Fall 2014

Effect of solid solutions and second phases on the thermal conductivity of zirconium diboride ceramics

Gregory John Kenneth Harrington

Department: Materials Science and Engineering

EFFECT OF SOLID SOLUTIONS AND SECOND PHASES ON THE THERMAL CONDUCTIVITY OF ZIRCONIUM DIBORIDE CERAMICS

by

GREGORY JOHN KENNETH HARRINGTON

A DISSERTATION

Presented to the Graduate Faculty of the

MISSOURI UNIVERSITY OF SCIENCE AND TECHNOLOGY

In Partial Fulfillment of the Requirements for the Degree

DOCTOR OF PHILOSOPHY

in

CERAMIC ENGINEERING

2014

Approved
Gregory E. Hilmas, Advisor
William G. Fahrenholtz
Wayne Huebner
Jeffrey D. Smith
George D. Waddill

PUBLICATION DISSERTATION OPTION

This dissertation consists of the following four articles that have either been submitted or will be submitted for publication as follows:

Pages 57-92 represent the manuscript titled “Effect of Carbon and Oxygen on the Densification and Microstructure of Hot Pressed Zirconium Diboride.” This manuscript was published in the *Journal of the American Ceramic Society* in volume 96, number 11 in 2013.

Pages 93-127 encompass the manuscript titled “Effect of Carbon on the Thermal and Electrical Transport Properties of Zirconium Diboride.” As of September 2014 this article was accepted for publication in the *Journal of the European Ceramic Society*.

Pages 128-151 are intended for submission to the *Journal of Testing and Evaluation* for publication following revisions based on the dissertation committee’s comments. The manuscript is titled “High Temperature Electrical Testing of Zirconium Diboride.”

Pages 152-184 contain the manuscript titled “Thermal Conductivity Modifications to $(Zr,W)B_2$ by ZrC Additions.” Submission of this document is intended for the *Journal of the European Ceramic Society* following revisions based on the input of the dissertation committee.

In addition to the four manuscripts presented within this dissertation, a fifth manuscript titled “Thermal Conductivity of the $(Zr,Hf)B_2$ Solid Solution System” is planned for publication in the *Journal of the American Ceramic Society*.

ABSTRACT

The research presented in this dissertation is focused on the thermal conductivity (k) of ZrB_2 ceramics. The goal was to develop a better understanding of how various solid solutions and second phases affect the thermal and electrical transport in ZrB_2, with a focus on the effect of C, W, and ZrC. The first study showed C additions improved densification and it was proposed that the reduction of boria was the impetus for this result. Boron carbide was formed by the reaction of excess C with reduced B and its formation was mitigated by the addition of ZrH_2. This allowed the ZrB_2-C binary system to be evaluated for study two. Study two showed the k of ZrB_2 is reduced by C in solid solution and as a second phase due to the decrease in the electron contribution to thermal conductivity. Conductivities of 99 (25°C) and 76 W/m·K (2000°C) were obtained for the most pure ZrB_2 (0.026 wt% C in solution and 0.2 vol% zirconia) produced in this study, which are the highest reported values for ZrB_2 processed using commercial powders since 1980.

The third study evaluated the electrical resistivity of ZrB_2 up to 1860°C using the van der Pauw technique. Separate linear regimes were observed below and above 950°C, whereas, previous studies assumed a linear relation. Finally the effect of ZrC on the $(Zr,W)B_2$ solid solution was evaluated in study four. The formation of (Zr,W)C initially increased k, but further ZrC additions resulted in decreased thermal conductivities.

In the end, this research provides both: (1) usable information for the design of future ultra-high temperature ceramic systems; and (2) fundamental research that lays the groundwork for future studies aimed at understanding thermal transport in diboride based materials.

ACKNOWLEDGMENTS

I would like to start off by thanking my advisor, Dr. Gregory Hilmas, for everything he has done for me and allowed me to do over the course of my time here at MST. Thanks to the opportunities he has provided, the experiences for me to learn have been wide ranging and in the end, priceless. Whether I've believed in my abilities, I know he has from the start and for me this was invaluable to my success. I would also like to thank my co-advisor, Dr. William Fahrenholtz, for his support and guidance, especially in honing my writing style (whether or not it shows). Drs. Brown-Shaklee, Thompson, and Watts are in my debt and I thank them for the tools (literally and figuratively) they provided, which got me on my feet and kept me going. I would also like to thank all of the other grad students from the UHTC group who have all been great friends and collaborators. The students who worked for me as undergrads also deserve thanks. Beyond the tedious lab work I hope you all got something out of it, as I know I learned a lot from the experience.

I would also like to thank the remainder of my committee: Drs. Jeff Smith, Wayne Huebner, and Dan Waddill. There is much more I could have learned from all of you, but I appreciate everything you provided me.

All of my research was funded by the National Science Foundation (DMR-0906584) and I thank all those who I don't know who made this a possibility.

I'd like to acknowledge some of the most influential people in my life. Without my sister, Emily; mom, Suzanne; dad, Greg; and stepmom, Marsha, I wouldn't be the person I am today, and for that I cannot thank them enough.

Last but not least I would like to dedicate this work to the two most important people in my life. One, my wife Heather followed me here and the other, our son Owen, showed up along the way. Heather, thank you for making me a better person, for supporting me no matter what, and most of all, for putting up with me. Owen, thank you for being so cute, smart, and inquisitive. You don't know it and may never realize it but you have taught me so much so far, you will continue to teach me, and I thank you for every moment.

TABLE OF CONTENTS

LIST OF ILLUSTRATIONS

Figure Page

LIST OF TABLES

1. INTRODUCTION

In large part, due to its high melting point (T_m) of ~3245°C[1], zirconium diboride (ZrB_2) is classified as an ultra-high temperature ceramic (UHTC) and its therefore of primary interest in high temperature structural ceramic applications.[2] However, in general ZrB_2 has been investigated for potential use in numerous high tech applications due to a broader set of thermal and mechanical properties. ZrB_2 has been shown to have good stability in contact with molten metals, making it a viable candidate for crucibles and submerged casting nozzles.[3,4] A high hardness of up to 23 GPa is a beneficial property for any use in high wear environments.[5] Similar to HfB_2, the ability to enrich the boron isotope concentration of ZrB_2 can enable its use in nuclear applications depending on the need for a low or high neutron absorption cross-section.[6,7] Low reported electrical resistivities for single crystal ZrB_2 (6.1 μΩ-cm for $[1\bar{1}00]$ and 7.2 μΩ-cm for [0001])[8] and the coincidence of a well matched lattice spacing and thermal expansion for ZrB_2 $(1\bar{1}00)$ with respect to the $(1\bar{1}00)$ of GaN have resulted in interest in ZrB_2 as an electronic substrate material.[9] Most importantly, the high T_m, moderate density (6.09 g/cm³)[3], and high flexure strengths (560±50 MPa at 25°C), especially at elevated temperatures (210±40 MPa at 2300°C)[10], make ZrB_2 a leading candidate for airfoil leading/trailing edge materials in hypersonic or atmospheric reentry vehicles and other propulsion engine components.[2,11-13]

The proposed design of these airfoil structures also makes the thermal conductivity an important property.[12,14] Specifically for the example of a leading edge, structures with a lower radius of curvature are intended to increase the maneuverability of vehicles in flight.[12,15] Combined with hypersonic speeds (>Mach 5), aero-frictional heating will cause leading edge temperatures to reach 2000°C or higher.[15,16] This heat

will be conducted away from the tip of the edge, through the bulk, to be re-radiated to the surroundings from the airfoil surface, behind the stagnation point of the hypersonic flow.[14,15] Therefore, the proposed design dictates that the material of choice have as high a thermal conductivity as possible.[12,14,16] In addition, higher thermal conductivities will decrease the possibility of thermal shock.[17] Other proposed high temperature applications dictate the need for lower thermal conductivities. Engine components may need to shield the airframe in situations where active cooling is limited.[16]

At the present, a large range of thermal conductivities are reported for ZrB_2. At room temperature, thermal conductivities vary from 133 W/m-K[18] down to 33 W/m-K[19]. At 2000°C this range narrows to between 55 [20] and 82 W/m-K[21]. From these reports and other published studies, some explanations are given for the observed variations. However, the majority of studies offer little to no insight into the range of results. Of the studies that do, few of them systematically investigate the changes in composition and microstructure that are associated with the resulting properties.

With the proposed needs in mind, and consideration to the established understanding with respect to the thermal conductivity of ZrB_2, this research looks to investigate the thermal conductivity of ZrB_2, particularly with respect to ZrB_2 processed using commercially available raw materials and the effect of common additives used to process ZrB_2-based ceramics. The work presented will focus on answering the following questions.

1. How do carbon and oxygen contents relate to the densification and resulting phase equilibria in the ZrB_2-C binary?
2. What is the effect of carbon (with specific emphasis on the ZrB_2+C solid solution) on the thermal conductivity of ZrB_2 and the electron/phonon contributions to k?
3. What is the achievable upper limit to the thermal conductivity of ZrB_2, produced from current commercial powders, when phase purity in the system is controlled?

In addition, how do these results compare to the examples from the literature and what is causing the differences?

4. Does the electrical resistivity of ZrB_2 change linearly from room temperature to 2000°C?
5. Can the $(Zr,W)B_2$ solid solution resulting from WC milling contamination be mitigated to produce ZrB_2 with increased thermal conductivities and improved microstructures?
6. Is the theoretical Lorenz number valid for ZrB_2 and how can it be evaluated experimentally?

Understanding what controls the thermal conductivity of ZrB_2 ceramics will enable the appropriate design of materials to fill its proposed applications. This research is intended to expand upon this understanding by relating the chemistry and phase equilibria of ZrB_2 to the resulting thermal conductivities and related properties.

2. LITERATURE REVIEW

This section is a review of the literature with regard to subjects pertaining to the articles in sections 3 through 7. The phase equilibria of ZrB_2 and ZrB_2 with C, ZrC, and B_4C are discussed first. Next an overview of the crystal structure and bonding is presented. The densification behavior is then discussed. Finally the properties and testing of thermal conductivity and electrical resistivity are reviewed.

2.1. ZrB_2 PHASE EQUILIBRIA

Zirconium and boron form the stable borides of ZrB_2 and ZrB_{12} (see Figure 2.1)[1], while some studies also report the existence of a ZrB phase[22,23]. ZrB_2 is the only congruent melting compound in this system. Its melting temperature is reported to be near 3245°C[1], with other reports centered on this value[22-24]. As indicated by the Zr-B phase diagram, the stoichiometry of ZrB_2 varies at most by 1 to 2 at% from the ideal 33 at% Zr/66 at% B.

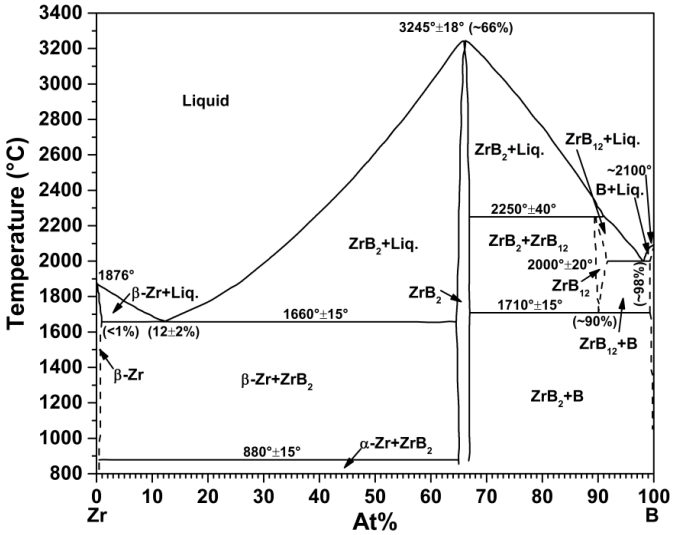

Figure 2.1. The Zr-B phase diagram featuring ZrB_2 (redrawn from Rudy and Windisch).[1]

ZrB_2 does not form in nature and instead is synthesized under inert conditions through various reactions involving Zr, B, or compounds thereof, typically oxides. Some of the possible routines for forming zirconium diboride are by the direct reaction of Zr and B[3,25,26] (reaction(1)), borothermal reduction[27,28] (reaction (2)), carbothermal reduction[3,29-31] (reaction (3)), boro-carbothermal reduction[32-34] (reaction (4)), reduction with boron carbide[33] (reaction (5)), and electrolysis[3] (reaction(6)).

$$Zr(s) + 2B(s) \rightarrow ZrB_2(s) \quad (1)$$

$$3ZrO_2(s) + 10B(s) \rightarrow 3ZrB_2(s) + 2B_2O_3(g) \quad (2)$$

$$ZrO_2(s) + B_2O_3(l) + 5C(s) \rightarrow ZrB_2(s) + 5CO(g) \quad (3)$$

$$2ZrO_2(s) + B_4C(s) + 3C(s) \rightarrow 2ZrB_2(s) + 4CO(g) \quad (4)$$

$$7ZrO_2(s) + 5B_4C(s) \rightarrow 7ZrB_2(s) + 3B_2O_3(g) + 5CO(g) \quad (5)$$

$$2ZrO_2(s) + 2B_2O_3 \rightarrow 2ZrB_2(s) + 5O_2(g) \quad (6)$$

Reactions (3) and (4) are most commonly used for the commercial production of ZrB_2.[35,36] These reactions are typically performed at upwards of 2000°C to facilitate a complete reduction of the oxides and to drive off excess boria.[29,37] Due to the use of free carbon or boron carbide in the synthesis of ZrB_2, commercial powders typically have carbon contents ranging from 0.25 to 1.5 wt%.[38-41]

The starting zirconia in these reactions typically comes from naturally occurring zircon or white baddeleyite.[42] Unfortunately, these minerals contain from 1% to 3% hafnium.[42] Due to the related chemical characteristics of Zr and Hf, difficult and expensive solvent extraction processes are necessary to isolate the two elements.[42] The

absorption cross-section for thermal neutrons is ~560 times higher for Hf (104.1 b for natural isotope abundance) than it is for naturally occurring Zr (0.185 b for natural isotope abundance)[43], making purified Zr beneficial for the nuclear industry.[42] However, with this exception, most Zr sources used in the commercial production of ZrB_2 contain Hf. Hf forms a diboride just like ZrB_2 and they are completely miscible[44] due to the similar metal radii for Zr (1.61 Å) and Hf (1.58 Å) within the same preferred AlB_2 prototype structure (see next section).[2] Therefore, commercial ZrB_2 powders are actually a $(Zr,Hf)B_2$ solid solution which depends on the purity of the starting materials. Some of the effects of this solid solution on the microstructure, thermal properties and electrical properties will be discussed in the following sections.

In addition to the solid solution with HfB_2, ZrB_2 also has ranges of solid solubility with other boride forming transition metals. Post et al. indicate ZrB_2 forms complete solid solutions with diborides of: Ti, Nb, Ta, and Mo due to the presence of only one set of peaks from XRD studies.[45] In the same study, both VB_2 and CrB_2 are shown to only be soluble up to 5 mol%. This was explained in terms of the different metal ions having, as a rule, >15% difference in their radii; where V is 16% and Cr is 17% smaller than Zr.[45] Some of these results differ with those by Otani et al.[44], while others were confirmed. TiB_2, NbB_2, and TaB_2 are instead shown to have solid solution limits of 24, 10 and 8 mol% in ZrB_2, respectively. Despite the presence of one set of peaks, Otani observed broadening of the peaks past these concentrations. The limited solubility of VB_2 (<3 mol%) and CrB_2 (<1 mol%) are confirmed but are reported to be lower in concentration.[44] Also of note is the $(Zr,W)B_2$ solid solution. Tungsten is reported to be soluble between 11 and 17 wt% (2.6 to 4.3 mol%). Once beyond the solid solution limit and in the presence of carbon W pulls B from the ZrB_2 forming WB and the free Zr reacts to form ZrC.[46] As with the solid solution of Hf, the role of other solid solutions with ZrB_2 will be elaborated on further.

2.1.1. ZrB_2 with C, B_4C, and ZrC. As shown in Figure 2.2, ZrB_2 forms a simple binary eutectic with C[47] (a), B_4C[48] (b), and ZrC[49] (c).

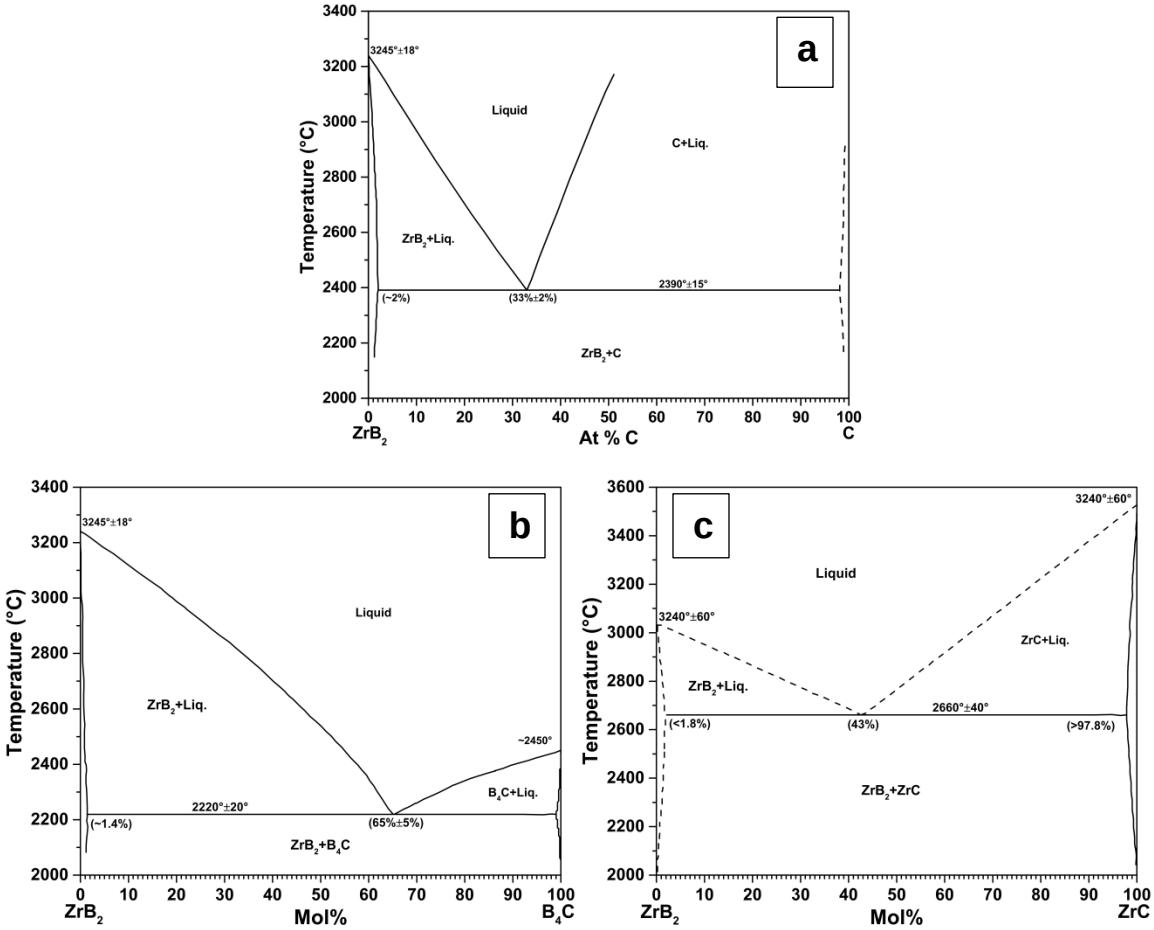

Figure 2.2. Binary phase diagrams of (a) ZrB_2-C, (b) ZrB_2-B_4C, and (c) ZrB_2-ZrC. (reproduced from work by Rudy and Winisch (C[47] and B_4C[48] and Ordan'yan and Unrod (ZrC[49])).

These phases are often added to ZrB_2 for reasons based on their compatibility as sintering aids and as secondary reinforcing phases. The solid solution limits are all low (~2 mol% C, ~1.4 mol% B_4C, and <1.8 mol% ZrC), even at the highest concentration near the eutectic. Therefore, minimal material is consumed allowing for second phases

to be readily formed. Eutectic temperatures of ZrB_2 with C (2390°C), B_4C (2220°C), and ZrC (2660°C) make all of these compositions high temperature materials, but depending on the concentration they may fail to be considered UHTCs.

2.1.1.1. Analysis of C and B_4C in ZrB_2. Detection of second phases of C and B_4C in ZrB_2 is difficult using energy dispersive spectroscopy (EDS) and X-ray diffraction (XRD); and these phases are often indistinguishable from each other by SEM. The signal intensity of each of these techniques is highly dependent on the number of electrons per atom which is related to the atomic number for elements (Z) or average atomic number ($\bar{Z}$) for compounds.[50,51] Carbon (Z=6) and B_4C ($\bar{Z}$=5.2) are similar but much lower compared ZrB_2 ($\bar{Z}$=16.7). One analysis technique which resolves these phases is confocal Raman spectroscopy. In the case of Raman, ZrB_2 can be regarded as "invisible", while C and B_4C are both Raman active and have characteristic peaks related to their structure and bonding.

2.1.1.1.1. Raman spectroscopy. Raman spectroscopy uses a source of monochromatic photons, usually a laser, to excite a given amorphous or crystalline solid.[52,53] Any resulting shift in frequency (i.e. change in energy, up or down) of a reemitted photon from that of the incident photons is a result of a molecule shifting into a different energy state due to inelastic scattering.[54,55] For the Raman processes, these states correspond to vibrational, rotational, or electronic levels.[55] Therefore, the resulting Raman pattern is specific to the bonding within a material. Substances are only Raman active if the molecular polarization potential changes, which is related to the deformation of the "electron cloud".[54] This change requires localized electrons.[55] As a result, materials with metallic bonding (i.e. ZrB_2) are not Raman active. This is beneficial when analyzing Raman active second phases within ZrB_2, as its presence is naturally excluded from the resulting spectra.

2.1.1.1.2. <u>Raman spectroscopy of boron carbide.</u> Boron carbides have been heavily studied via Raman spectroscopy to understand the bonding and distribution of carbon within the structure.[56] Boron carbide exhibits a large homogeneity range, from carbon rich $B_{4.3}C$ to boron rich $B_{\sim 11}C$.[57] The structural elements of B_{12} and $B_{11}C$ icosahedra; and C-B-C, C-B-B, and B□B (□; vacancies) chains vary throughout this range.[56,58] This results in observable changes in the Raman spectra as a function of carbon content (see Figure 2.3).[59] In Figure 2.3, the loss of narrow peaks near 500 cm^{-1} as carbon content decreased was related to the loss of C-B-C chains.

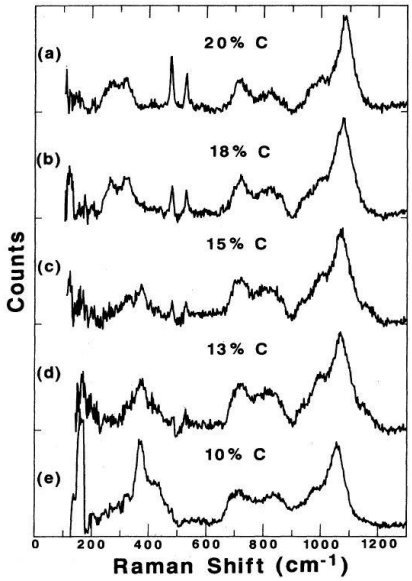

Figure 2.3. Raman spectra reported by Tallant et al. for boron carbides with carbon contents ranging from 10 to 20 at%.[59]

These chains were replaced by C-B-B chains as indicated by the increase in broad bands near 400 cm^{-1}. The remaining broad bands >600 cm^{-1} are due to icosahedral modes and these show little dependence on carbon content compared with the chains.[59] Thanks to research correlating Raman spectra to the stoichiometry of boron carbide, the

composition of boron carbide in a given system can be interpreted. In particular for diboride systems, Brown-Shaklee et al.[60] has reported the use of Raman spectroscopy in identifying boron carbide within HfB_2 which should be analogous to its use with ZrB_2 systems.

2.1.1.1.3. <u>Raman spectroscopy of carbon.</u> Like boron carbide, the various forms of carbon (i.e. amorphous, graphitic, diamond, nanotubes, Fullerenes, etc.) are Raman active (see Figure 2.4) and the spectra are related to the structure/bonding of each given form.[52]

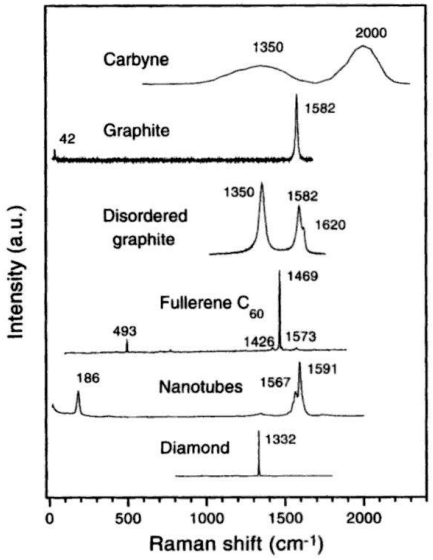

Figure 2.4. Representative Raman spectra for various forms of carbon.[52]

The presence of second phase carbon in ZrB_2 with carbon additions is reported by Thompson et al.[61] The reported Raman spectra are shown in Figure 2.5.

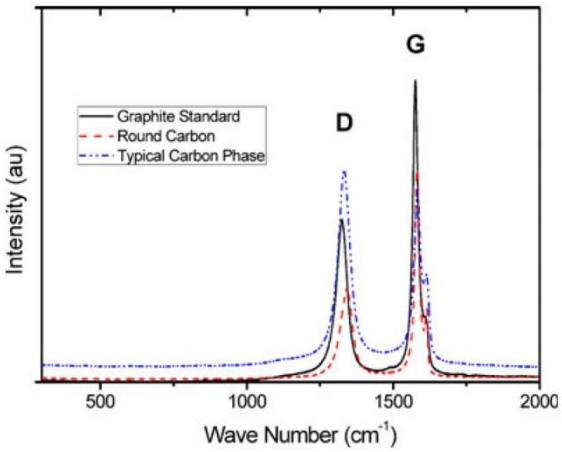

Figure 2.5. Experimental Raman spectra from disordered graphite formed at ZrB_2 grain boundaries as discussed by Thompson et al.[61]

Carbon within these materials was concluded to be a form of disordered graphite based on the studies by Ferrari et al.[62] and Antunes et al.[63] The D (diamond) peak typically located near 1350 cm^{-1} is related to sp^3 bonding and the G (graphite) peak near 1580 cm^{-1} is related to sp^2 bonding.[52,63] In addition, a shoulder off of the G peak representing the D' peak is often found near 1620 cm^{-1}.[63] The relative intensity between the D and G peaks (I_D/I_G) was correlated to the disorder of the graphitic carbon structure.[62,63] In this case, the disorder was linked to an increase in this ratio. It is important to note that the disorder is related to the size of the graphitic domains, where increased disorder relates to smaller domains or crystallite dimensions.[52,62] However, this analysis is only a first approach, as other factors such as the structural arrangement (i.e. probing the edge of graphite layers vs. the faces) may correlate to differences in the I_D/I_G ratio.[63] Regardless, Raman of C, like that of boron carbide, has been shown to be effective for phase identification and understanding the nature of the second phase within a diboride matrix.

2.2. ZrB_2 CRYSTAL STRUCTURE AND BONDING

AlB_2 is the prototype structure for ZrB_2, as with the other diborides, and the space group symmetry for this structure is P6/mmm.[64-66] One ZrB_2 formula unit makes up the unit cell.[64,65] The lattice is made up of equally spaced alternating layers of close packed hexagonal Zr atoms and graphite like hexagonal boron rings (see Figure 2.6).[64-66] As viewed perpendicular to the planes, each Zr atom is centered with respect to the boron hexagons.[64,67] Therefore, each Zr has 12 nearest B neighbors along with 6 nearest in-plane Zr. The position of a B atom at the junction of three separate hexagons results in 3 nearest neighbor B atoms for each B. Each B is also adjacent to 6 nearest neighbor Zr atoms (3 from both surrounding planes).[64]

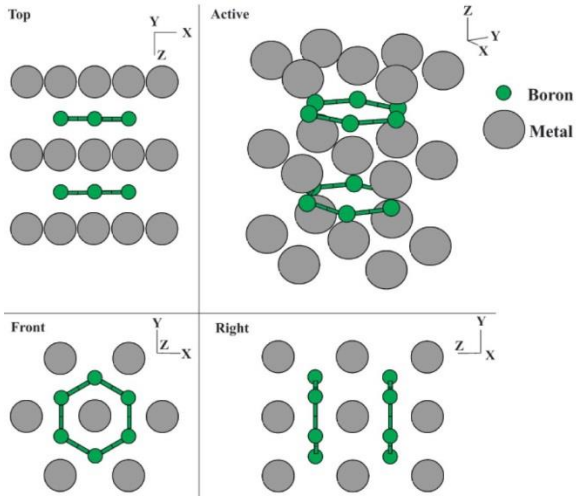

Figure 2.6. Representative views of the hexagonal AlB_2 structure. The pictures were taken from the Crystal Lattice Structures Web page thanks to the Center for Computational Materials Science of the United States Naval Research Laboratory.

Due to this crystal structure, many of the intrinsic properties of ZrB_2 (i.e. elastic properties, thermal expansion, thermal conductivity, electrical resistivity, lattice parameters, etc.) are anisotropic. Vajeeston et al. report experimental lattice parameters

of a=b=3.170 Å and c=3.533 Å.[64] Using equations (7) and (8) a theoretical density of 6.095 g/cm³ can be calculated for ZrB_2 from these lattice parameters, using the interaxial angles (hexagonal α=β=90° and γ=120°), molecular weights (M for Zr and B), number of atoms per unit cell (Z; 2 B and 1 Zr), and Avogadro's number (N_0=6.022*10^{23}).[68]

$$\rho = \frac{MZ}{N_0 V} = \frac{M_{Zr}Z_{Zr} + M_B Z_B}{N_0 V} \tag{7}$$

$$V = abc\left(1 - \cos^2\alpha - \cos^2\beta - \cos^2\gamma\right) \tag{8}$$

As mentioned in section 2.1 the presence of Hf in the structure can have an effect on various properties and density is no exception. Neuman et al. performed a similar calculation but accounted for the 1.9 wt% Hf content of the ZrB_2 used in the study. As a result of the Hf a theoretical density of 6.15 g/cm³ was reported.[10] This is one example where the presence of solid solutions should not be ignored.

The nature of the B-B, Zr-Zr, and Zr-B bonds has been studied by numerous researchers, typically through modeling of the density of states (DOS).[64,69-71] Despite some conflicting conclusions, it is generally established that the B-B bonds are covalent, the Zr-Zr bonding is metallic, and the Zr-B bonds are primarily ionic.[64,66,71] Some covalent nature has also been attributed to the Zr-B and Zr-Zr bonds but this conclusion is not universal.[64] In ZrB_2 there are 10 valence electrons per unit cell[66,71] which leads to an average of 3.33 electrons/atom (e^-/a)[64] without any donation of electrons associated with the ionic bonding. Due to the ionic nature of the Zr-B bonds, electrons are donated from the Zr atoms to the B.[64,66] Lawson et al. reports the charge transfer to be 2.57 e^-/a for Zr and 3.72 e^-/a for B.[71] Regardless of the electron distribution, Vajeeston et al. explains the importance of the average 3.33 e^-/a based on the density of states.[64] As seen in

Figure 2.7, the Fermi level (E_f) falls near the minima of the DOS for ZrB_2 (which is also true for TiB_2 and HfB_2).[64,66]

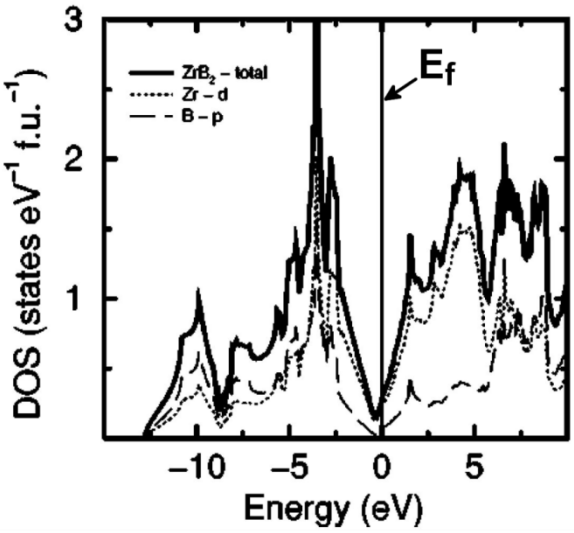

Figure 2.7. The site projected and total density of states (DOS) for ZrB_2 as reported by Vajeeston, where the Fermi level (E_f) can be seen to lie at the minima in the DOS curve.[64]

This indicates all of the bonding states are filled without any electrons occupying anti-bonding states for the group IVB transition metals diborides. A shift to the left of group IVB results in a shift of E_f to the left of the DOS minimum and an emptying of the bonding states. On the other hand, diborides composed of transition metals to the right of group IVB have an E_f to the right of the minima in the DOS which is related to the filling of anti-bonding states. Either shift in the filled states results in a decrease in the cohesive properties of the diborides from those composed of group IVB transition metals.[64,66] Therefore, important characteristics of ZrB_2, like its high melting temperature and high achievable hardness, are a direct consequence of the complete filling of bonding states by the valence electrons.

2.3. DENSIFICATION

As a structural ceramic, densification of ZrB_2 is critical for optimizing its most important properties, i.e. strength, modulus, oxidation resistance, thermal conductivity, and electrical conductivity. The sintering of ZrB_2 is limited by a large activation energy (678±114 kJ/mol) due to the aforementioned strong covalent and/or ionic bonding between the B and Zr/B atoms.[72] Therefore researchers have investigated the use of various sintering methods and aids for improving the densification of ZrB_2.

2.3.1. Sintering Methods. Nominally pure as-received ZrB_2, densified via pressureless sintering (PS) has only achieved densities as high as 78% of theoretical when held for 2 hr at 2100°C.[73] Multiple techniques have been used to improve the densification of ZrB_2 beyond this level. Additive assisted PS and pressure assisted densification (i.e. hot pressing (HP) and spark plasma sintering (SPS)) improve sintering by increasing the driving force for densification mechanisms, which are in competition with coarsening mechanisms.[74] Near full density (>98%) has been reported for pure ZrB_2 hot pressed at 2250°C under 36 MPa for 30 min.[75]

2.3.2. Particle Size Reduction. Improvements in densification are also realized by increasing the free energy of the system, through reductions in particle size. Thompson et al. has shown this effect on ZrB_2 (with added carbon) via PS (1900°C), HP (1900°C) and SPS (2000°C). Powder with an average particle size of 2 µm resulted in densities of 86%, 89%, and 85% for each respective process and 0.2 µm powder reached 97%, 99%, and >99%, respectively.[76] Self-propagating high-temperature synthesis (SHS) reactions have also been used to produce powders with reduced particle sizes (on the order of nanometers). Pressureless densification of these powders at 1800°C resulted in 93% dense ZrB_2.[31]

2.3.3. Sintering Aids. Densification of ZrB_2 can be improved by additions of various sintering aids. Carbon and carbides are often used due to their compatibility with diboride systems. The different additives will be discussed separately based on their role in facilitating densification.

2.3.3.1. Reactive additives. Displacement reaction additions (carbon, carbides, or boron) are beneficial thanks to their ability to remove Zr and B surface oxides from ZrB_2 powders. Dole et al. concluded that eliminating B_2O_3 reduced vapor phase assisted coarsening in B_4C[77], which should be analogous to ZrB_2. Evaporation-condensation mechanisms have also been shown to take place at higher temperatures due to the metal oxide, as in the case of TiB_2.[78] Therefore, densification is improved by preventing surface diffusion which contributes to coarsening at temperatures below where the diboride begins to densify.

Similar to their use in reducing oxides to produce ZrB_2, B_4C and C are predicted to remove ZrO_2 and/or B_2O_3 surface oxides via reactions (3), (4), (5), and (9) (see Table 2.1). The reaction which only involves ZrO_2 (reaction(9)) assumes that B_2O_3 has left the system through vaporization. As gaseous species are produced in each reaction, the favorability increases as the pressure of the system is decreased. This leads to reduced reaction temperatures under vacuum. Numerous researchers have evaluated the use of these reactions in improving the densification of pure ZrB_2 by performing vacuum assisted reaction holds, at or above temperatures specific to the desired reaction.[73,76,79-81] Zhang et al. reported a maximum density of 98% for PS ZrB_2 with 4 wt% B_4C (2000°C for 2 hr).[81] Similar results for an addition of 1 wt% C (96% dense at 2100°C) are detailed by Fahrenholtz et al.[73] A combination of 2 wt% B_4C and 1 wt% C was determined to be even more effective than the individual additives, resulting in >99% relative density at 1900°C.[80] Thompson et al. densified attrition milled ZrB_2 with 0, 1, and 3 wt% carbon, added in the form of phenolic resin. The 0% carbon material reached >99% relative

density in 35 min at 1900°C by HP and the densification time was reduced to 10 min with an addition of 1 wt% carbon.[61] It should be noted that, besides the reduction of oxides facilitated by the added carbon, densification for all the compositions was also attributed to reduced particle sizes and WC contamination.

Table 2.1. Oxide Removal Reactions Associated with the Densification of ZrB_2, Involving C and B_4C in Addition to the Evaporation of B_2O_3.

Rxn. #	Reaction Equation	Reaction Temperature	
		1 ATM	Vacuum
(3)	$ZrO_2 + B_2O_{3(g)} + 5C \rightarrow ZrB_2 + 5CO_{(g)}$	1140°C[73]	1044°C (25 Pa)[80]
(4)	$2ZrO_2 + B_4C + 3C \rightarrow 2ZrB_2 + 4CO_{(g)}$	1440°C[73]	1000°C (25 Pa)[80]
(5)	$7ZrO_2 + 5B_4C \rightarrow 7ZrB_2 + 3B_2O_3 + 5CO_{(g)}$	1219°C[73]	928°C (25 Pa)[80]
(9)	$ZrO_2 + 3C \rightarrow ZrC + 2CO_{(g)}$	-	1166°C (13 Pa) [82]
(10)	$B_2O_{3(l)} \rightarrow B_2O_{3(g)}$	2060°C[81]	1340°C (150 mTorr)[81]

2.3.3.2. ZrC and WC additions. The effect of the carbides of W and Zr have been studied in terms of their role as second phases within ZrB_2. Reports of the benefit of ZrC vary, but for the most part the conclusion is that ZrC reduces coarsening by pinning grain growth, allowing the free energy of the system to be reduced by sintering mechanisms. Kats et al. used PS to produce ZrB_2 and ZrB_2+ZrC at 2100°C and showed that 20 wt% ZrC was effective in reducing the porosity to 2.9% compared to 10.6% for ZrB_2 alone. There was little benefit to further additions of ZrC as porosity was only reduced by 0.6% (45 wt% ZrC) and 1.1% (51 wt% ZrC) from that of the 20% addition.[83] Similar results were observed by Gropyanov et al. who studied the PS of ZrB_2, ZrB_2+10wt% ZrC, and ZrB_2+50wt% ZrC.[84] Densification was only improved from ~96% to ~99.5% at 1900°C with the 10% addition[84] but the benefit of the ZrC may not be as apparent due to the improved densification of the ZrB_2 from that of Kats. Gropyanov reported no additional improvement in densification for the 50% ZrC composition. This

was also evident in the reported activation energies for densification. The 10% material dropped to 126.8±2.1 kJ/mol from 184.1±2.1 kJ/mol for the ZrB_2, but the activation energy for the 50% material (132.6±2.9 kJ/mol) was essentially the same as the 10%.[84] The benefit of ZrC as a sintering aid is less evident in the work by Fridlender et al. Densification of pure ZrB_2 (89% of theoretical) was only increased to 93% with the addition of 20% ZrC but was improved to 98% with another 20% of ZrC.[20] The densification of ZrB_2+ZrC is also reported for HP and SPS processing. Neuman et al. was successful in producing >99.9% dense ZrB_2 with 10 vol% ZrC by hot pressing under 32 MPa at 1900°C[85] and Tsuchida et al. was able to densify ZrB_2+20vol% ZrC to 97.5% of theoretical with SPS at 1800°C and 40 MPa.[86] All of these studies do indicate the benefit of ZrC additions in producing dense ZrB_2 ceramics, and based on Figure 2.2 the ZrB_2+ZrC system could be beneficial over others due to its eutectic of ~2660°C.

Reports of the benefit of WC as a sintering aid have mixed results. The presence of WC in ZrB_2 ceramics is often associated with contamination resulting from milling with WC media (typically bonded with 6% Co).[5,73,76,79,80,87-89] Chamberlain et al.[88], Fahrenholtz et al.[73], and Zhang et al.[81] discuss the benefits of WC in reducing oxide impurities, similar to that discussed above for C and B_4C additions. However, a systematic study of the effect of WC, Co, and WC/Co by Choi et al. indicates that densification is influenced more by Co than WC.[90] Choi reports the use of SPS at 1600°C under 60 MPa densified ZrB_2 to ~87% of theoretical. Additions of 0.1 to 1 wt% Co resulted in densities >99% but the relative density with added WC (5, 10 and 15%) steadily decreased compared to the additive free ZrB_2. In addition, ZrB_2 compositions with 5, 10, and 15% WC-6%Co only densified to between 95 and 96% under the same conditions. Co was concluded to improve densification through liquid phase sintering while WC had a negative impact through the introduction of WO_3 and WB which were credited with disturbing the mass transfer between ZrB_2.[90] Similar to the use of Co, 4%

Ni was shown by Bellosi and Monteverde to enable ZrB_2 to be hot pressed to 98% of theoretical at 1850°C, compared with pure ZrB_2 in the same study which only reached 87% when hot pressed at 1870°C.[91]

2.4. THERMAL AND ELECTRICAL TRANSPORT

The metallic bonding in ZrB_2 gives it characteristics like a metal, due to the presence of free electrons, allowing ZrB_2 to conduct electricity under the driving force of an electric field. More importantly for the current research, ZrB_2 will conduct heat via the same free electrons in the presence of a thermal gradient.[92] Whereas a net flow of electrons is established under an applied electric field, electrons as thermal conductors have no net flux. Instead, electrons gain energy in proportion to the temperature of the region where they experience a collision.[92] Their random motion ensures heat will be transported under a thermal gradient. The net charge in the material is maintained as carriers of the same charge, but having lower energy on average, replace higher energy electrons. Despite the differences in the transport of heat and electricity, the electrons involved are ultimately governed by similar phenomena. Therefore, the properties of electrical resistivity (ρ_e) and electron thermal conductivity (k_e) associated with these processes go hand in hand. In addition to transport by electrons, heat within ZrB_2 is also carried by phonons and is characterized by the phonon thermal conductivity (k_p). The summation of k_e and k_e, by equation (11), is equal to the total thermal conductivity (k).[93]

$$k = k_e + k_p \tag{11}$$

Equation (11) and the interrelation between k_e and ρ_e establish the need to study ρ_e, k_e, and k_p to understand k. This section will first look at the theoretical basis for these phenomena. With this established, published properties of ZrB_2 will be reviewed with an

emphasis on factors controlling thermal conductivity. Along the way, the evaluation and testing required to obtain k and ρ_e, and eventually k_e and k_p from these properties, will be discussed.

2.4.1. Electrical and Thermal Transport by Electrons. The relationship between the electrical resistivity of a material and the electron thermal conductivity is called the Wiedemann-Franz law and is displayed as equation (12).[93]

$$k_e = \frac{L_o T}{\rho_e} \tag{12}$$

The Wiedemann-Franz law states that at a given temperature k_e is inversely proportional to ρ_e. The term L_o is the proportionality constant between the two properties referred to as the Lorenz number.[93] Drude initially calculated the theoretical value for L_o using what is now called the Drude model.[94] This work made assumptions, such as treating the electrons as a "gas of electrons" using the kinetic theory of gasses.[92] Although flawed, Drude's calculations were close to the currently accepted theory, as a result of the two short comings of his theory offsetting. The magnitude in the mean square electron speed and the electronic heat capacity were each off by nearly two orders of magnitude. Fortunately, for the calculation of L_o these errors nearly canceled one another.[92,93] Eventually Fermi-Dirac statistics were used by Sommerfeld to recalculate L_o (equation (13); often called the Sommerfeld value due to his contribution) and this treatment corrected the issues of Drude's model by properly accounting for the mean square electron speed and the electron heat capacity.[93,94]

$$L_o = \frac{\pi^2}{3}\left(\frac{k_B}{e}\right)^2 = 2.44x10^{-8}\Omega \cdot W \cdot K^{-2} \tag{13}$$

This relationship only holds true if the relaxation times for ρ_e and k_e are identical.[92,93] As more aspects of the theory are presented, the bases for this limitation, and where it remains valid or fails, will be covered.

It is necessary to discuss the scattering mechanisms which prevent electrons from traveling unimpeded through a periodic lattice, in order to understand what controls ρ_e and k_e in metallic conductors. Matthiessen's rule (equation (14)) is typically used to account for the overall ρ_e of a material with multiple distinct scattering mechanisms. In the case of equation (14), the possible mechanisms of electron-phonon scattering ($\rho_{e\text{-}p}$), scattering from imperfections (ρ_{imp}), and electron-electron scattering ($\rho_{e\text{-}e}$), are presented[95], and each will be discussed in detail.

$$\rho_e = \rho_{e-p} + \rho_{imp} + \rho_{e-e} \tag{14}$$

These resistivity terms can be represented by equation (15) which is the standard relationship for resistivity:

$$\rho = \frac{m\bar{v}}{ne^2\ell_e} \tag{15}$$

where n is the number of electrons per volume, e is the electron charge, m is the effective mass of an electron, $\bar{v}$ is the mean electron velocity, and ℓ_e is the mean free path between collisions.[93,96] The mean free path and the mean electron velocity are related to the relaxation time (τ) by equation (16), therefore, equation (15) can also be represented as equation (17).[93]

$$\tau = \frac{\ell_e}{\bar{\nu}} \tag{16}$$

$$\rho = \frac{m}{ne^2\tau} \tag{17}$$

The common treatment of these equations in the literature with respect to the relaxation time approximation then leads to equation (18), where each resistivity in equation (14) is represented in terms of an individual τ.[93,95]

$$\frac{1}{\tau_e} = \frac{1}{\tau_{e-p}} + \frac{1}{\tau_{imp}} + \frac{1}{\tau_{e-e}} \tag{18}$$

Therefore, as the discussion of electron scattering continues, the relaxation time will remain an important factor.

It should be noted that there are instances where Matthiessen's rule breaks down when an interdependency exists between the components. Positive deviations from Matthiessen's rule have been shown for changes in alloying impurities. In this case, the function of $\rho_{e\text{-}p}$ with respect to temperature increased proportionally to ρ_{imp}. A negative deviation is reported for cases of deformation induced strain. The strain increased ρ_{imp} but caused a decrease in $\rho_{e\text{-}p}$.[93]

Now that the possible scattering mechanisms have been introduced, along with a basic equation for resistivity, the role of each mechanism can be discussed.

2.4.1.1. Electron-phonon scattering. For a perfect, periodic lattice, the wave nature of electrons dictates there would be no resistance to their motion.[93] Phonons are elastic waves of the atomic nuclei within the lattice. Their motion creates deviations in the lattice periodicity which can scatter electrons.[97] The magnitude of these waves is a function of increasing temperature which leads to increases in scattering. This

dependence on temperature is important when looking back at Matthiessen's rule as neither ρ_{imp} nor $\rho_{e\text{-}e}$ has an intrinsic temperature dependency.[93]

The temperature dependence of $\rho_{e\text{-}p}$ has been derived for the limiting cases of high (equation (19)) and low (equation (20)) temperatures. The constant A is dependent upon: Planck's constant, the effective electron mass, the speed of sound in a given medium, the electron density, the charge on an electron, the lattice parameter, the ion mass, the Debye temperature, and the Fermi energy.[93]

$$\rho_{e-p}(T) = \frac{A}{4}\frac{T}{\Theta_D}, for\left(T \geq \Theta_D\right) \tag{19}$$

$$\rho_{e-p}(T) = 124.4A\left(\frac{T}{\Theta_D}\right)^5, for\left(T \ll \Theta_D\right) \tag{20}$$

These equations indicate that at high temperatures $\rho_{e\text{-}p}$ should increase linearly with temperature. As temperature decreases well below the Debye temperature, $\rho_{e\text{-}p}$ precipitously drops off as a function of T^5. At low temperatures (below Debye) $\rho_{e\text{-}p}$ typically becomes insignificant compared with ρ_{imp}. However at high temperatures (above Debye) when no deviations to Matthiessen's rule exist $\rho_{e\text{-}p}$ is significant and leads to the common result of linear electrical resistivities as a function of temperature.[93]

Similar solutions for the temperature dependence of thermal transport have been made for the same limiting temperature conditions (equations (21) and (22)). In these equations the electron-phonon controlled thermal resistivity ($W_{e\text{-}p}$; where $W = k^{-1}$) was used as the thermal analogue to ρ_e.[93]

$$W_{e-p}\left(T\right) = \frac{\rho_{e-p}\left(H.T.\right)}{L_o T}, for\left(T \geq \Theta_D\right) \tag{21}$$

$$W_{e-p}(T) = \frac{A}{L_o \Theta_D}\left(\frac{k_F}{q_D}\right)^2 \left(\frac{T}{\Theta_D}\right)^2, for\left(T \ll \Theta_D\right) \quad (22)$$

At high temperatures these results indicate conductivity should be independent of temperature and this is shown in Figure 2.8 for four different types of metals (Cu, K, Ni, and Gd).[93] Thermal conductivity should increase as a function of T^2 at low temperatures and this is represented in Figure 2.8 by the rapid initial rise in k, especially for Cu.[93]

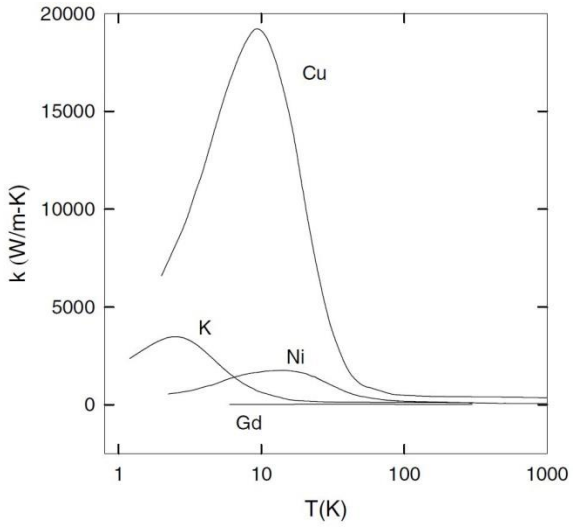

Figure 2.8. Thermal conductivity as a function of log temperature of Cu, K, Ni, and Gd showing the temperature dependence for metallic conductors.[93]

The following Lorenz ratios are derived (equations (23) and (24)) when the starting formulae, from which equations (19) and (20), along with (21) and (22) are obtained, are combined using the Wiedemann-Franz law, and again solved at low and high temperatures.[93]

$$\frac{L}{L_o} = 1, for\left(T \geq \Theta_D\right) \tag{23}$$

$$\frac{L}{L_o} \cong \frac{\pi^2}{3}\left(\frac{q_D}{k_F}\right)^2\left(\frac{T}{\Theta_D}\right)^2, for\left(T \ll \Theta_D\right) \tag{24}$$

From this, the theory dictates that the Lorenz number reaches the Sommerfeld value ($L=L_o$) at high temperatures due to the equalization of the relaxation times between the electrical resistivity and thermal conductivity.[92,93] This is due to high temperature phonons being energetic enough to effectively scatter electrons through large angles (elastic process) regardless of its conduction nature (i.e. thermal or electrical).[93] The low temperature result indicates that, as temperature decreases, the Lorenz number also decreases. Therefore, the Wiedemann-Franz law should deviate at lower temperatures due to a decrease in the relaxation time for thermal conduction (or mean free path) as indicated by equation (25) (subscripts denote thermal or electrical conduction).[93,94]

$$L = L_o \frac{\tau_T \bar{\upsilon}_T}{\tau_E \bar{\upsilon}_E} = L_o \frac{\ell_T}{\ell_E} \tag{25}$$

The result of equation (24) is related to the lower energy of the phonons at lower temperatures. Electrically conducted electrons cannot be scattered through large angles by these phonons.[94] However, thermal conducting electrons have another process by which they can more effectively decrease their energy via an inelastic route, and any inelastic scattering of electrons will result in deviations from the Wiedemann-Franz law.[92,93] Both the high and low temperature theoretical results for equations (23) and (24) are displayed in Figure 2.9 for the $\rho_{imp}/A = 0$ curve. This $\rho_{imp}/A = 0$ curve is for the result

with no impurities and therefore is not representative of real materials. As will be discussed in the next section, impurities play a significant role at low temperatures.

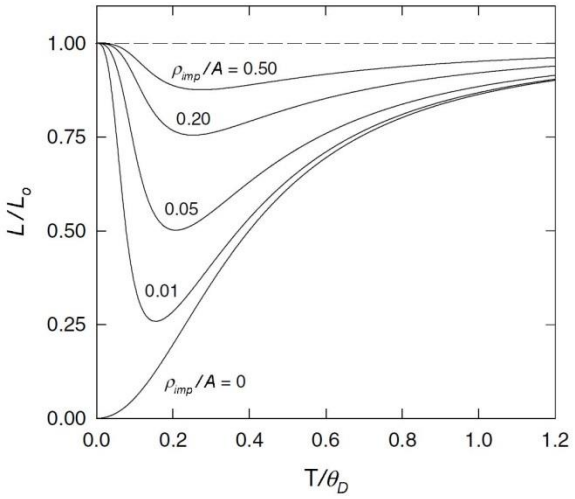

Figure 2.9. L/L_o plotted as a function of temperature normalized by the Debye temperature. Also included is the effect of impurities where the fractional concentration is varied from 0 to 0.5.[93]

2.4.1.2. Imperfection induced scattering. As mentioned before, scattering of electrons can result from inhomogeneities in the lattice. Imperfections are static deviations in the crystal that can come from grain boundaries, dislocations, impurities (solid solutions), vacancies, etc.[93,95] Inherently, in a material the effect of these features on electron conduction are typically invariant with temperature. Based on the Wiedemann-Franz law, the contribution from the imperfections to the electron thermal conductivity is then a linear function with temperature.[93]

The effect of imperfections is more significant at low temperatures where e-p scattering decreases significantly.[95] In most cases, impurities cannot absorb or return energy to an electron, making them responsible for only elastic scattering.[93] This leads to any given imperfection affecting the electrical and thermal processes identically.

Therefore at lower temperatures, as e-p scattering becomes less significant the inelastic scattering they induce decreases. As a result the Lorenz ratio typically begins to increase as temperature decreases, resulting in a return of the validity of the Wiedemann-Franz law.[93] This is displayed in Figure 2.9. The cases involving increased impurity contents (increasing ρ_{imp}/A) show a decrease in the magnitude of the difference between L and L_o. In addition, the temperature range over which L_o would be a valid assumption increases.

2.4.1.3. Electron-electron scattering. Despite the significance of electrons with respect to all other aspects of conduction within metallic materials, e-e scattering is actually an ineffective process. Theory dictates that the Pauli exclusion principle limits the allowed states necessary for e-e scattering. A solution for the dependence of $\rho_{e\text{-}e}$ on temperature is given in equation (26).[93]

$$\rho_{e-e}(T) = A_{ee}T^2 \tag{26}$$

Values for $A_{e\text{-}e}$ have been experimentally measured for various materials and ranges are reported from 2.8×10^{-16} to 1.35×10^{-10} W-Ω-K^{-2} (Cu and Bi). The magnitude of these values indicates that the effect of $\rho_{e\text{-}e}$ is insignificant with respect to the e-p and imperfection related processes.[93] Therefore, $\rho_{e\text{-}e}$ will not be discussed with respect to the effect on ZrB_2.

2.4.2. Phonon Conduction in Metals. As phonons are lattice vibrations, they are ubiquitous in contributing to thermal conduction in crystalline materials regardless of the nature of the electrons. However, when discussing the extent of phonon conduction in metals, as opposed to insulators, the presence of free electrons is important.[93,95] Therefore, the treatment of the phonon conduction in metals requires an understanding of electron-phonon scattering, in addition to phonon-phonon and defect scattering.

2.4.2.1. Conductivity due to phonon-electron scattering. Similar to the limiting temperature cases for electron-phonon scattering, the phonon-electron limited phonon portion of thermal conductivity ($k_{p\text{-}e}$) can be derived (equations (27) and (28)).[93]

$$k_{p-e} \cong \frac{G}{2}, for\left(T \geq \Theta_D\right) \tag{27}$$

$$k_{p-e}\left(T\right) \cong 7.18G\left(\frac{T}{\Theta_D}\right)^2, for T \ll \Theta_D \tag{28}$$

The G term is a constant related to the coupling between electrons and phonons, summed for the three acoustic phonon modes. There is no temperature dependency for G. This leads to the high temperature solution for $\rho_{p\text{-}e}$ to be independent of temperature. Although, the high temperature regime will be shown to be limited by the lattice scattering and therefore conductivities predicted by equation (27) are never realized in real materials.[93]

The low temperature result is more significant in contributing to k_p. Conductivity changes as function of T^2, effectively limiting phonon conduction at lower temperatures. Without this result, as will be shown in the next section, phonon-phonon conduction would otherwise lead to higher low temperature conductivities. Due to the scattering induced upon the lattice by electrons, the phonon contribution in metals is typically disregarded all together. Even at intermediate temperatures, k_p is typically not more than 2% of the total conductivity.[93] However, the presence of solid solutions can cause the phonon contribution to increase. This is due to the decreased mobility of electrons which makes them a less effective source of phonon-electron scattering.[93]

2.4.2.2. Phonon-phonon scattering. Where phonon-electron scattering was shown to be important at low temperatures, Umklapp processes (phonon-phonon scattering) can be shown to dominate at high temperatures. Slack et al.[98] derived equation (29) based on this scattering process.

$$k_p^U(T) = \frac{3x10^{-5} M_a a \Theta_o^3}{\gamma^2 n_c^{2/3}} \frac{1}{T} \tag{29}$$

The phonon conductivity is a function of the average atomic mass (M_a), the lattice parameter (a), the number of atoms in the unit cell (n_c), the high-temperature Gruneisen constant (γ), and Θ_o is from the low-temperature heat capacity.[98] Most importantly, k_p^U is a function of 1/T. This is why the phonon conduction is limited by thermal scattering of the lattice at high temperatures.

2.4.2.3. Defect scattering. Defects for phonons are the same as those for electrons, i.e. impurities, grain boundaries, etc. It turns out that because of the significant contribution of phonon-phonon and phonon-electron scattering in reducing the relaxation time, defects play a limited role in the k_p of metals.[93] This is in contrast to the great importance of these features when discussing dielectric materials. Regardless, the scattering of phonons by defects still contributes to the decrease in k_p for similar reasons in metals as insulators. Impurities lead to a decrease in the relaxation time by increasing the anharmonicity in the lattice. This effect can come from the substitution of atoms of different size or mass, and strain induced in the lattice from interstitials is also important. The inherent crystal structure of a material can also lead to reductions in the achievable phonon contribution. Anharmonicities are increased as the difference in atomic weight of the constituent atoms increases (e.g. 91.22 g/mol Zr vs. 10.81 g/mol B).[99]

2.4.3. Electrical Resistivity. Electrical resistivity is an important property which can be used in the evaluation of thermal conductivity. The electronic portion of thermal conductivity can be derived from measured electrical resistivities using the Wiedemann-Franz law, if assumptions regarding the Lorenz number are made. Because of its importance in calculating k_e, the testing of electrical resistivity will be discussed followed by a review of the ZrB_2 electrical resistivity technical literature.

2.4.3.1. Measurement of resistivity. Electrical resistivity testing of ZrB_2 at elevated temperatures has been reported by a handful of researchers. The highest evaluated testing temperature is reported by Samsonov et al.[100] In this study, resistivities for ZrB_2 are reported from room temperature up to 2000°C. The maximum testing temperature of all other studies ranges from 370 to 1300°C.[19,61,87,89,101-103] Where Samsonov used molybdenum to make high temperature contacts, the other researchers have been restricted to lower temperatures by the physical limitations of the conductors or contacts used (e.g. Pt[61,89,103], Ag[87,101], Cu[19], and Ni[61]). ZrB_2 resistivities have been measured using either a 2-point bar[100], 4-point bar[87,89,102,103], or 4-point van der Pauw[19,61,101] technique. Because of its use in the research presented in sections 4, 5, and 6; the specifics of the van der Pauw method will now be discussed.

2.4.3.1.1. <u>van der Pauw electrical testing.</u> L. J. van der Pauw, the namesake of the technique, developed this method as a way of testing electrical resistivity and the Hall effect. Any thin 2D shape can be evaluated and the only important dimension is the specimen thickness (x).[104] Figure 2.10 represents the current application and voltage measurement for one of eight different testing permutations required for the full van der Pauw method. These permutations allow for the evaluation of resistivity regardless of the specimen shape and electrical contact positioning.[104]

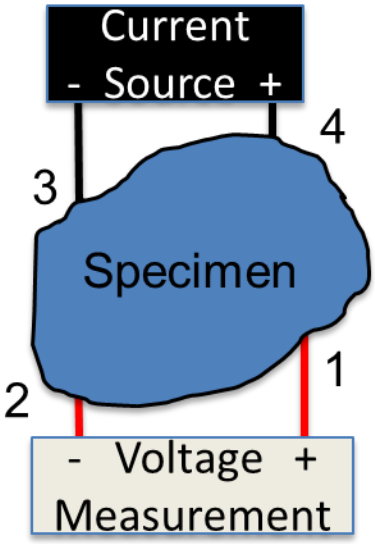

Figure 2.10. Representative schematic of the van der Pauw method, showing one of the eight testing permutations of current application/voltage measurement configured on a specimen of arbitrary 2D shape.

Two separate resistivities ($\rho_{e,A}$ and $\rho_{e,B}$) are calculated from equations (30) and (31) by measuring the resulting voltage drop ($V_{ab,cd}$) across the sample under a given current (I) for each permutation. The subscripts denote the positioning of the positive current leg (a), negative current leg (b), positive voltage leg (c), and negative voltage leg (d) on the numbered positions for the specimen in Figure 2.10.[105]

$$\rho_{e,A} = \frac{1.1331 f_A x}{I}[V_{21,34} - V_{12,34} + V_{32,41} - V_{23,41}] \quad (30)$$

$$\rho_{e,B} = \frac{1.1331 f_B x}{I}[V_{43,12} - V_{34,12} + V_{14,23} - V_{41,23}] \quad (31)$$

The parameter f (for A or B) in each equation is an empirically derived shape factor that can be solved via equation (32) using the resistance ratios calculated from equations

(33) and (34) (as current should be constant these ratios can be calculated directly from the voltages).[105]

$$\frac{Q-1}{Q+1}=\frac{f}{0.693}\operatorname{arcosh}\left[\frac{1}{2}\exp\left(\frac{0.693}{f}\right)\right] \tag{32}$$

$$Q_A=\frac{R_{21,34}-R_{12,34}}{R_{32,41}-R_{23,41}}=\frac{V_{21,34}-V_{12,34}}{V_{32,41}-V_{23,41}} \tag{33}$$

$$Q_A=\frac{R_{43,12}-R_{34,12}}{R_{14,23}-R_{41,23}}=\frac{V_{43,12}-V_{34,12}}{V_{14,23}-V_{41,23}} \tag{34}$$

The average of $\rho_{e,A}$ and $\rho_{e,B}$ can then be calculated, giving a single resistivity. A material is considered uniform and homogenous if $\rho_{e,A}$ and $\rho_{e,B}$ are within 10%.[105] Valid testing also requires the sample be free of geometrical holes and that the contacts remain small ($0.05 \cdot x_p$) with respect to peripheral length (x_p) of the specimen.[104,105] In addition, it is best to place the contacts on the specimen edge.[105] This technique is advantageous over 4-point resistivity testing of a bar as there is no need to account for the contact separation.

2.4.3.1.2. <u>The electrical resistivity of ZrB_2.</u> As can be seen from Figure 2.11, for the most part, ρ_e is linear with respect to temperature. This is a reasonable result based on the linear temperature dependence for resistivity given by equation (19). At room temperature, the reported resistivities range from 6.8[101] to 23[89] μΩ-cm. The relative increase in resistivities between the different materials presented is a good example of increases in scattering due to imperfections. For these materials, the imperfections are most likely impurity related due to differences in processing. The lower resistivity material by Zhang et al.[101] was reaction processed from Zr and B, whereas the higher resistivity material by Zimmermann et al.[89] was produced from commercial powder attrition milled with WC media.

The slope of ρ_e as a function of temperature for each dataset appears to increase as a function of the magnitude of the resistivities. Matthiessen's rule implies that the temperature dependent term ($\rho_{e\text{-}p}$) should be independent of changes in imperfections. Therefore, the resistivity of ZrB_2 may deviate from Matthiessen's rule.

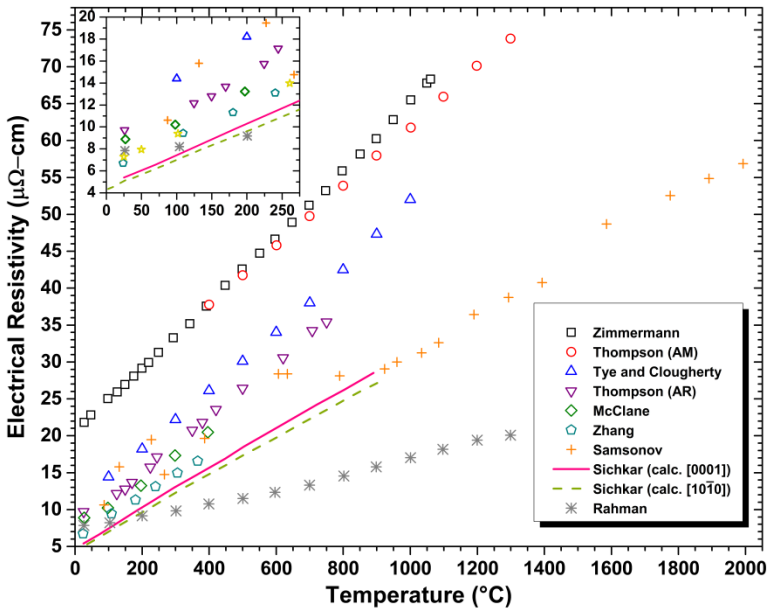

Figure 2.11. Experimental and calculated electrical resistivities of ZrB_2 with respect to temperature from the technical literature.[19,61,70,87,89,100-103]

Electrical resistivity is one material property affected by the anisotropic crystal structure of ZrB_2. Gasparov et al. measured the single crystal electrical resistivities for zone refined ZrB_2 at room temperature.[8] The a-direction was 6.1 μΩ-cm and 7.2 μΩ-cm was reported for the c-direction. These values bound the lowest resistivity ZrB_2 from Figure 2.11. The results by Gasparov clearly indicate electrical conduction is more favorable along the planes of Zr atoms rather than crossing the B planes. Calculated values for single crystal ZrB_2 are plotted in Figure 2.11. The data by Sichkar et al.

indicates a smaller anisotropic effect (5.1 μΩ-cm, a-direction and 5.5 μΩ-cm, c-direction) but still shows the appropriate trend between each direction.[70]

2.4.4. Thermal Conductivity of ZrB_2. This section reviews the technical literature, with respect to the thermal conductivity of ZrB_2. The discussion is divided into sections covering phase pure ZrB_2, solid solution effects, the role of C and ZrC as second phases, and finally the electron and phonon contributions to the total thermal conductivity. In addition, the evaluation of diffusivity and heat capacity is covered.

2.4.4.1. Pure ZrB_2. Few nominally phase pure ZrB_2 materials (referred to hereafter as "pure ZrB_2") have been produced and have had k characterized. Table 2.2 summarizes the reported room temperature and highest evaluated temperature thermal conductivities, along with details of the powder processing, material purity, densification techniques, special notes regarding grain size and sintering aids, and relative densities for ZrB_2 from the technical literature. As can be seen from Table 2.2, starting with the work by Sindeband et al.[106] in 1950, to the present, k has been reported for only 20 pure, single phase ZrB_2 ceramics. This is likely due to the difficulty of densifying ZrB_2 without sintering aids and the frequency with which second phases are added to ZrB_2 to improve strength, fracture toughness, resistance to oxidation, and thermal shock performance. From this point on, reports before 1980 are referred to as "historic" while anything after is considered "current".

Table 2.2. Thermal Conductivity of Pure ZrB_2 with Information on Starting/Final Materials, Processing, and Density

Powder Processing	% Purity	Densification Technique	Special Notes (gs in µm)	$\rho_{relative}$	Thermal Conductivity (k, W/m-K)		Ref.
					25°C	@ max temp	
fused-salt electrolysis	-	PS	-	85%	24	-	106
-	96.3	HP	-	70%	-	29 @ 2200°C†	107
"fluid energy milled"	99.2	HP	gs=28.5µm	100%	-	82 @ 1000°C†	21
"fluid energy milled"	99.2	HP	gs=28.5µm	100%	-	82 @ 2000°C	21
-	-	HP	-	100%*	-	133 @ 2020°C†	108
-	99.1 (final)	HP	gs=11µm	97.4%	-	92 @ 1143°C	109
-	-	HP	gs=13µm	100%*	-	84 @ 885°C	110
"vibrogrinding"	-	CVD	Pyrolytic	100%*	-	84 @ 2150°C	20
"vibrogrinding"	-	PS, 2100°C	Ni sintering aid	100%*	-	55 @ 2200°C	20
-	-	RF FZR	SX - a-direction	100%	132-145	-	111
-	-	RF FZR	SX - c-direction	100%	95-102	78-82 @ 200°C	111
BM w/ZrO_2	99.5	HP, 2000°C	gs=5µm	75%	-	43 @ 2000°C	112
AM w/WC	-	HP, 1900°C	gs=6µm*	100%	56	67 @ 1325°C	89
BM w/SiC	98	SPS, 1900°C	gs=3.0µm	95.6%	113	-	113
BM ZrH_2+B w/SiC	99 ZrH_2, 95.9 B	rxn-SPS, 1800°C	gs=5.35µm	97%	133	-	18
HM, Zr+B	99.7 Zr, 99 B	rxn-SPS	gs=5.6µm	92.5%	-	92 @ 435°C	101
BM w/ZrO_2	-	SPS, 2000°C	gs=6-11µm	95%	50†	-	114
AM w/WC	-	HP, 1900°C	gs=3.3µm	100%	-	59 @ 2000°C	61
BM w/ZrB_2	-	HP, 2100°C	gs=22µm	97%	93	67 @ 2000°C	87
BM w/ZrB_2	98.7	HP, 2150°C	gs=21, 0.5wt%C sintering aid	100%*	88	86 @ 200°C	115

AM ≡ Attrition milling
BM ≡ Ball milling
HM ≡ Hand milling
HP ≡ Hot pressing
PS ≡ Pressureless sintering
RF FZR ≡ Radio frequency float zone refinement
SPS ≡ Spark plasma sintering
gs ≡ Grain size
* density has been corrected to 100% by publication author
† direct conductivity measurement

Most studies have evaluated the k of ZrB_2 indirectly using the bulk density (ρ), thermal diffusivity (D), and the constant pressure heat capacity (C_p), via equation

(35).[18,20,21,61,87,89,101,109-113,115] However, several exceptions exist. Studies have measured k directly using steady state methods[21,107,108] or a direct dynamic method[114] and these exceptions to have been noted in Table 2.2.

$$k = \rho * D * C_p \tag{35}$$

2.4.4.1.1. <u>Thermal diffusivity.</u> For those studies utilizing equation (35), D was evaluated by one of three dynamic methods: xenon flash [18,113], laser flash[21,61,87,89,109,111,112,115], or a plane temperature wave approach [20,101]. Overall this is the most important parameter involved in calculating k. Compared to C_p and ρ, D is the property most affected by changes in parameters such as grain size and purity.

2.4.4.1.1.1. <u>Flash diffusivity measurement.</u> As the flash method is most common (and because of its use in the research presented in sections 4 and 6) it has been chosen for discussion.

The flash method for measuring thermal diffusivity is performed by irradiating the front face of a thin disk or plate specimen with a finite energy pulse as represented by Figure 2.12.[116] As noted above, laser and xenon flash lamps are examples of possible radiant energy sources. The resulting temperature profile on the back face of the specimen is subsequently evaluated using either contacting (thermocouple) or non-contacting (optical pyrometery) thermal analysis instrumentation.[116,117]

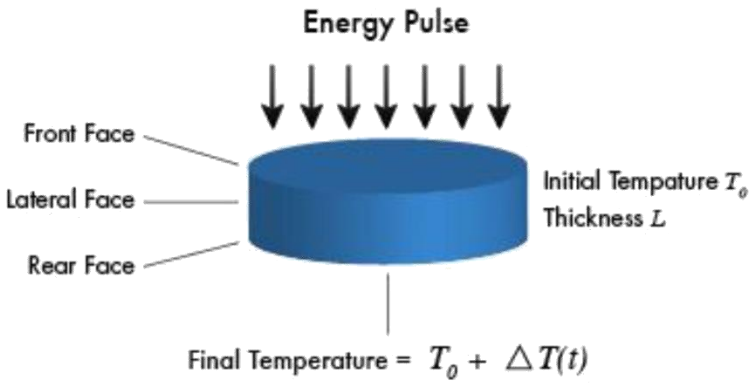

Figure 2.12. Schematic representation of the impinging energy pulse of a flash thermal diffusivity technique on a specimen disk. Image courtesy of TA Instruments.

Parker et al. developed the flash method and the research presented discusses the development of the heat flow equations which are the basis for the flash technique. The solution to these equation, with the appropriate boundary conditions, yields a simple relation (equation (36)) between D, the specimen thickness (x), and the time ($t_{1/2}$) to reach half of the maximum in the overall temperature rise.[116]

$$D = 1.38\frac{x^2}{\pi^2 t_{1/2}} \tag{36}$$

The theoretical form of the temperature rise profile determined by Parker et al. is shown as the solid “mathematical model” line in Figure 2.13. Multiple assumptions have to remain valid for this curve to match any experimental results and they are as follows.[116]

- One dimensional heat flow is maintained
- No heat is lost from the lateral faces
- The pulse must be uniformly absorbed
- The pulse duration is short with respect to the temperature rise time
- Energy is absorbed within a minimal thickness
- Materials properties are nearly constant over the range of specimen temperature excursion (i.e. no phase changes occur)

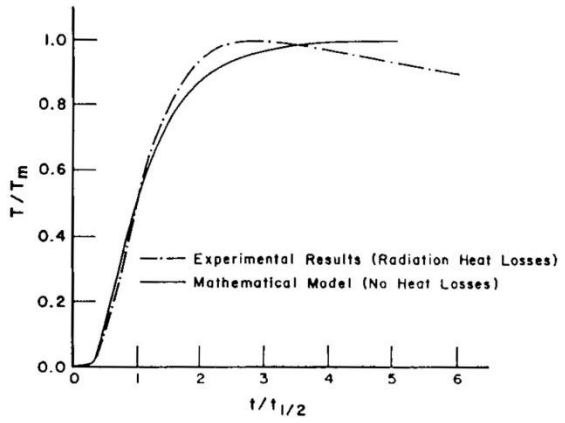

Figure 2.13. Normalized temperature rise shown as a function of normalized time for both the theoretical temperature profile by Parker et al.[116] and representative experimental results showing the effect of radiant heat loss. Image copied from ASTM Standard E 1461-07, "Standard Test Method for Thermal Diffusivity by the Flash Method".

In reality, it would be difficult to satisfy all of these conditions so that the experimental results matched the model. Therefore, multiple researchers have studied various aspects of the assumptions to produce equations that better model the experimental conditions. Treatments by Cowan[118], and Clark and Taylor[119] specifically looked at the heat loss from the lateral face(s). This heat loss is evident at the end of the experimental temperature rise curve in Figure 2.13. Beyond the peak, temperature decreases in contrast to the constant rise for the theoretical curve by Parker. Heckman discusses a correction for the pulse time assuming an experimental pulse width is not short enough, with respect to the rise time, to be negligible.[120] Corrections can also be combined to more fully account for the possible discrepancies in experimental results from Parker's analysis. One such example is the work by Koski which describes the application of a pulse width correction to the work by both Cowan; and Clark and Taylor.

In addition, the author includes a treatment to account for the heat loss from the front face.[121]

Accuracy of the flash method will always rely on having a mathematical model which most closely follows the experimental results. Regardless, the technique does offer benefits which make it advantageous, and they are as follows.[117]

- Only small specimen sizes are required
- Specimens need only be made into basic geometric shapes (i.e. flat disks)
- The technique requires no calibration
- A broad temperature range (cryogenic to 2000°C+) may be evaluated with the appropriate systems

2.4.4.1.2. <u>Heat capacity.</u> In some cases, C_p values for ZrB_2 have either been measured by drop calorimetry[21], DSC[89,112], or one of the flash techniques[18,111,113]. More commonly, C_p values have been taken from thermochemical tables [20,61,87,101,109,115], like historic literature by either Schick[122] or Bolgar et al.[123] or more recent sources such as the NIST-JANAF[124] tables or HSC Chemistry[125] (HSC primarily derives its ZrB_2 equations from the NIST-JANAF). Figure 2.14 shows C_p data for ZrB_2 plotted with respect to temperature from several of the conductivity experiments[18,21,89,112,113] as well as the thermochemical tables.[122,124-126]

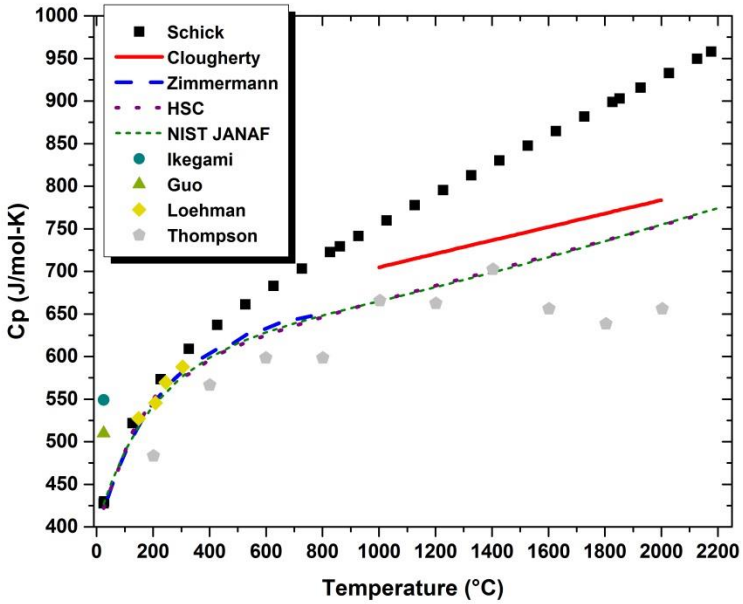

Figure 2.14. Heat capacities as a function of temperature used in the technical literature to calculate thermal conductivity.

Upon inspection of Figure 2.14, it obvious that discrepancies exist among reported values of $C_{p.}$ Despite the divergence at higher temperatures, data from Schick et al., the NIST-JANAF/HSC, and more recent DSC data by Zimmermann et al.[89] appear to agree between room temperature (RT) and ~200°C (430 to 550 J/kg-K). In contrast, the room temperature values reported by Guo et al.[18] and Ikegami et al.[113], which were obtained via a comparison method using xenon flash, are ~20% and ~29% higher, respectively. The cause of the discrepancies in the C_p values is unclear and not discussed by the researchers. Recent findings by Jason Lonergan at Missouri S&T indicate reducing Hf content, even from that of the natural concentration, may increase C_p. This would make sense given the lower C_p of HfB_2 at 25°C (220 to 250 J/mol-K)[122,125,127] The material produced by Guo et al. could have a decreased Hf content since it was produced by reactively processing ZrB_2 from 99% pure ZrH_2 and 95.9% pure B. Regardless of the mechanism, it goes without saying that reliable heat capacity data are

of utmost importance when evaluating C_p, as measurement errors will propagate into k when calculated via equation (35).

2.4.4.1.2.1. <u>Flash heat capacity measurement.</u> One benefit of flash thermal diffusivity measurement is the ability to evaluate C_p simultaneously with D.[116,128] This analysis is similar to DSC in that the temperature response of a reference standard of known heat capacity ($C_{p,R}$) is first evaluated and compared to the response of the experimental specimen. With the evaluation of the total temperature rise for the reference (ΔT_R) and experimental (ΔT_E) specimens the experimental specimen heat capacity ($C_{p,E}$) can be calculated from equation (37) using the known densities (ρ_R and ρ_E) and sample thicknesses (x_R and x_E) of each specimen.[128]

$$C_{p,E} = \frac{x_R \Delta T_R \rho_R}{x_E \Delta T_E \rho_E} C_{p,R} \tag{37}$$

Unlike the flash diffusivity measurement, the use of a standard to evaluate C_p eliminates the issues of properly modeling the heat transfer to obtain accurate results. However, some assumptions have to be made and accounted for as follows:[129]

- The intensity of the energy source must be reproducible (note: sampling the intensity can also allow for an appropriate correction)
- The detector has to maintain sensitivity over time
- Reference and experimental specimens should be similar in size, emissivity, and opacity to be comparable (note: graphite coatings are typically used to equilibrate emissivity)
- Both specimens must be homogeneous and isotropic
- Both specimens should be tested closely in terms of time and temperature

2.4.4.1.3. <u>Density.</u> Density is the final aspect of the calculation of k from equation (35). The Archimedes method is almost unanimously used for the evaluation of density. If and when densities of ZrB_2 were corrected for the effects of thermal expansion, researchers used either tabulated data[61,87,115] or experimental dilatometry results [21,89,107,109,111,112]. The most cited tabulated thermal expansion data for ZrB_2 has been reported by Touloukan et al. and the linear thermal expansion for polycrystalline ZrB_2 is given as equation (38).[130]

$$\frac{\Delta L}{L_o}(\%) = -0.135 + 3.94x10^{-4}(T+273) + 2.39x10^{-7}(T+273)^2 - 3.97x10^{-11}(T+273)^3 \quad (38)$$

Bulk polycrystalline ZrB_2 can typically be considered isotropic with respect to thermal expansion. Therefore, equation (39) can be used to calculate the volumetric thermal expansion from the linear expansion and used to correct density for thermal expansion.[99]

$$\frac{\Delta V}{V_o} = 3\frac{\Delta L}{L_o} + 3\left(\frac{\Delta L}{L_o}\right)^2 + \left(\frac{\Delta L}{L_o}\right)^3 \quad (39)$$

2.4.4.1.4. <u>Materials processing from ZrB_2 k literature</u>. Most of the studies reported some type of milling procedure for particle size reduction, combining starting materials, or both. Contamination from milling media is common and can affect the properties of the densified ceramics. Only the modern reports provide much detail on the types of media used. The use of WC [61,89], SiC [18,113], ZrO_2 [112,114] and ZrB_2 [87,115] are the most common media types reported. Pressure assisted densification techniques such as

hot pressing (HP) or spark plasma sintering (SPS; also known as field assisted sintering (FAST) or pulsed electric current sintering (PECS)) were most often employed for the densification of ZrB_2 [18,21,61,87,89,101,107-110,112-115], but pressureless sintering (PS) [20,106], chemical vapor deposition [20], and float zone refinement [111] have also been utilized. More often than not, researchers were successful at producing ≥95% dense ceramics with several achieving full density.

2.4.4.1.5. Historic ZrB_2. Figure 2.15 summarizes all of the thermal conductivity data reported as a function of temperature for the historic, pure ZrB_2. The lowest historic thermal conductivity ceramics were produced by Sindeband et al. (~25W/m-K)[106] and Neel et al. (20-46 W/m-K)[107], likely due to their low relative densities of 85 and 70%, respectively. The effect of density is especially evident at elevated temperatures where k begins to rise, presumably due to photon heat transport across pores. Despite the low density of the ceramics, research carried out by Neel et al. was significant in that ZrB_2 was tested up to 2200°C, which has since only been equaled by Fridlender et al.[20]. In addition to high testing temperatures, Neel et al., along with Samsonov et al.[108] and Clougherty et al.[21], are the only researchers to perform direct steady-state measurements of thermal conductivity for any ZrB_2 based materials.

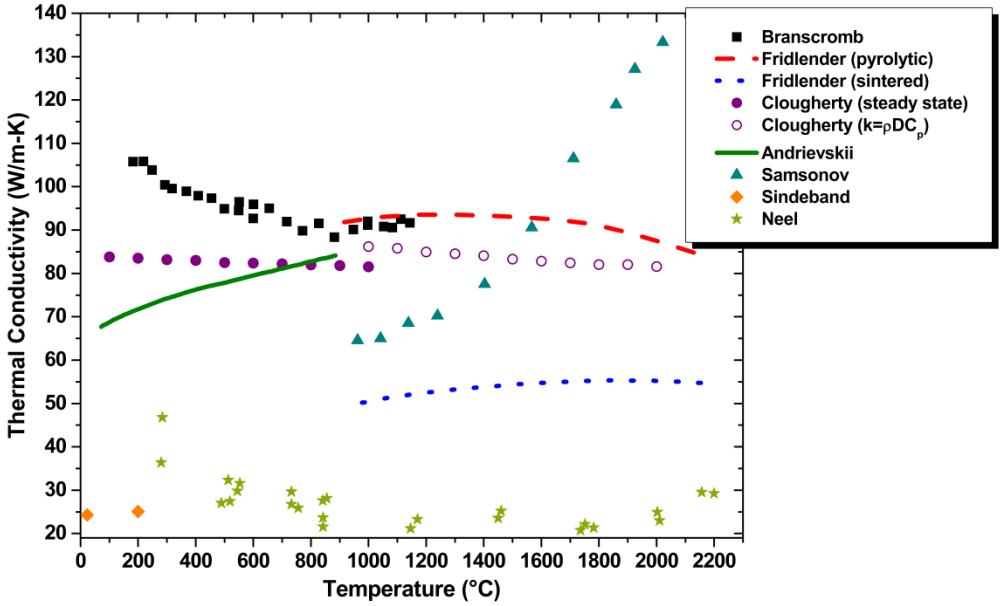

Figure 2.15. Thermal conductivity as a function of temperature from the historic pure ZrB_2 technical literature.

Besides Neel et al. and Sindeband et al., the historic data were obtained from ceramics that were either >97% dense [109], fully dense [21], or had the thermal conductivities corrected for porosity [20,108,110]. No clear trend in thermal conductivity as a function of temperature emerges from these dense ceramics; as k increases as temperature increases for some and decreases for others. The k values also vary widely, from as low as ~35 W/m-K at 200°C to ~80 W/m-K at 2000°C. This range excludes the data by Samsonov et al. In comparison to the other historic literature values in Figure 2.15, the values reported by Samsonov et al. are likely not representative of ZrB_2, as k steadily increases from ~60 W/m-K at 1000°C to ~130 W/m-K at 2000°C.

Andrievskii et al.[110] also reported k increasing with temperature, which was not explained in their paper. In contrast, Fridlender reported the addition of 1 wt% carbonyl nickel for densification of “sintered” ZrB_2, which led to Ni being a significant impurity. This

was the most likely cause of the relatively low k values (50 to 54 W/m-K), and a positive trend. Fridlender et al. also investigated pyrolytic ZrB_2 produced by CVD that led to a "columnar microstructure with semi-coherent crystallite boundaries". No overall temperature trend was apparent, but the higher conductivity (84 to 93 W/m-K) compared to sintered material was attributed to decreased phonon scattering from more coherent grain boundaries.[20]

Finally, ZrB_2 produced by Branscomb and Hunter[109] and Clougherty et al.[i] [21] had the highest k values of the historic ceramics, also exhibiting negative slopes with respect to increasing temperature. This behavior is consistent with high relative density and purity. Further, Branscomb and Hunter reported the highest k at low temperature (105 W/m-K @ 200°C) and the highest conductivity above 1000°C (~91 W/m-K @ 1143°C, excluding Fridlender's pyrolytic ZrB_2). Branscomb and Hunter analyzed the metallic impurity content and found their ceramics to be ~99.1 at% pure with the largest impurities being Fe (0.7 at%), Si (0.07 at%), and Nb (0.05 at%) and all other individual elements being <0.02 at%.[109] However, the analysis did not include Hf (which as discussed earlier is a common impurity in ZrB_2), C (typically introduced during processing), or O (from native powder surface oxide layers), which are also likely impurities. Despite this, the ZrB_2 by Branscomb and Hunter was likely one of the purest historic ceramics resulting in its high k values.

2.4.4.1.6. <u>Current ZrB_2.</u> Like the thermal conductivities for the historic Studies in Figure 2.15, the data from the current ZrB_2 studies have been compiled and are summarized in Figure 2.16. Thermal conductivity at the highest temperatures measured for current ZrB_2 ceramics[61,87,89] ranged from 43 W/m-K[112] to 67 W/m-K. Room temperature k values are all >85 W/m-K [18,87,101,111,113,115] with one exception at 56 W/m-

[i] It should be noted that the discontinuity at 1000°C for data by Clougherty et al.[94] is likely due to a change in testing method.

K[89]. With such wide ranges of conductivities for ZrB_2, it may first be important to evaluate the intrinsic thermal conductivity of ZrB_2, which could then be used a baseline for comparison to other materials.

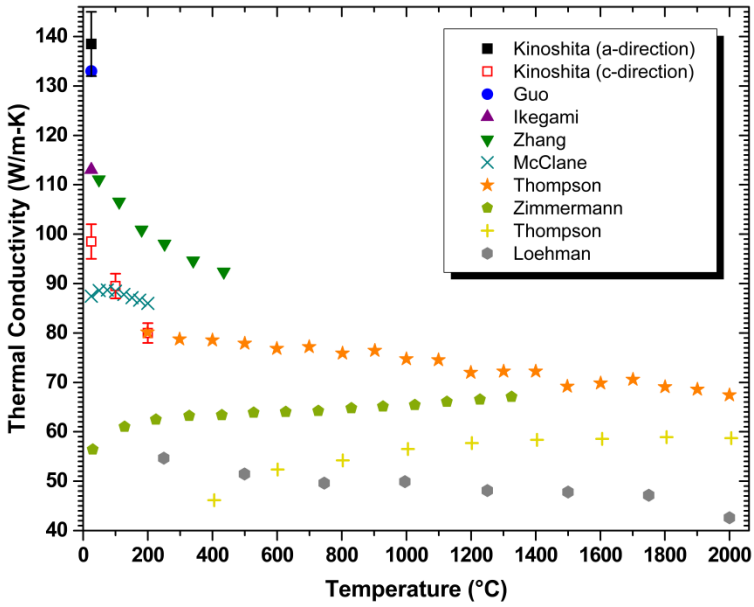

Figure 2.16. Thermal conductivity as a function of temperature from the current pure ZrB_2 technical literature.

To investigate ZrB_2 as a possible lattice-matched substrate for GaN, Kinoshita et al. produced single crystal (SX) ZrB_2 via float zone refinement (Table 2.2). ZrB_2 is a hexagonal material, as discussed earlier, resulting in an anisotropic as a result the thermal conductivity is anisotropic. Therefore, measurements ranged from 132-145 W/m-K parallel to the a-axis and 95-102 W/m-K parallel to the c-axis (Figure 2.16).[111] The differences can be explained by dissimilar phonon and electron scattering for different directions. Phonon scattering increases as the ratio of atomic masses increases between constituent elements.[131] Therefore, phonon conduction will be highest for directions with B-B and Zr-Zr bonds, which is the basal plane. In addition, the electron

contribution to k should be higher along the basal plane due to the close-packed planes of metallically bonded Zr atoms.[64]

The SX values reported by Kinoshita et al. provided insight into the theoretical limits of the thermal conductivity of ZrB_2 ceramics. Equations (40) and (41) have been used to estimate the arithmetic mean (k_{AM}, upper bounds) and harmonic mean (k_{HM}, lower bounds) polycrystalline thermal conductivities from SX values .[132,133]

$$k_{AM} = \tfrac{1}{3}\left(k_1 + k_2 + k_3\right) \tag{40}$$

$$\frac{1}{k_{HM}} = 1/3\left(\frac{1}{k_1} + \frac{1}{k_2} + \frac{1}{k_3}\right) \tag{41}$$

Using values from Kinoshita, the theoretical k for ZrB_2 is between 117 and 131 W/m-K. These values do not account for grain boundary resistances, which are influenced by both grain size and boundary impurities, and would decrease thermal conductivity. Therefore, the predicted k values should be upper limits for polycrystalline ZrB_2 ceramics.

The ZrB_2 by Guo et al.[18] (Figure 2.16) has a higher k than the theoretical bounds calculated above. This makes it the best representation of the intrinsic conductivity of polycrystalline ZrB_2 from the technical literature. In addition, at 133 W/m-K this value is the highest room temperature thermal conductivity reported to date for ZrB_2. The next two highest conductivity materials only approached the lower limit by 4 to 6 W/m-K.[101,113] It is interesting to note that of the three highest conductivity materials two of them (Guo et al.[18] and Zhang et al.[84]) were reaction processed. While the ZrB_2 produced by Ikegami, and the other current ZrB_2 from the literature, were produced from commercial powder. Reaction processing from B and either Zr or ZrH_2 is believed to result in high purities for the resulting diboride, therefore leading to higher thermal conductivites.

The material by Loehman et al.[112] likely has an uncharacteristically low conductivity due to its low density (75%). Disregarding this material, an obvious division in room temperature k values occurs at ~67 W/m-K for the data plotted in Figure 2.16. Above this value, the reported k values decrease as temperature increases.[87,101,115] The two other materials below 67 W/m-K exhibit an increase in k with increasing temperature.[61,89] These two low conductivity ceramics contained WC impurities from milling and, in both cases, the researchers indicate that W from the media was a likely cause for the differing slopes and reduced thermal conductivities. The detrimental effect of W has since been confirmed by McClane et al.[19], and this research will be discussed in more detail in the next section. It is interesting to note that despite the differences in room temperature k, and the change in k with temperature, the conductivities appear to converge to a narrow range (within ~14 W/m-K) above 1300°C. This indicates that factors resulting in large changes in the k at lower temperatures may give way to a common mechanism that controls k at elevated temperatures.

For the current ZrB_2 ceramics, the major differences in conductivity appear to be independent of grain size. Grain sizes can be divided into two separate ranges, fine grains with average sizes below 10 μm[18,61,89,101,112,113] or coarse grains with average sizes over 20 μm.[87,115] Fine grains have resulted in either high k (>111 W/m-K at 25°C) ZrB_2 [18,101] or low k (<57 W/m-K at 25°C) for conventionally processed ZrB_2.[61,89] Thermal conductivities for the coarse grained materials fell between those values.[87,115] Therefore, the differences in k apparent in Figure 2.16 are not significantly affected by grain size. However, differences in purity, which are reported much less often, are a more likely explanation for the observed variations. Unfortunately, none of the current studies report chemical analysis of the final ceramics, although some assays of starting powders are provided.[18,101,112,113,115] As a result, analysis of the effect of purity is difficult. However,

some studies have systematically evaluated the effects of solid solution additions of various species as discussed in the next section.

2.4.4.2. ZrB_2 and transition metal solid solutions. Systematic evaluations of the effects of transition metal solid solutions were carried out by McClane et al.[19] and Thompson[87]. The thermal conductivities from these two are summarized in Table 2.3 and plotted in Figure 2.17. The conductivity data for the reaction hot pressed ZrB_2 reported by Zhang et al.[101] have been included for comparison as they are the highest conductivities reported above room temperature. These studies were self-consistent since similar processing was used for pure, baseline ZrB_2 ceramics and those with subsequent solid solution additions. This is important, as can be seen in Figure 2.17, because the true effects of the solid solutions would be misleading if only compared to ZrB_2 from other studies, like that by Zhang.

Table 2.3. Summary of the Transition Metal Solid Solutions by McClane et al.[19] and Thompson.[87]

Composition	Hot Pressing Temperature	Special Notes	Relative Density (%)	Thermal Conductivity (k, W/m-K)	
				25°C	@ max temp
ZrB_2[19]	I	gs=22µm, 0.5wt%C added	100*	88	86 @ 200°C
ZrB_2+2.8mol%HfB_2	I	gs=29µm, 0.5wt%C added	100*	81	82 @ 200°C
ZrB_2+2.9mol%NbB_2	2150°C I	gs=8µm, 0.5wt%C added	100*	74	76 @ 200°C
ZrB_2+2.9mol%W_2B_5	I	gs=19µm, 0.5wt%C added	100*	34	39 @ 200°C
ZrB_2[87]	I	gs=22µm	97.2	93	68 @ 2000°C
ZrB_2+5vol%TiB_2	I	gs=13µm	96.7	85	68 @ 2000°C
ZrB_2+10vol%TiB_2	2100°C I	gs=10µm	96	76	68 @ 2000°C
ZrB_2+50vol%TiB_2	I	gs=7µm	99.6	58	65 @ 1900°C

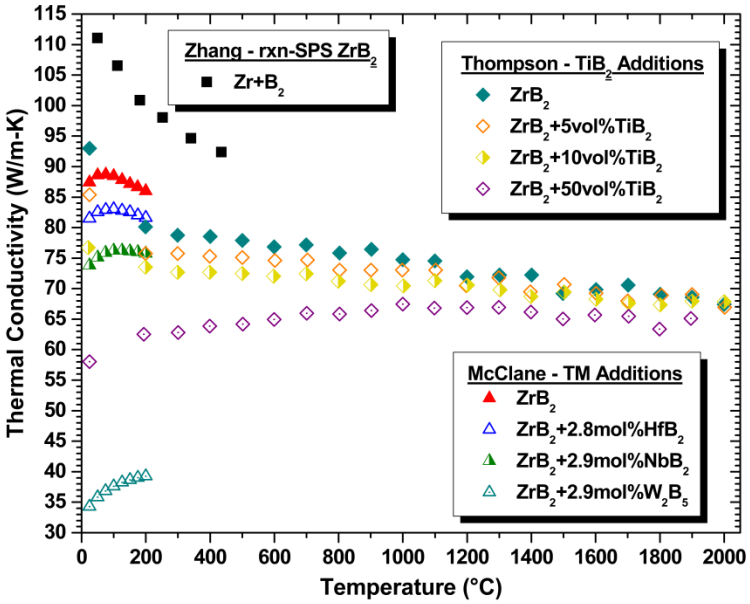

Figure 2.17. Thermal conductivity as a function of temperature for the transition metal solid solutions by McClane et al.[19] and Thompson[87] with the rxn-SPS ZrB_2 for reference.

All solid solution additions decreased the thermal conductivity of ZrB_2 ceramics from the respective baselines, especially at room temperature. The trend in k as a function of temperature depends on both the type and amount of addition. For example, Thompson et al. showed that a solid solution addition of 10 vol% TiB_2 reduced k resulting in an almost linear, shallow, negative trend with temperature. In contrast, the addition of 50 vol% TiB_2 resulted in a decrease in k of ~23 W/m-K at 25°C compared to the addition of 10 vol% TiB_2.[87] Both Thompson et al.[61] and McClane et al.[115] found that smaller additions of TiB_2 (data by McClane not shown in Figure 2.17) have a minimal effect on conductivity. In contrast, other transition metal additions such as W or Nb evaluated by McClane had a much larger effect at the same concentration.[115] McClane confirmed that the solid solution of tungsten in ZrB_2 does significantly contribute to the reduction in k (~53 W/m-K drop at 25°C for 3.1 mol% W). Evaluation of k for different solid solution additions was also shown to correlate to changes in lattice parameters for

the Hf and Nb additions.[115] However, W had a lower thermal conductivity than expected based on the lattice shift. This was attributed extra strain induced in the ZrB_2 lattice by the W, since WB_2 has a different crystal structure.

2.4.4.3. Second phase C and ZrC. In addition to studies concerned with the role of solid solutions on the conductivity of ZrB_2, thermal conductivity has been evaluated for ZrB_2 with second phase additions. These second phases are primarily limited to carbon[21,61,110], carbides (ZrC[68,77] and SiC[21,101,112,113,134-140]), and silicides ($MoSi_2$[141,142] and $ZrSi_2$[143]). The following discussion will be limited to additions of C and ZrC as they pertain to the research presented in sections 4 and 6. The thermal conductivities of these materials as a function of temperature are plotted in Figure 2.18 and specific details regarding the processing, grain size, and porosity are given in Table 2.4.

A broad range of conductivity values are reported depending on the specific additive and its content. For ZrB_2 containing 20 vol% C, the material from Clougherty et al. is the only composition plotted in Figure 2.18 that had a negative slope with temperature. Like other materials evaluated by Clougherty, there was again a discontinuity at 1000°C where the test method switched from a steady state cut bar method to a calculation based on measured D values. Overall the conductivity dropped from ~85 W/m-K at 100°C to ~64 W/m-K at 2000°C.[21] The form of the carbon in this material, either before or after processing, is not discussed. Given the small decease in k at room temperature between this material and the ZrB_2 studied by Clougherty, the C is likely to be graphitic in nature. The conductivity of amorphous carbon is lower and would have decreased k considerably more than for graphitic carbon which is typically on the order of ZrB_2.[144,145]

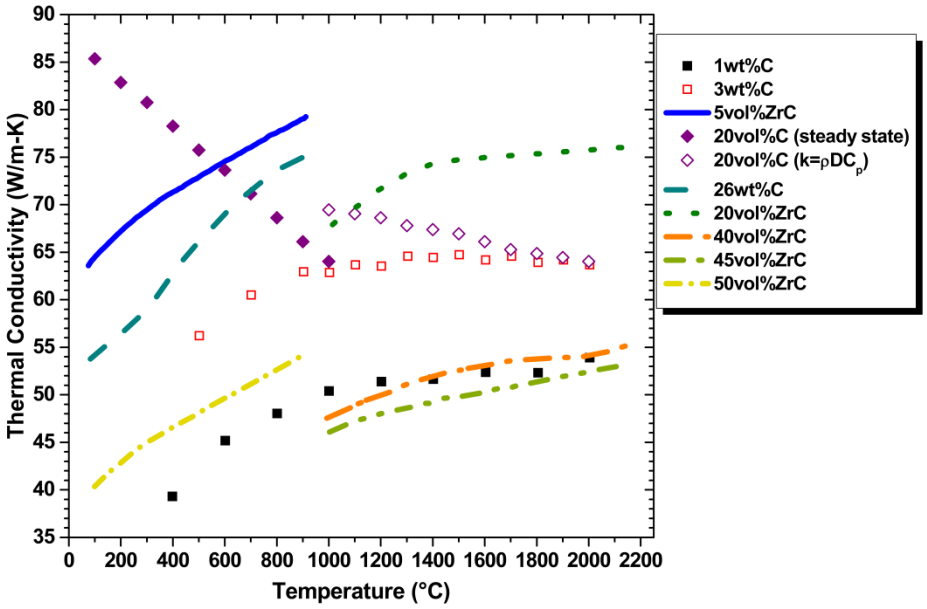

Figure 2.18. Thermal conductivity as a function of temperature for ZrB_2 with C or ZrC as a second phase.[20,21,61,110]

Table 2.4. Summary of the Processing, Grain Size, Density and Thermal Conductivity Data Reported for ZrB_2 with C and ZrC Additions.

2nd Phase	Powder Processing	Densification Technique	Special Notes (gs in µm)	$\rho_{relative}$	Thermal Conductivity (k, W/m-K) @ min temp	Thermal Conductivity (k, W/m-K) @ max temp
1wt%C[61]	AM w/WC	HP, 1900°C	gsZrB_2=2.4	100%	39.3 @ 400°C	53.9 @ 2000°C
3wt%C[61]	AM w/WC	HP, 1900°C	gsZrB_2=1.8	100%	56.2 @ 500°C	63.7 @ 2000°C
20vol%C[21]	VM w/plastic	HP	-	100%	85.4 @100°C	64.0 @ 1000°C
20vol%C[21]	VM w/plastic	HP	-	100%	69.5 @1000°	64.0 @ 2000°C
26vol%C[110]	-	HP	gsZrB_2=20	100%*	53.8 @ 83°C	75 @ 900 °C
5vol%ZrC[110]	-	HP	gsZrB_2=27	100%*	63.6 @75°C	79.3 @ 910°C
50vol%ZrC[110]	-	HP	gsZrB_2=10	100%*	40.4 @ 99.3°C	54.3 @ 905°C
20vol%ZrC[20]	"vibrogrinding"	PS, 2100°C	gsZrB_2=5, gsZrC=6, 1% Ni sintering aid	100%*	67.9 @ 1014°C	76.1 @ 2200°C
40vol%ZrC[20]	"vibrogrinding"	PS, 2100°C	gsZrB_2=3, gsZrC=4, 1% Ni sintering aid	100%*	47.5 @ 992°C	55.5 @ 2200°C
45vol%ZrC[20]	"vibrogrinding"	PS,2100°C	gsZrB_2=1, gsZrC=3, 1% Ni sintering aid	100%*	46.1 @ 1002°C	53.2 @ 2150°C

VM ≡ Vibratory mixing

Thompson et al.[61] and Andrievskii et al.[110] also reported thermal conductivities of ZrB_2 with carbon additions. The thermal conductivities for these materials all increased with increasing temperature. Considering the ZrB_2 was the majority constituent for these ceramics, the slope indicates something was inherently altering the conductivity of the diboride phase. For Andrievskii et al., 26 vol% carbon was added as graphite, which reduced the conductivity ~10 W/m-K at all temperatures with respect to the pure ZrB_2 of the same study.[110] Thompson et al. added carbon in the form of phenolic resin, resulting in 1 and 3 wt% amorphous carbon after pyrolysis. After hot pressing, a disordered, graphitic carbon was identified at the grain boundaries. The 1 wt% C material experienced a decrease in k compared to pure ZrB_2. It is theorized that the graphite was aligned with its basal plane parallel to the grain boundaries, thus disrupting phonon transport between ZrB_2 grains. However, k did not continue to decrease when C content was increased to 3 wt% C. It should be noted that 2.9 wt% of ZrC was also identified in the 3 wt% material. The increase in thermal conductivity for this composition was attributed to the preferential segregation of W into ZrC after testing up to 2000°C. The ZrC phase, produced due to carbon additions, served as a sink for W, reducing the W content in the ZrB_2 grains and boosting the overall thermal conductivity of the composite.[61]

Both Andrievskii et al. and Fridlender et al. discuss the effect of intentional additions of ZrC on conductivity. The addition of ZrC to ZrB_2 typically reduces k, due to the lower k of ZrC compared to ZrB_2. Andrievskii et al. evaluated both 5 and 50 vol% ZrC from 100-900°C while Fridlender et al. added 20, 40, and 45 vol% ZrC and tested up to 2150°C or 2200°C. The higher ZrC additions resulted in k values for the two studies to be between 40 and 55 W/m-K while the lower additions resulted in k values between 64 and 80 W/m-K, despite the different testing temperatures and compositions. The decrease in k with increasing ZrC content was due to the lower conductivity of ZrC (20 to

45 W/m-K at 25°C and 30 to 50 W/m-K at 2000°C)[146] compared to ZrB_2. It may be speculated that the wide range of possible conductivities for both ZrB_2 and ZrC could be contributing to the specific differences between the materials presented by Andrievskii et al. and Fridlender et al.

2.4.4.4. Electron and phonon contributions to k. Utilizing the Wiedemann-Franz law, the summation of k_e and k_p, and measured values for k and ρ_e several researchers have evaluated the contributions to thermal conductivity for ZrB_2.[19,61,87,89,101,102] The values of k_t, k_e, and k_p from these studies are plotted as a function of temperature in Figure 2.19. Comparing k_t and k_e, the positive or negative trends with temperature for k_e data are identical to those of the k_t, except for data from Tye and Clougherty[ii] [102]. On the other hand, k_p shows little variation with temperature. This is understandable, as k_p is expected to be limited by phonon-electron scattering at lower temperatures and then by phonon-phonon scattering at higher temperatures.

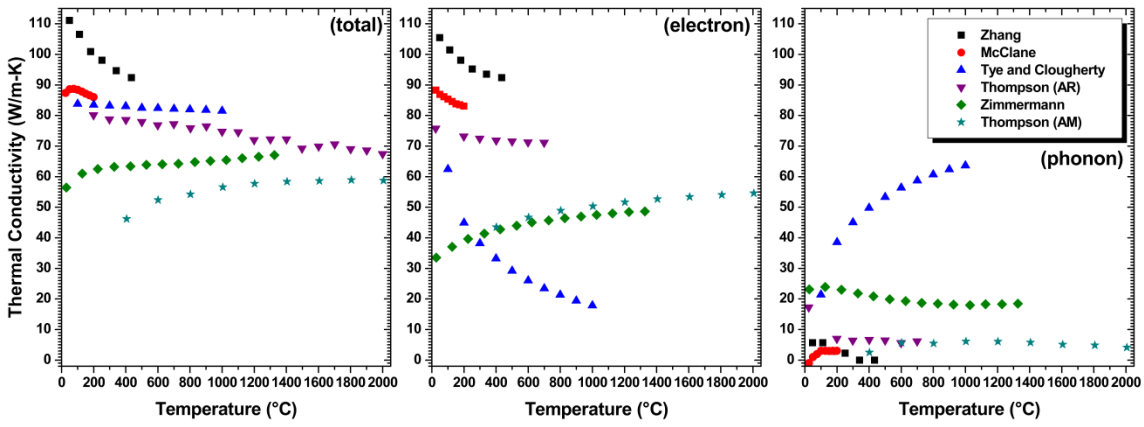

Figure 2.19. Total, electron, and phonon conductivities plotted as a function of temperature phase pure ZrB_2 from the literature.[19,61,87,89,101,147]

[ii] This reference was used for separation of the contributions to thermal conductivity in place of Clougherty et al. [9] which is the original reference for the k_t data.

The relatively small differences between k_e and k_t (excluding Tye and Clougherty and Zimmermann et al.[89]) indicate that electrons are the dominant thermal carrier for diborides. Little indication is given as to why k_p is so much higher and has a positive trend (and conversely k_e so much lower) for the material studied by Tye and Clougherty. When compared with other reports, this does not seem to be characteristic of ZrB_2. Zimmermann et al. found k_p values as high as ~24 W/m-K below 200°C. However, most of the other research[61,87,101] indicated that k_p was less than ~12 W/m-K for either ZrB_2.

Because k_e and k_p are estimated using equations (11) and (12), this method may be prone to error. One assumption, that permeates the studies to date, is the use of the theoretical Lorenz number to calculate k_e. Calculation of negative k_p values for materials produced by McClane et al. (Figure 2.19), indicate that a lower Lorenz number may be more representative of the behavior of some ZrB_2 ceramics. As discussed in section 2.4.1.1, it is possible for thermal conduction electrons to scatter inelastically. This would result in a decreased mean free path ℓ_t compared with ℓ_e. This is plausible as equation (25) indicates the Lorenz number for a material would decrease from L_o with a decrease in ℓ_t/ℓ_e.

2.4.4.4.1. <u>Evaluation of the Lorenz number.</u> The discussion above would be made more complete with a better understanding of the Lorenz number of ZrB_2. However, the evaluation of L typically requires k_p or k_e be directly measured. This is difficult to accomplish above the boiling point of liquid He without measurements of electrical resistivity and thermal conductivity under high or varied magnetic fields.[94,148]

Other researchers have reported the calculation of negative k_p values, like mentioned above. Sharma discusses this phenomena for the transition metals: Zr, Ru, Ir, Ta, Re, Os, and Pt.[149] Morgan et al. presents a similar discussion for several conductive ceramics including ZrC.[150] These studies report the calculation of L by combining

equations (11) and (12), and substituting C/T (C is a constant) for k_p which gives equation (42). Multiplying through by T results in equation (43). This indicates that if kT is plotted with respect to T^2/ρ_e the slope is equal to the Lorenz number. The 1/T relation for k_p is the same relation indicated by the solution for k_p^U by equation (29). Therefore this is likely a good assumption at elevated temperatures ($T \geq \Theta_D$) at which phonon-electron scattering is dominant.

$$k = \frac{LT}{\rho_e} + \frac{C}{T} \tag{42}$$

$$kT = \frac{LT^2}{\rho_e} + C \tag{43}$$

This analysis may be beneficial in allowing Lorenz values to be calculated when their direct measurement may not be an option. These values of L may be more representative than the theoretical value if deviations in the Wiedemann-Franz law exist for a material. In addition, for previously presented research where the data exists, the Lorenz number could be evaluated and used to re-evaluate the contributions to k.

PAPER

I. Effect of Carbon and Oxygen Content of the Densification and Microstructure of Hot Pressed Zirconium Diboride

Gregory J. K. Harrington, Greg E. Hilmas, and William G. Fahrenholtz

Department of Materials Science and Engineering, Missouri University of Science and Technology, Rolla, Missouri 65409

Abstract

The role of carbon additions and oxygen content on the densification of zirconium diboride (ZrB_2) was studied. ZrB_2 with up to 1 wt% added carbon was hot pressed at temperatures of 2000 and 2100°C. Nominally pure ZrB_2 hot pressed at 2100°C achieved relative densities >95.5%. Carbon and oxygen analysis indicate that oxygen removal was facilitated by the reduction of oxides with carbon or the removal of boria (B_2O_3) as a vapor. Therefore, by removing oxides from the particle surfaces, carbon additions of ≥0.5 wt% enabled densification to proceed to >96.5% of theoretical at 2000°C. Raman spectroscopy revealed the formation of boron carbide ($B_{4.3}C$) in specimens with carbon additions of ≥0.75 wt%. The formation of $B_{4.3}C$ was eliminated via a 1 wt% addition of zirconium hydride (ZrH_2), as a source of zirconium, resulting in the formation of carbon as the only residual second phase. Grain sizes were in the range of 7-10 μm (2000°C) and 12-16 μm (2100°C) and only appeared to be controlled by temperature, as no trends due to the evaluated carbon or oxygen contents were observed.

1. Introduction

Zirconium diboride, because of its 3250°C melting point, is typically grouped in a family of materials deemed ultra-high temperature ceramics.[1] Attractive properties such as the melting temperature, high strength (565 MPa) and hardness (23 GPa), high thermal (88 W/m-K @ 100°C) and electrical conductivities (8.6×10^6 S-m^{-1}) relative to other ceramics, and good corrosion resistance to molten metals have spurred interest in

ZrB_2 research.[2-4] Development of ZrB_2 has sought to fill diverse applications such as molten metal crucibles, electronic substrates, nuclear cladding, and most heavily for thermal protection materials in future hypersonic aviation systems.[5-9]

Most of the proposed applications require fully dense and relatively pure ZrB_2 which can be difficult to fabricate because of various factors inherent to this material system. The typical transport mechanisms characteristic of solid-state sintering are grain boundary and lattice diffusion. Both cases proceed due to a reduction in surface free energy. Sintering requires significant mobility of the appropriate species to facilitate densification and inhibit the typical mechanisms associated with grain coarsening.[10] Coarsening reduces the driving force for densification, also resulting in the reduction of surface free energy, but without reducing porosity.[11] For ZrB_2, strong ionic (Zr to B) and covalent (B to B) bonding results in a large barrier to the diffusional processes necessary for densification.[12]

To promote solid state sintering of ZrB_2 and other similar diborides, many approaches have been taken. Kalish et al. employed uniaxial hot pressing to densify hafnium diboride (HfB_2) at pressures of ~410 MPa (60 ksi), ~790 MPa (115 ksi), and ~1150 MPa (225 ksi) at 1790°C and achieved relative densities of 93.2%, 98.6%, and 100% respectively.[13] Kalish demonstrated that extreme pressures promoted densification, especially compared to results by Brown-Shaklee et al. where hot pressing of HfB_2 at 2200°C and 32 MPa only resulted in 85.3% dense material.[14] Many researchers have evaluated the effect of temperature on densification and as expected, based on the kinetics of diffusion limited sintering, densification increases with increasing processing temperatures.[13,15,16] Fahrenholtz et al. and Thompson et al. have shown that particle size reduction by milling promotes densification of ZrB_2, in pressureless and pressure assisted densification respectively, due to the increased driving force of powders with higher surface free energy.[17,18] However, milling also

introduces contamination from the media (typically tungsten carbide (WC) or silicon carbide), which may adversely affect other properties. In addition to particle reduction by milling, the decreased particle size of ZrB_2 powder produced by a self-propagating high-temperature synthesis (SHS) reaction has been shown to promote densification.[19] However, it was also proposed that an increased defect concentration in the SHS powder over material produced by replacement or carbothermal reduction reactions may have helped promote densification.[20]

The presence of surface oxides further complicates the densification of ZrB_2. These native oxides form in the presence of atmospheric O_2 and H_2O, due to the pyrophoric nature of ZrB_2, similar to that of TiB_2.[21] The deleterious role surface oxides play in promoting coarsening through vapor phase transport of boron oxides was discussed for B_4C by Dole et al.[22] That study concluded that removing boria from the surface of B_4C improved densification. Similarly, Baik and Becher's work on titanium diboride also indicated that surface oxide impurities promoted evaporation-condensation processes and that, at higher temperatures, the metal oxide species were responsible for surface diffusion at particle interfaces.[23] Their conclusion was that oxide species promoted coarsening mechanisms, by surface transport, at temperatures lower than those required for densification of the diboride.

Several different reactions have been proposed to remove oxide impurities from diborides.[14-16,18,21] Usually, these reactions only consider reduction of the metal oxide (i.e., ZrO_2 for ZrB_2) because B_2O_3 can be removed by evaporation under mild vacuum conditions (e.g., ~20 Pa (150 mTorr) via mechanical pumping) at moderate temperatures (e.g., above ~1340°C). [18,22] Both the transition metal oxide and boria can be removed by, carbothermal reduction. For example, reaction (1) becomes favorable above 1140°C at standard state conditions or 775°C under vacuum (15 Pa (~110 mTorr)).[18] Therefore,

reaction (1) is important to consider due the favorability of consuming B_2O_3 at lower temperatures under vacuum prior to its volatilization.

$$ZrO_2 + B_2O_3 + 5C \rightarrow ZrB_2 + 5CO_{(g)} \quad (1)$$

In addition to removing surface oxides during densification, reaction (1) is also used for the production of commercial ZrB_2 powders.[4,23] Powders produced via carbothermal reduction typically contain carbon as a major impurity, providing further motivation to study the effect of carbon content on the processing and properties of ZrB_2.[23] Typical carbon impurity contents for commercial powders can range between 0.25 and 1.5%, by weight, depending on the manufacturer.[24-27]

The purpose of this study was to evaluate the effect of oxygen and carbon contents on the densification, microstructure development, and second phase formation in ZrB_2 compositions with carbon additions.

2. Experimental Procedure

2.1 Powder Processing

Starting materials used in this study were ZrB_2 (Grade B, H. C. Starck, Goslar, Germany), phenolic resin (GP 2074, Georgia-Pacific, Atlanta, GA) with a 41 wt% carbon yield, and ZrH_2 (Grade C, Chemetall GmbH, Frankfurt, Germany). Separate processing routines, and starting ZrB_2 powder lots, were used to produce the starting powders for the ZrB_2+C (lot 77718) and ZrB_2+C+ZrH_2 (lot 79115) specimens. All ZrB_2+C powder compositions were produced by mixing as-received ZrB_2 powder with phenolic resin and acetone. The mixture was stirred for 30 min, subsequently ultrasonicated for 10 min to disperse the powder, and then dried by rotary evaporation (Roto-vapor R-124, Buchi, Flawil, Switzerland). Pyrolysis, of the phenolic resin, was performed in a retort furnace. After pulling a mild vacuum (~84 kPa) and establishing a flow of Ar-10%H_2, the chamber was heated at 10°C/min and held at 600°C for 4 h. The ZrB_2+C+ZrH_2 compositions were

mixed by low energy ball milling (60 rpm in HDPE bottles) the ZrB_2 and ZrH_2 powders together in acetone using ZrB_2 milling media. After 1.5 h, phenolic resin was added and mixing continued for another 0.5 h. Rotary evaporation was used to dry the powders. Before hot pressing, all powders produced were crushed and sieved to -50 mesh. Table I indicates the specimen identification scheme and corresponding carbon addition, hot pressing temperature, and ZrH_2 addition used to produce each composition. For example, 0.75-20 is ZrB_2+0.75 wt% C hot pressed at 2000°C and 1-21-5 is ZrB_2+1 wt% C and 5 wt% ZrH_2 hot pressed at 2100°C.

2.2 Hot Pressing and Billet Preparation

All compositions were hot pressed (HP20-3060, Thermal Technologies, Santa Rosa, CA) under 32 MPa of pressure in a 44.5 mm diameter cylindrical graphite die, lined with boron nitride coated graphite foil. The phenolic resin in the ZrB_2+C+ZrH_2 compositions was pyrolyzed in the hot press by heating at a rate of 20°C/min and holding at 600°C for 0.5 h under flowing Ar as the first step, whereas the ZrB_2+C compositions that were pyrolyzed in the retort were not held at this temperature. Prior to establishing the flowing Ar, the furnace was evacuated to a pressure of ≤26 Pa. Isothermal holds at 1450 and 1650°C were performed on every composition until the vacuum recovered to 26 Pa. Before pressing, the furnace was switched to flowing Ar. ZrB_2+C compositions were hot pressed at temperatures of either 2000°C or 2100°C while the compositions with ZrH_2 were only pressed at 2100°C. A 30°C/min ramp was used from 1650°C up to the densification temperature and this temperature was maintained until ram travel ceased for 10 min. Ram pressure was maintained during cooling until 1650°C and travel was recorded with respect to temperature. Ram travel data were then used to correct for thermal expansion during heating for densification curves.

2.3 Characterization

Each billet was surface ground to remove the outermost material from the faces and subsequently sectioned to produce specimens for characterization. The Archimedes method was used to obtain the bulk density. Specimens were ground and diamond polished to a 0.25 μm finish for electron microscopy (S-570, Hitachi, Ibaraki, Japan) and confocal Raman spectroscopy (Aramis Labram, Horiba Jobin Yvon, Edison, NJ). Polished specimens were also thermally (1500°C for 10 min in vacuum) or chemically (100% molten KOH for <1 sec) etched for grain size analysis. SEM images of as-polished and etched specimens were analyzed using image analysis software (ImageJ, National Institutes of Health, West Bethesda, MD) to obtain second phase volume fractions and grain sizes. Minimum and maximum grain size values from at least 500 grains were averaged to obtain the grain sizes reported for each composition. X-ray diffraction (XRD; X'Pert Pro, PANalytical, Almelo, Netherlands) analysis was also used for phase identification. Quantification of carbon content (CS600, Leco, St. Joseph, MI) in the densified materials was performed on each composition after grinding to -200 mesh using an alumina mortar and pestle. Whereas, oxygen content (TC500, Leco, St. Joseph, MI) was evaluated using coarsely crushed densified material. Finally, the carbon and oxygen contents of the as-pyrolyzed ZrB_2+C and ZrB_2+C+ZrH_2 compositions and starting as-received powders were also evaluated.

3. Results and Discussion

3.1 Formation of Boron Carbide

Second phase formation was observed in all compositions with carbon additions of 0.75 wt% or above (specimens 0.75-20, 0.75-21, 1-20, and 1-21). In a representative image of specimen 1-20 (Fig 1), the second phase appeared as black, non-spherical particles. Raman spectra, of the second phase, (Fig 2) match $B_{4.3}C$ as reported by Werheit et al.[28],

indicating that the second phase is likely carbon saturated boron carbide. Areal analysis showed the compositions formulated with 0.75 wt% carbon contained between 0.40 and 0.43 vol% $B_{4.3}C$ (Table II). An increase in the carbon addition from 0.75 wt% to 1 wt% produced an increase in the total volume of $B_{4.3}C$ to, between 0.6 and 1.1 vol%. In addition, the average size of the $B_{4.3}C$ inclusions appeared to grow, with increasing carbon additions, from ~1.9 µm for the 0.75 wt% C specimens to between 2.6 and 2.9 µm for the 1 wt% specimens. Therefore, because the amount and size of the $B_{4.3}C$ increased as the carbon addition increased, the formation of $B_{4.3}C$ appears to be controlled by the presence and amount of carbon. Also, since $B_{4.3}C$ formation was only identified in the two highest carbon addition compositions, it is possible that the presence of residual carbon (to be described later in the discussion) allowed for a reaction with boron, either from B_2O_3 or ZrB_2, to form a significant amount of second phase.

A thorough review of the diboride literature revealed that the formation of boron carbide, as the result of adding carbon to a diboride, has not been reported to date. Two explanations are possible. First, the formation of $B_{4.3}C$ may have been ignored or missed since the volume fraction is small and $B_{4.3}C$ is difficult to detect by XRD. Second, other impurities, such as WC which is commonly introduced through milling, could have inhibited $B_{4.3}C$ formation. As discussed by Brown-Shaklee et al., based on the B-W-C ternary phase diagram, WC and $B_{4.3}C$ are not compatible and, therefore, $B_{4.3}C$ formation is not likely in materials with WC contaminants.[14]

To eliminate the formation of $B_{4.3}C$, a second set of compositions was formulated with ZrH_2 (Table I). According to the Zr-B-C ternary phase diagram, B_4C and Zr are not chemically compatible as indicated by the lack of an Alkemade line (i.e., a true binary join) between the two compositions. A system with B_4C and Zr could result in the formation of various combinations of compatible phases, depending on the relative

amounts of the two reactants, which can be represented by a line drawn from Zr to B_4C. Most notably, this line intersects the Alkemade line between ZrB_2 and carbon, so an appropriate Zr addition should produce only ZrB_2+C as represented by Reaction (2). Smaller additions of Zr would result in overall compositions that lie in the ZrB_2+B_4C+C compatibility region.[29]

$$B_4C + 2Zr \rightarrow 2ZrB_2 + C \quad (2)$$

Despite the addition of 0.25 wt% ZrH_2, $B_{4.3}C$ was present in specimen 1-21-0.25 after hot pressing. However, the volume fraction of $B_{4.3}C$ was ~0.6 vol%, which was lower than the $B_{4.3}C$ content of ~1.5 vol% found in specimen 1-21 that was not formulated with ZrH_2 (Table I). The reduction in $B_{4.3}C$ content indicated Reaction (2) proceeded, but that the Zr addition was insufficient to completely eliminate the formation of $B_{4.3}C$. With the addition of 5 wt% ZrH_2 (composition 1-21-5), XRD analysis (Fig 3) identified peaks corresponding to zirconium carbide (ZrC, PDF 73-0477[30]). Thus, while insufficient Zr content left residual $B_{4.3}C$, the addition of excess Zr resulted in a reaction with free carbon to produce ZrC represented by Reaction (3).

$$B_4C + 3Zr \rightarrow 2ZrB_2 + ZrC \quad (3)$$

To produce ZrB_2 with only carbon as a second phase, an appropriate addition of Zr is required to inhibit $B_{4.3}C$ formation without adding enough to produce ZrC. Based on the volume fractions of $B_{4.3}C$ and ZrC from specimens 1-21-0.25 and 1-21-5, it was determined that an addition of 1 wt% ZrH_2 should be adequate and specimen 1-21-1 (Fig 4) was prepared based on this analysis. The microstructure of 1-21-1 was free of $B_{4.3}C$ and ZrC. Instead, only dark particles with an acicular morphology (Fig. 4) were observed as a second phase. Based on the two peaks in the Raman spectra (Fig 2) that match results by Vidano et al., the second phase appears to be carbon with a disordered

graphitic structure.[31] Further, this carbon seemed to form at the grain boundaries and was evenly distributed throughout the microstructure. Even though both carbon and $B_{4.3}C$ show up as dark particles in the SEM micrographs, the carbon morphology was significantly different than the $B_{4.3}C$ that was observed in specimen 1-20 (Fig 1) which appeared as larger, equiaxed particles. Based on the analysis of the second phase in 1-21-1, the addition of 1 wt% ZrH_2 supplied sufficient Zr to allow Reaction (2) to go to completion without producing ZrC by Reaction (3). The expected phase equilibria, as a result of Reactions (2) and (3), are consistent with prediction made based on the Zr-B-C phase diagram, but are not meant to indicate the actual reactions occurring. For example, Wang et al. reports that Reaction (3) should proceed at temperatures ≥900°C.[32] Therefore, B and C species may react with Zr without the actual formation of $B_{4.3}C$.

3.2 Effect of Temperature and Carbon Additions on Densification

Relative densities, of the specimens produced in this study, (Table III) were calculated based on measured bulk densities and calculated theoretical densities. The constituent theoretical densities used were 6.15 g/cm^3 for ZrB_2[33], 2.20 g/cm^3 for carbon[34], 2.49 g/cm^3 for $B_{4.3}C$[35], and 6.73 g/cm^3 for ZrC[30]. Finally, the volume fractions of the second phases were assumed to be equivalent to the area fractions determined using image analysis. The two lowest carbon content addition materials (0-20 and 0.125-20) had relative densities of less than 80% after hot pressing at 2000°C. In contrast, higher carbon contents resulted in relative densities of 96% or higher after hot pressing at 2000°C. Increasing the hot pressing temperature to 2100°C resulted in relative densities greater than 95% for all compositions regardless of carbon content. Aside from the change in amount or type of second phase produced, the ZrH_2 additions had no effect on densification, where all compositions had relative densities greater than 99%. It is clear from these density results that carbon is an effective sintering aid for ZrB_2.

Curves of relative density, as a function of time, for specimens hot pressed at 2000°C and 2100°C (Fig 5 and Fig 6) indicate the positive effect that carbon additions and hot pressing temperatures had on the densification of ZrB_2. In general, the rate of densification increased as the starting carbon content increased, for both temperatures. The exceptions to this were the 0 wt% C material at both 2000 and 2100°C and composition 1-21. Densification of specimen 1-21 was clearly different from the trends observed for other compositions; however, the reason for the decrease in densification is not clear. Compared to the 0.125 wt% C compositions hot pressed at 2000°C and 2100°C, and the 0.5 wt% C specimen at 2100°C, the 0 wt% C materials had higher densification rates that would suggest a difference between the as-received powder and those that went through processing to add carbon.

Figures 5 and 6 also show the interconnected role of carbon and temperature on the densification of ZrB_2. The difference in density was up to ~7% at time zero between the compositions with the highest and lowest carbon additions, for example ~47% for 1-20 compared to ~40% for 0.125-20. This indicates significant densification may have occurred at or below the 1650°C isothermal hold for the higher carbon content compositions. Also, increasing the processing temperature proved to have the greatest effect on densification for the 0 and 0.125 wt% C compositions, which only densified to 77-79% of theoretical at 2000°C, but reached densities greater than 95% when processed at 2100°C. All of the compositions containing 0 and 0.125 wt% C densified to between 56-59% at the 10 min (2000°C) mark. However, beyond this point the densification rate tapered off for these compositions hot pressed at 2000°C, as compared with the same powders pressed at 2100°C, which experienced a continuing higher rate of densification, promoted by the increase in processing temperature.

Figure 7 provides another view of the effect of carbon on the densification of the various compositions, by showing the time at temperature required to reach full density

as a function of the amount of carbon added. In general, the hold times needed for densification decreased as carbon content and temperature increased. The maximum hold times for 2000°C and 2100°C were 65 and 35 min, respectively, both for the 0.125 wt% C compositions. A lower threshold in the time for densification was apparent for the higher carbon additions. Compositions with at least 0.75 wt% C densified within 20 min at 2000°C or 10 min at 2100°C (it should be noted that all specimens were pressed until ram travel ceased for 10 min making this the lowest possible time by default). This may indicate that for the highest carbon additions the carbon content was sufficient to fully reduce any surface oxides that would have inhibited densification. In addition, the appearance of a second phase for the higher carbon contents (i.e., ≥0.75 wt% C) supports this hypothesis because $B_{4.3}C$ can only form after enough carbon is added to leave excess carbon after the surface oxides are removed. The densification times for 0-20 (52 min) and 0-21 (19 min) went against the trend of decreasing time at temperature with increasing carbon additions, which again suggests a difference between the as-received material and the compositions that went through the carbon addition process, which involved dispersion in acetone and pyrolysis within the retort.

3.3 Carbon and Oxygen Content

Figure 8 shows the carbon content measured after densification as a function of the amount of carbon added to the compositions without ZrH_2. Without any reactions, a continuous linear increase in the measured carbon content would be expected with increased carbon additions. However, the final carbon contents appeared to exhibit two regimes of behavior, with the transition between additions of 0.75 and 1 wt% carbon. For carbon additions from 0 to 0.75 wt% C, the measured carbon contents were all below 0.04 wt% and did not appear to increase as the amount of carbon added was increased. In contrast, both of the compositions with 1 wt% C had significantly higher final carbon contents of 0.1 wt% for 1-20 and 0.075 wt% for 1-21. This observation gives further

support to the hypothesis that carbon reacts with surface oxides. For the lower carbon additions, carbon was the limiting reactant and nearly all of the carbon that was added was consumed. After the carbon additions increased to a point where the surface oxides had been reduced to some equilibrium level, the final carbon content increased in proportion to the amount added. Because $B_{4.3}C$ was formed for carbon additions of 0.75 wt% or higher, this composition was believed to have reached the necessary carbon addition threshold for maximum oxide removal based on what is known about the stability of Zr/B oxide species in the presence of $B_{4.3}C$.[18,36-38]

For compositions that densified, more than 95 wt% of the initial oxygen content was removed during hot pressing. The final oxygen contents for the dense compositions were all less than 0.03 wt% with no systematic variations in oxygen content with carbon additions. Because Reaction (1) was thought to control oxygen removal, the initial assumption was that the molar ratio of carbon consumed to oxygen removed (C/O) would be one. However, as can be seen in Table IV, C/O was less than one for every composition. This indicates that more oxygen was removed than what should have been possible if Reaction (1) were the only oxygen removal process. The most likely explanation for the greater-than-expected loss of oxygen is B_2O_3 evaporation by Reaction (4) during heating under vacuum. Compositions with carbon additions <0.75 wt% did not have enough carbon to consume all the B_2O_3 via Reaction (1), so Reaction (4) was necessary to achieve the final measured oxygen contents. Finally, as a boron source was needed for the formation of $B_{4.3}C$ in the 0.75 and 1 wt% carbon compositions, Reaction (5) is likely to have proceeded in reducing the B_2O_3 after the ZrO_2 had been exhausted by Reaction (1).

$$B_2O_3 \rightarrow B_2O_{3(g)} \tag{4}$$

$$2B_2O_3 + 7C \rightarrow B_4C + 6CO_{(g)} \tag{5}$$

Evaluation of the powder compositions prior to powder processing and hot pressing (Table IV) revealed differences in the oxygen contents that can explain variations observed between the densified materials. All ZrB_2+C compositions were produced with the same lot of powder (lot 77718) but oxygen analysis showed that, after powder processing, the oxygen level increased between 29-79% over the 1.25 wt% O (Table IV) that was present in the starting powder. This increase is the most likely cause of the improved densification of the unprocessed 0 wt% C material over that of the 0.125 wt% C compositions (i.e., processing the 0.125 wt% C addition powder increased the oxygen content relative to the as-received powder while not providing enough carbon to improve densification). In addition to effects of processing on oxygen content, the use of separate powder lots for the ZrB_2+C (lot 77718, 1.25 wt% O) and ZrB_2+C+ZrH_2 (lot 79115, 0.85 wt% O) compositions showed the importance of the oxygen content of the starting powder. The increased starting oxygen content within lot 77718 carried through the powder processing steps leaving oxygen contents higher within the as-processed ZrB_2+C compositions than those made with lot 79115. Because an increase in the oxygen content of the powder will consume more carbon by reaction with oxygen, these differences in oxygen contamination explain the significant variance in as-hot pressed carbon contents between specimen 1-21 (0.076 wt% C) and the ZrH_2 addition material (0.55-0.58 wt% C) (Table IV). Through the evaluation of densification results and final carbon contents, the importance of oxygen content within the powder has been further demonstrated.

3.4 Microstructure and Grain Size

For compositions that were nearly fully dense, the ZrB_2 grain size did not vary significantly with the amount of carbon added (Fig 9). The 2100°C ZrB_2+C materials all had grain sizes between 12 and 17 μm with no statistically significant variations. SEM images of the 0 and 1 wt% carbon contents hot pressed at 2100°C (Fig 10) demonstrate

the similarity in the grain sizes across the range of carbon additions. The main difference was the decrease in porosity from ~4.4% (specimen 0-21) to ~1.5% (specimen 1-21), clearly showing the benefit of carbon as a sintering aid. When carbon was not added, the majority of residual porosity was trapped within grains, with little or no porosity present at the grain boundaries, suggesting that 0-21 had reached a limiting value of relative density. The entrapped porosity was likely the result of rapid grain coarsening from the starting average ZrB_2 particle size (~2 μm) to the final grain size of the densified material (≥12 μm) at some point during the densification cycle. Since little porosity was observed at the grain boundaries for any composition, the practice of ending the high temperature hold (2000°C or 2100°C) during hot pressing after ten minutes of zero travel was successful in densifying ZrB_2 while minimizing further grain growth.

On average, the grain size of the ZrB_2+C compositions hot pressed at 2000°C (7-10 μm) was smaller than the same or similar compositions hot pressed at 2100°C (12-19 μm). This would be expected due to the lower driving force for grain coarsening at the lower processing temperatures. This increase in grain size with increasing hot pressing temperature can be observed by comparing the microstructures of 0.75-20 and 0.75-21 (Fig 11). With the exception of the 5 wt% ZrH_2 composition, which was nearly identical in grain size to the 2100°C ZrB_2+C specimens, the other two ZrB_2+C+ZrH_2 compositions had grain sizes that were identical to the 2000°C ZrB_2+C compositions despite being hot pressed 100°C higher in temperature. Apparently, the ZrB_2+C+ZrH_2 compositions with 0.25 or 1 wt% ZrH_2 exhibited a reduction in the driving force for grain coarsening compared to compositions formulated with only carbon. Similar to the conclusion reached by Brown-Shaklee et al. for densification of HfB_2,[14] grain growth in ZrB_2 does not appear to be pinned by carbon additions, at least for the composition range for this study.

3.5 Processing map

Figure 12 is a processing map produced to help visualize the regimes of densification and second phase formation as well as the trends in grain coarsening. The behavior was mapped according to carbon and ZrH_2 additions. Densification is favorable for all compositions at 2100°C but additions of at least 0.5 wt% C helped achieve the same results at 2000°C while producing finer final grain sizes. The bottom (blue) hatched region corresponds to $B_{4.3}C$ formation which was a result of the reaction between carbon and excess boron. Stability moves into the ZrB_2+C (red) or ZrB_2+ZrC (green) regions depending on the total addition of the Zr source. In addition, these conditions likely apply for any ZrB_2 powders with oxygen contents of <2 wt% prior to densification. Variations in starting oxygen content would increase the amount of carbon and/or ZrH_2 needed to facilitate oxygen removal, promote densification, and stabilize the desired phases, but the trends should be consistent for any standard commercial ZrB_2 source.

4. Summary and Conclusions

The purpose of this study was to evaluate the effects of carbon and oxygen contents on the densification behavior, microstructure development, and phase equilibria of ZrB_2. Both ZrB_2+C and ZrB_2+C+ZrH_2 compositions were densified via hot pressing under 32 MPa with the former being densified at 2000 and 2100°C and the later only at 2100°C. $B_{4.3}C$ was present in ZrB_2+C compositions with ≥0.75 wt% added C. Additions of ZrH_2 either decreased $B_{4.3}C$ formation or produced C or ZrC second phases, depending on whether the system was deficient, neutral, or rich in Zr.

Only compositions with ≥0.5 wt% C reached relative densities of >96% when hot pressed at 2000°C. However, at 2100°C all compositions were densified to at least 95.6%. Densification curves indicated that the highest carbon additions resulted in a lower onset temperature for densification. Carbon additions were shown to have little

effect on grain size and hot pressing temperatures played the largest role in changing the resultant grain size when the hot pressing time was determined by the cessation of ram travel. As a result, ZrB_2+C specimens densified at 2000°C had grain sizes between 7 and 10 µm on average and specimens processed at 2100°C had grain sizes of 12-19 µm.

With increasing carbon additions up to 0.75 wt%, the resulting C content was 0.04 wt% or below, while the final carbon increased to between 0.075 and 0.1 wt% C for the 1 wt% C compositions. Final oxygen contents for all specimens >95% dense were <0.03 wt% despite the differing C contents. Several conclusions can be drawn about removal of O from ZrB_2 based on the results in this study.

1. Carbon reacts with oxide impurities due to the carbothermal reduction reaction and decreases the oxygen content of the resulting ceramics.
2. Oxygen can also be removed by the evaporation of B_2O_3.
3. Reduction of B_2O_3 is the most likely source of boron for the subsequent formation of the observed $B_{4.3}C$.
4. Improved densification of ZrB_2 was, at the least, facilitated by the reduction B_2O_3 (due to C additions) which at higher temperatures, as either a liquid or vapor, could have led to detrimental grain coarsening.

References

1. R.A. Cutler, "Engineering Properties of Borides," pp. 787-803 in Engineered Materials Handbook, Vol. 4, *Ceramics and Glasses.* Edited by S.J. Schneider Jr. ASM International, Materials Park, OH, 1991.

2. A.L. Chamberlain, W.G. Fahrenholtz, G.E. Hilmas, and D.T. Ellerby, "High-Strength Zirconium Diboride-Based Ceramics," *J. Am. Ceram. Soc.,* **87** [6] 1170-2 (2004).

3. R.P. Tye and E.V. Clougherty, "The Thermal and Electical Conductivities of Some Electrically Conducting Compounds," *Proceedings of the Fifth Symposium on Thermophysical Properties, New York American Society of Mechanical Engineers,* Boston, MA, September 30-October 2, 396-401 (1970).

4. C. Mroz, "Zirconium Diboride," *Am. Ceram. Soc. Bull.,* **73** [6] 141-2 (1994).

5. N. Kaji, H. Shikano, and I. Tanaka, "Develpment of ZrB_2-Graphite Protective Sleeve for Submerged Nozzle," *Taikabutsu Overseas,* **14** [2] 39-43 (1992).

6. N.L. Okamoto, M. Kusakari, K. Tanaka, H. Inui, M. Yamaguchi, and S. Otani, "Temperature dependence of thermal expansion and elastic constants of single crystals of ZrB_2 and the suitability of ZrB_2 as a substrate for GaN film," *J. Appl. Phys.,* **93** [1] 88-93 (2003).

7. P. Rogl and H. Bittermann, "On the Ternary System Hafnium–Boron–Carbon," *J. Solid State Chem.,* **154** [1] 257-62 (2000).

8. M.M. Opeka, I.G. Talmy, and J.A. Zaykoski, "Oxidation-based materials selection for 2000°C + hypersonic aerosurfaces: Theoretical considerations and historical experience," *J. Mater. Sci.,* **39** [19] 5887-904 (2004).

9. M.J. Gasch, D.T. Ellerby, and S.M. Johnson, "Ultra High Temperature Ceramic Composites " pp. 197-224 in *Handbook of Ceramic Composites.* Edited by N.P. Bansal. Springer, New York, 2005.

10. N. Rahaman, *Ceramic Processing*. CRC/Taylor & Francis, Boca Raton, 2007.

11. W.D. Kingery, H.K. Bowen, and D.R. Uhlmann, *Introduction to ceramics*. John Wiley and Sons, New York, 1976.

12. P. Vajeeston, P. Ravindran, C. Ravi, and R. Asokamani, "Electronic structure, bonding, and ground-state properties of AlB_2-type transition-metal diborides," *PhRvB,* **63** [4] 045115-(1-12) (2001).

13. D. Kalish and E.V. Clougherty, "Densification Mechanisms in High-pressure Hot-Pressing of HfB_2," *J. Am. Ceram. Soc.,* **52** [1] 26-30 (1969).

14. H.J. Brown-Shaklee, W.G. Fahrenholtz, and G.E. Hilmas, "Densification Behavior and Microstructure Evolution of Hot-Pressed HfB_2," *J. Am. Ceram. Soc.,* **94** [1] 49-58 (2011).

15. A.L. Chamberlain, W.G. Fahrenholtz, and G.E. Hilmas, "Pressureless Sintering of Zirconium Diboride," *J. Am. Ceram. Soc.,* **89** [2] 450-6 (2006).

16. S. Zhu, W.G. Fahrenholtz, G.E. Hilmas, and S.C. Zhang, "Pressureless sintering of carbon-coated zirconium diboride powders," *Materials Science and Engineering: A,* **459** [1–2] 167-71 (2007).

17. M. Thompson, W.G. Fahrenholtz, and G. Hilmas, "Effect of Starting Particle Size and Oxygen Content on Densification of ZrB_2," *J. Am. Ceram. Soc.,* **94** [2] 429-35 (2011).

18. W.G. Fahrenholtz, G.E. Hilmas, S.C. Zhang, and S. Zhu, "Pressureless Sintering of Zirconium Diboride: Particle Size and Additive Effects," *J. Am. Ceram. Soc.,* **91** [5] 1398-404 (2008).

19. S.K. Mishra (Pathak), S. Das, S.K. Das, and P. Ramachandrarao, "Sintering studies on ultrafine ZrB_2 powder produce by a self-propagating high-temperature synthesis process," *J. Mater. Res.,* **15** [11] 2499-504 (2000).

20. S.K. Mishra, S. Das, and L.C. Pathak, "Defect structures in zirconium diboride powder prepared by self-propagating high-temperature synthesis," *Materials Science and Engineering: A,* **364** [1–2] 249-55 (2004).

21. H.R. Baumgartner and R.A. Steiger, "Sintering and Properties of Titanium Diboride Made from Powder Synthesized in a Plasma-Arc Heater," *J. Am. Ceram. Soc.,* **67** [3] 207-12 (1984).

22. S.L. Dole, S. Prochazka, and R.H. Doremus, "Microstructural Coarsening During Sintering of Boron Carbide," *J. Am. Ceram. Soc.,* **72** [6] 958-66 (1989).

23. V.I. Matkovich, G.V. Samsonov, and P. Hagenmuller, *Boron and Refractory Borides*. Springer, Berlin; New York [etc.], 351-76, 1977.

24. D. Sciti, S. Guicciardi, A. Bellosi, and G. Pezzotti, "Properties of a Pressureless-Sintered ZrB_2–$MoSi_2$ Ceramic Composite," *J. Am. Ceram. Soc.,* **89** [7] 2320-2 (2006).

25. S.-H. Lee, Y. Sakka, and Y. Kagawa, "Dispersion Behavior of ZrB_2 Powder in Aqueous Solution," *J. Am. Ceram. Soc.,* **90** [11] 3455-9 (2007).

26. T. Baldridge, M.C. Gupta, and C.-N. Sun, "Nanostructures from Zirconium Diboride and Alumina Ceramics," *J. Am. Ceram. Soc.,* **93** [9] 2891-6 (2010).

27. Treibacher Industrie Ag, Zircnoium Diboride data sheet/chemical analysis, Auer von Welsbach Straße 1, A9660 Althofen, Austria, www.treibacher.com.

28. H. Werheit, V. Filipov, U. Schwarz, M. Armbruster, A. Leithe-Jasper, T. Tanaka, and S.O. Shalamberidze, "On surface Raman scattering and luminescence radiation in boron carbide," *J. Phys.: Condens. Matter,* **22** [4] 045401 (2010).

29. E. Rudy and S. Windisch, Figure No. 08874 - Zr-B-C Ternary System, ACerS-NIST Phase Equilibria Diagrams Online, ACerS-NIST Phase Equilibria Diagrams Online, (1966).

30. Card number 73-0477, Powder Diffraction File, International Centre for Diffraction Data.

31. R. Vidano and D.B. Fischbach, "New Lines in the Raman Spectra of Carbons and Graphite," *J. Am. Ceram. Soc.,* **61** [1-2] 13-7 (1978).

32. X.-G. Wang, W.-M. Guo, Y.-M. Kan, and G.-J. Zhang, "Hot-Pressed ZrB_2 Ceramics With Composite Additives of Zr and B_4C," *Adv. Eng. Mater.,* **12** [9] 893-8 (2010).

33. E.W. Neuman, G.E. Hilmas, and W.G. Fahrenholtz, "Strength of Zirconium Diboride to 2300°C," *J. Am. Ceram. Soc.,* **96** [1] 47-50 (2013).

34. D. Lide, *CRC Handbook of Chemistry and Physics,* 88th ed. CRC, Boca Raton, 2007.

35. F. Thévenot, "Boron carbide—A comprehensive review," *J. Eur. Ceram. Soc.,* **6** [4] 205-25 (1990).

36. S.C. Zhang, G.E. Hilmas, and W.G. Fahrenholtz, "Pressureless Densification of Zirconium Diboride with Boron Carbide Additions," *J. Am. Ceram. Soc.,* **89** [5] 1544-50 (2006).

37. S. Zhu, W.G. Fahrenholtz, G.E. Hilmas, and S.C. Zhang, "Pressureless Sintering of Zirconium Diboride Using Boron Carbide and Carbon Additions," *J. Am. Ceram. Soc.,* **90** [11] 3660-3 (2007).

38. A. Goldstein, Y. Geffen, and A. Goldenberg, "Boron Carbide–Zirconium Boride In Situ Composites by the Reactive Pressureless Sintering of Boron Carbide–Zirconia Mixtures," *J. Am. Ceram. Soc.,* **84** [3] 642-4 (2001).

Fig 1. SEM image of specimen 1-20 showing dark (low Z) second phase boron carbide particles in addition to the smaller finely dispersed pores.

Fig 2. Raman spectroscopy verifying the presence of $B_{4.3}C$ and C in samples 1-20 and 1-21-1, respectively.

Fig 3. XRD of specimen 1-21-5 showing the presence of ZrC formed from the addition of excess Zr.

Fig 4. Micrograph of 1-21-1 showing the formation of carbon in the microstructure as finely distributed elongated second phase particles which appear to have formed along grain boundaries.

Fig 5. Relative density and furnace temperature as a function of hot pressing time for 2000°C ZrB_2+C specimens.

Fig 6. Relative density and furnace temperature as a function of hot pressing time for 2100°C ZrB_2+C and ZrB_2+C+ZrH_2 specimens.

Fig 7. Time at temperature to achieve maximum densification as a function of carbon additions for all carbon and C+ZrH_2 compositions

Fig 8. Measured carbon content as a function of added carbon for both 2000 and 2100°C ZrB_2+C material.

Fig 9. Average grain size as a function of carbon additions for ZrB_2+C (squares and triangles, bottom axis) and ZrH_2 addition for ZrB_2+C+ZrH_2 (stars, top axis).

Fig 10. SEM micrographs of 0-21 (A) and 1-21 (B) showing no differences in grain size as carbon content is increased.

Fig 11. SEM images of 0.75-20 (A) and 0.75-21 (B) showing the increase in grain size resulting from an increase in densification temperature.

Fig 12. Processing map detailing conditions for densification, second phase formation, and grain growth for ZrB_2, with a nominal initial oxygen content of <2 wt% for hot pressing at 32 MPa with respect to additions of carbon and zirconium.

Table I. Compositions, Temperatures, and Corresponding Specimen ID Format for Each Material

Sample ID	Carbon Addition (wt%)	Pressing Temperature (°C)	ZrH_2 Addition (wt%)
x-20	x = (0, 0.125, 0.5, 0.75, or 1)	2000	--
x-21	x = (0, 0.125, 0.5, 0.75, or 1)	2100	--
x-21-y	x = 1	2100	y = (0.25, 1, or 5)

Table II. Volume Fraction and Particle Size for Second Phases Formed in 0.75 and 1 wt% C and ZrH_2 Material

Sample ID	2nd Phase(s)	Volume %	Particle Size (μm)	
			Average	Maximum
0.75-20	$B_{4.3}C$	0.43	1.93	5.81
0.75-21	$B_{4.3}C$	0.40	1.97	8.15
1-20	$B_{4.3}C$	0.99	2.60	6.91
1-21	$B_{4.3}C$	1.46	2.92	7.27
1-21-0.25	$B_{4.3}C$, (C)	0.59 (2.02)	2.63 (-)	9.11 (-)
1-21-1	C	2.23	-	-
1-21-5	ZrC, (C)	4.74 (0.70)	3.36 (-)	17.66 (-)

Table III. Bulk, Theoretical, and Resulting Relative % Density Values

Sample ID	Bulk Density (g/cm^3)	Theoretical Density (g/cm^3)	$\rho_{relative}$ (%)
0-20	4.89	6.15	79.5
0.125-20	4.73	6.15	76.9
0.5-20	5.98	6.15	97.3
0.75-20	5.93	6.13	96.6
1-20	5.93	6.11	96.9
0-21	5.88	6.15	95.6
0.125-21	5.90	6.15	95.9
0.5-21	5.96	6.15	96.9
0.75-21	5.94	6.14	96.8
1-21	6.00	6.10	98.5
1-21-0.25	6.03	6.05	99.7
1-21-1	6.03	6.06	99.5
1-21-5	6.09	6.15	99.1

Table IV. Carbon and Oxygen Content Analysis of Starting Powders and As-Hot Pressed Material Separated by Lot # and Pyrolysis Procedure

ZrB_2 Powder Lot	Pyrolysis	Sample ID	Carbon Content (wt%)		Oxygen Content (wt%)		% of Material Lost or Consumed		Removed C/O Molar Ratio
			Starting Powder	Hot Pressed	Starting Powder	Hot Pressed	Carbon	Oxygen	
77718	NA	0-20	0.088±0.002	0.025±0.003	1.25	0.19	71.7	85.2	0.079
	Retort	0.125-20	0.17±0.03	0.019±0.008	1.79	0.084	88.7	95.3	0.12
		0.5-20	0.56±0.03	0.037±0.008	1.62	0.025	93.3	98.4	0.44
		0.75-20	0.80±0.06	0.037±0.002	2.24	0.005	95.4	99.8	0.46
		1-20	1.28±0.10	0.098±0.001	1.74	0.015	92.4	99.1	0.92
	NA	0-21	0.088±0.002	0.031±0.003	1.25	0.044	64.5	96.5	0.06
	Retort	0.125-21	0.17±0.03	0.035±0.002	1.79	0.028	79.1	98.4	0.10
		0.5-21	0.56±0.03	0.032±0.005	1.62	0.028	94.3	98.3	0.44
		0.75-21	0.80±0.06	0.041±0.004	2.24	0.009	94.9	99.6	0.45
		1-21	1.28±0.10	0.076±0.006	1.74	0.012	94.1	99.3	0.94
79115	As-received powder analysis		0.087±0.003	NA	0.85	NA	NA	NA	NA
	Hot Press	1-21-0.25	1.34±0.004	0.58±0.01	1.21	0.007	57.5	99.4	0.86
		1-21-1	1.36±0.03	0.55±0.02	1.19	0.006	58.8	99.5	0.88
		1-21-5	X	0.56±0.01	X	0.070	X	X	X

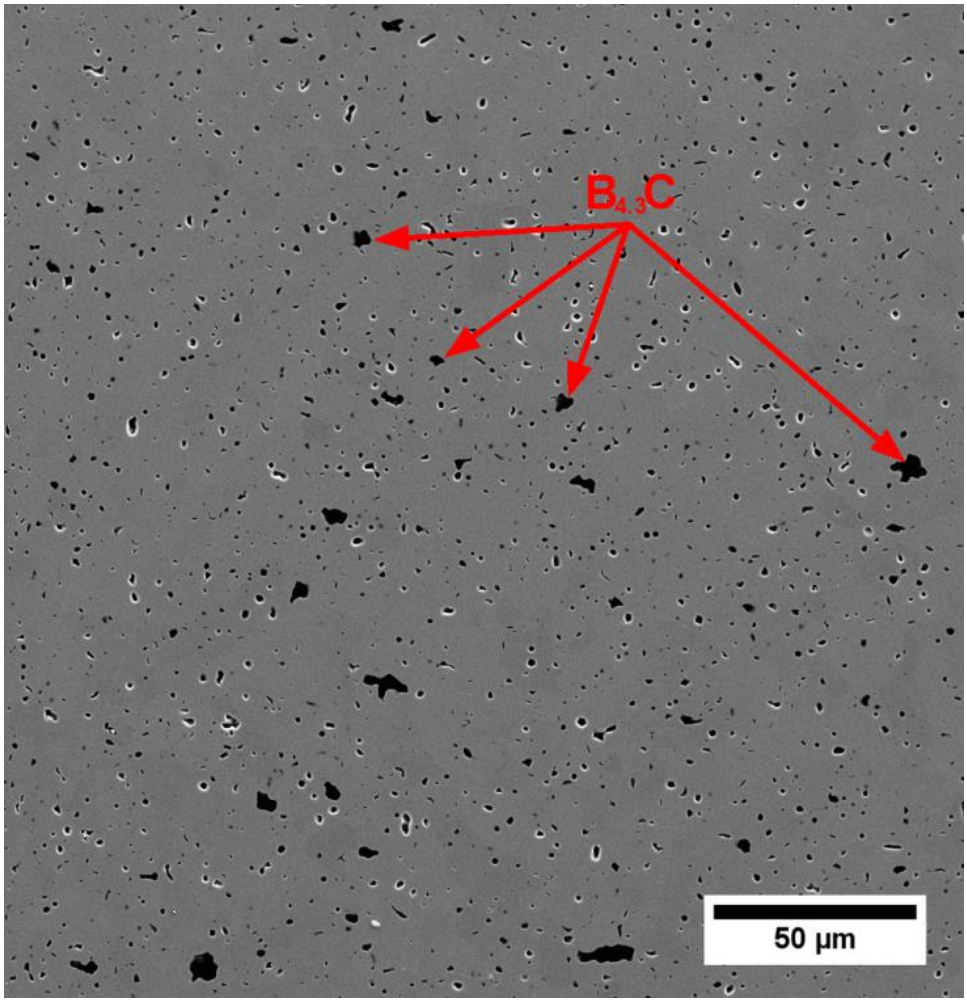

Fig 1. SEM image of specimen 1-20 showing dark (low Z) second phase boron carbide particles in addition to the smaller finely dispersed pores.

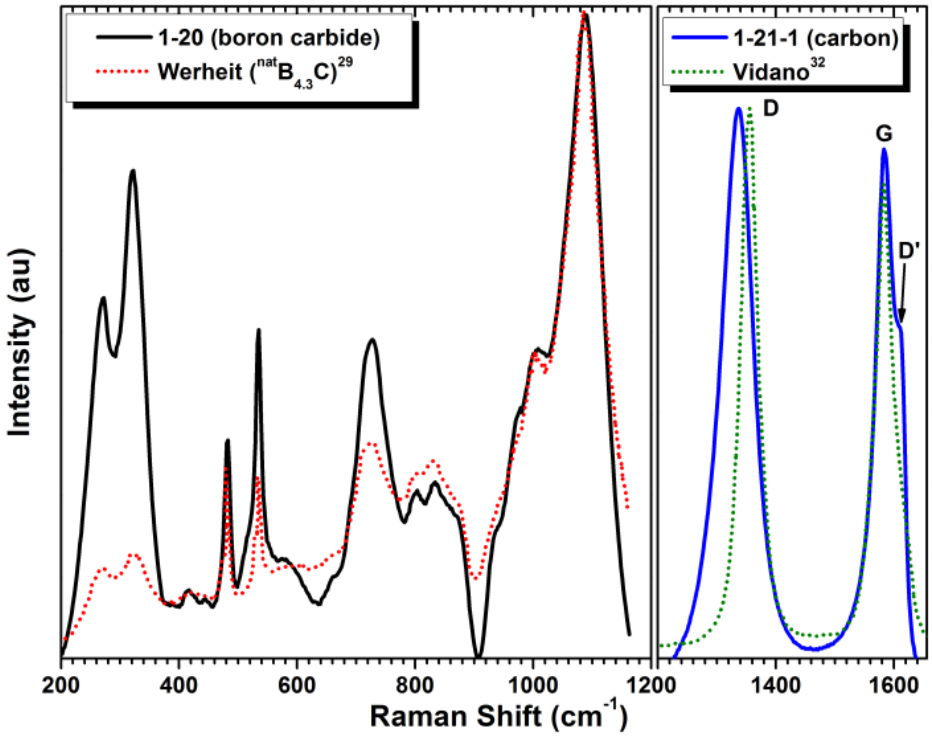

Fig 2. Raman spectroscopy verifying the presence of $B_{4.3}C$ and C in samples 1-20 and 1-21-1, respectively.

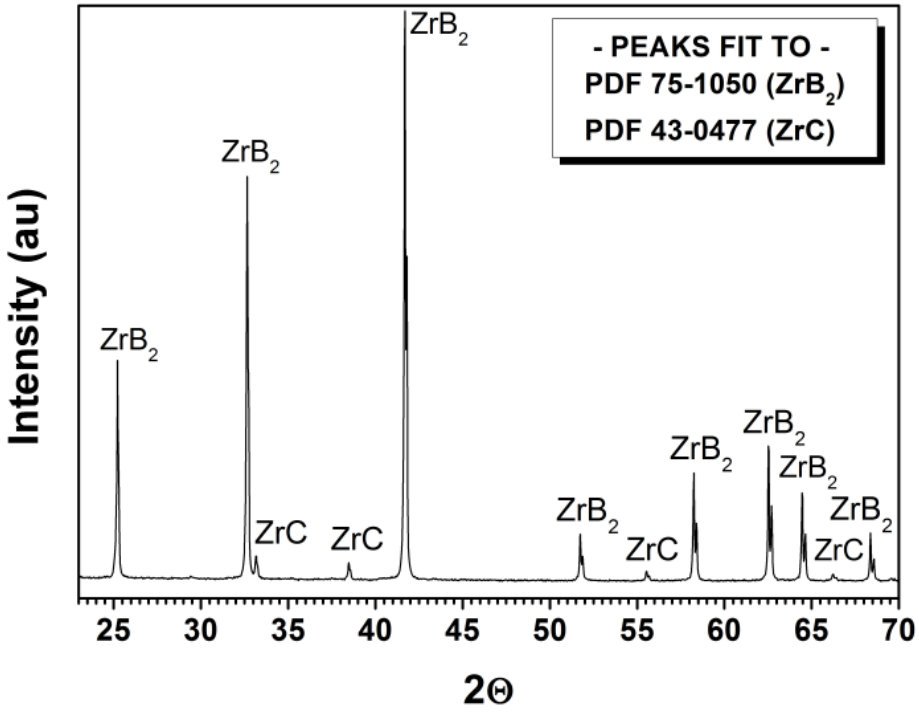

Fig 3. XRD of specimen 1-21-5 showing the presence of ZrC formed from the addition of excess Zr.

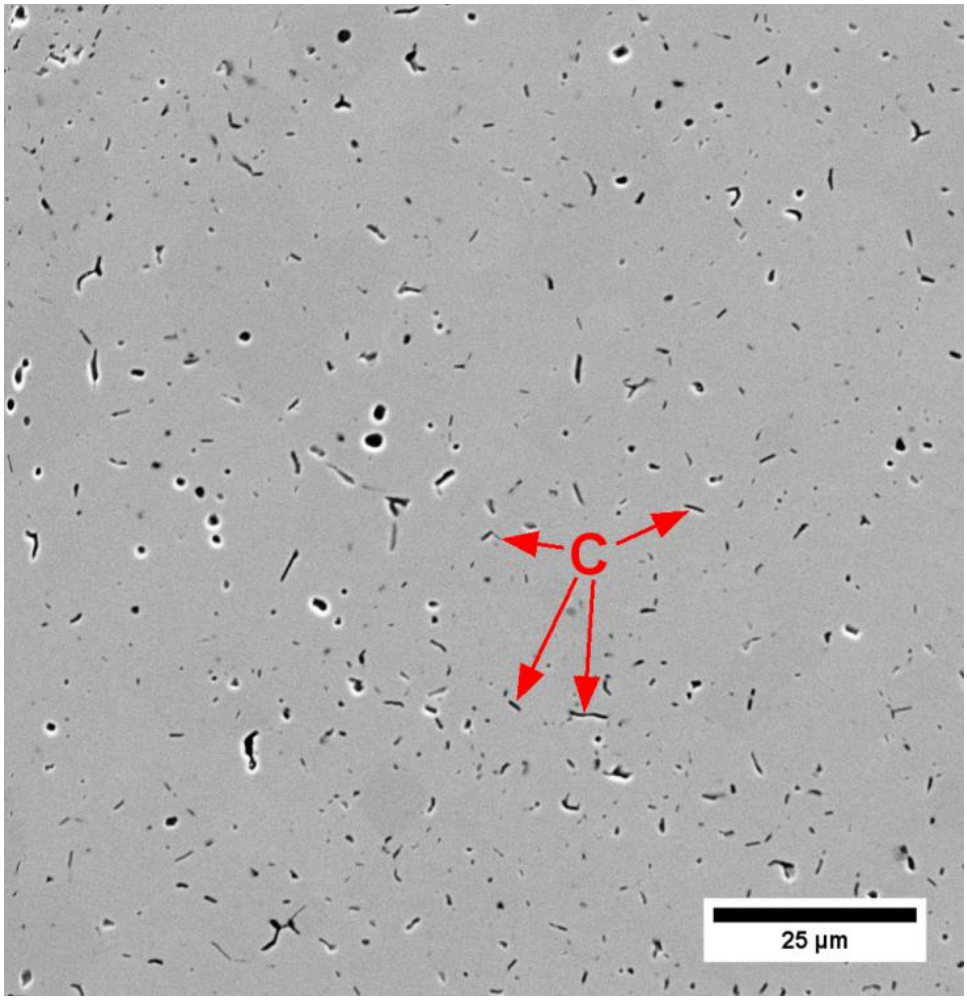

Fig 4. Micrograph of 1-21-1 showing the formation of carbon in the microstructure as finely distributed elongated second phase particles which appear to have formed along grain boundaries.

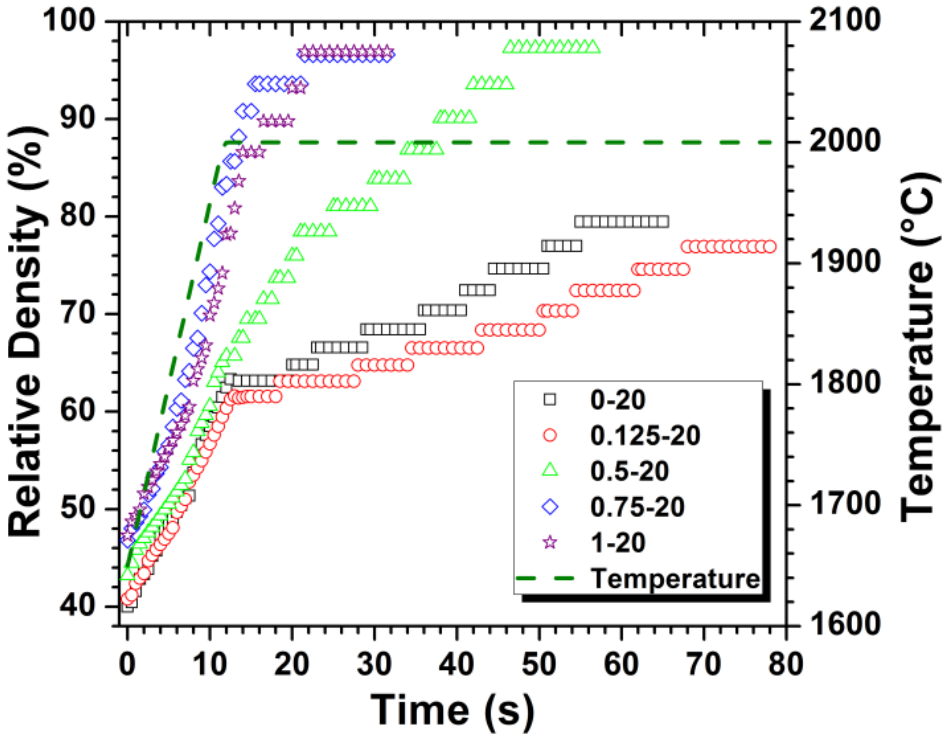

Fig 5. Relative density and furnace temperature as a function of hot pressing time for 2000°C ZrB_2+C specimens.

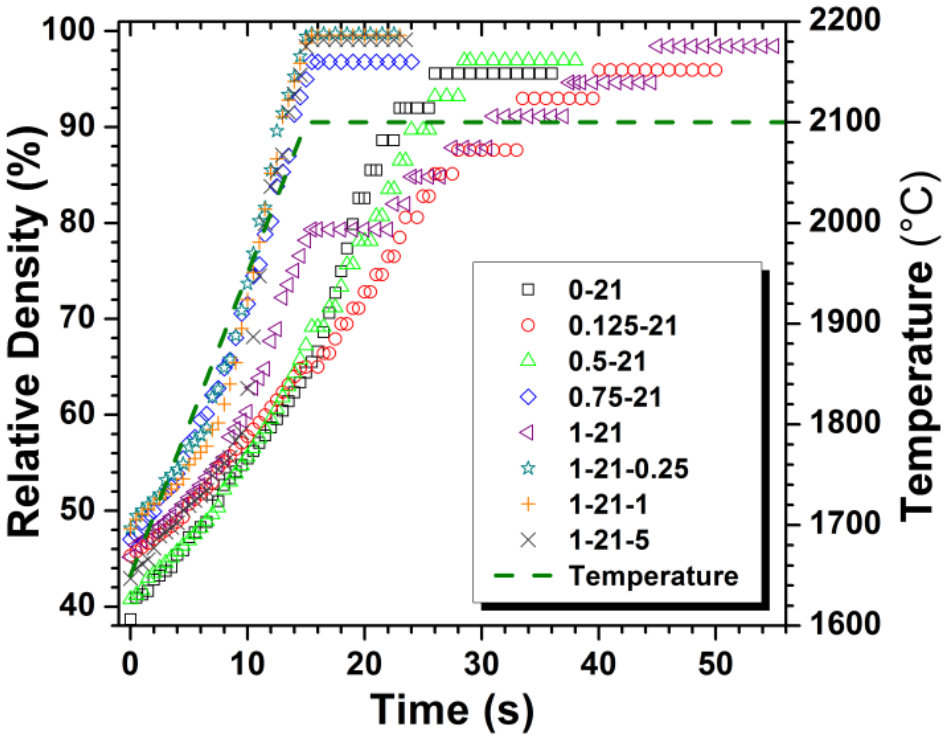

Fig 6. Relative density and furnace temperature as a function of hot pressing time for 2100°C ZrB_2+C and ZrB_2+C+ZrH_2 specimens.

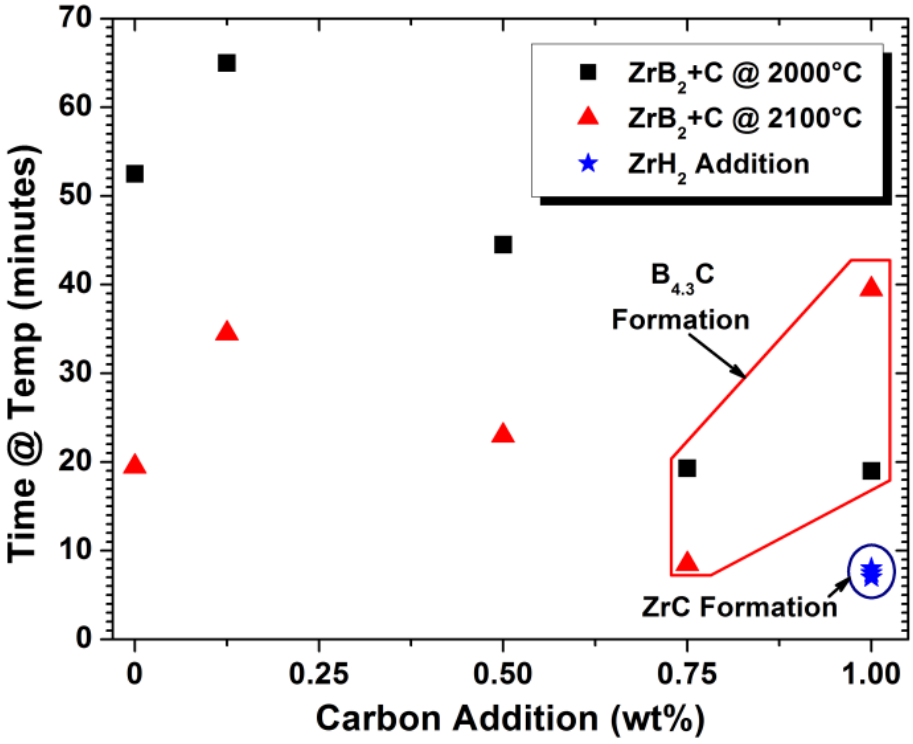

Fig 7. Time at temperature to achieve maximum densification as a function of carbon additions for all carbon and C+ZrH_2 compositions

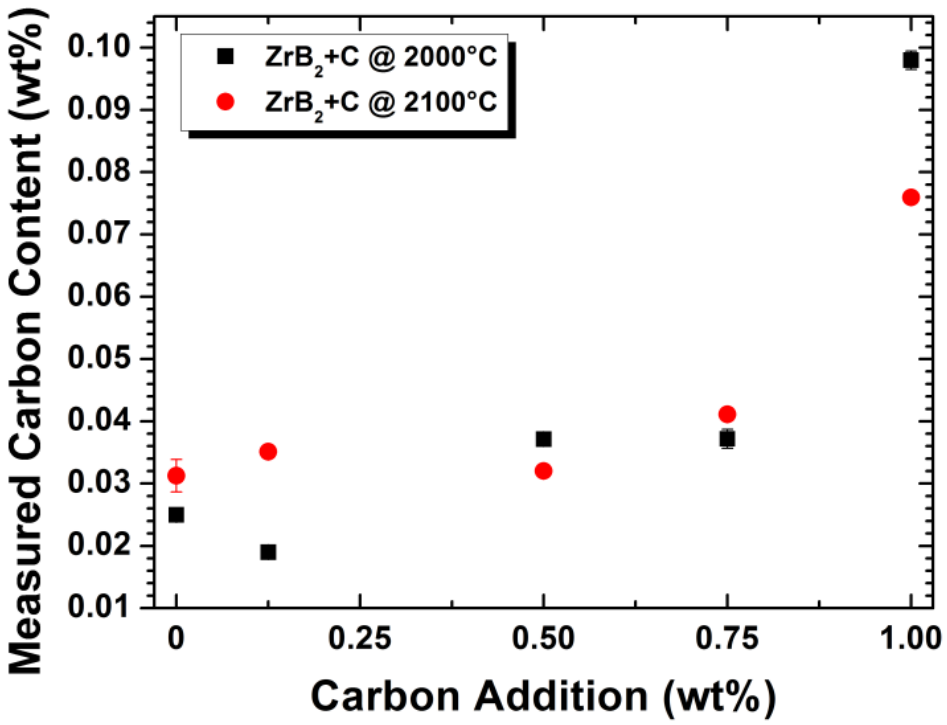

Fig 8. Measured carbon content as a function of added carbon for both 2000 and 2100°C ZrB_2+C material.

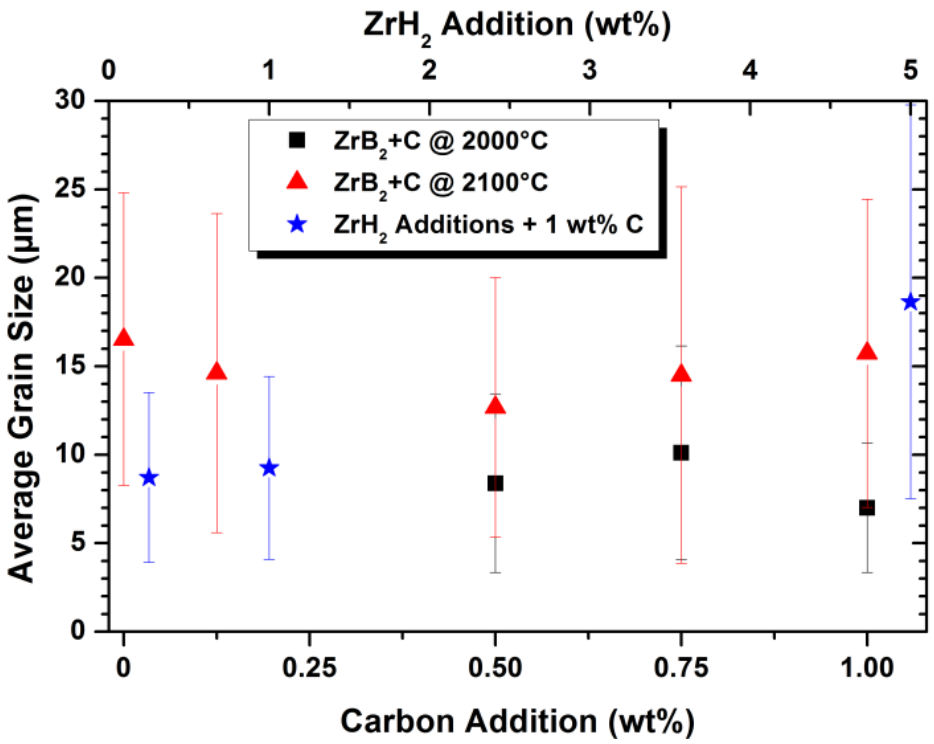

Fig 9. Average grain size as a function of carbon additions for ZrB_2+C (squares and triangles, bottom axis) and ZrH_2 addition for ZrB_2+C+ZrH_2 (stars, top axis).

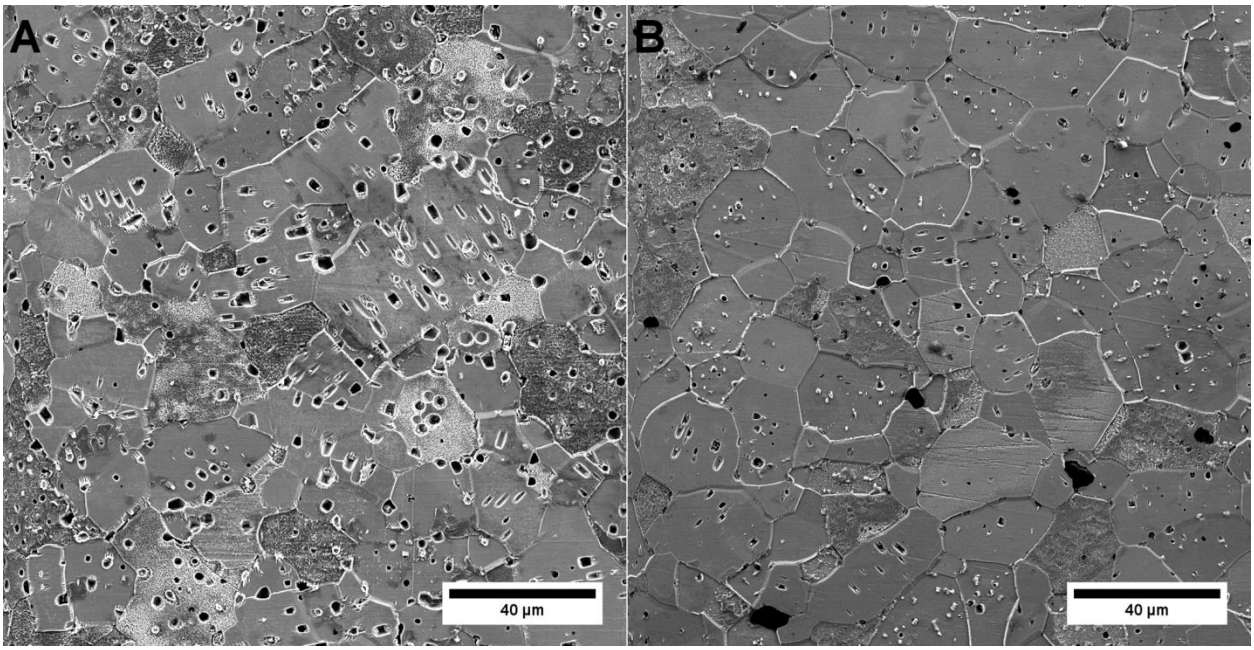

Fig 10. SEM micrographs of 0-21 (A) and 1-21 (B) showing no differences in grain size as carbon content is increased.

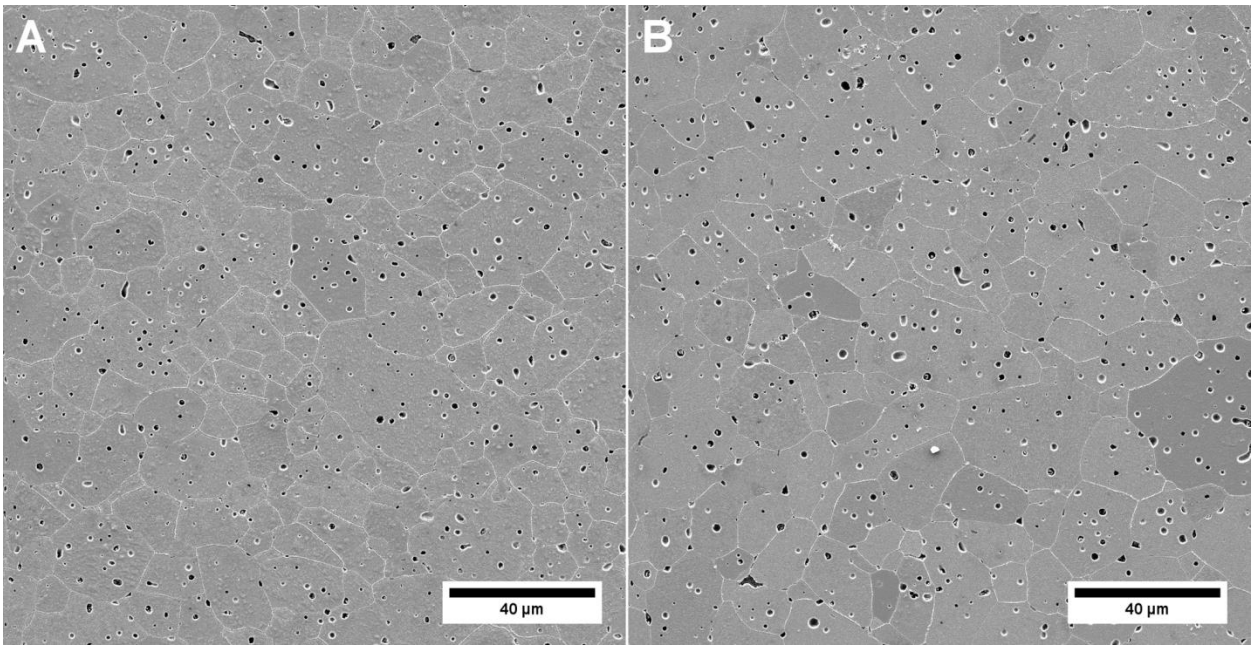

Fig 11. SEM images of 0.75-20 (A) and 0.75-21 (B) showing the increase in grain size resulting from an increase in densification temperature.

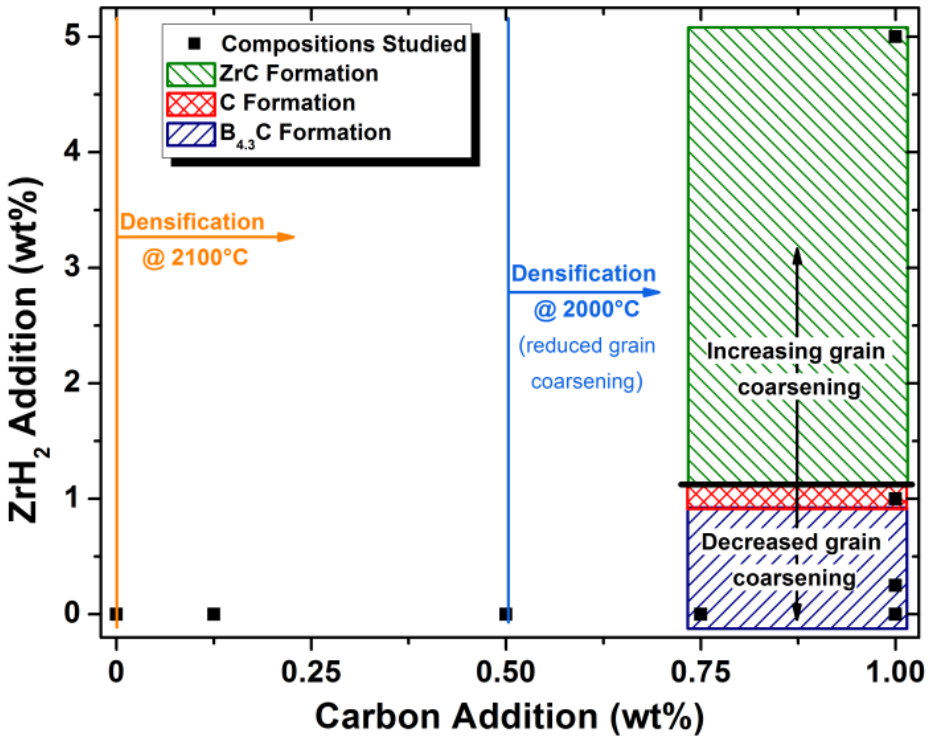

Fig 12. Processing map detailing conditions for densification, second phase formation, and grain growth for ZrB_2, with a nominal initial oxygen content of <2 wt% for hot pressing at 32 MPa with respect to additions of carbon and zirconium.

II. Effect of Carbon on the Thermal and Electrical Transport Properties of Zirconium Diboride

Gregory J. K. Harrington*, Greg E. Hilmas, and William G. Fahrenholtz

Department of Materials Science and Engineering, Missouri University of Science and Technology, Rolla, Missouri 65409

***Corresponding author Tel.: +1 573 341-7205**
E-mail address: gjhmf4@mst.edu
Mail: 223 McNutt Hall, 1400 N. Bishop, Rolla, MO 65409

Abstract

The thermal and electrical properties were studied for zirconium diboride (ZrB_2) containing 0 to 2 wt% carbon. Thermal conductivity was evaluated from 25 to 2000°C and electrical resistivity measured from 25 to 800°C and linearly extrapolated to 2000°C. Estimated values for the Lorenz number for each composition ranged from 2.04×10^{-8} to 2.26×10^{-8} W•Ω•K^{-2} and were used to separate the electron (84-95%) and phonon (5-16%) contributions to thermal conductivity. The estimated Lorenz numbers were lower than the theoretical value, which indicated the electron mean free path for thermal conduction in ZrB_2 was less than the mean free path for electrical conduction. Thermal conductivities ranged from 99 to 87 W/m•K at 25°C and 76 to 72 W/m•K at 2000°C. Increasing carbon content, either as a second phase or in solid solution, decreased thermal conductivity across the entire temperature range by decreasing the electron contribution to thermal transport.

Keywords: UHTC, Zirconium Diboride, Thermal Conductivity, Lorenz number, Carbon,

1. Introduction

Zirconium diboride is a prospective material for use in applications involving extreme physical and chemical environments, such as leading/trailing edges of hypersonic and re-entry vehicles.[1,2] High thermal conductivities (k) are one of the properties that make ZrB_2 an attractive material for these applications, and others such as electronic substrates.[3,4] Thermal conductivity values up to 133 W/m•K at room temperature[5], and as high as 82 W/m•K at 2000°C[6] (nearing the highest evaluated temperatures), have been reported for nominally phase pure ZrB_2. In contrast, k values as low as 56 W/m•K[7] at 25°C and 55 W/m•K[8] at 2000°C have also been reported. Other applications, which may be best served by a material with lower conductivities, are molten metal crucibles and scram jet engine components.[9,10] Additives and impurities can have a strong influence on the thermal conductivity of ZrB_2.

The bonding of ZrB_2 is a mix of covalent, ionic, and metallic types.[11] Due to the metallic bonding, ZrB_2 exhibits low electrical resistivities (6 to 23 μΩ•cm at 25°C).[7,12] Therefore, the total k includes significant phonon (k_p) and electron (k_e) contributions. Typically, phonon and electron conductivities are separated by evaluating k and electrical resistivity (ρ_e, or electrical conductivity ($\sigma_e=\rho_e^{-1}$)). Then, k_e is calculated using the Wiedemann-Franz law (equation (1)) while k_p is estimated using equation (2).[13]

$$k_e = \frac{TL_o}{\rho_e} \tag{1}$$

$$k = k_e + k_p \tag{2}$$

Equation (1) uses the theoretical Lorenz number (L_o, equation (3)) that was derived by Sommerfeld[14] as a combination of constants, π, Boltzmann's constant (k_B), and the charge on an electron (e).

$$L_o = \frac{\pi^2 k_B^2}{3e^2} = 2.44 \times 10^{-8} W \bullet \Omega \bullet K^{-2} \tag{3}$$

However, L_o assumes that the mean free paths for thermal transport (ℓ_t) and electrical transport (ℓ_e) by electrons are the same.[15] However, ℓ_t and ℓ_e can differ depending on the inelastic scattering events experienced by electrons, which would cause the Lorenz number to vary from the theoretical value.[13,16]

Separation of phonon and electron contributions can be used to study the effects of processing and composition on the total thermal conductivity. For example, McClane et al. showed that the solid solution of transition metals (including Hf, a common, natural impurity in commercial ZrB_2 powder and thus ceramics produced using this powder) results in a decrease in k for ZrB_2 based ceramics due to a reduction in k_e.[17] Like Hf, carbon is commonly present in ZrB_2-ceramics and may also affect k. Commercial ZrB_2 powders are commonly produced using boro-carbothermal and carbothermal reduction processes, which result in typical commercial C contents between 0.25 and 1.5 wt%.[18-21] In addition, carbon is a sintering aid that is often added intentionally to ZrB_2-ceramics to react with and remove surface oxide impurities from powder particles.[22-24] Previous researchers have investigated the effect of carbon additions, showing that increasing the volume fraction of carbon (typically graphitic in nature), as a second phase, decreases k.[6,23,25] The overall decrease in k was attributed to the orientation of the graphite between the ZrB_2 grains.[21] The structure and orientation of graphite as a second phase is significant due to the highly anisotropic nature of pyrolytic graphite. Differences in bonding between the graphene layers ($\perp$ to a-direction) vs. along the sheets ($\parallel$ to a-direction), can result in thermal conductivities of ~2 W/m•K ($\perp$) to ~500 W/m•K ($\parallel$) at 300K.[26] Therefore, if the graphite is preferentially oriented such that the $\perp$ direction dominates, it would be expected to decrease the overall k of the composite. The same should be true if the graphite were disordered, due to the increase in incomplete bonding within the structure.

The role of the carbon in solid solution in ZrB_2 has not been evaluated. In addition, previous studies, such as the one performed by Thompson et al., did not evaluate the effects of C on “pure” ZrB_2. Those ceramics contained WC contamination that was introduced by a milling process. In Thompson’s study, the presence of WC reduced the overall k[23] and the role of the $(Zr,W)B_2$ solid solution on k has been supported by McClane et al.[17]

The present study investigated the thermal conductivity of nominally pure ZrB_2 with additions of carbon from 0 to 2 wt%. Thermal diffusivity and electrical resistivity were measured to determine the electron and phonon contributions to total thermal conductivity. Second phase and compositional analyses were performed to relate changes in k to the effects of the carbon additions.

2. Experimental Procedure

2.1. Powder Processing

Materials used in this study were ZrB_2 (Grade B, H.C. Starck, Goslar, Germany), phenolic resin (GP 2074, Georgia-Pacific, Atlanta, GA) with a 41 wt% carbon yield, and ZrH_2 (Grade S, Chemetall GmbH, Frankfurt, Germany). All powder batches were ball milled for 2 hours at 60 rpm using ZrB_2 media and acetone as the liquid. The ZrB_2 and ZrH_2 (1 wt% based on previous research[24]) were dispersed together for the first 1.5 hours and the desired phenolic amount was introduced for the final 30 minutes. After mixing, slurries were dried by rotary evaporation (Roto-vapor R-124, Buchi, Flawil, Switzerland). Before densification, the dried powders were ground and sieved to -100 mesh.

2.2. Hot Pressing and Billet Preparation

Processed powders were loaded in a 5.08 cm diameter graphite die lined with graphite foil that had been coated with BN spray. The dies were then loaded in a graphite

element furnace (HP50-7040G, Thermal Technologies LLC, Santa Rosa, CA) for hot pressing. A low temperature isothermal hold was performed under flowing Ar-10%H_2 at 600°C for 30 min to pyrolyze the phenolic. The atmosphere was then switched to a mild vacuum (≤200 mTorr or ~27 Pa) for three isothermal reaction holds at 1250, 1450, and 1600°C for 1 hour each. After the final hold, a flow of Ar-10%H_2 was established and the furnace was heated under full power to 2150°C where the heating rate steadily decreased from ~130 to ~80°C/min. Upon stabilization of the furnace temperature, the force was applied to achieve 50 MPa of pressure. After pressing for 70 min, the furnace was shut off and allowed to cool naturally and the force was released at 1600°C. Hot pressed billets were fabricated to be ~8 mm thick to allow for the removal >1.5 mm of material from the top and bottom faces of each billet to eliminate the sampling/testing of any of the reaction layer between the ZrB_2 and the graphite spacers. The billets were then diamond machined to produce specimens that were 1.27 cm square and 0.27-0.28 cm thick for thermal diffusivity and one disk 2.5 cm in diameter and 0.1 cm thick for electrical resistivity testing.

2.3. Characterization

Bulk densities (ρ) were evaluated using the Archimedes method with water as the immersing medium. Density values were corrected for temperature for use in thermal conductivity calculations using thermal expansion data from Touloukian.[27] Specimens were ground and polished to a 0.05 µm finish for scanning electron microscopy (SEM; S-570, Hitachi, Ibaraki, Japan) and confocal Raman spectroscopy (633 nm He-Ne laser, Aramis LabRAM, Horiba Jobin Yvon, Edison, NJ). Image analysis (ImageJ, National Institutes of Health, West Bethesda, MD) was performed on SEM images to analyze the volume fractions of porosity and second phases. Transmission electron microscopy (TEM; Tecnai F20, FEI, Hillsboro, OR) was also performed to identify a second phase in the composition with the lowest carbon addition. The TEM specimen was produced by

focused ion beam (FIB; Helios Nanolab 600, FEI) lift-out. X-ray diffraction (XRD; X'Pert Pro, PANalytical, Almelo, Netherlands) analysis was also used for phase identification. Carbon content was quantified (CS600, Leco Corporation, St. Joseph, MI) for the densified materials after grinding to -200 mesh using an alumina mortar and pestle. In addition, several other impurities were analyzed for the highest conductivity material (0.2 wt% added C) to allow for direct comparisons with ZrB_2 ceramics from other studies. Four common impurities in ZrB_2 were analyzed, including O, N (TC500, Leco), Hf, and Fe (inductively coupled plasma mass spectroscopy (ICPMS) performed by NSL Analytical, Warrensville Heights, OH). In addition, W and Co contents were measured (ICPMS, NSL Analytical) to detect possible contamination from the ZrB_2 milling media used in this study, which was produced from powders milled with Co bonded WC media.

The thermal diffusivity (D) of each composition was evaluated on duplicate specimens using the laser flash technique from 25 to 200°C† and from 200 to 2000°C‡ (S-2† and FL5000‡, Anter Corporation, New Castle, DE). Specimens were coated with graphite (dry film graphite lubricant, Sprayon, Cleveland, OH) to increase laser absorption (for both units) and thermal emission (for the FL5000). Testing was carried out under flowing Ar at a gauge pressure of ~41 kPa. Each D value is the average of three separate tests and these results were calculated using the Clark and Taylor method.[28] The calculated thermal conductivity (k_{cal}) was obtained using equation (4), where values for the constant pressure heat capacity (C_p) were taken from the NIST-JANAF thermochemical tables.[29]

$$k_{cal} = \rho D C_p \tag{4}$$

k_{cal} was corrected to account for porosity (v_p = pore volume fraction) to obtain a final value of k using the Maxwell-Eucken relation (equation (5)) with the conductivity of the pores assumed to be zero (k_p=0) to isolate differences due to carbon.[30]

$$k = k_{cal}\frac{2k_{cal} + k_p - 2v_p\left(k_{cal} - k_p\right)}{2k_{cal} + k_p + v_p\left(k_{cal} - k_p\right)} \quad (5)$$

Electrical resistivity (ρ_e) testing was performed from room temperature to 800°C using a 4-point van der Pauw setup following ASTM standard F76-08.[31] The measured resistivities were corrected for porosity, similarly to k, using a modification of equation (5). Fixturing, for the 4-point measurements, consisted of an insulating hexagonal-BN setter supported on the hearth of a metal element furnace (1100-4080-W3; Thermal Technologies LLC.). Four copper wire leads extended from an electrical feedthrough in the furnace body up to the setter within the hotzone and were physically crimped to four copper bars. The bars were angled and made contact with the thin disk specimens through four copper rollers which were kept in constant electrical contact by gravity. Current application (Sorensen DLM 40-15, AMETEK Corp., San Diego, CA) and voltage measurement (NI 9211 DAQ w/NI USB-9162, National Instruments Corporation, Austin, TX) were then controlled by a LabVIEW program (LabVIEW 12, National Instruments Corporation, Austin, TX). Applied currents ranged from 0.1 to 0.4 A and were measured using the DAQ and a 0.05 Ω 4-point current sense resistor (CS3JR050E, Ohmite Mfg. Co., Arlington Heights, IL). Temperature was measured with a k-type thermocouple situated ~0.5 cm above the specimen in the center of the hotzone. Three separate currents were applied at each temperature to confirm that all contacts in the testing circuit were ohmic. An average testing voltage was obtained from the difference in measured voltages from at least three on/off cycles of each current. These measured voltages, along with the testing current and specimen thickness, were used to calculate the resistivity for multiple permutations of the 4-point electrical configuration as described in ASTM F76-08.

3. Results and Discussion

3.1. Microstructure and Carbon Content

Table 1 summarizes the bulk, theoretical, and relative densities for the nine compositions produced for this study. The specimen identification (ID) reflect the added carbon content where the number after the “C” stands for the values to the right of the decimal (0.1 wt% → C1) and the number preceding the “C” to values left of the decimal (2.0 wt% → 2C). Theoretical densities were calculated based on second phase volume fractions using values of 6.15 g/cm³ (ZrB_2[32]), 5.99 g/cm³ (ZrO_x from Rietveld refinement of XRD), and 2.2 g/cm³ (C[33]).

The calculated relative densities decreased from 97.8% to 93.4% between C0 and C3, but increased from 96.1% to near full density (>99.9%) from C4 to 2C. SEM micrographs of C0, C2, C3, C4, C5, and 2C are shown in Fig. 1, where the grains are apparent due to channeling contrast. Compositions C0 to C5 contain between 1% and 7% porosity, which can be seen in dark contrast. The pores range in size from 0.5 to 2 µm for C5 and 1 to 3 µm for C3. Pores were typically round, except for C3, and exhibited some edge charging. The measured volume fractions of porosity were in good agreement with the calculated relative densities (Table 1).

In addition to porosity, two additional phases were identified in C0 through C2 and C5 through 2C. In the specimens with carbon contents of 0.2 wt% or less, a second phase appears as bright regions due to charging in the SEM. Roughly 0.85 vol% of this phase was found in C0, decreasing to ~0.22 vol% in C2 (Table 1). For carbon additions ≥0.5 wt%, a second phase appeared black in contrast to the ZrB_2 and had an elongated acicular morphology. The amount of this phase was between 0.3 vol% (C5) and 4.7 vol% (2C) (Table 1). The decrease in relative density in the middle of the carbon addition range (minima for C3) appeared to be linked to the occurrence of these secondary phases, indicating that their presence initially improved densification.

In addition to the strong ZrB_2 pattern, XRD analysis of C0 through C2 revealed faint peaks at ~29.41°, ~30.07°, and ~37.51° 2Θ (Fig. 2). The peaks at 29° and 37° were due to Cu-Kβ (λ = 1.39 Å) radiation in the incident beam that produced extra peaks for ZrB_2. The peak at ~30° was likely attributed to the second phase observed by SEM. With consideration to potential phases containing Zr, B, O, and C, this peak appeared to be from substoichiometric, tetragonal zirconia (ZrO_x; x<2). The primary peak from the (101) plane of zirconia is reported to be at 30.11° (PDF card 81-1545), which matched well with the experimental data. No other peaks were observed as the second strongest peak for ZrO_x (the (112) at 50.05°) is reported to have a relative intensity of only 30% compared to the primary peak. Analysis by TEM was performed to confirm the hypothesis that ZrO_x was present. A TEM specimen was extracted from a region containing the second phase in composition C0 (Fig. 3). Both zirconium and oxygen were identified by EDS in the regions labeled ZrO_x and electron diffraction patterns (single pattern inset in Fig. 3) confirmed that the phase was tetragonal. The presence of ZrO_x in C0, C1, and C2 indicated that the reduction of oxide impurities was not complete for the lowest carbon additions. Previous research utilizing similar carbon additions discussed the removal of surface oxides from the ZrB_2 but showed no signs of visible oxide inclusions.[24] Therefore, the formation of zirconia was believed to be related to the use of ZrH_2, which if oxidized could have led to the formation of a discreet second phase. The TEM analysis also revealed a crystalline phase that was found between the ZrO_x and ZrB_2. Nitrogen was the major constituent (small zirconium peaks were also present) of this phase according to EDS. Based on the material system, and similar findings by Eakins et al.[34], this grain boundary phase was likely boron nitride.

For carbon additions of more than 0.4 wt%, (C5 (Fig. 1), C6, C8, and 2C (Fig. 1)), carbon was believed to be the only second phase present, although some porosity (<1.1 vol%) was also observed. Raman spectroscopy confirmed that the carbon inclusions

were a form of disordered graphite, similar to that previously identified [23,24] in ZrB_2 based ceramics. No quantitative analysis was performed as part of the present study, but the ZrB_2 grain sizes appeared to range from 10 to 50 μm for C5 and decreased to 3 to 15 μm for higher carbon contents (e.g., 2C shown in Fig. 1). These observations indicated that specimen 2C experienced grain pinning due to the carbon second phase. This conclusion is consistent with results shown for carbon additions by Thompson et al.[23] and SiC additions by Guo et al.[35]

Carbon analysis for each of the hot pressed compositions (Fig. 4) showed little variation (0.026 to 0.033 wt% C) in the final carbon contents for the specimens with ≤0.4 wt% added C. In contrast, carbon additions of more than 0.4 wt% increased the C concentration in the final ceramics in proportion to the increase in added carbon. This is indicated by the linear trend for the C5 and 2C compositions where the retained carbon content increases from 0.05 to 1.36 wt%. These results are nearly identical to the carbon addition analysis from a previous study.[24] The observed trends are attributed to the carbon/oxygen reactions taking place in the system. The carbon content (Fig. 4) increases slightly (0.026 to 0.033 wt%) from C2 to C4. In this range, the apparent lack of carbon inclusions in the ZrB_2 indicates that any carbon that did not react with oxide species dissolved into the ZrB_2 matrix.

From the carbon analysis and resulting microstructures, several conclusions can be drawn. First, the solid solution limit for C within ZrB_2 (after cooling from 2150°C) is between 0.03 and 0.05 wt%. This is lower than the limit indicated by the ZrB_2-C binary phase diagram (~0.134 wt% C), near the processing temperature of 2150°C. However, these specimens were cooled slowly in the hot press, and not quenched, so the observed dissolved carbon content may represent equilibrium at a temperature <2150°C. Second, despite the efforts to vary the dissolved C concentration in ZrB_2, a minimum solid solution threshold was reached (~0.026 wt%) regardless of the presence

of residual oxides for compositions C0 to C2. The minimum carbon limit is, therefore, likely set by the processing environment (i.e., graphite die, furnace element, and insulation), regardless of attempts to exclude carbon from the system by pressing thicker billets.

3.2. Thermal Conductivity

Thermal conductivities for C2, C5, and 2C are compared to other reported ZrB_2 ceramics in Fig. 5. These three compositions represented the range in thermal conductivities observed for the materials produced in the present study. For all of the materials produced, k decreased as temperature increased. The highest k was for C2, which was 99 W/m•K at 25°C, decreasing to 75 W/m•K at 2000°C. The k values at 25°C were 93 W/m•K for C5 and 88 W/m•K for 2C, but converged to 72 to 73 W/m•K at 2000°C. Despite the differences in composition and microstructure, the range in k values was narrow at the higher temperatures (Fig. 5), similar to numerous previous reports. For example, the reaction processed material, densified by spark plasma sintering (rxn-SPS) by Zhang et al., has one of the highest reported conductivities near room temperature (108 W/m•K at 46°C)[12]. Alternatively, one of the lowest (56 W/m•K at 27°C) was reported by Zimmermann et al.[7] for hot pressed ZrB_2 produced from commercial ZrB_2 powder that was attrition milled with WC media. However, despite their differences near room temperature, they both converge towards the data for C2, C5, and 2C.

Purity is believed to be the biggest difference between the materials in this study and those previously reported. This assumption is largely based on the results by McClane et al., who demonstrated that metallic additives such as W, Hf, and others decreased the thermal conductivity of ZrB_2.[17] Based on the conclusions of those studies, C2 was analyzed for metallic and non-metallic impurities thought to be the biggest concern. The measured impurity contents along with reported/estimated impurity contents for materials from the present and previous studies are summarized in Table 2.

The rxn-SPS material produced by Zhang et al. had a higher thermal conductivity due to its high nominal purity and its decreased Hf content (0.001 wt%), compared with C2, which had a Hf content of 1.65 wt%. The ZrB_2 ceramics produced by Zimmermann et al. and Thompson et al.[23] should have comparable Hf contents to the current study due to their use of the same commercial ZrB_2 powder (H.C. Starck, Grade B). Their decreased thermal conductivities, and the increase in k with increasing temperature, are instead due to tungsten introduced by attrition milling.

Across the compositional range studied, the change in thermal conductivity can be divided into three regimes. Regime I includes compositions C0, C1, and C2, where k increased with the carbon addition but the measured carbon content was constant. Regimes II (C2 through C4) and III (C5 through 2C) both span the range of decreasing k as a function of increasing C content but were differentiated by the presence of carbon as a second phase. These regimes will now be discussed individually with respect to the specific relation between thermal conductivity and the carbon content and/or second phase formation.

Based on Fig. 6, the thermal conductivity of the ZrB_2 in Regime I (C0, C1, and C2), for the lowest temperatures, increased as added carbon increased (Fig. 6; right) despite a negligible change in the measured carbon content (Fig. 6; left) Although, through this range the oxide second phase content decreased as the amount of carbon added increased. The thermal conductivity of zirconia was reported to be in the range of 0.6 to 2.4 W/m•K[36] and would likely cause the thermal conductivity to decrease from C2 to C0. However, the effect of the zirconia was only important at temperatures below ~600°C. Above this temperature, any clear trend between these specimens disappeared. These results indicate that for a material intended to be used >600°C zirconia may be a beneficial second phase, allowing for improved densification with negligible changes to the thermal conductivity at high temperatures.

In Regime II, the thermal conductivity at room temperature decreased from 99 W/m•K for C2 to 94 W/m•K for C3 and 93 W/m•K for C4. This coincided with a small variation in C content between C2 (0.027 wt% C), C3 (0.028 wt% C), and C4 (0.033 wt%) without any visible second phase. Therefore, in this range, the decrease in k was attributed to carbon solid solution in ZrB_2. No published reports discuss the role of C in solution with the thermal conductivity of ZrB_2, or any other diborides. Carbon most likely forms a substitutional solid solution, replacing boron atoms. The effect of the solid solution on k remains as temperature increases. However, the values of k converge in Regime II as temperature increases (Fig. 5), as discussed previously. Therefore, the negative effect of the solid solution decreased as temperatures approached the proposed use temperatures of ZrB_2 for hypersonic applications.

Finally, for Regime III (C5 through 2C), k continued to decrease as carbon content increased (Fig. 6). As discussed previously, the carbon second phase was disordered graphite with an elongated morphology lying along grain boundaries. For the carbon to decrease the conductivity of the composite, it must have a lower k than ZrB_2. This is possible if the lower k c-direction of the graphitic structure is dominating the thermal transport of the second phase. In addition, the disordered nature is likely to decrease k by the presence of an increased number of broken bonds within the structure.

Thompson et al. also reported a decrease in thermal conductivity of ZrB_2 as carbon content increased. Comparison of the decrease in k due to C contents between specimens C2 and 2C and Thompson's 0 wt% C and 1 wt% C materials (Fig. 5) showed a smaller decrease in k for the material in the current study. In the present study, 4.7 vol% C (2C) reduced k by only 2.4 to 3.4 W/m•K (3 to 4%) between 600 and 2000°C. In comparison to the work of Thompson, 1.4 vol% C resulted in a 5 to 7 W/m•K (8 to 14%) drop in k. The difference between these materials could come from the morphology of

the carbon second phase or its relative dispersion in the microstructure and these will be discussed below.

Thompson et al. proposed that second phase carbon may increase conductivity when the percolation threshold is met due to the high thermal conductivity of aligned graphite structures.[23] However, percolation was not achieved in 2C. The aspect ratio for the carbon in 2C was ~3. Based on the relative sizes of ZrB_2 grains and carbon inclusions, along with the aspect ratio of the carbon, a carbon content of ~22 vol% would be required for percolation.[37] This is well above the measured content of 4.7 vol% C (Table 1). Therefore, the dispersion of the carbon second phase, in this range, is not likely to have resulted in the differences observed between the current material and that by Thompson.

The nature of the carbon in the current study differed from that reported by Thompson according to the Raman analysis. As mentioned previously, Raman spectroscopy revealed the carbon, in the specimens in the present study, was a disordered form of graphite. This was indicated by the combination of characteristic D (sp^3 bonding) and G (sp^2 bonding) peaks in spectra from individual particles.[23,24] Peak fitting of the Raman spectra (from eight scans of separate regions) for carbon in 2C revealed peak positions of 1333 cm^{-1} for the D peak and 1586 cm^{-1} for the G peak along with a D/G intensity ratio of 1.6. The peak positions were nearly identical to those reported by Thompson et al. (1333 cm^{-1} and 1585 cm^{-1}), but Thompson's intensity ratio was lower at 1.28.[23] The evaluation of the D/G intensity ratio is a first approach to investigating the amount of disorder/size of the graphitic domains.[38] A larger ratio, like that for 2C, is an indication that the carbon is characterized by smaller graphitic regions and more disorder, but other factors like the structural arrangement of the graphite may also influence peak intensity.[38,39] The differences in graphite structure could have led

to a higher conductivity carbon in 2C compared with Thompson's material, resulting in the reduced effect of the carbon on the thermal conductivity of the composite.

3.3. Electron and Phonon Contributions to Thermal Conductivity

The electron and phonon contributions to total thermal conductivity (using equations 1 to 3) were evaluated by measuring electrical resistivities. Table 3 shows the measured room temperature measurements and 2000°C values obtained through linear extrapolation of the measurements from 25 to 800°C. For this study, a continuous linear trend was assumed based on previous high temperature studies of ZrB_2[23,40] and TiB_2[41]. Resistivities ranged from 7.29 to 9.26 μΩ•cm at room temperature and 67 to 76 μΩ•cm at 2000°C for C2 and 2C, respectively. The trends for ρ_e as a function of composition and temperature were inverse of those discussed for thermal conductivity, due to the relation between ρ_e and k (equations (1) and (2)), with the exception of higher than expected values for C3 and C4. This may be due to the density correction that was used rather than intrinsic differences in the specimens.

The k, k_e, and k_p values as a function of temperature for C2, C5, and 2C are plotted in Fig. 7. Using the theoretical Lorenz number (L_o), some calculated k_e values were higher than the total k. An example of this can be seen for C2, C5, and 2C in Fig. 7, where k, k_e, and k_p were plotted side by side. The overestimation of k_e resulted in negative values of k_p for C2 at all temperatures, >500°C for C5, and >1300°C for 2C. Negative values are not possible and are an indication that L_o is not appropriate for the determination of k_e from ρ_e data, for ZrB_2.

A corrected Lorenz number (L_c) was estimated for ZrB_2 based on previous similar evaluations.[42,43] The previous studies sought to determine Lorenz values for various transition metals[42] or conductive ceramics[43] which displayed k_e>k, similar to the ZrB_2 ceramics in the current study. With the assumption that L should reach a constant value

above the Debye temperature (as is typically discussed for the case of L_o[13]) equation (6) was used to evaluate L_c.

$$k = L_c T \rho_e^{-1} + CT^{-1} \quad (6)$$

Equation (6) is the combination of equations (1) and (2) along with the assumption that k_p is proportional to T^{-1} and represented by C/T (C is a constant). Rearrangement of equation (6) gives equation (7).

$$kT = L_c T^2 \rho_e^{-1} + C \quad (7)$$

From this equation, L_c is the slope of kT plotted as a function of $T^2\rho_e^{-1}$. In this case, values were plotted starting from 600°C (within the reported range of Debye temperatures for ZrB_2 of 457°C to 692°C) [7,44-46] to 2000°C. Table 3 contains the L_c values estimated for each composition. These values range from 2.04×10^{-8} (C6) to 2.26×10^{-8} W•Ω•K^{-2} (2C) without any systematic trends between compositions. While not as accurate as direct measurements of Lorenz numbers (beyond the scope of this research), use of these values results in calculation of k_p values that were positive for all compositions at all temperatures. Although L_c may only be valid at higher temperatures, it was used for the entire temperature range for the present study to recalculate k_e and k_p for C2, C5, and 2C, which are plotted as dashed lines in Fig 7.

The values of k_e were higher for C2 (88 to 72 W/m•K) than for either C5 (79 to 69 W/m•K) or 2C (76 to 68 W/m•K). The relative magnitudes of the resulting k_p values showed the opposite trend. This may be an indication of improved phonon conduction due to the increased carbon content, but a slight change in L_c (~3%) would negate any difference. Hence, the phonon contributions could be considered the same for C2, C5, and 2C. The peak in k_p (~14 W/m•K for C5 and 2C, and ~12 W/m•K for C2) between 200 to 300°C may indicate a minima in phonon scattering processes for each composition. However, the peak also coincides with a change from the low temperature to high

temperature units for laser flash diffusivity measurements, which could also account for the inflection.

Beyond the form of the absolute values of k, and the trends with temperature, an important aspect of this analysis is the relative contribution of each transport mechanism to k. For all compositions, k_e is clearly dominant, comprising ~87% (300°C) to ~95% (2000°C) of the total k for C2 and ~84% and ~94% at the same temperatures for C5 and 2C. Therefore, when considering the thermal conductivity of ZrB_2, and how it may be modified, future studies should consider additives and impurities that affect the electron contribution to thermal conductivity, especially at the highest temperatures.

Comparison of L_c and L_o by equation (8) can also be used to evaluate the mean free paths of electrons acting as thermal conductors, ℓ_T, and electrical conductors, ℓ_E.[15]

$$L_c = L_o \frac{\ell_T}{\ell_E} \tag{8}$$

Differences in mean free paths for the two transport mechanisms is ultimately what leads to a breakdown in the validity of equations (1) and (3) for the Lorenz number for metallic conductors to deviate from theoretical.[13,16] The ratio of ℓ_T/ℓ_E appears to range from 0.84 to 0.93, but most values result in an average of 0.88 (Table 3). This negative deviation in ℓ_T/ℓ_E from unity can be attributed to one or more inelastic scattering processes, which affect the thermal transport of electrons more negatively than the electrical transport of electrons in ZrB_2. This analysis does not elucidate the mechanism of scattering, but further investigation could provide a more complete understanding of thermal transport in ZrB_2 and similar diboride based ceramics.

4. Summary and Conclusions

The role of carbon content on the thermal conductivity of ZrB_2 was studied. The three lowest carbon additions (0 to 0.2 wt% C) had a residual second phase of zirconia, which

appear to aid densification, resulting in final relative densities between 98% and 96%, respectively. Two intermediate compositions (0.3 and 0.4 wt% C) had no visible second phases, achieving relative densities of 93% and 96%, respectively. Finally, improved densification (>98.9%) was observed for carbon contents of 0.5 wt% and higher along with the formation of carbon as a second phase.

The variations in thermal conductivity of ZrB_2 with carbon content were divided into three regimes based on compositional and microstructural changes to the ZrB_2. Regime I was characterized by the presence of zirconia in the lowest carbon compositions (C0, C1 and C2), with zirconia content decreasing as carbon was added. Elimination of zirconia increased k and resulted in the highest k values for compositions produced in this study (99 W/m•K at 25°C to 75 W/m•K at 2000°C for C2). In Regime II, k values decreased as C content increased across the limited carbon solid solution range for ZrB_2. The drop was most significant at 25°C, where k changed from 99 W/m•K for C2 to 93 W/m•K for C5. Thermal conductivity continued to decrease in Regime III due to increasing content of a second phase that was characterized as disordered graphite. The lowest k values in Regime III were 88 W/m•K at 25°C and 72 W/m•K at 2000°C for 2C. Carbon lowers thermal conductivity due to its disordered morphology.

Thermal conductivity values were separated into k_e and k_p using measured electrical resistivities and the Wiedemann-Franz law. The theoretical Lorenz number, L_o, overestimated k_e and resulted in negative k_p values. Values for a corrected Lorenz number, L_c, were estimated by plotting kT as a function of $\rho_e^{-1}T^2$, using the assumption that k_p is proportional to T^{-1} above the Debye temperature. This evaluation led to the following conclusions:

1. L_c ranged from 2.04×10^{-8} to 2.26×10^{-8} with no trends related to composition

2. k_p values were all positive using L_c and ranged from 12-14 W/m•K at 200°C and 4-5 W/m•K at 2000°C. Values were slightly higher for compositions with carbon as a second phase
3. Trends in k_e were similar to k and 84% to 95% of total thermal conductivity was due to electron transport in these materials
4. Comparison of L_c to L_o indicated that the mean free path of the electrons for thermal conduction was, on average, 0.88 of the mean free path of electrons for electrical conductivity.

Acknowledgements

This research was funded by the National Science Foundation (DMR-0906584).

References

[1] Opeka MM, Talmy IG and Zaykoski JA. Oxidation-based materials selection for 2000°C + hypersonic aerosurfaces: Theoretical considerations and historical experience. J Mater Sci 2004;**39**(19):5887-904.

[2] Gasch MJ, Ellerby DT and Johnson SM. Ultra High Temperature Ceramic Composites In: Bansal NP, editor Handbook of Ceramic Composites, New York: Springer; 2005, p. 197-224.

[3] Kinoshita H, Otani S, Kamiyama S, Amano H, Akasaki I, Suda J and Matsunami H. Zirconium diboride (0001) as an electrically conductive lattice-matched substrate for gallium nitride. Japanese Journal of Applied Physics, Part 2: Letters 2001;**40**(12 A):L1280-L2.

[4] Okamoto NL, Kusakari M, Tanaka K, Inui H, Yamaguchi M and Otani S. Temperature dependence of thermal expansion and elastic constants of single crystals of ZrB_2 and the suitability of ZrB_2 as a substrate for GaN film. J Appl Phys 2003;**93**(1):88-93.

[5] Guo S, Nishimura T and Kagawa Y. Preparation of zirconium diboride ceramics by reactive spark plasma sintering of zirconium hydride-boron powders. Scripta Mater 2011;**65**(11):1018-21.

[6] Clougherty EV, Wilkes KE and Tye RP. Research and Development of Refractory Oxidation-Resistant Diborides, Part II, Volume V: Thermal, Physical, Electrical, and Optical Properties. Air Force Materials Laboratory, Air Force Systems Command, Wright-Patterson Air Force Base, Ohio, Technical Report AFML-TR-68-190, Part II, Volume V 1969;

[7] Zimmermann JW, Hilmas GE, Fahrenholtz WG, Dinwiddie RB, Porter WD and Wang H. Thermophysical Properties of ZrB_2 and ZrB_2–SiC Ceramics. J Am Ceram Soc 2008;**91**(5):1405-11.

[8] Fridlender BA, Neshpor VS, Ordan'yan SS and Unrod VI. Thermal Conductivity and Diffusivity of Binary Alloys of the ZrC-ZrB_2 System at High Temperatures. High Temperature 1980;**17**(6):1001-5.

[9] Mroz C. Zirconium Diboride. Am Ceram Soc Bull 1994;**73**(6):141-2.

[10] Van Wie DM, Drewry DG, King DE and Hudson CM. The hypersonic environment: Required operating conditions and design challenges. J Mater Sci 2004;**39**(19):5915-24.

[11] Vajeeston P, Ravindran P, Ravi C and Asokamani R. Electronic structure, bonding, and ground-state properties of AlB_2-type transition-metal diborides. PhRvB 2001;**63**(4):045115-(1-12).

[12] Zhang L, Pejaković DA, Marschall J and Gasch M. Thermal and Electrical Transport Properties of Spark Plasma-Sintered HfB_2 and ZrB_2 Ceramics. J Am Ceram Soc 2011;**94**(8):2562-70.

[13] Uher C. Thermal Conductivity of Metals. In: Tritt TM, editor Thermal Conductivity: Theory, Properties, and Applications, Springer; 2004, p. 21-91.

[14] Sommerfeld A. Zur Elektronentheorie der Metalle. NW 1927;**15**(41):825-32.

[15] Kumar GS, Prasad G and Pohl RO. Experimental determinations of the Lorenz number. J Mater Sci 1993;**28**(16):4261-72.

[16] Ashcroft NW and Mermin ND. Solid State Physics. Cengage Learning; 2011.

[17] McClane DL, Fahrenholtz WG and Hilmas GE. Thermal Properties of (Zr,TM)B_2 Solid Solutions with TM = Hf, Nb, W, Ti, and Y. J Am Ceram Soc 2014;**97**(5):1552-8.

[18] Sciti D, Guicciardi S, Bellosi A and Pezzotti G. Properties of a Pressureless-Sintered ZrB_2–$MoSi_2$ Ceramic Composite. J Am Ceram Soc 2006;**89**(7):2320-2.

[19] Lee S-H, Sakka Y and Kagawa Y. Dispersion Behavior of ZrB_2 Powder in Aqueous Solution. J Am Ceram Soc 2007;**90**(11):3455-9.

[20] Baldridge T, Gupta MC and Sun C-N. Nanostructures from Zirconium Diboride and Alumina Ceramics. J Am Ceram Soc 2010;**93**(9):2891-6.

[21] Treibacher Industrie AG. Zirkonium diboride data sheet/chemical analysis. Auer von Welsbach Straße 1, A9660 Althofen, Austria, www.treibacher.com

[22] Thompson M, Fahrenholtz WG and Hilmas G. Effect of Starting Particle Size and Oxygen Content on Densification of ZrB_2. J Am Ceram Soc 2011;**94**(2):429-35.

[23] Thompson MJ, Fahrenholtz WG and Hilmas GE. Elevated Temperature Thermal Properties of ZrB_2 with Carbon Additions. J Am Ceram Soc 2012;**95**(3):1077-85.

[24] Harrington GJK, Hilmas GE and Fahrenholtz WG. Effect of Carbon and Oxygen on the Densification and Microstructure of Hot Pressed Zirconium Diboride. J Am Ceram Soc 2013;**96**(11):3622-30.

[25] Andrievskii RA, Korolev LA, Klimenko VV, Lanin AG, Spivak II and Taubin IL. Effect of zirconium carbide and carbon additions on some physicomechanical properties of zirconium diboride. Powder Metall Met Ceram 1980;**19**(2):93-4.

[26] Klein CA and Holland MG. Thermal Conductivity of Pyrolytic Graphite at Low Temperatures. I. Turbostratic Structures. PhRv 1964;**136**(2A):A575-A90.

[27] Touloukian YS, Kirby RK, Taylor RE and Desai PD. Thermal Expansion: Nonmetallic Solids. IFI/Plenum; 1977.

[28] Clark III LM and Taylor RE. Radiation loss in the flash method for thermal diffusivity. J Appl Phys 1975;**46**(2):714-9.

[29] Chase MW. NIST-JANAF Thermochemical Tables. American Chemical Society and the American Institute of Physics. 4th ed. Woodbury, NY: 1998.

[30] Levy FL. A modified Maxwell-Eucken equation for calculating the thermal conductivity of two-component solutions or mixtures. International Journal of Refrigeration 1981;**4**(4):223-5.

[31] ASTM Standard F76, 2008, "Standard Test Methods for Measuring Resistivity and Hall Coefficient and Determining Hall Mobility in Single-Crystal Semiconductors". West Conshohocken, PA: ASTM International; 2008, DOI: 10.1520/F0076-08.

[32] Neuman EW, Hilmas GE and Fahrenholtz WG. Strength of Zirconium Diboride to 2300°C. J Am Ceram Soc 2013;**96**(1):47-50.

[33] Lide D. CRC Handbook of Chemistry and Physics. 88th ed. Boca Raton: CRC; 2007.

[34] Eakins E. Nanoscale characterization of effect of SiC on microstructure and oxidation behaviour of ZrB_2-based ceramics [dissertation]. Imperial College London; 2011.

[35] Guo W-M, Zhang G-J and Wang P-L. Microstructural Evolution and Grain Growth Kinetics in ZrB_2–SiC Composites During Heat Treatment. J Am Ceram Soc 2009;**92**(11):2780-3.

[36] Schneider Jr. SJ and committee AH. Engineered Materials Handbook, Volume 4, Ceramics and Glasses. ASM International; 1991.

[37] Garboczi EJ, Snyder KA, Douglas JF and Thorpe MF. Geometrical percolation threshold of overlapping ellipsoids. PhRvE 1995;**52**(1):819-28.

[38] Antunes E, Lobo A, Corat E, Trava-Airoldi V, Martin A and Verissimo C. Comparative study of first-and second-order Raman spectra of MWCNT at visible and infrared laser excitation. Carbon 2006;**44**(11):2202-11.

[39] Ferrari AC and Robertson J. Interpretation of Raman spectra of disordered and amorphous carbon. PhRvB 2000;**61**(20):14095-107.

[40] Samsonov GV and Sinel'nikova VS. The resistivity of refractory compounds at high temperatures. Powder Metall Met Ceram 1962;**1**(4):272-4.

[41] McLeod AD, Haggerty JS and Sadoway DR. Electrical Resistivities of Monocrystalline and Polycrystalline TiB_2. J Am Ceram Soc 1984;**67**(11):705-8.

[42] Sharma RG, Chari MSR and Reddy DK. The electronic Lorenz number in some transition metals at high temperatures. JPhF 1986;**16**(5):603-7.

[43] Morgan PED. Wiedemann-Franz-Lorenz Relation in Metallic Conducting Ceramics. J Am Ceram Soc 1975;**58**(7-8):349.

[44] Samsonov GV, Serebryakova TI and Neronov VA. Borides. Atomizdat, Moscow 1975;

[45] Wiley DE, Manning WR and Hunter Jr O. Elastic properties of polycrystalline TiB_2, ZrB_2 and HfB_2 from room temperature to 1300°K. Journal of the Less Common Metals 1969;**18**(2):149-57.

[46] Bernstein H. Met Soc AIME Inst Metals Div Spec Rept Ser 1964;(13):609.

Fig. 1. SEM images, of specimens C0, C2, C3, C4, C5, and 2C, showing the transitions in density, grain size, and second phase fractions as carbon additions are increased.

Fig. 2. XRD patterns from specimens C0, C1, C2, and C3 that show a peak at ~30° 2Θ for specimens up to C2. This peak has been attributed to a second phase of sub-stoichiometric form of tetragonal zirconia.

Fig. 3. TEM image of C0 showing zirconia and boron nitride. The inset SADP is of the zirconia 111 zone axis, indexed to a tetragonal phase.

Fig. 4. Measured carbon content after hot pressing displayed as a function of the carbon addition.

Fig. 5. Thermal conductivity as a function of temperature for C2, C5, and 2C compared to values reported by Zhang et al.[12], Zimmermann, et al.[7], and Thompson et al.[23]

Fig. 6. Thermal conductivity as a function of measured carbon content (right) and carbon addition amount.

Fig. 7. Total, electron, and phonon thermal conductivities for specimens C2, C5, and 2C showing the separate contributions to k calculated using L_o (shapes) and then L_c (dashed lines) from each composition.

Table 1. The specimen ID is given for each composition along with: carbon addition, second phase and density information (bulk, theoretical and relative) and volume percent measured porosity results.

Specimen ID	Carbon Addition (wt%)	ρ_{bulk} (g/cc)	$\rho_{theoretical}$ (g/cc)	$\rho_{relative}$ (%)	Second Phase (vol% C or ZrO_x)	Porosity vol%
C0	0	6.01	6.15	97.8	0.85 (ZrO_x)	1.43
C1	0.1	5.97	6.15	97.1	0.40 (ZrO_x)	1.67
C2	0.2	5.93	6.15	96.4	0.22 (ZrO_x)	2.03
C3	0.3	5.75	6.15	93.4	N/A	5.31
C4	0.4	5.91	6.15	96.1	N/A	3.18
C5	0.5	6.07	6.14	98.9	0.26 (C)	0.56
C6	0.6	6.10	6.12	99.5	0.64 (C)	0.34
C8	0.8	6.07	6.11	99.3	0.92 (C)	0.20
2C	2	5.97	5.96	>99.9	4.68 (C)	0

Table 2. Measured elemental impurity concentrations for C2, along with reported or estimated impurities for ZrB_2 reported by Zhang et al.[12], Zimmermann et al.[7], and Thompson et al.[23]

Elemental Impurity	Specimen C2 (wt%)	Zhang (wt%)	Zimmermann (wt%)	Thompson 0 wt% C (wt%)
C	0.027	-	-	0.42
O	0.13	-	-	0.40
N	0.078	-	-	-
Co	<0.001	-	-	-
Fe	<0.001	-	-	-
Hf	1.65	<0.001 (<200 ppm)[iii]	1.5-2[iv]	1.5-2[b]
W	0.005	-	~3	2
Total Purity	98.1	~99.6[v]	≤95.5	≤95.7

[iii] according to Cerac Inc. product information
[iv] typical range of H. C. Starck, Grade B, ZrB_2
[v] based on reported Zr (99.7%) and B (99%) purities [12]

Table 3. Room temperature and extrapolated 2000°C electrical resistivities in addition to the evaluated Lorenz constant (L_c) and mean free path ratio (ℓ_T/ℓ_E) for each composition.

Specimen ID	ρ_e @ 25°C ($\mu\Omega\bullet$cm)	ρ_e @ 2000°C*[vi] ($\mu\Omega\bullet$cm)	L_c (x 10^{-8} $W\bullet\Omega\bullet K^{-2}$)	ℓ_T/ℓ_E -
C0	7.34	68.8	2.12	0.87
C1	7.32	68.4	2.20	0.90
C2	7.29	67.1	2.11	0.87
C3	8.59	71.3	2.20	0.90
C4	8.92	70.8	2.14	0.88
C5	7.99	69.4	2.10	0.86
C6	8.49	70.2	2.04	0.84
C8	8.49	70.4	2.13	0.87
2C	9.26	75.9	2.26	0.93

[vi] estimated using a linear fit from ρ_e measurements in the range of 25 to 800°C

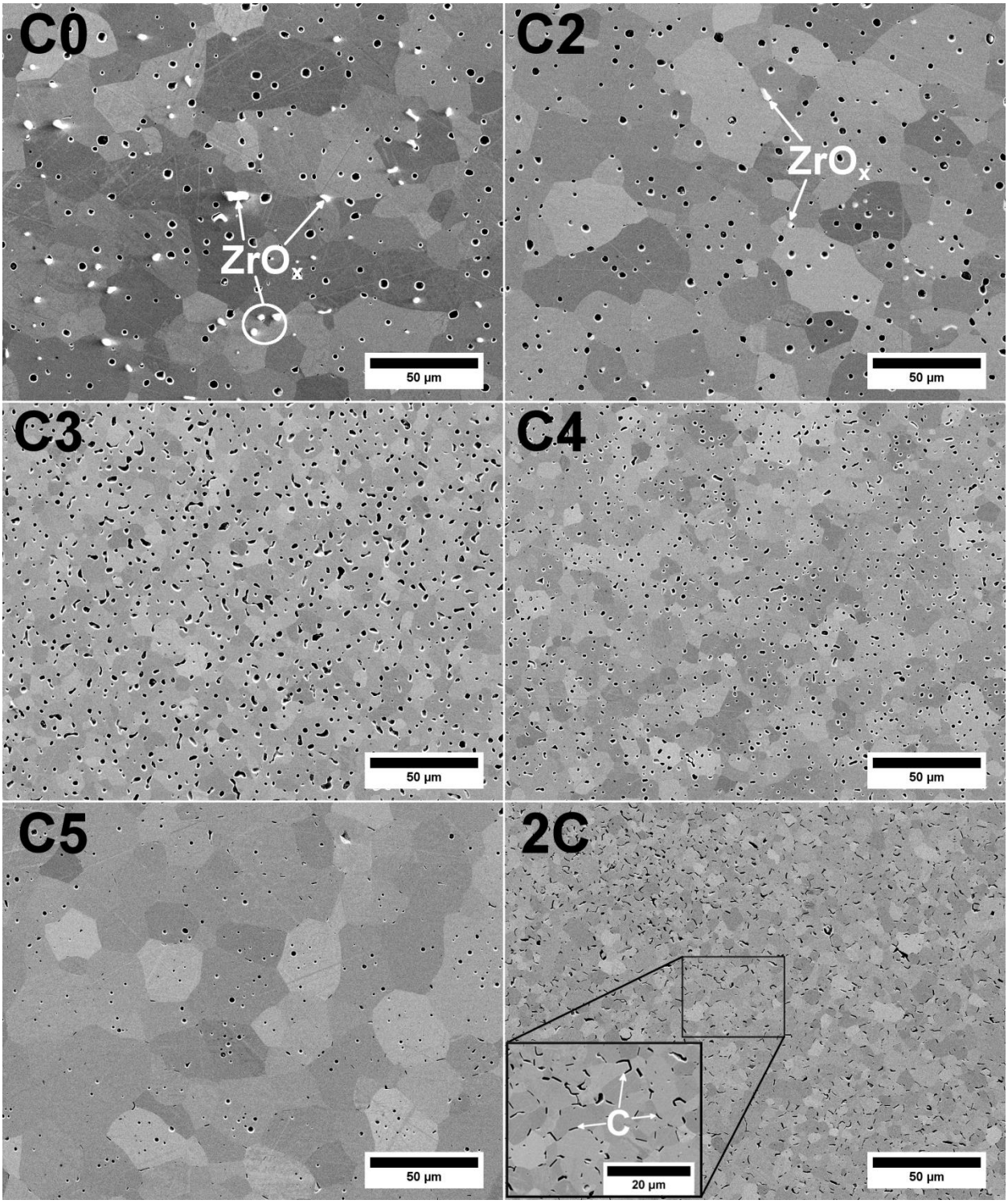

Fig. 1. SEM images, of specimens C0, C2, C3, C4, C5, and 2C, showing the transitions in density, grain size, and second phase fractions as carbon additions are increased.

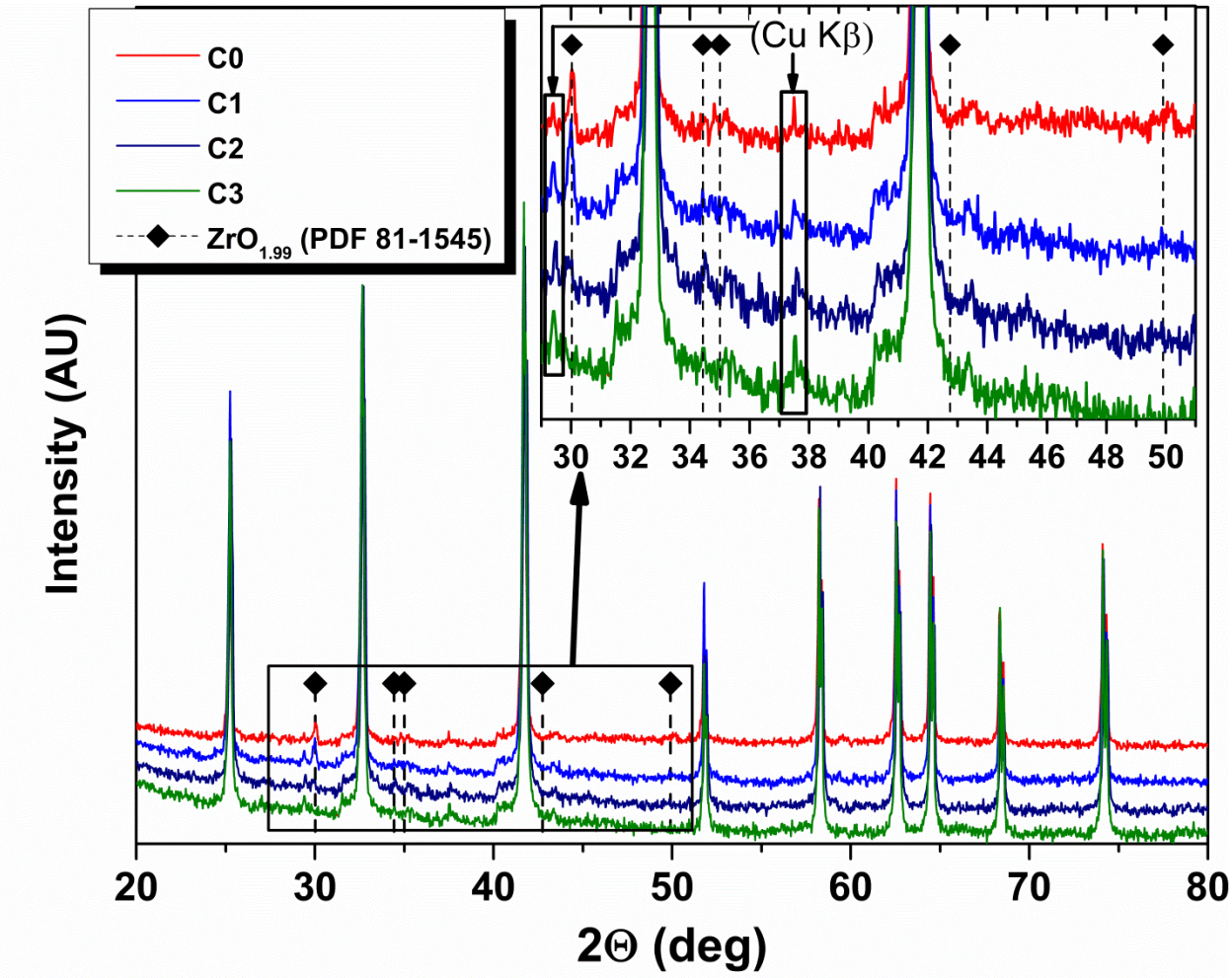

Fig. 2. XRD patterns from specimens C0, C1, C2, and C3 that show a peak at ~30° 2Θ for specimens up to C2. This peak has been attributed to a second phase of sub-stoichiometric form of tetragonal zirconia.

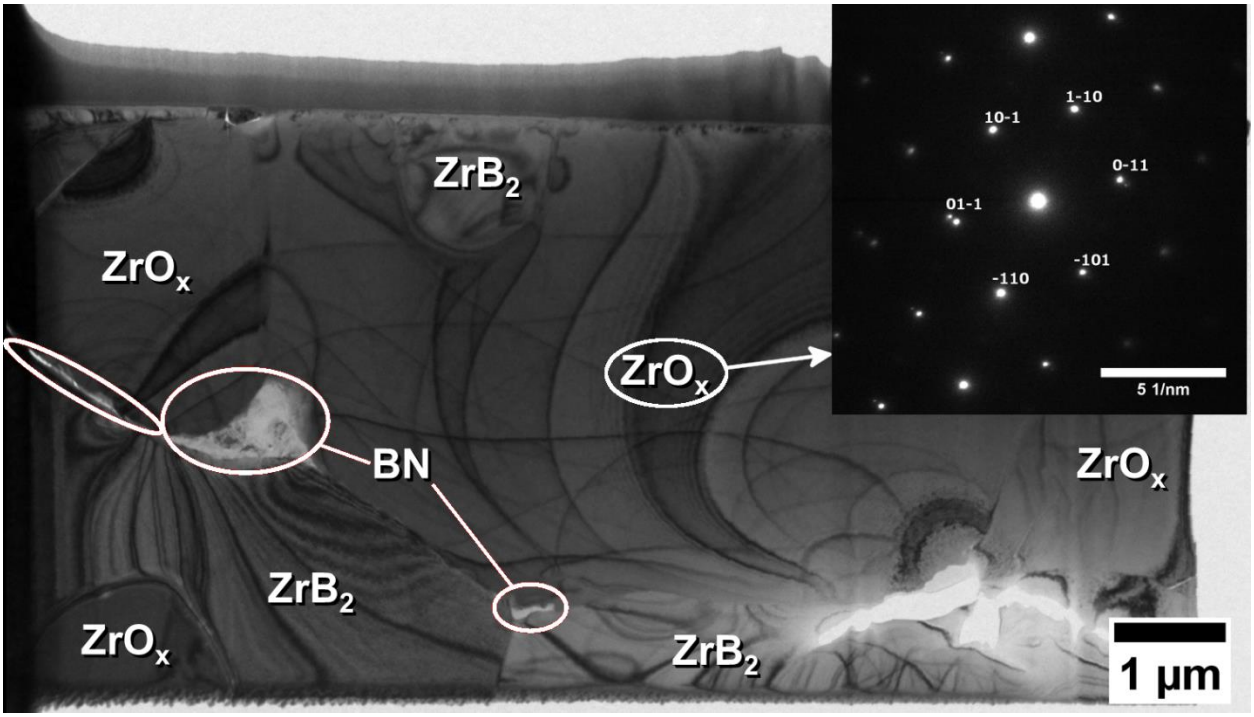

Fig. 3. TEM image of C0 showing zirconia and boron nitride. The inset SADP is of the zirconia 111 zone axis, indexed to a tetragonal phase.

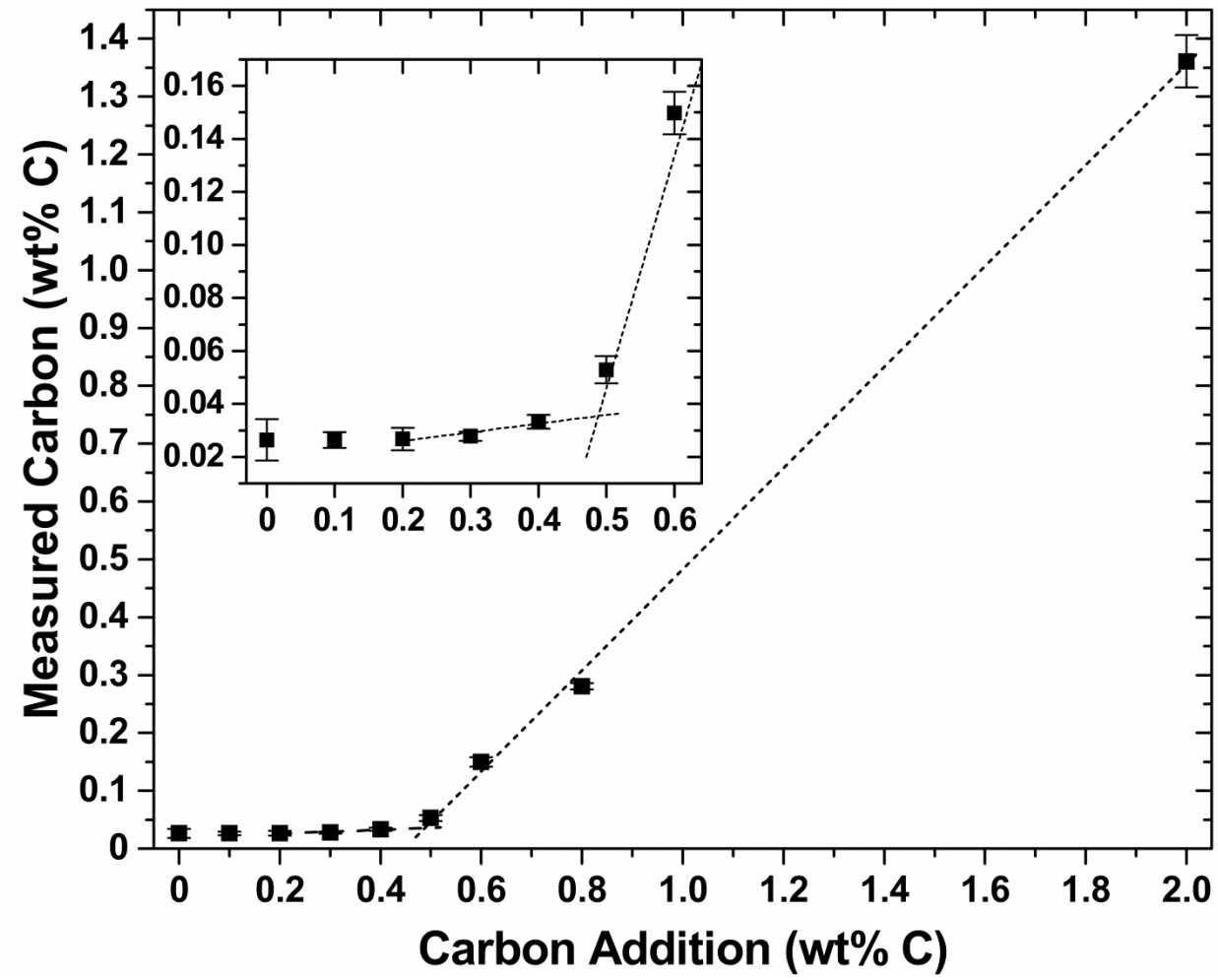

Fig. 4. Measured carbon content after hot pressing displayed as a function of the carbon addition.

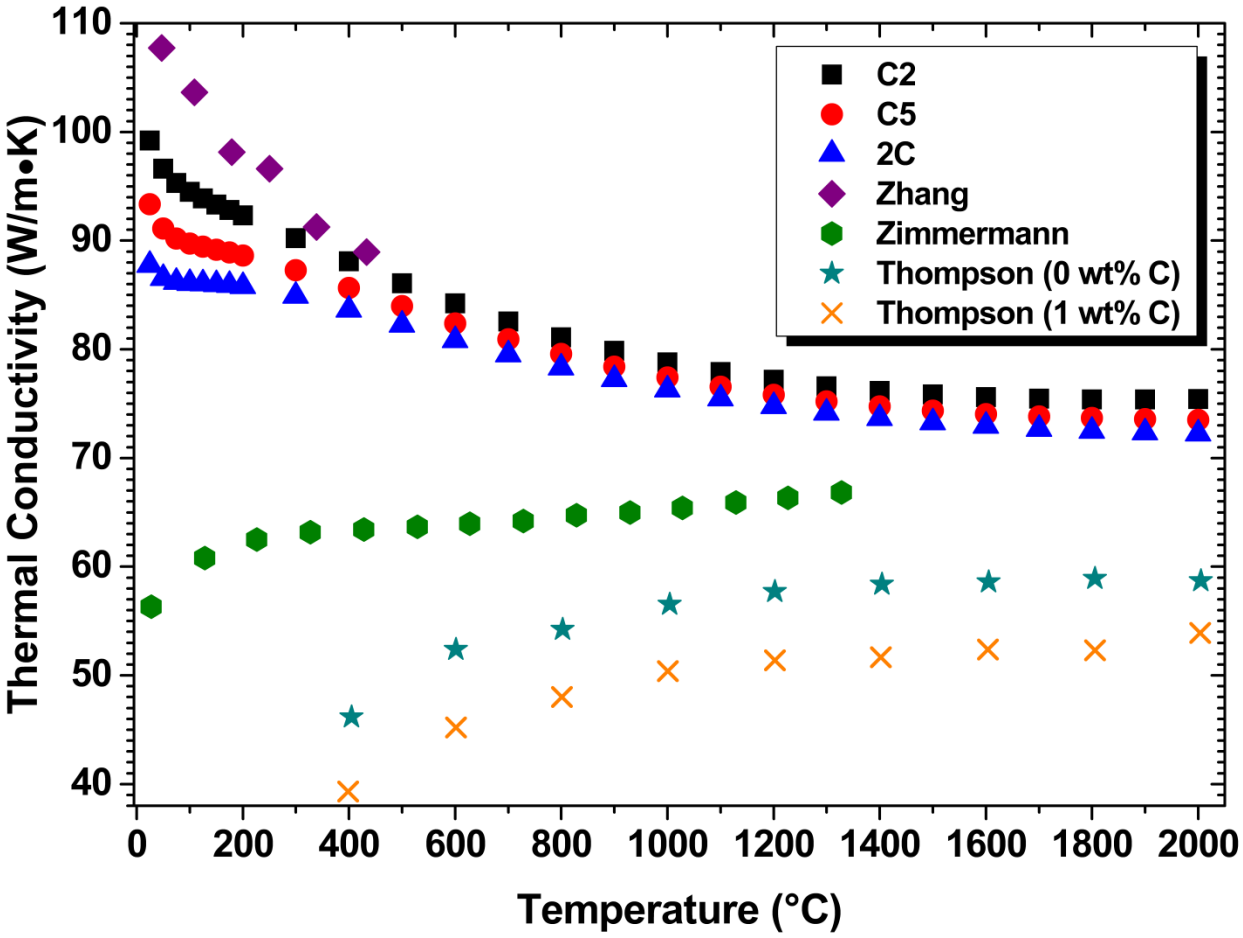

Fig. 5. Thermal conductivity as a function of temperature for C2, C5, and 2C compared to values reported by Zhang et al.[12], Zimmermann, et al.[7], and Thompson et al.[23]

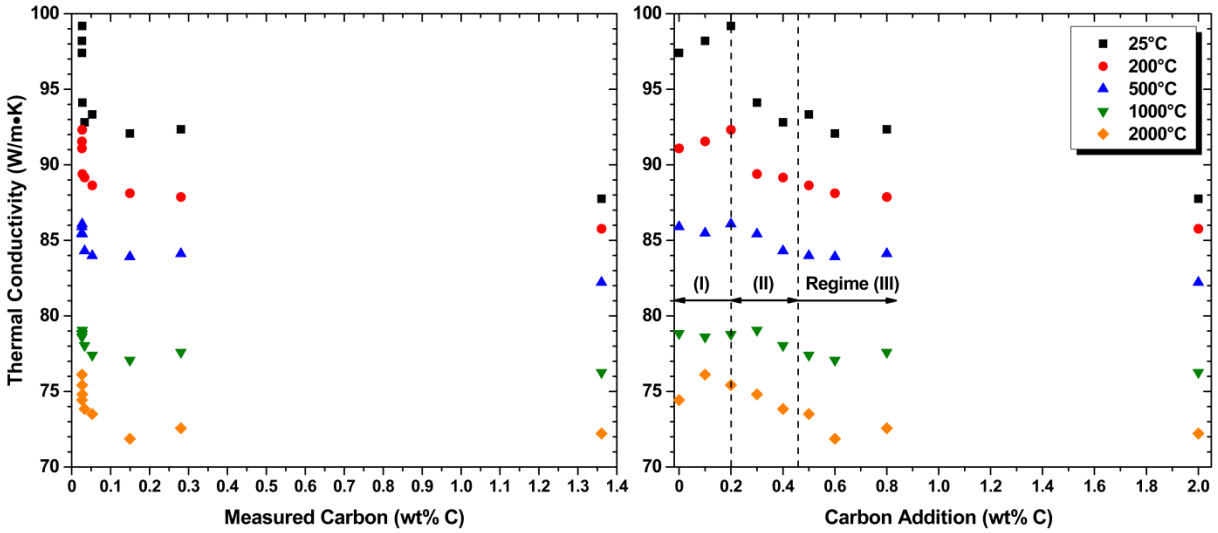

Fig. 6. Thermal conductivity as a function of measured carbon content (right) and carbon addition amount.

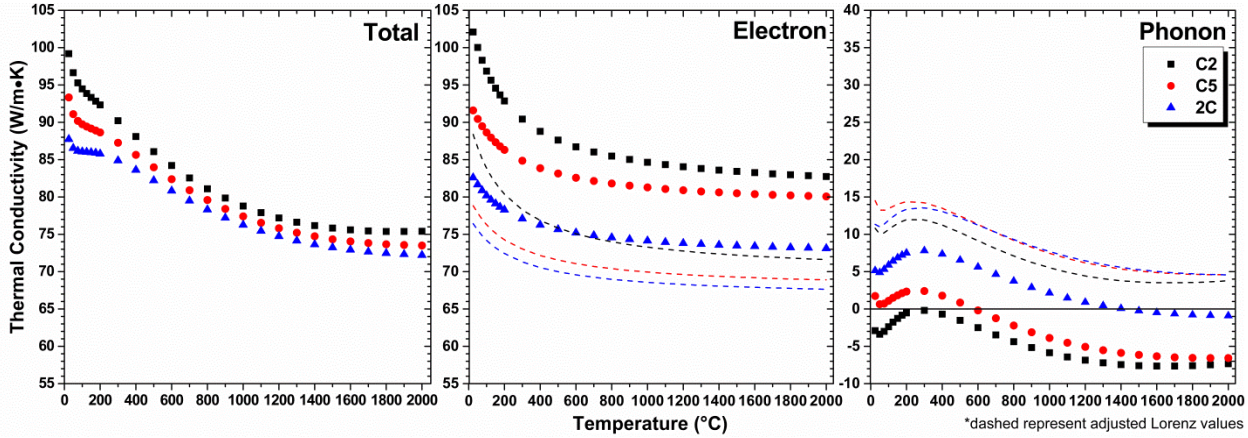

Fig. 7. Total, electron, and phonon thermal conductivities for specimens C2, C5, and 2C showing the separate contributions to k calculated using L_o (shapes) and then L_c (dashed lines) from each composition.

III. High Temperature Electrical Testing of Zirconium Diboride

Gregory J. K. Harrington, Greg E. Hilmas, and William G. Fahrenholtz

Department of Materials Science and Engineering, Missouri University of Science and Technology, Rolla, Missouri 65409

Abstract

Electrical resistivity of ZrB_2 was measured from room temperature to 1860°C using the van der Pauw method. The ZrB_2 was produced from commercial powder with additions of 1 wt% ZrH_2 and 0.2 wt% carbon and densified to ~96% of theoretical via hot pressing. X-ray diffraction and microscopy confirmed the final material was phase pure with the exception of 0.2 vol% of zirconia. The electrical testing was performed utilizing fixturing designed and fabricated in-house and the temperatures evaluated are believed to be the highest reported for the use of the van der Pauw technique. The high temperature setup proved effective as the fixturing eliminated the need for more complex specimen, contacts and geometries. Whereas previous studies have assumed a single continuous linear trend, the electrical resistivity of the ZrB_2 exhibited two linear trends with respect to temperature, increasing from 7.3 to 35.7 μΩ-cm between 25 and ~950°C and then from 35.7 to 76 μΩ-cm between ~950 and 1860°C. These results may indicate a change in the bonding nature or compositional distribution of the ZrB_2.

1. Introduction

Zirconium diboride (ZrB_2) is an attractive material for multiple advanced ceramic applications, including leading edges for hypersonic and reentry vehicles, nuclear cladding, molten metal crucibles, and electronic substrates.[1-4] These potential applications can be realized because ZrB_2 possesses a unusual set of properties at temperatures above which most structural ceramics have lost the majority of their room

temperature mechanical properties (i.e., >1500°C). The attractive attributes of ZrB_2 include high strengths (216±40 MPa at 2300°C) [5], high thermal conductivities for a ceramic (34-133 W/m-K at room temperature [6, 7] and 59-82 W/m-K at 2000°C [8, 9]), and good chemical stability in contact with molten metals.[10] The structure of ZrB_2 is hexagonal with Zr atoms arranged in hexagonal close packed layers and graphite like rings of B atoms positioned halfway between Zr layers.[11] ZrB_2 is characterized by a mix of covalent, ionic, and metallic bonding. The metallic bonding gives rise to electrical conduction in ZrB_2 and is localized to the metal atoms in the diborides.[12] The continuous layer of metallically bonded Zr atoms in the basal plane should lead to lower electrical resistivities (ρ_e) in the a-direction of ZrB_2 crystals. Indeed, Gasparov et al. reports a single crystal resistivity in the a-direction to be 6.1 μΩ-cm at 25°C and 7.2 μΩ-cm in the c-direction for zone refined ZrB_2.[13]

For hypersonics, use temperatures of leading and trailing edge structures have been proposed to be 2000°C or higher.[14, 15] To achieve this goal, aerospace designers require an understanding of the thermal conductivity (k) of the leading edge material. For ZrB_2, and other diborides, k is controlled by the summation of both phonon (k_p) and electron (k_e) thermal conduction mechanisms (equation (1)) due to the aforementioned bonding characteristics.

$$k = k_e + k_p \tag{1}$$

Because neither k_p nor k_e can be directly measured at temperatures above the boiling point of liquid He without the use of high or varied magnetic fields [16, 17], an indirect analysis is typically used. The electron contribution can be calculated from measurements of ρ_e using the Wiedemann-Franz law (equation (2)) [18] and then subtracted from k to obtain k_p.

$$k_e = \frac{TL}{\rho_e} \quad (2)$$

From the Wiedemann-Franz law, k_e is related to ρ_e at a given temperature (T) by a fitting parameter L otherwise known as the Lorenz number. If the mean free path for electrons as thermal and electrical conductors are equal, then L is defined as the constant L_o.[17] Using Fermi-Dirac statistics, Sommerfeld derived L_o to be equal to 2.44×10^{-8} $W\Omega K^{-2}$.[18] Multiple researchers report the calculation of k_e and k_p for ZrB_2 using equations (1) and (2), while utilizing the L_o term.[6, 8, 19-22] Two of these studies report estimations of negative k_p values from this analysis which indicates an $L<L_o$ may be more appropriate for these materials.[6, 19] Due to this, calculated Lorenz values (L_c) have been derived previously for ZrB_2.[19] In addition, similar evaluations have been made for various transition metals [23] and other conductive ceramics.[24] Assuming $k_p = C/T$ (C is a constant), equations (1) and (2) can be combined to give equation (3) and multiplying each side by T gives equation (4). A value L_c is then obtained from the slope of kT plotted with respect to T^2/ρ_e.[23]

$$k = \frac{L_c T}{\rho_e} + \frac{C}{T} \quad (3)$$

$$kT = \frac{L_c T^2}{\rho_e} + C \quad (4)$$

Because of the importance of evaluating thermal conductivity up to 2000°C, and the limited means by which this can be accomplished, the measurement of ρ_e approaching 2000°C is a necessity. The evaluation of ρ_e for ZrB_2, up to these temperatures, has only been carried out by Samsonov et al.[25], where other researchers have only tested in the range of 370 to 1300°C (Fig. 1).[8, 20, 21, 26-28] These researchers have been restricted from testing to higher temperatures due to the physical limitation of the metals used as the conductors or contacts (e.g. platinum [8, 21,

28], silver [20, 27], and nickel [8]). Any k_e values reported up to 2000°C in these studies have therefore been extrapolated using linear fits of ρ_e vs. T from lower temperatures. Reported values for ρ_e at room temperature (Fig. 1), range from 6 to 28 μΩ-cm at 25°C.[20, 21] The reported resistivity values increase linearly as temperature increases. Calculated resistivities for single crystal ZrB_2 by Sichkar et al. also displayed a linear trend over the same temperature range. Samsonov's data were not linear below ~920°C but starting at this temperature the trend appeared to be linear, resulting in a resistivity of ~57 μΩ-cm at the highest reported test temperature for ZrB_2 of 2000°C.

It is this deviation from linearity, for the only reported resistivity measurements at 2000°C, and the assumed linearity of $\rho_e(T)$, for all other research, which emphasizes the need for further high temperature evaluations of the electrical resistivity of ZrB_2. This study focuses on the development of a high temperature fixture for measuring ρ_e as a function of temperature up to 2000°C for nominally phase pure ZrB_2.

2. Experimental Procedure

2.1 Processing

The zirconium diboride evaluated in this study was produced from commercial ZrB_2 (Grade B; H.C. Starck, Goslar, Germany), phenolic resin (GP 2074; Georgia-Pacific, Atlanta, GA) as a source of 0.2 wt% C and zirconium hydride (ZrH_2, 1 wt% based on previous research [29]). The ZrB_2 and ZrH_2 were ball milled for 1.5 hours in acetone, then the phenolic was added followed by milling for an additional 30 minutes. The slurry was dried by rotary evaporation (Roto-vapor R-124; Buchi, Flawil, Switzerland) and the powder was ground and sieved to -100 mesh. Densification was carried out by isothermal hot pressing (HP50-7040G; Thermal Technology LLC, Santa Rosa, CA) at 2150°C for 70 minutes at 50 MPa. Before pressing, isothermal reaction holds were performed at 600°C (30 minutes in Ar-10%H_2 to pyrolyze the phenolic), 1250°C, 1450°C,

and 1600°C (1 hour each under vacuum for removal of surface oxides). The billet was sectioned using diamond machining (FSG-3A818; Chevalier, Santa Fe Springs, CA) and a disk for 4-point van der Pauw electrical testing was produced on a cylindrical grinder (608 Plain Grinder; Crystal Lake Grinders, North Fork, CA). The relative density was calculated from the bulk density measured using the Archimedes method assuming a theoretical density of 6.15 g/cm³. Measured electrical resistivities were then adjusted for porosity using the empirical relation (equation (5)).[30]

$$\rho_{e,\exp}^{-1} = \rho_{e,ZrB_2}^{-1} \frac{2\rho_{e,ZrB_2}^{-1} + \rho_{e,p}^{-1} - 2\nu_p\left(\rho_{e,ZrB_2}^{-1} - \rho_{e,p}^{-1}\right)}{2\rho_{e,ZrB_2}^{-1} + \rho_{e,p}^{-1} + \nu_p\left(\rho_{e,ZrB_2}^{-1} - \rho_{e,p}^{-1}\right)} \quad (5)$$

Where $\rho_{e,exp}$, ρ_{e,ZrB_2}, and $\rho_{e,p}$ are the electrical resistivities for the experimental measurements, ZrB_2 phase, and porosity, respectively, and v_p represents the volume fraction porosity. Equation (5) has been rewritten with inverse resistivities, in place of the conductivities, and $\rho_{e,p}^{-1}$ has been assumed to be zero.

2.2 Electrical Testing

Electrical resistivity testing was performed following ASTM Standard F-76-08. To test samples in the 4-point van der Pauw configuration from room temperature to 2000°C, a fixture was designed to be placed on the pneumatic elevating hearth of a metal element furnace (1100-4080-W3; Thermal Technology, Santa Rosa, CA). The fixture (used from 950 to 1860°C) is pictured in Fig. 2, along with a schematic depicting its design. A complimentary low temperature setup (25 to 800°C) was also used, where all W and ZrB_2 components were replaced with copper. A hexagonal-BN setter (Fig. 2.a.) was used to hold the four contacting bars (Fig. 2.d.) which then supported the contacting rollers (Fig. 2.d.). The slope of the bars was designed to keep the rollers in contact with the specimen (Fig. 2.h.) while allowing for thermal expansion during testing. In addition, the use of rollers to contact a thin disk eliminated any need to correct for effects of the

contact size.[31] Four tungsten wires (Fig. 2.e.) extended through the thermal shielding of the hearth to reach the testing fixture within the hot zone. Successful contacts between the W wires and contacting bars were made utilizing two methods. The first approach involved spot welding the wire to the ZrB_2-20vol% zirconium carbide (ZrC) contacting bars (Fig. 2.f.) via plasma arc welding. This proved effective, but time consuming to produce. A second approach involved pinning the hooked end of a W wire into a notch (Fig. 2; lower-left image), produced by electrical discharge machining (EDM; DS-2, Hansvedt, Orlando, FL), in the end of a ZrB_2 bar (Fig. 2.g.).

Current input (DLM 40-15; Sorensen, AMETEK Corp., San Diego, CA) and voltage measurement (NI 9211 DAQ w/NI USB-9162; National Instruments Corporation, Austin, TX) were controlled by a LabVIEW program (LabVIEW 12; National Instruments Corporation, Austin, TX). The applied current (typically 0.1-0.5 A) through the circuit was verified using a 0.05 Ω current sense resistor (CS3JR050E; Ohmite Mfg. Co., Arlington Heights, IL), which was also read by the DAQ. Eight separate permutations of current application and voltage measurement were performed for each temperature as part of the van der Pauw technique. Each permutation was also evaluated at three different currents to ensure the contacts were Ohmic. The resistivity obtained from the average of the eight permutations was further averaged with the resistivity from each testing current. In order to confirm the validity of the test setup, measurements were also made on a 2.54 cm diameter by 0.053 cm thick piece of molybdenum sheet (99.95% molybdenum; lot L22X005, Alfa Aesar, Ward Hill, MA). All electrical testing within the tungsten furnace was carried out under flowing Ar-10%H_2 following a vacuum purge of ≤60 mTorr (~8 Pa). Prior to entering the furnace, the gas was passed through an oxygen getter containing Ti turnings while being heated to 800°C (2B-20-Q-120; Centorr Vacuum Industries, Inc., Nashua, NH). Heating of the furnace was carried out at 15°C/min and the baseline voltage signal across the specimen was allowed to stabilize

before any measurements were performed. Room temperature test specimen thicknesses were corrected for thermal expansion using tabulated data for ZrB_2 and molybdenum from Touloukian et al.[32, 33]

2.3 Characterization

Bulk densities (ρ) were evaluated using the Archimedes method. ZrB_2 specimens were ground and polished to a 0.05 μm finish for electron microscopy (S-570; Hitachi, Ibaraki, Japan). X-ray diffraction (XRD; X'Pert Pro, PANalytical, Almelo, Netherlands) and transition electron microscopy (TEM; Tecnai F20, FEI, Hillsboro, OR) analysis were used for phase identification. Elemental analysis was also performed to measure C (CS600; Leco Corporation, St. Joseph, MI); N and O (TC500; Leco); and W, Co, Fe, and Hf (inductively coupled plasma mass spectroscopy; performed by NSL Analytical, Warrensville Heights, OH).

3. Results and Discussion

3.1 Evaluation of Molybdenum

The measured resistivity of the molybdenum sheet is plotted as a function of temperature in Fig. 3. Measurements using the low temperature setup (open triangles) are differentiated from those using the high temperature setup during heating to 1900°C (open triangles w/dot) and then cooling (closed triangles). In addition, the "recommended" values and upper/lower bounds for the ρ_e of Mo, as reported by Desai et al., are plotted for comparison.[34] Higher than expected resistivities were measured during heating for the Mo specimens. For an unknown reason data collection failed above 1900°C during heating but resumed upon cooling, with the highest evaluated temperature at 1860°C. Resistivity values obtained during cooling were lower than those made during heating. Values obtained during cooling lie along the upper bound for the reported values but appear to deviate to values slightly higher than the upper bound

starting at 1760°C. This deviation, and the change in results between the heating and cooling measurements, is not well understood. However, anecdotal evidence indicates it may be due to the high temperature fixturing. Visible oxidation was present on the exposed surfaces of the ZrB_2 fixturing after testing. This oxidation was a coherent layer which was thin enough to be removed by polishing with 15 µm diamond abrasive. In the oxidized regions, electrical continuity (verified with a multimeter) with the underlying ZrB_2 was disrupted. In a separate exploratory furnace run, unoxidized surfaces were realized by cooling directly to room temperature from high temperatures (>1900°C). Therefore, the belief is that the physical contacts were changing due to oxidation at low temperatures (600 to 1000°C), transitioning to removal of oxidation at higher temperatures. To support this hypothesis, the favorability of oxidation in the furnace environment was evaluated by calculating the oxygen partial pressure (pO_2). The pO_2 metal-oxide equilibrium values for Ti/TiO_2 and Zr/ZrO_2 were calculated using equation (6) [35], and compared with the oxidation of ZrB_2 presented by Chamberlain et al.[36]

$$\Delta G^{o}_{rxn} = RT \ln\left(pO_2\right) \tag{6}$$

The NIST-JANAF thermochemical tables [37] were used to obtain ΔG and R is the ideal gas constant. The pO_2 of the gas flow should be 10^{-37} atm due to the titanium getter that was operated at 800°C. This puts the oxidation range of ZrB_2, at or below ~670°C but at this pO_2, Zr should oxidize to form ZrO_2 up to ~970°C. These estimates assume no other source of oxygen, therefore oxidation of ZrB_2 or Zr at the surface may remain favorable up to even higher temperatures if any other source of oxygen exists. Regardless, the thermodynamics predict that the pO_2 of the system should allow oxidation at low temperatures, but not at elevated temperatures.

3.2 ZrB_2 Resistivity

A secondary electron image of the ZrB_2 ceramic prepared for this study is shown in Fig. 4. Based on Archimedes measurements, the ZrB_2 was determined to be ~96% of the theoretical density and the corresponding porosity (~4%) can be seen as the dark, nearly spherical features within the microstructure. In addition to porosity, a minor phase (0.2 vol%) of zirconia is visible (white, 1 to 5 μm features) and was identified via XRD and TEM as previously reported.[19] Besides these two features, the ZrB_2 appears to be free of other phases or impurities.

Like the molybdenum, resistivities of the ZrB_2 (Fig. 5) were also measured using the low temperature (open squares) and high temperature fixtures. The high temperature measurements were again made during heating (open square w/dot) and cooling (closed squares) after reaching a final temperature of 1900°C. The resistivity at room temperature was 7.3 μΩ-cm and increased to 76 μΩ-cm at 1860°C. Similar to the testing of the molybdenum, the resistivities measured during heating were higher than those measured during cooling. The data appear to fit two separate linear trends which deviate close the 36 μΩ-cm data point at 950°C. Previously, the resistivity of ZrB_2 has only been measured at the lower temperatures and then extrapolated to the higher temperatures. Direct measurements in the present study show that a linear fit through the data from 25 to 950°C is very good (R^2=0.9995) but the change in slope above this temperature would lead to the underestimation of resistivities by 16 μΩ-cm (19%) at 2000°C.

The change in slope for the current resistivity data is unexpected based on previous reports. Measurements for ZrB_2 by Zimmermann et al., Thompson et al., Tye and Clougherty, and Rahman et al. all indicated that the electrical resistivity of ZrB_2 was linear through this same range (Fig. 1). It is not clear exactly what may cause ZrB_2 to remain linear or change at a given temperature. As the bonding nature of ZrB_2 has both shared and delocalized electrons, a change in the distribution of electrons with

temperature is one possibility. The change in behavior may also be linked to a change in impurity content as temperature increases. Zirconia was identified as a second phase and the solubility of the excess oxygen and/or zirconium may alter the lattice resulting in an increased source of electron scattering. At this point these possibilities are merely speculation. Regardless of the mechanisms at work, the range of resistivities displayed in Fig. 1 deserve discussion with respect to the current material.

Comparison of this study with experimental values from the literature (Fig. 1) shows the current ZrB_2 to have a lower electrical resistivity than most of the materials, except for those by Zhang et al.[20], Rahman et al.[28], and Samsonov et al.[25]. Most of the reported values have similar slopes (excluding the data by Rahman et al.) and primarily differ in their magnitudes. Initially the resistivity obtained at 25°C in the current study (7.3 μΩ-cm) starts lower than for the ZrB_2 produced by Rahman et al., but the shallower slope results in the values crossing over between 25 and 100°C. In fact, ≥100°C, Rahman reports the lowest elevated temperature resistivities eventually increasing to ~20 μΩ-cm at 1300°C. As discussed in the introduction, the resistivities by Samsonov are the highest reported temperature measurements and at 800°C the resistivity (~28 μΩ-cm) falls below that of the current study (~31 μΩ-cm). The material by Zhang et al. are the only experimental resistivity values that were consistently lower than the current study. Zhang also had the lowest reported room temperature electrical resistivity for polycrystalline ZrB_2 at 6.7 μΩ-cm. In contrast, the highest resistivity at room temperature (22 μΩ-cm) is for ZrB_2 reported by Zimmermann et al. Zimmermann's material, along with that by Thompson et al. (AM) also have the highest resistivities at elevated temperatures where values of ~68 μΩ-cm at 1060°C and ~74 μΩ-cm at 1300°C were reported, respectively.

The differences in the resistivity values between the current and prior studies, outlined above, appear to primarily come from small compositional differences that stem

from processing. All materials underwent pressure assisted densification (hot pressing [8, 21, 25, 28] or SPS [20]) but different starting materials and powder processing routines were used. ZrB_2 produced in the current study used commercial powders, milled only to combine the raw materials prior to densification not to reduce particle size. Chemical analysis of this material indicated that it was ~98.1% pure based on C (0.03 wt%), O (0.13 wt%), N (0.08 wt%), Co (<0.001), Fe (<0.001), Hf (1.65 wt%), and W (0.005 wt%). In contrast, Zhang et al. produced ~99.6% pure ZrB_2 from the direct reaction of Zr (99.7% pure with <200 ppm Hf according to the manufacturer) and B (99%) powders. A second phase of ZrC was identified in the Zhang et al. study, making it the only other material besides the current study to report the presence of a second phase.[20] Attrition milling of commercial powders was responsible for contamination in the materials produced by both Thompson et al. (~2 wt% tungsten) [8] and Zimmermann et al. (~3 wt% tungsten) [21], resulting in ZrB_2 that was ≤95.7% pure. Results by McClane et al. showed increased concentrations of hafnium and tungsten (in addition to niobium, yttrium, and titanium) in solid solution led to increases in the ρ_e of ZrB_2. Therefore, the low hafnium content within the reaction processed material by Zhang likely resulted in its lowest resistivities and the tungsten contamination for Thompson's and Zimmermann's milled ZrB_2 were responsible for the marked increase in ρ_e. The results for the ZrB_2 by Rahman et al. are less clear and details regarding the material by Samsonov et al. were not provided. Rahman tested ZrB_2 with 2 wt% iron added as a sintering aid.[28] McClane's work indicates that transition metals should increase the resistivity of ZrB_2, but the effect of Fe has not been tested. Based on these comparisons, the change in magnitudes of ρ_e is influenced by the purity of the ZrB_2, where solid solutions, rather than second phases, had the most significant effect on resistivity.

3.3 Electrical Resistivity and Thermal Conduction

The thermal conductivity of the material examined in the present study was reported previously [19] and has been included herein as Fig. 6. The electron contributions were calculated from the low temperature resistivity data using L_o (solid line) and an L_c of 2.11 x 10^{-8} $W\Omega K^{-2}$ (dotted line) derived using equation (4). The forms of k and k_e as a function of temperature are similar, but the analysis of k_e changes in light of the high temperature resistivity data presented in the current study.

Using the linear fit of ρ_e above 950°C, k_e is plotted in Fig. 6 using L_o (dashed line) and a recalculated L_c of 3.78 x 10^{-8} $W\Omega K^{-2}$ (dashed/dotted line). The increased slope of ρ_e as a function of temperature translates to a more negative slope, which no longer trends well with k. Calculation of a Lorenz value using equation (4) appears to be invalid for two reasons. First, the resulting k_e values were higher than k which is a physical impossibility. Second, the intercept (C) from this evaluation was negative. As this constant represents the lattice conductivity at a given temperature, it must be positive to have a physical meaning. At elevated temperatures k and k_e should be similar as k_p is not expected to vary significantly above the Debye temperature. Therefore, at temperatures above 950°C the Lorenz number for ZrB_2 may be better characterized by a dynamic value which increases with increasing temperature. This is consistent with previous reports of Lorenz values that increase at elevated temperatures.[18] The change in the slope of ρ_e with temperature and an increasing Lorenz number could then be an indication of an increase in an inelastic scattering process for the electrons as electrical conductors for ZrB_2 at elevated temperatures.

4. Summary and Conclusions

An electrical testing fixture was used to evaluate the resistivity of ZrB_2 up to 1860°C using the van der Pauw technique. This is the highest temperature reported for the

measurement of electrical resistivities utilizing this technique. A molybdenum disk was evaluated as a standard from room temperature (6.0 μΩ-cm) to 1860°C (62 μΩ-cm). These values agreed well with the upper limits for the accepted resistivities for molybdenum from the literature (~5.8 and ~60 μΩ-cm at room temperature and 1860°C, respectively). The electrical resistivity of ZrB_2 increased from 7.3 μΩ-cm at 25°C to 76 μΩ-cm at 1860°C. This rise in the resistivity is characterized by two separate linear regions, which transition near 950°C. It is not understood why the ZrB_2 did not exhibit a continuous linear trend through the entire temperature range, but it is proposed that either a change in the electron distribution, or an increase in the solid solution of oxygen or zirconium from a minor (0.2 vol%) zirconia second phase occurred. In the end, this testing setup shows promise for the evaluation of the elevated temperature electrical resistivity of ceramics by utilizing specialized fixturing that provides repeatable electrical contacts to be made without the need to establish permanent connections to the specimen.

Acknowledgments

The authors would like to thank Ryan Grohsmeyer for his help in fabricating, and Dr. Jeremy Watts for his collaboration in developing and fabricating, the high temperature electrical fixturing. This research was funded by the National Science Foundation (DMR-0906584).

References

[1] Okamoto NL, Kusakari M, Tanaka K, Inui H, Yamaguchi M and Otani S, "Temperature dependence of thermal expansion and elastic constants of single crystals of ZrB_2 and the suitability of ZrB_2 as a substrate for GaN film," *J Appl Phys* 2003; **93**(1):88-93.

[2] Rogl P and Bittermann H, "On the Ternary System Hafnium–Boron–Carbon," *J Solid State Chem* 2000; **154**(1):257-62.

[3] Gasch MJ, Ellerby DT and Johnson SM, "Ultra High Temperature Ceramic Composites," In: Bansal NP, editor *Handbook of Ceramic Composites*, New York: Springer; 2005, p. 197-224.

[4] Kaji N, Shikano H and Tanaka I, "Develpment of ZrB_2-Graphite Protective Sleeve for Submerged Nozzle," *Taikabutsu Overseas* 1992; **14**(2):39-43.

[5] Neuman EW, Hilmas GE and Fahrenholtz WG, "Strength of Zirconium Diboride to 2300°C," *J Am Ceram Soc* 2013; **96**(1):47-50.

[6] McClane DL, Fahrenholtz WG and Hilmas GE, "Thermal Properties of (Zr,TM)B_2 Solid Solutions with TM = Hf, Nb, W, Ti, and Y," *J Am Ceram Soc* 2014; **97**(5):1552-8.

[7] Guo S, Nishimura T and Kagawa Y, "Preparation of zirconium diboride ceramics by reactive spark plasma sintering of zirconium hydride-boron powders," *Scripta Mater* 2011; **65**(11):1018-21.

[8] Thompson MJ, Fahrenholtz WG and Hilmas GE, "Elevated Temperature Thermal Properties of ZrB_2 with Carbon Additions," *J Am Ceram Soc* 2012; **95**(3):1077-85.

[9] Clougherty EV, Wilkes KE and Tye RP, "Research and Development of Refractory Oxidation-Resistant Diborides, Part II, Volume V: Thermal, Physical, Electrical, and Optical Properties," *Air Force Materials Laboratory, Air Force Systems Command,*

Wright-Patterson Air Force Base, Ohio, Technical Report AFML-TR-68-190, Part II, Volume V 1969;

[10] Mroz C, "Zirconium Diboride," *Am Ceram Soc Bull* 1994; **73**(6):141-2.

[11] Fahrenholtz WG, Hilmas GE, Talmy IG and Zaykoski JA, "Refractory Diborides of Zirconium and Hafnium," *J Am Ceram Soc* 2007; **90**(5):1347-64.

[12] Vajeeston P, Ravindran P, Ravi C and Asokamani R, "Electronic structure, bonding, and ground-state properties of AlB_2-type transition-metal diborides," *Phys Rev B* 2001; **63**(4):045115-(1-12).

[13] Gasparov VA and Suslov A, "Electron Transport and Superconducting Properties of ZrB_{12}, ZrB_2 and MgB_2," *AIP Conference Proceedings* 2006; **850**(1):637-8.

[14] Opeka MM, Talmy IG and Zaykoski JA, "Oxidation-based materials selection for 2000°C + hypersonic aerosurfaces: Theoretical considerations and historical experience," *J Mater Sci* 2004; **39**(19):5887-904.

[15] Van Wie DM, Drewry DG, King DE and Hudson CM, "The hypersonic environment: Required operating conditions and design challenges," *J Mater Sci* 2004; **39**(19):5915-24.

[16] Lukas KC, Liu WS, Joshi G, Zebarjadi M, Dresselhaus MS, Ren ZF, et al., "Experimental determination of the Lorenz number in $Cu_{0.01}Bi_2Te_{2.7}Se_{0.3}$ and $Bi_{0.88}Sb_{0.12}$," *Phys Rev B* 2012; **85**(20):205410.

[17] Kumar GS, Prasad G and Pohl RO, "Experimental determinations of the Lorenz number," *J Mater Sci* 1993; **28**(16):4261-72.

[18] Uher C, "Thermal Conductivity of Metals," In: Tritt TM, editor *Thermal Conductivity: Theory, Properties, and Applications*, Springer; 2004, p. 21-91.

[19] Harrington GJK, Hilmas GE and Fahrenholtz WG, "Effect of Carbon on the Thermal and Electrical Transport Properties of ZrB_2," *J Eur Ceram Soc* late 2014;

[20] Zhang L, Pejaković DA, Marschall J and Gasch M, "Thermal and Electrical Transport Properties of Spark Plasma-Sintered HfB_2 and ZrB_2 Ceramics," *J Am Ceram Soc* 2011; **94**(8):2562-70.

[21] Zimmermann JW, Hilmas GE, Fahrenholtz WG, Dinwiddie RB, Porter WD and Wang H, "Thermophysical Properties of ZrB_2 and ZrB_2–SiC Ceramics," *J Am Ceram Soc* 2008; **91**(5):1405-11.

[22] Patel M, Prasad VVB and Jayaram V, "Heat conduction mechanisms in hot pressed ZrB_2 and ZrB_2–SiC composites," *J Eur Ceram Soc* 2013; **33**(10):1615-24.

[23] Sharma RG, Chari MSR and Reddy DK, "The electronic Lorenz number in some transition metals at high temperatures," *J Phys F* 1986; **16**(5):603-7.

[24] Morgan PED, "Wiedemann-Franz-Lorenz Relation in Metallic Conducting Ceramics," *J Am Ceram Soc* 1975; **58**(7-8):349.

[25] Samsonov GV and Sinel'nikova VS, "The resistivity of refractory compounds at high temperatures," *Sov Powder Metall* 1962; **1**(4):272-4.

[26] Fail L, "Narcolepsy and neurosis," *Med J Aust* 1973; **2**(5):223-5.

[27] Thompson MJ, "Densification and Thermal Properties of Zirconium Diboride Based Ceramics," *Material Science and Engineering*, **PhD**(228, 2012.

[28] Rahman M, Wang CC, Chen W, Akbar SA and Mroz C, "Electrical Resistivity of Titanium Diboride and Zirconium Diboride," *J Am Ceram Soc* 1995; **78**(5):1380-2.

[29] Harrington GJK, Hilmas GE and Fahrenholtz WG, "Effect of Carbon and Oxygen on the Densification and Microstructure of Hot Pressed Zirconium Diboride," *J Am Ceram Soc* 2013;

[30] Sun C-N, Gupta MC and Porter WD, "Thermophysical Properties of Laser-Sintered Zr–ZrB2 Cermets," *J Am Ceram Soc* 2011; **94**(8):2592-9.

[31] Chwang R, Smith BJ and Crowell CR, "Contact size effects on the van der Pauw method for resistivity and Hall coefficient measurement," *Solid-State Electronics* 1974; **17**(12):1217-27.

[32] Touloukian YS, Kirby RK, Taylor RE and Desai PD, *Thermal Expansion: Nonmetallic Solids*, IFI/Plenum; 1977.

[33] Touloukian YS, Kirby RK, Taylor RE and Desai PD, *Thermal Expansion: Metallic Elements and Alloys*, IFI/Plenum; 1975.

[34] Desai PD, Chu TK, James HM and Ho CY, "Electrical Resistivity of Selected Elements," *J Phys Chem Ref Data* 1984; **13**(4):1069-96.

[35] Gaskell DR, *Introduction to thermodynamics of materials*, New York; London: Taylor & Francis; 2003.

[36] Chamberlain A, Fahrenholtz W, Hilmas G and Ellerby D, "Oxidation of ZrB_2-SiC ceramics under atmospheric and reentry conditions," *Refractories Applications Transactions* 2005; **1**(2):1-7.

[37] Chase MW, *NIST-JANAF Thermochemical Tables. American Chemical Society and the American Institute of Physics*, 4th ed, Woodbury, NY: 1998.

Fig. 1. Experimental and calculated electrical resistivities as a function of temperature for ZrB_2 from the literature and the current study, showing the wide variation in reported values.

Fig. 2. (left) Image of the electrical test setup supported on the W hearth of the furnace elevator door. (upper-right) A schematic of the high temperature electrical testing fixture in cross section, with the following parts: a. circular BN setter, b. BN samples support, c. ZrB_2-20%ZrC contacting bar, d. ZrB_2 contacting roller, e. W wire, f. contacting bar/wire spot weld, g. contacting bar/wire pin and slot connection, and h. sample disk. An identical set of wires, contacting bars and rollers rest 90° to the first set within the BN setter. (lower-right) Image of a contacting bar with a tungsten wire pinned into an machined notch.

Fig. 3. Measured resistivities of molybdenum (as a reference material) tested up to 1860°C from room temperature are plotted along with values for molybdenum from literature.[34] For each material the data is separated into the measurements made with the low temp fixture (open shapes), high temp fixture during heating (open shapes w/dot), and high temp fixture upon cooling from 1900°C (closed shapes).

Fig. 4. Secondary electron image of the ZrB_2 showing porosity (black with charging perimeters) and zirconia (white minority phase).

Fig. 5. Electrical resistivity with respect to temperature for the ZrB_2 specimen, showing the shift in linear trends near 950°C. For each material the data is separated into the measurements made with the low temp fixture (open shapes), high temp fixture during heating (open shapes w/dot), and high temp fixture upon cooling from 1900°C (closed shapes).

Fig. 6. Comparison of electron thermal conductivities calculated from the linear fit of resistivity via the low and high temperature fixturing. Both theoretical and calculated Lorenz values were used to calculate k_e and the total thermal conductivity is plotted for reference.

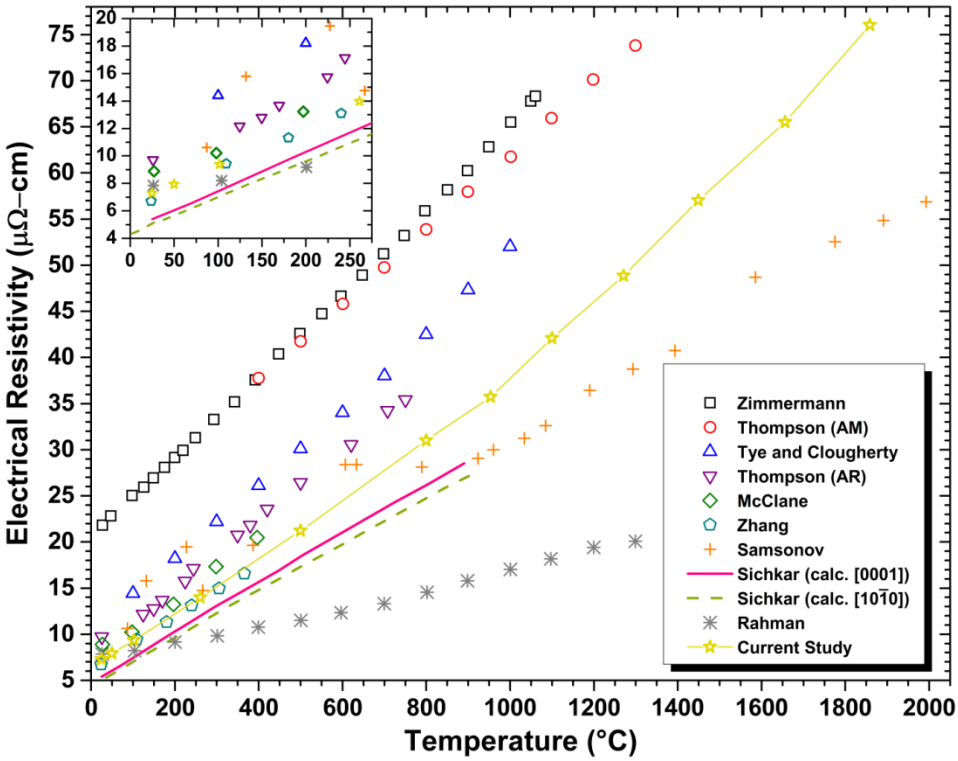

Fig. 1. Experimental and calculated electrical resistivities as a function of temperature for ZrB_2 from the literature and the current study, showing the wide variation in reported values.

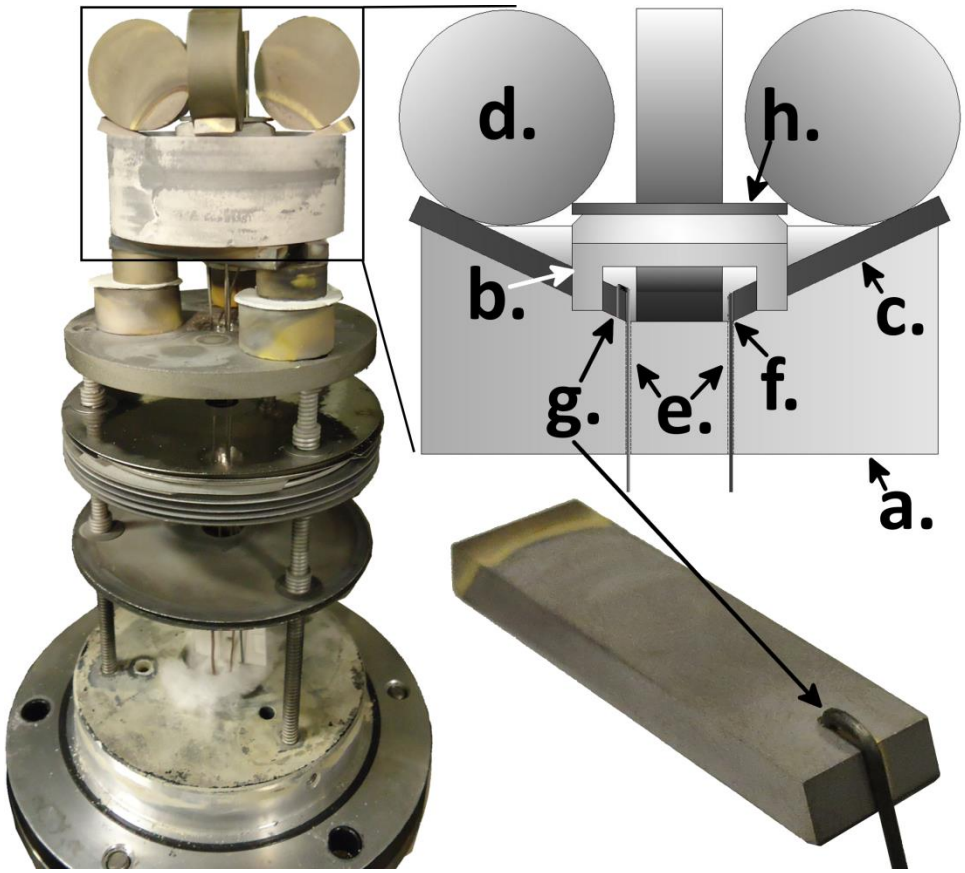

Fig. 2. (left) Image of the electrical test setup supported on the W hearth of the furnace elevator door. (upper-right) A schematic of the high temperature electrical testing fixture in cross section, with the following parts: a. circular BN setter, b. BN samples support, c. ZrB_2-20%ZrC contacting bar, d. ZrB_2 contacting roller, e. W wire, f. contacting bar/wire spot weld, g. contacting bar/wire pin and slot connection, and h. sample disk. An identical set of wires, contacting bars and rollers rest 90° to the first set within the BN setter. (lower-right) Image of a contacting bar with a tungsten wire pinned into a machined notch.

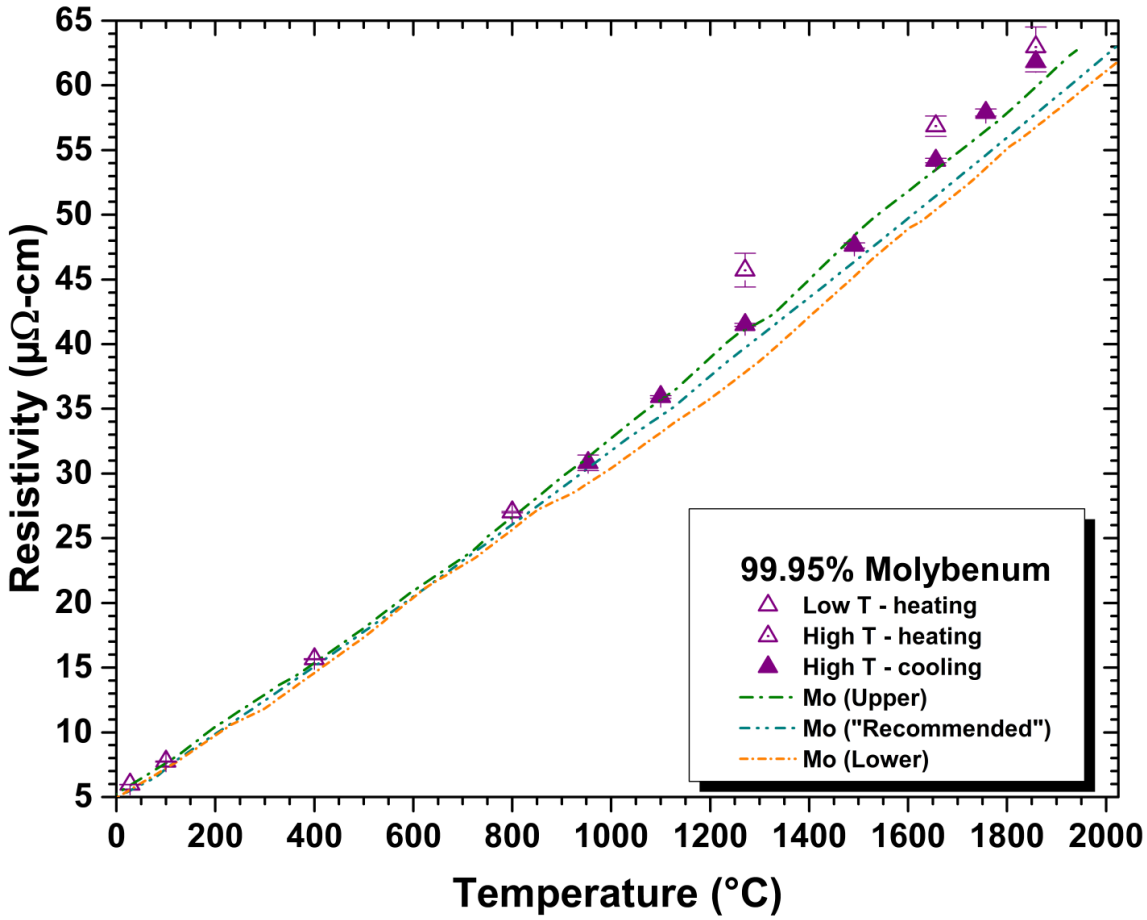

Fig. 3. Measured resistivities of molybdenum (as a reference material) tested up to 1860°C from room temperature are plotted along with values for molybdenum from literature.[34] For each material the data is separated into the measurements made with the low temp fixture (open shapes), high temp fixture during heating (open shapes w/dot), and high temp fixture upon cooling from 1900°C (closed shapes).

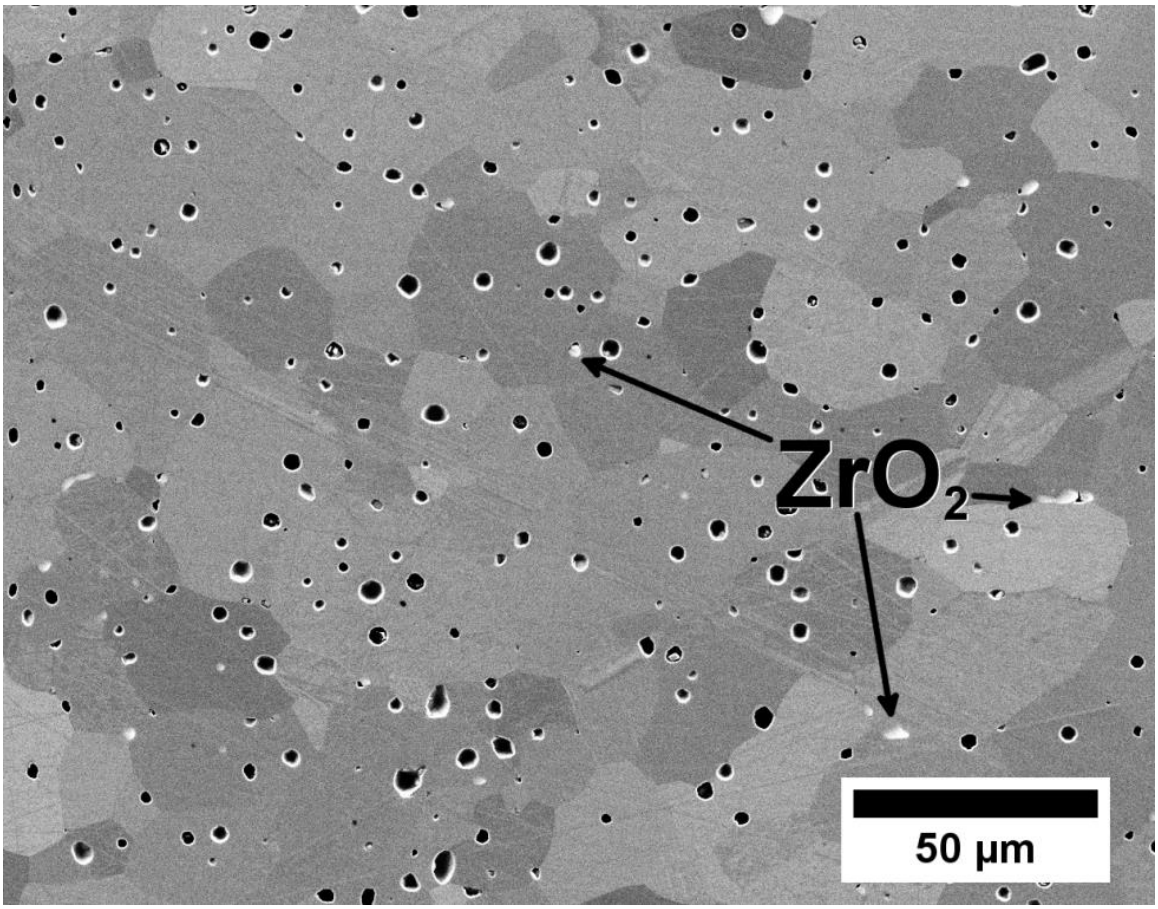

Fig. 4. Secondary electron image of the ZrB_2 showing porosity (black with charging perimeters) and zirconia (white minority phase).

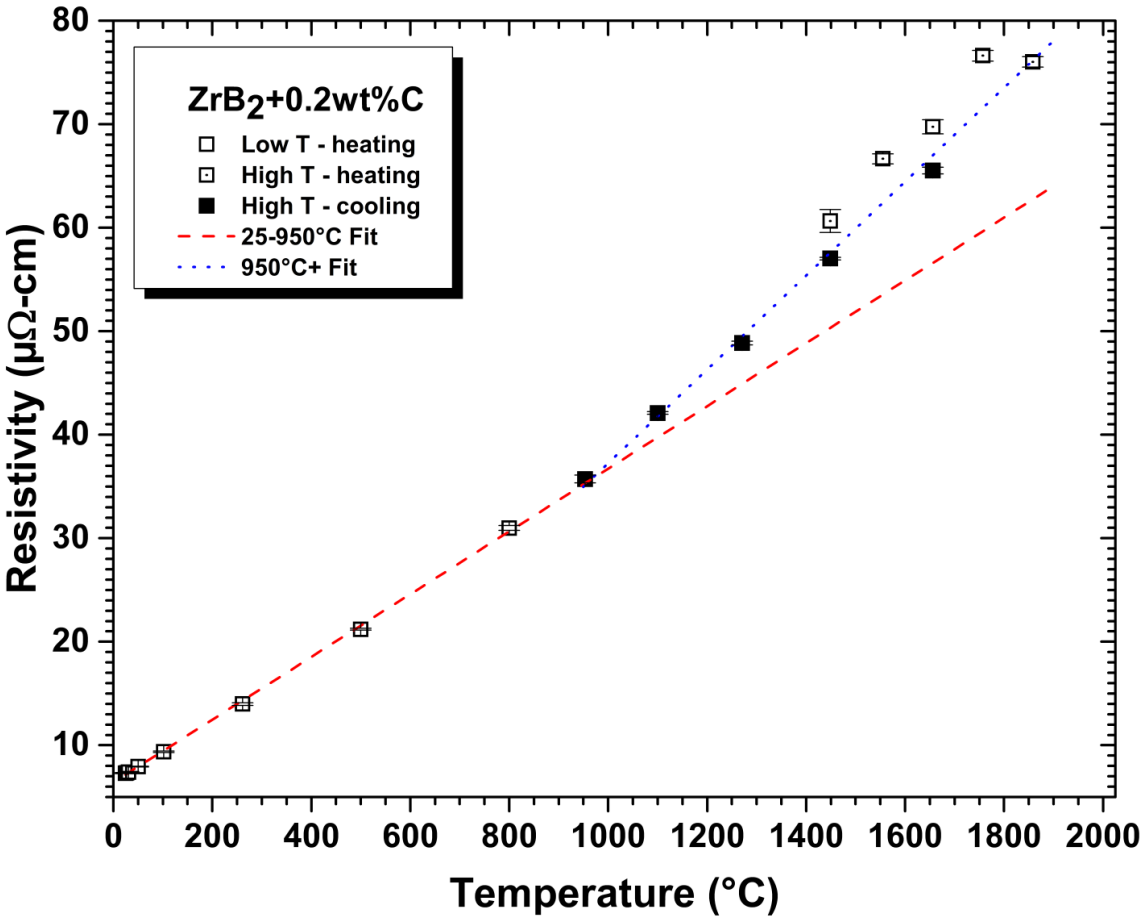

Fig. 5. Electrical resistivity with respect to temperature for the ZrB_2 specimen, showing the shift in linear trends near 950°C. For each material the data is separated into the measurements made with the low temp fixture (open shapes), high temp fixture during heating (open shapes w/dot), and high temp fixture upon cooling from 1900°C (closed shapes).

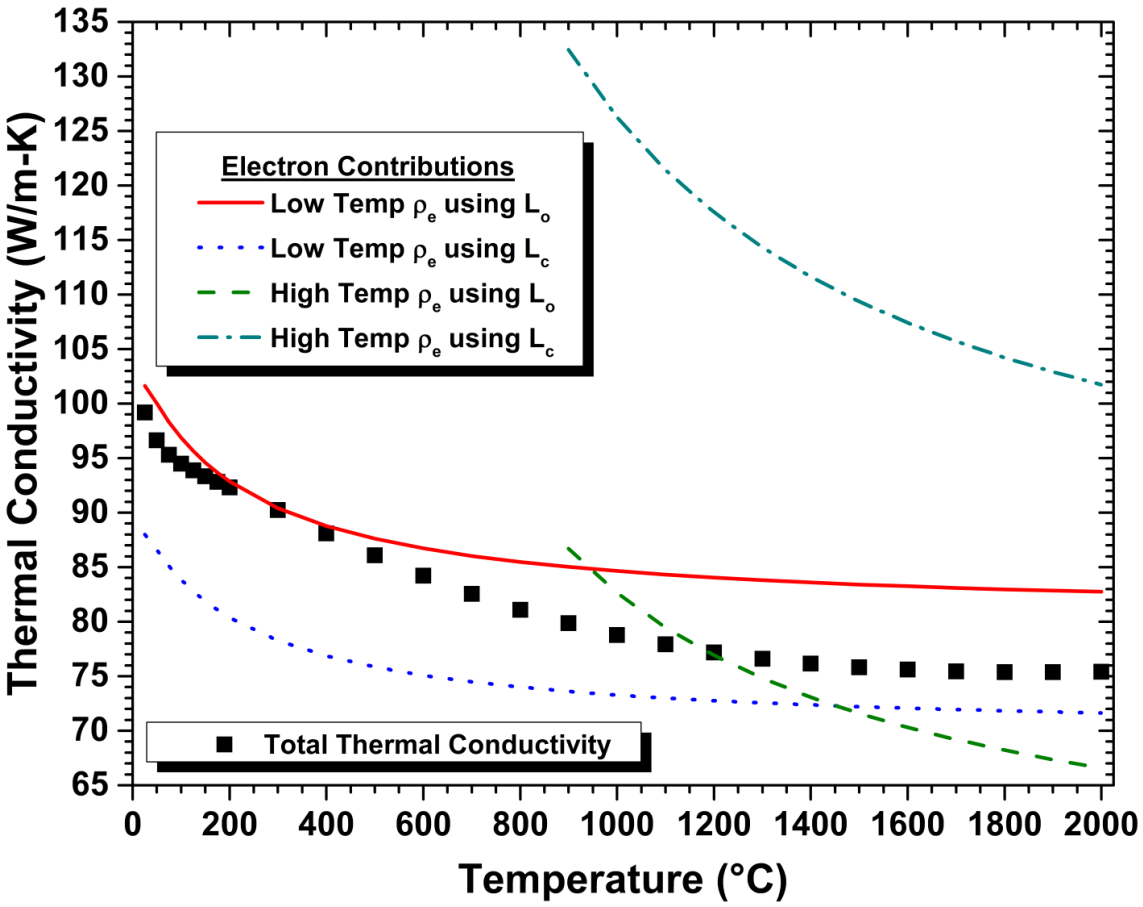

Fig. 6. Comparison of electron thermal conductivities calculated from the linear fit of resistivity via the low and high temperature fixturing. Both theoretical and calculated Lorenz values were used to calculate k_e and the total thermal conductivity is plotted for reference.

IV. Thermal Conductivity Modification to $(Zr,W)B_2$ by ZrC Additions

Gregory J. K. Harrington, Greg E. Hilmas, and William G. Fahrenholtz

Department of Materials Science and Engineering, Missouri University of Science and Technology, Rolla, Missouri 65409

Abstract

The thermal conductivity of ZrB_2 with WC and ZrC additions was studied from 25 to 2000°C. ZrC additions were made from 0 to 10 vol% based on reported interactions with $(Zr,W)B_2$ solid solutions. X-ray diffraction analysis showed changes in the lattice parameter of ZrC which were attributed to W diffusion from $(Zr,W)B_2$ into ZrC. (Zr,W)C second phase ZrC contents of 1.72, 4.47, and 9.37 vol% were concluded to have reduced the percentage of W in ZrB_2 by 31-34%, 68-71%, and 71-90%, respectively. Electrical resistivity was lowest (~9.9 μΩ•cm at 25°C) and thermal conductivity highest (78 and 72 W/m•K at 25 and 2000°C, respectively) for the 1 and 2.5 vol% additions of ZrC due to the decrease in W content in $(Zr,W)B_2$. Electrical resistivities were increased and thermal conductivities decreased at the ZrC compositional extremes. Without ZrC this was the result of the full amount of WC contamination being contained in the ZrB_2. For higher additions the higher resistivity, and lower thermal conductivity, ZrC second phase was the limiting factor. Evaluation of the electron and phonon contributions to the total thermal conductivity showed that the electron contribution was most affected by changes in composition, while the phonon conduction resulted in the change in conductivity as a function of temperature. Calculation of experimental Lorenz numbers shows that W solid solution contamination can increase the Lorenz value to near that of the theoretical number. Finally, grain growth in ZrB_2 was shown to be heavily influenced by the presence of ZrC. Starting ZrB_2 grain sizes were all 3.3 to 3.9 μm after hot pressing but heat treatment at 2100°C for 4 hours resulted in a five-fold increase in the

grain size of the ZrB_2 with 0 vol% ZrC and only a two-fold increase for the ZrB_2 with 10 vol% ZrC. Based on these results, the decrease in thermal conductivity due to the ZrC second phase could be an acceptable tradeoff for improved high temperature microstructural stability thanks to limiting the grain growth in these materials.

1. Introduction

Due to its extremely high melting temperature (~3250°C) [1], zirconium diboride (ZrB_2) is typically classified as an ultra-high temperature ceramic (UHTC).[2] In addition to its melting point, several other characteristics of ZrB_2 make it a top candidate for use in applications with extreme operating conditions, such as those encountered by, leading/trailing edges of hypersonic aerospace vehicles.[3,4] Strong Zr-B (ionic) and B-B (covalent) [5] bonding allows ZrB_2 to be a very high strength material with excellent hardness (565±53 MPa and 23±0.9 GPa, respectively) [6]. The tradeoff with this strong bonding comes as difficulties in densification. Reinforcing phases (SiC [6,7], ZrC [8,9], etc.) are typically used to improve both mechanical properties and densification, by limiting coarsening and keeping grain/particle sizes smaller. Thermal conductivity (k) is also an interesting property for zirconium diboride because it can be very high (up to 133 W/m•K at 25°C) [10], for a ceramic. However, thermal conductivities less than 100 W/m•K are more typical, mainly due to the effects of solid solutions [11-16] or second phase additions (SiC [12,16], ZrC [17,18], C [13,15], $MoSi_2$ [19] etc.) which have lower thermal conductivities than the ZrB_2 matrix. Because conditions which lead to improved (higher) thermal conductivities (higher purity and larger grain sizes) are most often in competition with improving mechanical properties, it is worth studying ways to improve both simultaneously.

Comminution of ZrB_2 improves densification by increasing the free energy of the system, which increases the driving force for solid state sintering.[20,21] Cobalt bonded

WC (typically 6% Co) is commonly utilized as media for attrition milling, as its hardness (12 to 20 GPa) [22] and density (14.94 g/cm³) [23] make it an ideal choice. WC can also serve as a reducing agent to remove surface oxides from ZrB_2, driving densification which has also been shown to improve the final density of diboride ceramics.[21,24] However, a study by Choi et al. indicated that WC alone may not be the most effective sintering aid. Choi made additions of WC, Co, and WC-6%Co to ZrB_2 and found that Co was the most significant contributing factor to the improved densification due to liquid phase sintering.[25]

Due to a reduction in grain sizes, milling with WC media has been used with great effectiveness to produce high strength ZrB_2.[6,26] Although, a tradeoff in using WC appears to be reduced ZrB_2 thermal conductivities. Zimmermann et al. reported ZrB_2 with ~2.8 wt% WC contamination (1.8 mol%, based on the reported bulk density of 6.27 g/cm³ and calculated assuming a density of 6.15 g/cm³ for ZrB_2 [27] and 19.3 g/cm³ for W [28]) to have a thermal conductivity of 56 W/m•K at 25°C.[12] While, a conductivity of 45 W/m•K (400°C) was presented by Thompson et al. for attrition milled ZrB_2 with 2.2 wt% WC (1.4 mol% WC).[13] Both Zimmermann and Thompson attributed their results to the formation of a $(Zr,W)B_2$ solid solution. Compared with thermal conductivities of 99 W/m•K (25°C) and 88 W/m•K (400°C) for "pure" ZrB_2 processed from the same manufacturer/grade of powder, their values were greatly reduced.[15] McClane et al. investigated the effect of several different transition metals, including W, on the k of ZrB_2. An addition of 5.1 wt% (3 mol%) W decreased k by 54 W/m•K (25°C) from that of the reference ZrB_2 (88 W/m•K) of the same study. W was reported to have the largest effect on k of the metals tested (Hf, Ti, Nb, Y, and W). The authors proposed that the presence of W in the ZrB_2 imposes a strain on the lattice due to the preferred structure of tungsten boride ($P6_3/mmc$ for W_2B_4).[11]

ZrC may be a beneficial second phase additive to ZrB_2 due to its affinity for W, and the resulting ability to getter W from $(Zr,W)B_2$ solid solutions. Thompson et al. detailed the formation of ZrC in ZrB_2, with added carbon, which was attrition milled with WC. X-ray diffraction (XRD) analysis indicated a decrease in the lattice parameter of the ZrC from that of pure ZrC due to the formation of a (Zr,W)C solid solution. The thermal conductivity of this material increased 5 to 6 W/m•K, across the entire temperature range, over the carbon free composition without ZrC.[13] As discussed by Andrievskii et al.[17] and Fridlender et al.[18], ZrC should lower the thermal conductivities due to its lower k than ZrB_2. In the end this may be an acceptable trade off, as ZrC has also been shown to improve densification and limit grain growth of ZrB_2 ceramics.[8]

This study has investigated the effect of ZrC additions on the grain growth, electrical resistivity and thermal conductivity of ZrB_2 based ceramics with WC contamination. The total thermal conductivity was separated using electrical resistivity to evaluate the electron and phonon contributions. These results were interpreted using XRD and scanning electron microscopy (SEM) analysis to understand the second phase and solid solution distributions within each composition.

2. Experimental Procedure

2.1 Powder Processing

The starting ZrB_2 and ZrC powders (both Grade B, H.C. Starck, Goslar, Germany) were attrition milled separately for 2 h in hexanes in a fluoropolymer lined bucket using 6%Co-bonded WC media and a spindle with arms of the same WC-6%Co. WC contamination was tracked by weighing both the spindle and media before and after milling. After drying (Roto-vapor R-124, Buchi, Flawil, Switzerland), nominal compositions of 0, 1, 2.5, 5, and 10 vol% ZrC were batched. The true calculated ZrC addition values are presented in Table I. The naming convention of #-ZrC has been used to identify each composition

where the # represents the value to the left of the decimal of the nominal ZrC vol% addition. Each composition was ball milled in acetone for 4 h with phenolic resin (GP 2074, Georgia-Pacific, Atlanta, GA), as a source of 0.5 wt% C (based on the ZrB_2), using ZrB_2 media. The powders were dried again and subsequently ground with an alumina mortar and pestle and sieved to -50 mesh.

2.2 Hot Pressing and Specimen Preparation

Powders were loaded in a 44.5 mm diameter graphite die, lined with graphite foil coated with BN spray. After loading the die into the hot press (HP20-3060, Thermal Technologies LLC, Santa Rosa, CA) isothermal vacuum holds of 600°C (30 min), 1250°C, 1450°C, and 1600°C (1 hr each) were performed. A pressure of 32 MPa was applied starting at 1600°C and the furnace was ramped at 30°/min to 1900°C for 30 min under flowing Ar to densify the material. After densification the furnace was allowed to cool naturally and the pressure was released upon reaching 1600°C. Each billet was sectioned using diamond machining to produce a thermal diffusivity specimen (nominally 12.7x12.7x2.5 mm) and a disk for electrical testing (nominally 23 mm in diameter by 1 mm thick). A separate piece of each billet was heat treated at 2100°C for 4 hr in a graphite element furnace (1000-4560-FP30, Thermal Technologies LLC, Santa Rosa, CA) to observe the grain growth characteristics of each composition above the processing temperature. Diamond grinding and polishing to 0.05 µm was performed for microscopy. Finally, each composition was crushed in a steel die then ground in an alumina mortar and pestle and finally sieved to -200 mesh in preparation for XRD.

2.3 Characterization

Bulk densities (ρ) were evaluated using the Archimedes method using water as the immersing medium. These values were corrected as a function of temperature, for use in thermal conductivity/electrical resistivity calculations, using thermal expansion data from Touloukian.[29] SEM (S-570, Hitachi, Ibaraki, Japan) was performed on specimens as-

polished and as-etched (2/3 KOH and 1/3 DI H_2O by weight @ 140°C for 1 to 3 minutes depending on grain size). Image analysis (ImageJ, National Institutes of Health, West Bethesda, MD) was performed on SEM images to determine the second phase volume fractions as well as grain sizes (min/max dimensions determined by fitting an ellipse). The analysis of grain sizes was performed by outlining the boundaries using image manipulation software (GIMP, GNU Image Manipulation Software, version 2.8.6). At least 500 ZrB_2 grains and 200 ZrC grains were outlined in each case. Confocal Raman spectroscopy (633 nm He-Ne laser, Aramis Labram, Horiba Jobin Yvon, Edison, NJ) was used to identify carbon and boron carbide. XRD (X'Pert Pro, PANalytical, Almelo, Netherlands) analysis was also used for phase identification and lattice parameters were determined using Rietveld refinement.

The thermal diffusivity (D) of each composition was evaluated using the laser flash technique from 25 to 200°C† and from 200 to 2000°C‡ (S-2† and FL5000‡, Anter Corporation, New Castle, DE). The specimens were coated with a thin layer of graphite (dry film graphite lubricant, Sprayon, Cleveland, OH) to increase absorption of the laser and reemission of the heat in the FL5000. Testing was carried out under flowing Ar at a gauge pressure of ~41 kPa. Each D value is the average of three separate laser pulses and these results were calculated using the Clark and Taylor method.[30] Diffusivity was fit as a function of temperature from 25°C to 300°C using the average of an Arrhenius (equation (1)) and natural log (equation (2)) relation.

$$D = D_o \exp\left(-\frac{E_a}{RT}\right) \tag{1}$$

$$D = A\ln(T) + B \tag{2}$$

Only the natural log fit was used above 300°C as it better characterized the raw data. The constant pressure heat capacity (C_p) of each composite was calculated as a

volumetric average of the individual phases and heat capacities for each phase (ZrB_2, ZrC, and either C or B_4C) were taken from the NIST-JANAF thermochemical tables.[31] The thermal conductivity (k) was then calculated using equation (3)

$$k = \rho \cdot D \cdot C_p \quad (3)$$

Electrical resistivity (ρ_e) testing was performed from room temperature to 800°C (measured with a k-type thermocouple) using a 4-point van der Pauw setup following ASTM standard F76-08.[32] The setup and specifics of testing are detailed in the preceding paper.[15] In order to compliment the high temperature thermal conductivity analysis, the measured ρ_e values were all fit to linear function of temperature and the corresponding linear regression slopes (a) and intercepts (b) were used to extrapolate ρ_e above 800°C.

3. Results and Discussion

3.1 Microstructure and Second Phase Content

Representative examples of the as-processed microstructures are shown for 0-ZrC, 2-ZrC and 10-ZrC in Fig. 1. All compositions contained a second phase of graphitic carbon (determined via Raman spectroscopy) as indicated in the micrographs (Fig. 1). Boron carbide was the only other second phase observed in 0-ZrC and is visible as larger (~1 µm), equiaxed second phase particles in comparison to the carbon. Instead of boron carbide, zirconium carbide was found in addition to the carbon within all compositions in which it was added. ZrC is visible as the bright phase in contrast to the ZrB_2 (Fig. 1).

Carbon second phase content increased between 0-ZrC (~1.48 vol%) and 1-ZrC (~1.89 vol%) but gradually decreased thereafter with ~1.05 vol% remaining in 10-ZrC (Table I). The increase in C content is likely tied to the loss of boron carbide between 0-ZrC and 1-ZrC as a result of the addition of ZrC. As indicated by the Zr-B-C ternary phase diagram, no binary join exists between B_4C and ZrC.[33] Therefore, the absence

of boron carbide in 1-ZrC through 10-ZrC is a result of the reaction of B_4C and ZrC to form ZrB_2 and C, which are the only phases that form a binary system between ZrC and B_4C on the phase diagram. In addition, the formation of C from this reaction is the most likely explanation for the observed increase in C content.

The final ZrC contents were lower than the starting additions for all compositions (Table I). As an example, 1-ZrC decreased by 0.82 vol% (1.03 to 0.21 vol%) after hot pressing but the difference gradually decreased with increasing ZrC additions. Thus, 10-ZrC only decreased by 0.29 vol% (9.65 to 9.37 vol%). It is possible some ZrC went into solid solution with the ZrB_2, however this effect would be minimal at 1900°C as the ZrB_2-ZrC binary phase diagram indicates the solubility limit is only ~0.08 mol% (0.07 vol%) even at 2000°C (lowest temperature given in the diagram).[34] As discussed in the previous paragraph, the $B_{4.3}C$ was removed via a reaction with ZrC. Therefore, this is the most likely cause for the decrease in ZrC content between the starting composition and after hot pressing.

WC contamination from milling increased from 0.68 wt% for 0-ZrC to 0.85 wt% for 10-ZrC. This is a result of the higher contamination in the ZrC powder (2.2 wt%) vs. that for the ZrB_2 (0.68 wt%). Along with the second phase volume fractions, the milling contamination was used to calculate the theoretical densities (Table I) which are all less than or equal to the measured bulk densities. The estimated $\rho_{theoretical}$ are therefore an underestimate but the micrographs (Fig. 1) confirm the samples are fully dense, as no porosity is visible.

Heat treatment of the hot pressed ZrB_2-ZrC ceramics (as-processed) showed ZrC was effective at limiting grain growth. The average of the maximum dimension (long dimension of fit ellipses) of the ZrB_2 grains for the as-processed and heat treated material are plotted in Fig. 2 as a function of the ZrC addition. In the as-processed condition, the ZrB_2 grains were between 3.3 and 3.9 μm. Any small differences in the

averages were within the standard deviations of 1.8 to 2.2 µm. After the 2100°C heat treatment the 0-ZrC grains grew to 20.4±10.2 µm which is more than a five-fold increase. Subsequent ZrC additions restricted ZrB_2 grain growth after heat treatment. The 10-ZrC material experienced the least grain growth, only doubling in size, with an average grain size of 6.3±2.8 µm.

The ZrC grains most likely pinned the growth of the ZrB_2, however the benefit of even the lowest ZrC addition may suggest another mechanism. It is interesting to note that even the lowest addition of ZrC (1-ZrC), with only 0.21 vol% ZrC in the microstructure after hot pressing (and no visible ZrC after heat treatment), still exhibited reduced grain growth. The grain size of 1-ZrC was ~8 µm lower than 0-ZrC and was only 2 to 3 µm larger than 5-ZrC and 2-ZrC, respectively. The complete absence of any ZrC in the microstructure after heat treatment of 1-ZrC would indicate that the remaining ZrC went into solid solution. If grain growth were only being restricted by grain pinning then this material would be expected to be more like 0-ZrC than either 2-ZrC or 5-ZrC. It is unclear what may have reduced the grain growth in 1-ZrC. At this point the speculation is that bulk diffusion was limited by the additional solid solution of ZrC within the ZrB_2. This may be similar to the reduction in Al_2O_3 grain growth due to the solid solution of MgO. Bennison and Harmer's evaluation of this system proposed that solute drag at the grain boundaries was sufficient to retard grain growth in MgO doped Al_2O_3 as compared to undoped material.[35]

Analysis of the ZrC clusters indicates that the average size increased as a function of the ZrC addition and due to growth during heat treatment. These effects are visible in Fig. 3, but are all within the standard deviations. The growth of the ZrC was negligible compared to that of the ZrB_2 as the grains only grew between 0.2 and 0.6 µm, whereas the standard deviations vary between 0.7 and 1 µm. The minimal ZrC growth is

assumed to be due to the increase in diffusion lengths for ZrC as a result of it being the minority constituent.

3.2 W Solid Solution

ZrC was identified as a second phase in 2-ZrC, 5-ZrC, and 10-ZrC by XRD, and the measured lattice parameters increased as a function of the ZrC content (Fig. 4). In addition, the lattice parameters (4.666, 4668, and 4.675 Å for 2, 5, and 10-ZrC, respectively) all decreased from the starting ZrC powder (4.691 Å). This is attributed to the formation of a (Zr,W)C solid solution. The increase in lattice parameters with the increase in final ZrC content is then a result of a dilution of WC within the ZrC as more ZrC is present for similar amounts of WC contamination. The solid solution of WC in ZrC and, in turn, the W content within the ZrB_2 was then calculated from the measured lattice parameters using analysis of ZrC lattice parameters as a function of WC content by Brun et al.[36] and Denbnovetskaya et al.[37]

The WC content in the ZrC was calculated to be 6.9 to 7.9 mol% for 2-ZrC and decreased to 5.7-5.9 mol% in 10-ZrC. These values are well under the reported 30 mol% solid solution limit for WC within ZrC at 1900°C[36] but the attainable solid solution will be limited due to competition with the $(Zr,W)B_2$ solid solution. It should be noted that even though other factors, like the Zr/C ratio, can also affect the lattice parameter of ZrC [38], a stoichiometric composition is assumed to have formed based on the presence of excess carbon in the system.

From the calculated WC concentration in ZrC, and known ZrC and WC contents, the amount of W sequestered from the ZrB_2 by the ZrC was estimated to be 31-34% (2-ZrC), 68-71% (5-ZrC), and 71-90% (10-ZrC), respectively (Fig. 4). In addition, the value for 1-ZrC was estimated to be ~4.5% based on a linear fit of the WC (mol%) content in the ZrC as a function of the ZrC volume percent. This results in an overall decrease in the W content of the $(Zr,W)B_2$ solid solution as the ZrC content is increased.

3.3 Electrical Resistivity

The total (k), electron (k_e), and phonon (k_p) thermal conductivities of all five compositions are plotted in Fig. 7 from 25 to 2000°C. The electron and phonon contributions were calculated from the total thermal conductivity values and ρ_e (from the linear fit parameters, Table II) using the Wiedemann-Franz law (equation (6)) and the summation of the contributions to k (equation (7))

$$k_e = \frac{LT}{\rho_e} \tag{6}$$

$$k = k_e + k_p \tag{7}$$

L is the Lorenz number which is a proportionality constant that for many metallic systems is close to the theoretical value of L_o=2.44E-8 and T is the temperature of interest.[40] Initial calculations of k_p for 2-ZrC, 5-ZrC, and 10-ZrC with L_o resulted in negative values above 900°C. Other authors report negative k_p values, from the same type of analysis, for ZrB_{2}[11,15,41] as well as for the related diboride, HfB_{2}[41]. However, as this is theoretically impossible, Lorenz values have been calculated (L_c, see Table II) for each material from a linear fit of kT with respect to $T^2\rho_e^{-1}$. L_c was taken as the slope of this fit based on equation (8),

$$kT = L_c T^2 \rho_e^{-1} + C \tag{8}$$

which is the combination of equations (6) and (7) multiplied through by T with k_p set equal to a constant (C) over T. This analysis has been presented for various transition metals, including those in group IV (Ti, Zr, and Hf)[42], for several electrically conductive ceramics[43], and for ZrB_{2}[15], which also showed negative deviations in the Lorenz number to make physical sense of k_p. This equation assumes k_p to be proportional to 1/T and is therefore, most likely valid at temperatures greater than the Debye temperature.

For this reason, the data were fit from 600 to 2000°C based on the reported range of Debye temperatures for ZrB_2 (457 to 692°C)[12,44-46]

0-ZrC has the largest L_c at $2.433x10^{-8}$ $W\Omega K^{-2}$ and the values decrease to $2.249x10^{-8}$ $W\Omega K^{-2}$ for 5-ZrC, before increasing to 2.261E-8 $W\Omega K^{-2}$ for 10-ZrC. These changes are likely tied to the purity of the ZrB_2 but they could also be affected by the ZrC second phase. The increase in the L_c for 10-ZrC may be a sign of the influence of the ZrC which has a wide range of reported Lorenz values ($2.06x10^{-8}$ $W\Omega K^{-2}$ [43], $2.36x10^{-8}$ to $3.08x10^{-8}$ $W\Omega K^{-2}$ (from 727 to 2727°C)[47], and 3.5E-8 $W\Omega K^{-2}$ [38]), some of which are large enough to positively influence value of the composite. L_c for 0-ZrC is very close (0.42%) to that of the theoretical value and this composition has the highest $(Zr,W)B_2$ solid solution. The Lorenz values then decrease as W is removed from solution in ZrB_2 (increasing ZrB_2 purity) up to 10-ZrC. Results by McClane et al. appear to indicate that the solid solution composition, and not just the concentration, has an effect on the Lorenz number of ZrB_2. As mentioned in the introduction McClane made several transition metal additions to ZrB_2 and the same concentration was used for each (3 mol%). In McClane's study, both the ZrB_2 and $(Zr,Hf)B_2$ compositions resulted in negative phonon contributions and had the lowest electrical resistivities. On the other hand, the two compositions which increased resistivities the most [$(Zr,W)B_2$ and $(Zr,Nb)B_2$] had the highest k_p values.[11] Based on the current results and the findings by McClane, it is proposed that the extent of the negative deviation in L from that of L_o for ZrB_2 is tied to the extent to which the electrical resistivity is affected. The relation between L and L_o is typically explained via equation (9), where ℓ is the mean free path of either the thermal (T) or electrical (E) conduction electrons.[48]

$$L = L_o \frac{\ell_T}{\ell_E} \tag{9}$$

Therefore, the “pure” ZrB_2 with $L<L_O$ has $\ell_E>\ell_T$ and the greater the degradation in the electrical conduction of ZrB_2 by a given solid solution leads to an accelerated decline in ℓ_E compared to ℓ_T, eventually leading to $L=L_o$.

Where 1-ZrC and 2-ZrC were the best electrical conductors, they were also the best thermal conductors. Both compositions were nearly constant between 25 and 300°C (~78 W/m•K) beyond this, k decreased to 72 W/m•K by 2000°C. 5-ZrC and 10-ZrC have similar trends compared with 1-ZrC and 2-ZrC but overall their conductivities decreased by 2 to 3 W/m•K (2% to 4% for 5-ZrC) and 4 to 6 W/m•K (5% to 8% for 10-ZrC) from the higher k compositions. These differences were higher at 25°C and diminished as temperature increased. Finally, 0-ZrC was close in conductivity to 5-ZrC between 25 and 300°C (~75 W/m•K) but decreased in k at a slower rate, eventually converging with 1-ZrC and 2-ZrC by ~1500°C, up through 2000°C. At temperatures below 1500°C, k is improved for 1-ZrC and 2-ZrC over that of 0-ZrC due to the reduced W solid solution. Conductivity then uniformly decreases across the entire temperature range for 5-ZrC and 10-ZrC due to the increasing carbide phase. Therefore, like ρ_e, the conductivity of each composition is influenced by the $(Zr,W)B_2$ solid solution and the ZrC second phase, in large part due to the relationship between ρ_e and k.

The thermal conductivities of the material from the present study, and those from previous reports, are plotted with respect to temperature in Fig. 8. As discussed in the introduction, Zimmermann et al. and Thompson et al. evaluated k for ZrB_2, attrition milled (AM) with WC. All of these materials exhibit an increase in k with increasing temperature, which is characteristic of solid solutions of transition metals with ZrB_2. With, 2.8 wt% and 2.2 wt% WC contamination it is understandable why the materials by Zimmermann and Thompson have significantly lower conductivities (up to ~32 W/m•K at 400°C for Thompson (AM)) than the current study. Despite the lower conductivities,

Thompson does show a much larger increase in k (with respect to the current study) over the entire temperature range from AM to AM+3%C. AM+3%C was reported to have formed 2.7 vol% ZrC which removed 20% of the W from the ZrB_2. Based on the current findings it is unlikely the entire increase can be attributed to the transfer of W from ZrB_2 to the ZrC. Instead, as the authors also propose, it may be the carbon second phase (which had reached percolation) that led to the thermal conductivity increase. It should be noted that despite the increased WC contamination, the as-processed grain sizes between the current study (3.3 to 3.9 µm, Fig. 2) and those by Zimmermann (~6 µm) and Thompson (2.4 to 3.3 µm) are similar. Considering the significant decrease in thermal conductivities from the extra WC contamination, it is important to optimize milling procedures to prevent unnecessary changes in k when WC milling is employed for particle size reduction.

From Fig. 7 it is apparent that changes in k_e and k_p across compositions, and with respect to temperature, have differing effects on the overall conductivity. In all cases, k_e increases from 25 to 2000°C, whereas k_p decreases similarly to k. Therefore, k_p is primarily controlling the temperature dependency of k. The change in k_e with temperature increases with ZrC content from 1-ZrC (0.08 W/m•K) to 10-ZrC (1.8 W/m•K). This increase is likely due to the ZrC because k_e vs. T for pure ZrC is reported have a positive trend.[38,47] As the change in k_e across each composition is larger than that for k_p (4 to 6 W/m•K vs. 1 to 2 W/m•K between 2-ZrC and 10-ZrC), k_e primarily controls the compositional dependency. In addition, k_e is between 87-89% (25°C) and 95-96% (2000°C) of the total thermal conductivity of these materials. This is similar to the range of values (84-97%)[11,13,15,16,41] reported for ZrB_2. Strong ionic and covalent bonding (as is characteristic for ZrB_2)[5] typically helps contribute to improved phonon conduction (like for SiC, diamond, and AlN)[49]. Despite this, the result is reasonable for an electrically conductive material. Similarly to other good electrical

conductors, the higher electron mobility, limits phonon conduction via increased phonon-electron scattering at “low” temperatures. Then, with increased temperatures, phonon-phonon scattering increases and limits k_p as the phonon-electron scattering diminishes.[40] With this in mind, the most likely way to alter the conductivity of a ZrB_2 based ceramic is to focus on those aspects which change k_e.

4. Summary and Conclusions

Attrition milled ZrB_2 and ZrC were combined from 0 to 10 vol% and densified to full density at 1900°C. Between 1.05 and 1.89 vol% carbon was present in each composition. ZrC additions reduced the formation of 0.24 vol% boron carbide which formed in 0-ZrC. This resulted in materials with between 0.21 and 9.37 vol% ZrC. WC contamination was present due to the milling procedure between 0.68 wt% (0-ZrC) and 0.85 wt% (10-ZrC). The increase was due to the greater amount of contamination in the ZrC powder. After hot pressing, ZrB_2 grain sizes were between 3.3 and 3.9 µm but after heat treating at 2100°C for 4 hours the grains increased in size for all compositions. The largest grain growth was experience by 0-ZrC (5x larger grains; 20.4±10.2 µm) and the least by 10-ZrC (2x larger; 6.3±2.8 µm). Reduced grain growth (compared with 0-ZrC) was not entirely attributed to grain pinning of the ZrB_2. This is based on the absence of ZrC in the microstructure of 1-ZrC after heat treatment. It is proposed that a solid solution of ZrC in ZrB_2 may have limited the grain growth.

A decrease in the ZrC lattice parameters from the starting powder was attributed to the formation of the (Zr,W)C solid solution. This solid solution was calculated to be 6.9 to 7.9 mol% in 2-ZrC, but was diluted by the increased ZrC content to 5.7-5.9 mol% for 10-ZrC. The percentage of tungsten sequestered from the ZrB_2 by the ZrC increased with the ZrC addition from 31 to 34% (2-ZrC) to, 71 to 90% for 10-ZrC. Electrical resistivities were lowest at all temperatures (25 to 800°C) for 1-ZrC and 2-ZrC (~9.9

μΩ•cm). The initial decrease in resistivity from 0-ZrC (10.8 μΩ•cm) was attributed to the reduced $(Zr,W)B_2$ solid solution. However, subsequent ZrC additions increased the electrical resistivity, due to the increased resistivity of the ZrC. This ultimately lead to 10-ZrC having a resistivity of 10.7 μΩ•cm.

The electron and phonon contributions to the total thermal conductivity were calculated using the Wiedemann-Franz law, electrical resistivities, and calculated Lorenz numbers (L_c). The compositions 1-ZrC and 2-Zrc had the highest conductivities at all temperatures (78 W/m•K at 25°C, decreasing to 72 W/m•K at 2000°C. Specimen 0-ZrC, was lower than 1-ZrC and 2-ZrC below ~1500°C due to the $(Zr,W)B_2$ solid solution. The additional ZrC in 5-ZrC, and 10-ZrC reduced k at all temperatures uniformly from that of 1-ZrC and 2-ZrC. 10-ZrC was the lowest k material, with conductivities of 72 W/m•K at room temperature and 69 W/m•K at 2000°C.

The decrease in conductivity, due to the compositional changes, was primarily due to changes in the electron contribution (up to 5 W/m•K) versus the phonon contribution (at most 2 W/m•K at 25°C). On the other hand, changes in conductivity with respect to temperature were due to the decrease in phonon contribution with temperature.

The calculated Lorenz numbers were 2.433×10^{-8}, 2.352×10^{-8}, 2.251×10^{-8}, 2.549×10^{-8}, and 2.261×10^{-8} $W\Omega K^{-2}$ for 0-ZrC, 1-ZrC, 2-ZrC, 5-ZrC, and 10-ZrC. It was predicted that L_c was highest (and nearly equal to the theoretical value) due to the increased W contamination in the ZrB_2. As the W was removed by the ZrC, L_c decreased from the value for 0-ZrC. Finally, the increase of L_c for 10-ZrC, may have been due to the contribution to L_c from the ZrC.

Several important conclusions can be drawn from this analysis:

1. In the end, the role of ZrC in improving the conductivity of ZrB_2 with W contamination was confirmed but its effect was less than previously thought.
2. ZrC is effective in preventing grain growth in ZrB_2 and this benefit may outweigh the drawback of reduced thermal conductivities.
3. By improving milling procedures, ZrB_2 with reduced grain sizes can be formed with higher thermal conductivities, as a result of reduced milling contamination when using WC media.

Acknowledgements

This research was funded by the National Science Foundation (DMR-0906584).

References

[1] Rudy E and Windisch S. *Figure 08824 - Zr-B System*. ACerS-NIST Phase Equilibria Diagrams. CD-ROM Database, Ver. 3.0.1. 2004.

[2] Fahrenholtz WG, Hilmas GE, Talmy IG and Zaykoski JA. Refractory Diborides of Zirconium and Hafnium. J Am Ceram Soc 2007;**90**(5):1347-64.

[3] Gasch MJ, Ellerby DT and Johnson SM. Ultra High Temperature Ceramic Composites. In: Bansal NP, editor Handbook of Ceramic Composites, New York: Springer; 2005, p. 197-224.

[4] Opeka MM, Talmy IG and Zaykoski JA. Oxidation-based materials selection for 2000°C + hypersonic aerosurfaces: Theoretical considerations and historical experience. J Mater Sci 2004;**39**(19):5887-904.

[5] Vajeeston P, Ravindran P, Ravi C and Asokamani R. Electronic structure, bonding, and ground-state properties of AlB_2-type transition-metal diborides. Phys Rev B 2001;**63**(4):045115-(1-12).

[6] Chamberlain AL, Fahrenholtz WG, Hilmas GE and Ellerby DT. High-Strength Zirconium Diboride-Based Ceramics. J Am Ceram Soc 2004;**87**(6):1170-2.

[7] Guo W-M, Zhang G-J and Wang P-L. Microstructural Evolution and Grain Growth Kinetics in ZrB_2–SiC Composites During Heat Treatment. J Am Ceram Soc 2009;**92**(11):2780-3.

[8] Gropyanov VM and Bel'tyukova LM. Sintering and recrystallization of ZrC-ZrB_2 compacts. Sov Powder Metall 1968;**7**(7):527-33.

[9] Neuman EW. Elevated Temperature Mechanical Properties of Zirconium Diboride Based Ceramics [dissertation]. Missouri University of Science and Technology; 2014.

[10] Guo S, Nishimura T and Kagawa Y. Preparation of zirconium diboride ceramics by reactive spark plasma sintering of zirconium hydride-boron powders. Scripta Mater 2011;**65**(11):1018-21.

[11] McClane DL, Fahrenholtz WG and Hilmas GE. Thermal Properties of (Zr,TM)B_2 Solid Solutions with TM = Hf, Nb, W, Ti, and Y. J Am Ceram Soc 2014;**97**(5):1552-8.

[12] Zimmermann JW, Hilmas GE, Fahrenholtz WG, Dinwiddie RB, Porter WD and Wang H. Thermophysical Properties of ZrB_2 and ZrB_2–SiC Ceramics. J Am Ceram Soc 2008;**91**(5):1405-11.

[13] Thompson MJ, Fahrenholtz WG and Hilmas GE. Elevated Temperature Thermal Properties of ZrB_2 with Carbon Additions. J Am Ceram Soc 2012;**95**(3):1077-85.

[14] Thompson MJ. Densification and Thermal Properties of Zirconium Diboride Based Ceramics [dissertation]. Missouri University of Science and Technology; 2012.

[15] Harrington GJK, Hilmas GE and Fahrenholtz WG. Effect of Carbon on the Thermal and Electrical Transport Properties of ZrB_2. J Eur Ceram Soc late 2014;

[16] Patel M, Prasad VVB and Jayaram V. Heat conduction mechanisms in hot pressed ZrB_2 and ZrB_2–SiC composites. J Eur Ceram Soc 2013;**33**(10):1615-24.

[17] Andrievskii RA, Korolev LA, Klimenko VV, Lanin AG, Spivak II and Taubin IL. Effect of zirconium carbide and carbon additions on some physicomechanical properties of zirconium diboride. Powder Metall Met Ceram 1980;**19**(2):93-4.

[18] Fridlender BA, Neshpor VS, Ordan'yan SS and Unrod VI. Thermal Conductivity and Diffusivity of Binary Alloys of the ZrC-ZrB_2 System at High Temperatures. High Temperature 1980;**17**(6):1001-5.

[19] Guo S, Kagawa Y, Nishimura T and Tanaka H. Thermal and Electric Properties in Hot-Pressed ZrB_2–$MoSi_2$–SiC Composites. J Am Ceram Soc 2007;**90**(7):2255-8.

[20] Thompson M, Fahrenholtz WG and Hilmas G. Effect of Starting Particle Size and Oxygen Content on Densification of ZrB_2. J Am Ceram Soc 2011;**94**(2):429-35.

[21] Fahrenholtz WG, Hilmas GE, Zhang SC and Zhu S. Pressureless Sintering of Zirconium Diboride: Particle Size and Additive Effects. J Am Ceram Soc 2008;**91**(5):1398-404.

[22] O'Quigley DGF, Luyckx S and James MN. An empirical ranking of a wide range of WC-Co grades in terms of their abrasion resistance measured by the ASTM standard B 611-85 test. Int J Refract Met Hard Mater 1997;**15**(1–3):73-9.

[23] Brookes KJA. World Directory and Handbook of Hardmetals and Hard Materials. International Carbide Data; 1996.

[24] Zhang SC, Hilmas GE and Fahrenholtz WG. Pressureless Densification of Zirconium Diboride with Boron Carbide Additions. J Am Ceram Soc 2006;**89**(5):1544-50.

[25] Choi S-K, Ui S-W, Choi I-S and Choi S-C. Densification behavior of ZrB_2 with Co-WC as additives. J Ceram Soc Jpn 2014;**122**(1423):198-203.

[26] Zhu S. Densification, Microstructure, and Mechanical Properties of Zirconium Diboride Based Ultra-High Temperature Ceramics [dissertation]. Missouri University of Science and Technology; 2008.

[27] Neuman EW, Hilmas GE and Fahrenholtz WG. Strength of Zirconium Diboride to 2300°C. J Am Ceram Soc 2013;**96**(1):47-50.

[28] Lide D. CRC Handbook of Chemistry and Physics. 88th ed. Boca Raton: CRC; 2007.

[29] Touloukian YS, Kirby RK, Taylor RE and Desai PD. Thermal Expansion: Nonmetallic Solids. IFI/Plenum; 1977.

[30] Clark III LM and Taylor RE. Radiation loss in the flash method for thermal diffusivity. J Appl Phys 1975;**46**(2):714-9.

[31] Chase MW. NIST-JANAF Thermochemical Tables. American Chemical Society and the American Institute of Physics. 4th ed. Woodbury, NY: 1998.

[32] ASTM Standard F76, 2008, "Standard Test Methods for Measuring Resistivity and Hall Coefficient and Determining Hall Mobility in Single-Crystal Semiconductors". West Conshohocken, PA: ASTM International; 2008, DOI: 10.1520/F0076-08.

[33] Rudy E and Windisch S. *Figure 08874 - Zr-B-C Ternary System*. ACerS-NIST Phase Equilibria Diagrams. CD-ROM Database, Ver. 3.0.1. 2004.

[34] Ordan'yan SS and Unrod V. *Figure 08875 - ZrB_2-ZrC - Quasibinary phase diagram*. ACerS-NIST Phase Equilibria Diagrams. CD-ROM Database, Ver. 3.0.1. 2004.

[35] Bennison SJ and Harmer MP. Effect of MgO Solute on the Kinetics of Grain Growth in Al_2O_3. J Am Ceram Soc 1983;**66**(5):90-2.

[36] Brun M and Stubican VS. Precipitation Studies in the System WC-ZrC. J Am Ceram Soc 1974;**57**(3):117-9.

[37] Denbnovetskaya EN. Preparation of solid solutions of some complex carbides of the transition metals. Sov Powder Metall 1967;**6**(3):194-7.

[38] Jackson HF and Lee WE. 2.13 - Properties and Characteristics of ZrC. In: Editor-in-Chief: Rudy JMK, editor Comprehensive Nuclear Materials, Oxford: Elsevier; 2012, p. 339-72.

[39] Grebenkina VG and Denbnovetskaya EN. Thermal Coefficient of the Electrical Resistivity of Carbides and Their Solid Solutions. In: Samsonov G, editor Refractory Carbides, Springer US; 1995, p. 269-74.

[40] Uher C. Thermal Conductivity of Metals. In: Tritt TM, editor Thermal Conductivity: Theory, Properties, and Applications, Springer; 2004, p. 21-91.

[41] Zhang L, Pejaković DA, Marschall J and Gasch M. Thermal and Electrical Transport Properties of Spark Plasma-Sintered HfB_2 and ZrB_2 Ceramics. J Am Ceram Soc 2011;**94**(8):2562-70.

[42] Sharma RG, Chari MSR and Reddy DK. The electronic Lorenz number in some transition metals at high temperatures. J Phys F 1986;**16**(5):603-7.

[43] Morgan PED. Wiedemann-Franz-Lorenz Relation in Metallic Conducting Ceramics. J Am Ceram Soc 1975;**58**(7-8):349.

[44] Samsonov GV, Serebryakova TI and Neronov VA. Borides. Atomizdat, Moscow 1975;

[45] Wiley DE, Manning WR and Hunter Jr O. Elastic properties of polycrystalline TiB_2, ZrB_2 and HfB_2 from room temperature to 1300°K. J Less Common MET 1969;**18**(2):149-57.

[46] Bernstein H. Met Soc AIME Inst Metals Div Spec Rept Ser 1964;13):609.

[47] Jean-Paul C. Origins of the high temperature increase of the thermal conductivity of transition metal carbides from atomistic simulations. J Phys: Condens Matter 2013;**25**(50):505501.

[48] Kumar GS, Prasad G and Pohl RO. Experimental determinations of the Lorenz number. J Mater Sci 1993;**28**(16):4261-72.

[49] Slack GA. Nonmetallic crystals with high thermal conductivity. J Phys Chem Solids 1973;**34**(2):321-35.

Fig. 1. Representative polished micrographs of 0-ZrC, 2-ZrC, and 10-ZrC which show no remaining porosity.

Fig. 2. The average, maximum ZrB_2 grain size dimensions (from the fitting ellipse) are plotted as a function of the ZrC addition for the as-processed and heat treated specimens.

Fig. 3. The average, maximum ZrC grain dimensions as a function of the ZrC addition for the as-processed and heat treated specimens.

Fig. 4. The measured lattice parameters and calculated percentage of W sequestered from ZrB_2 by the ZrC are plotted as a function of the final ZrC content.

Fig. 5. Measured electrical resistivities as a function of the final composite ZrC volume percent for each the test temperatures of 25, 100, 400, and 800°C.

Fig. 6. Electrical resistivity as a function of the mol% W in ZrB_2 as calculated for the matrix of 1-ZrC through 10-ZrC and as reported for 0-ZrC. In addition the literature data from McClane et al. (W additions to ZrB_2)[11] and Zimmermann et al. (W from WC milling)[12] are plotted for comparison. *1.8 mol% W based on reported density of 6.27 g/cm^3

Fig. 7. The total (filled symbols), electron (open), and phonon (open dot) thermal conductivities are plotted as a function of temperature for each as processed composition.

Fig. 8. Thermal conductivity as a function of temperature for the material from the current study displayed along with material by Zimmermann et al.[12] and Thompson et al.[13], which had been attrition milled (AM) with WC.

Table 1. Composition Name, Added and Final ZrC Content, Final C/$B_{4.3}C$ Content, Total WC Contamination, and Relative/Bulk Density Information for Each As-processed Specimen

Composition Name	ZrC Addition (vol%)	Final ZrC (vol%)	Final C ($B_{4.3}C$) (vol%)	WC (wt%)	$\rho_{theoretical}$ (g/cm^3)	ρ_{bulk} (g/cm^3)
0-ZrC	0	0	1.48 (0.24)	0.68	6.11	6.11
1-ZrC	1.03	0.21	1.89	0.70	6.10	6.12
2-ZrC	2.41	1.72	1.55	0.72	6.12	6.15
5-ZrC	4.82	4.47	1.33	0.76	6.15	6.16
10-ZrC	9.65	9.37	1.05	0.85	6.20	6.20

Table 2. Linear Fit Parameters a (slope) and b (intercept) Calculated for ρe(T) and the Calculated Lorenz (Lc) Number for Each Composition

Sample Name	a ρ_e/T	b ρ_e	L_c $W\Omega K^{-2}$
0-ZrC	0.0346	10.0613	2.433E-08
1-ZrC	0.0340	9.2918	2.352E-08
2-ZrC	0.0325	8.9705	2.251E-08
5-ZrC	0.0331	9.2402	2.249E-08
10-ZrC	0.0342	9.6701	2.261E-08

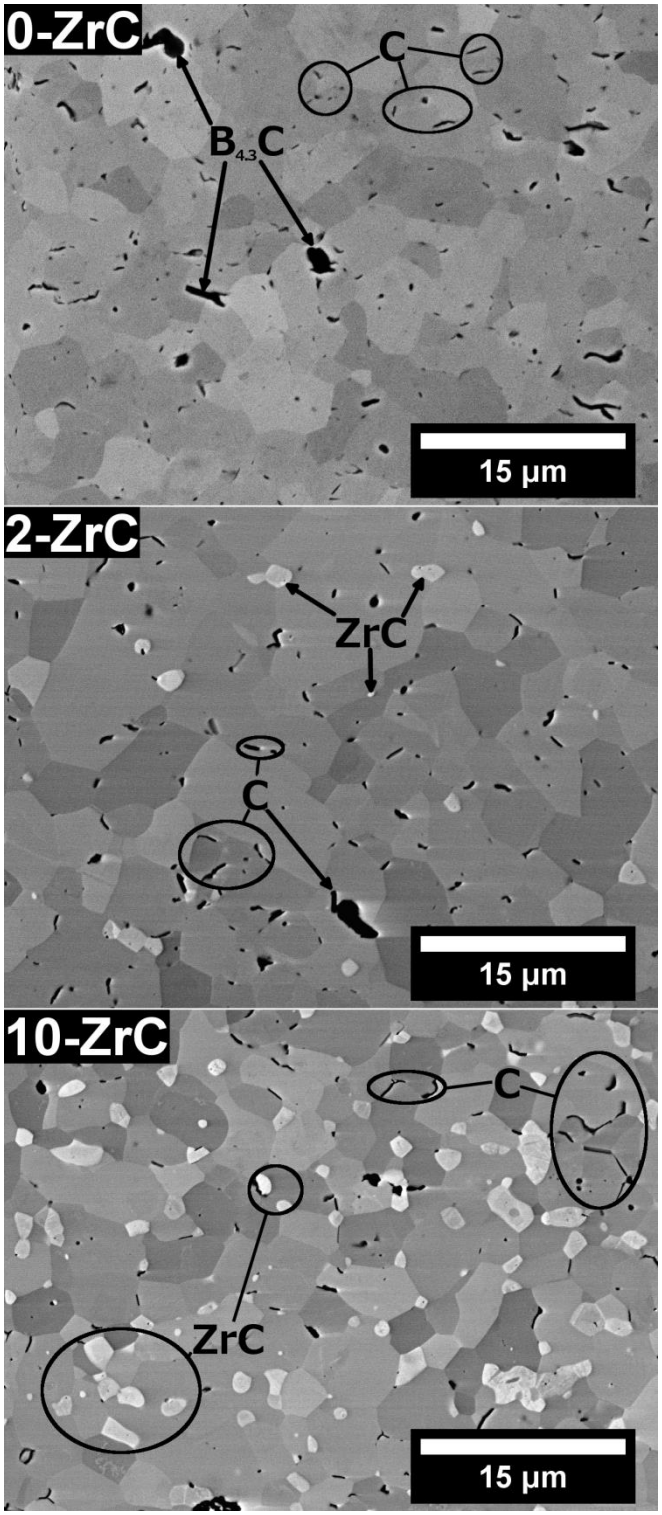

Fig. 1. Representative polished micrographs of 0-ZrC, 2-ZrC, and 10-ZrC which show no remaining porosity.

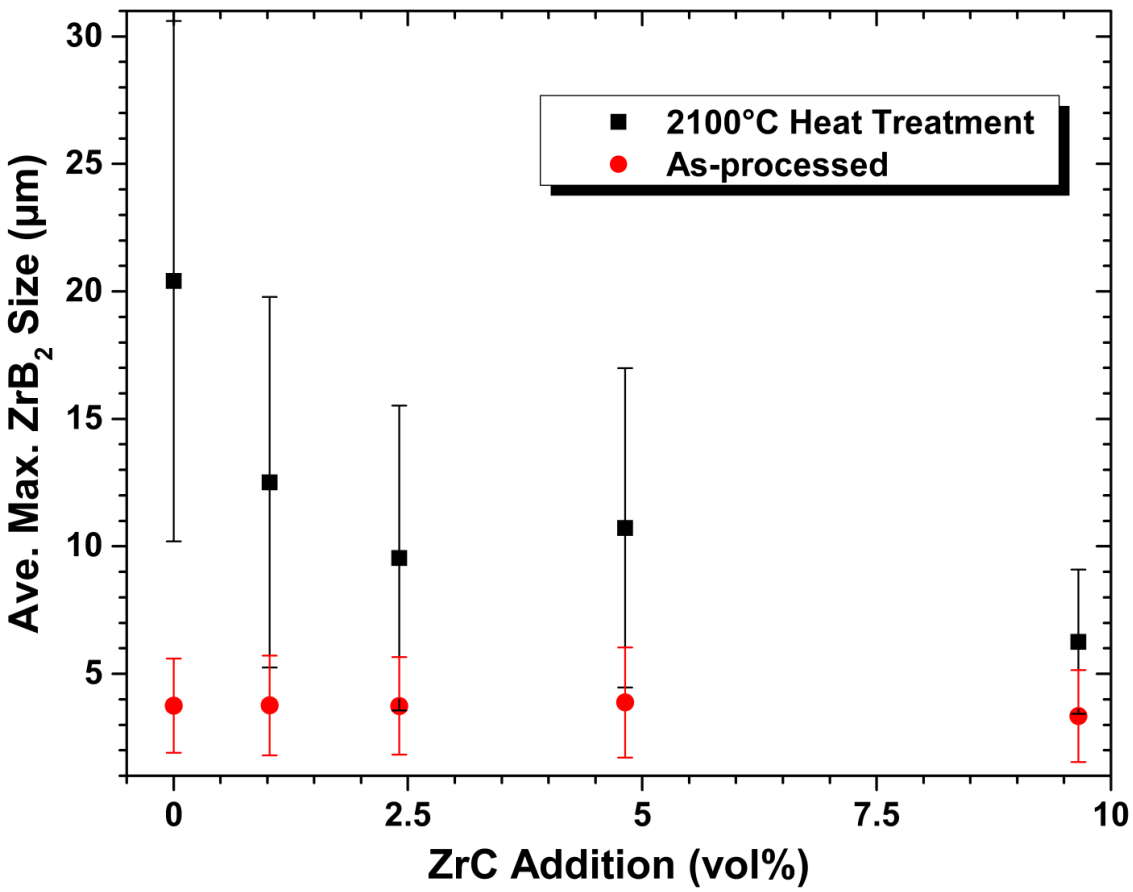

Fig. 2. The average, maximum ZrB_2 grain size dimensions (from the fitting ellipse) are plotted as a function of the ZrC addition for the as-processed and heat treated specimens.

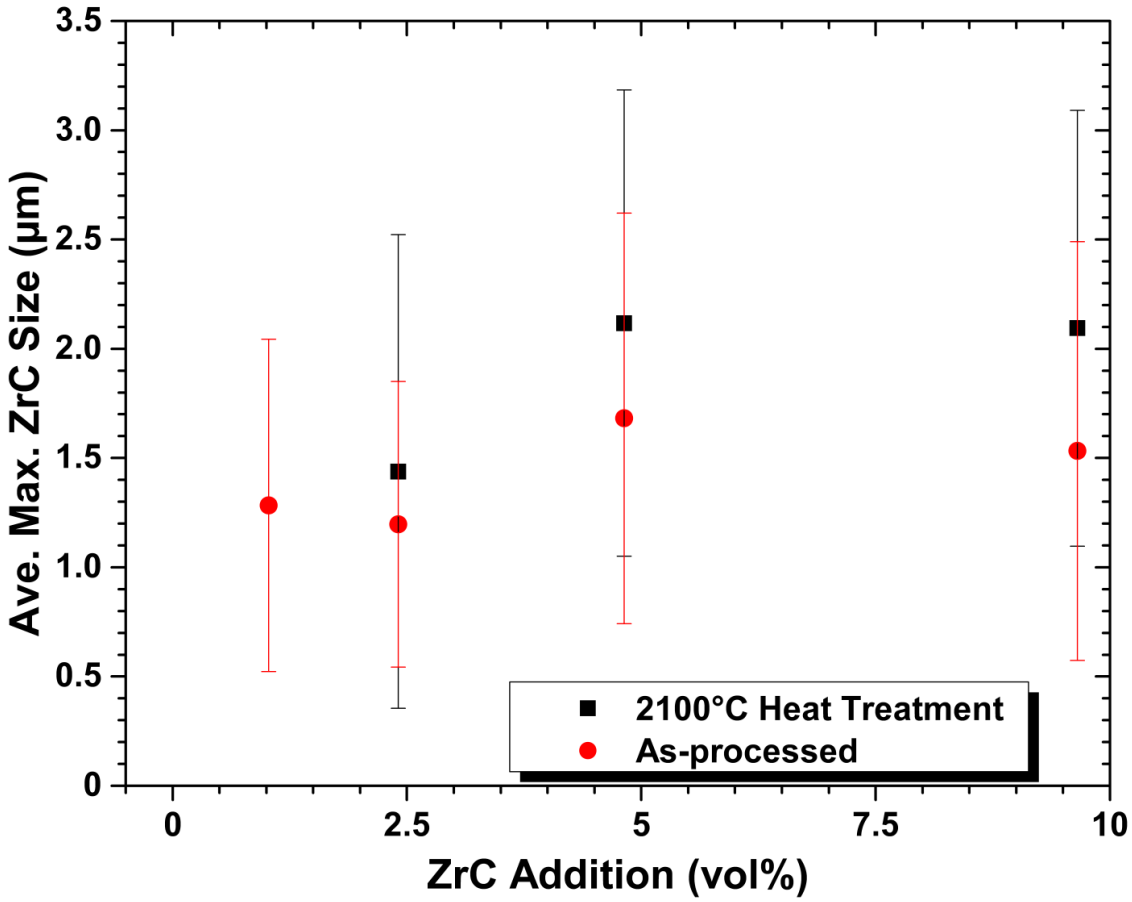

Fig. 3. The average, maximum ZrC grain dimensions as a function of the ZrC addition for the as-processed and heat treated specimens.

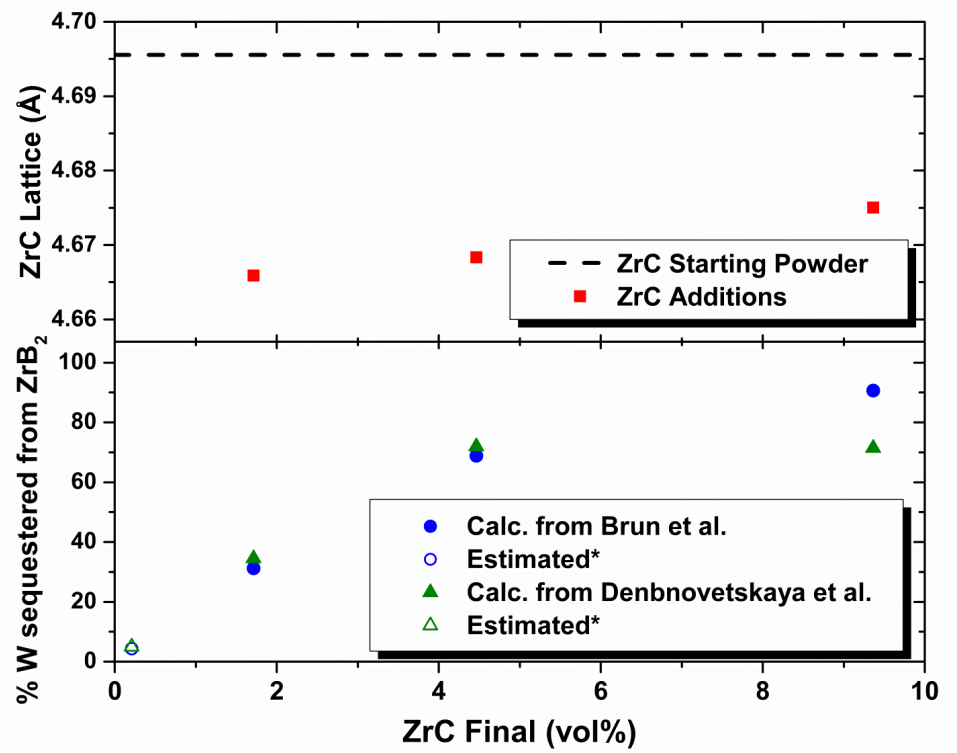

Fig. 4. The measured lattice parameters and calculated percentage of W sequestered from ZrB_2 by the ZrC are plotted as a function of the final ZrC content.

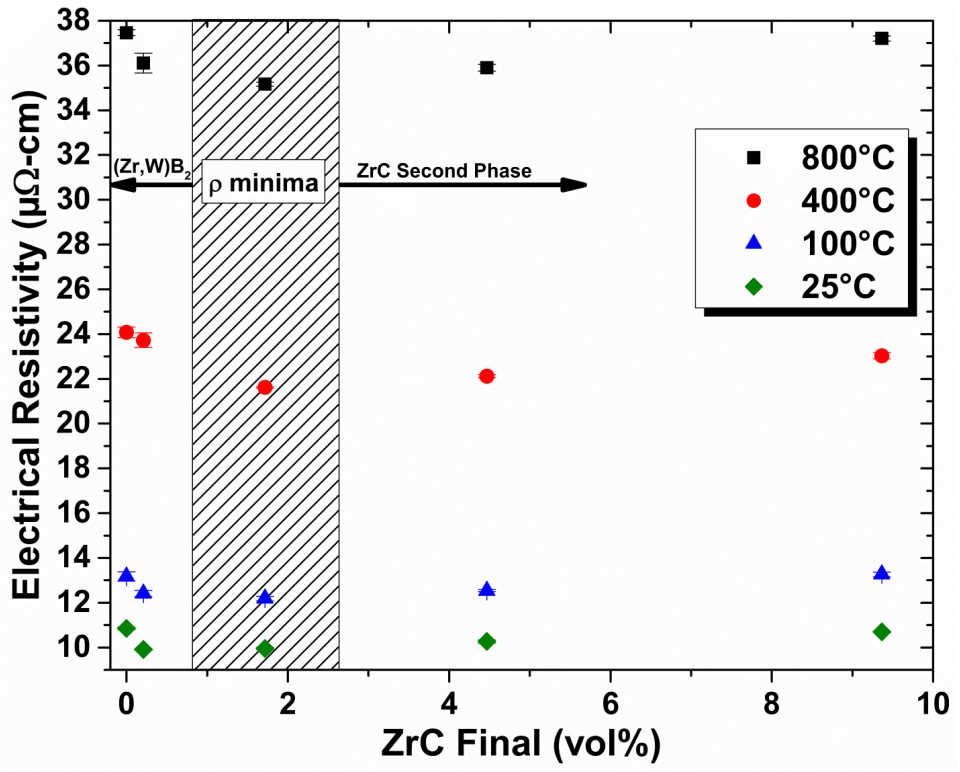

Fig. 5. Measured electrical resistivities as a function of the final composite ZrC volume percent for each the test temperatures of 25, 100, 400, and 800°C.

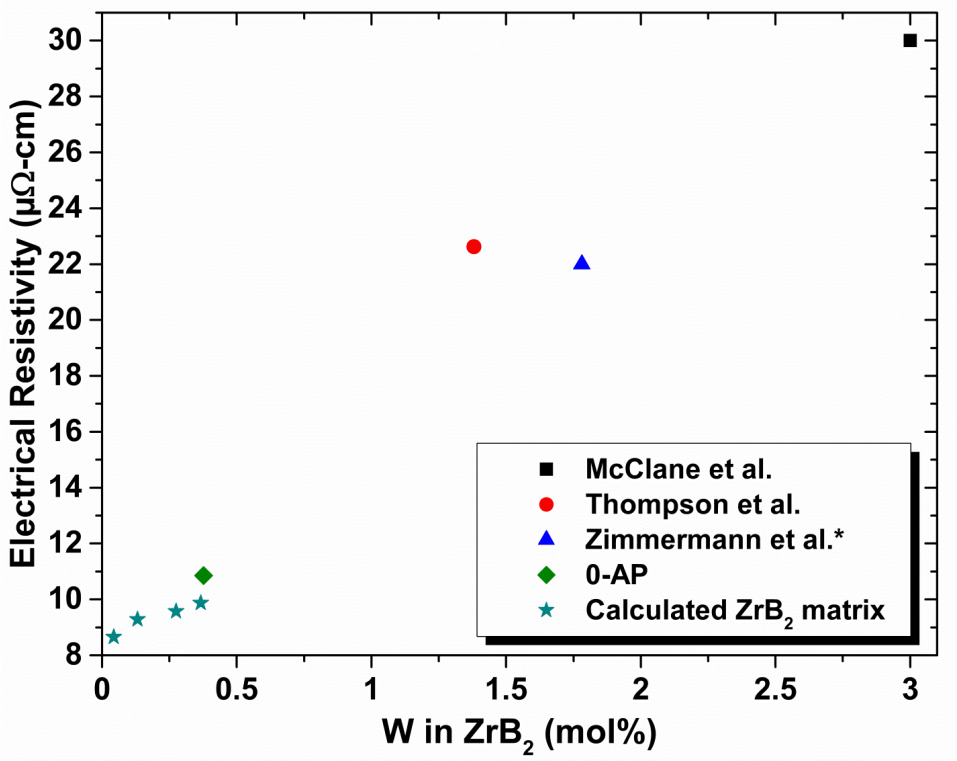

Fig. 6. Electrical resistivity as a function of the mol% W in ZrB_2 as calculated for the matrix of 1-ZrC through 10-ZrC and as reported for 0-ZrC. In addition the literature data from McClane et al. (W additions to ZrB_2)[11] and Zimmermann et al. (W from WC milling)[12] are plotted for comparison. *1.8 mol% W based on reported density of 6.27 g/cm³

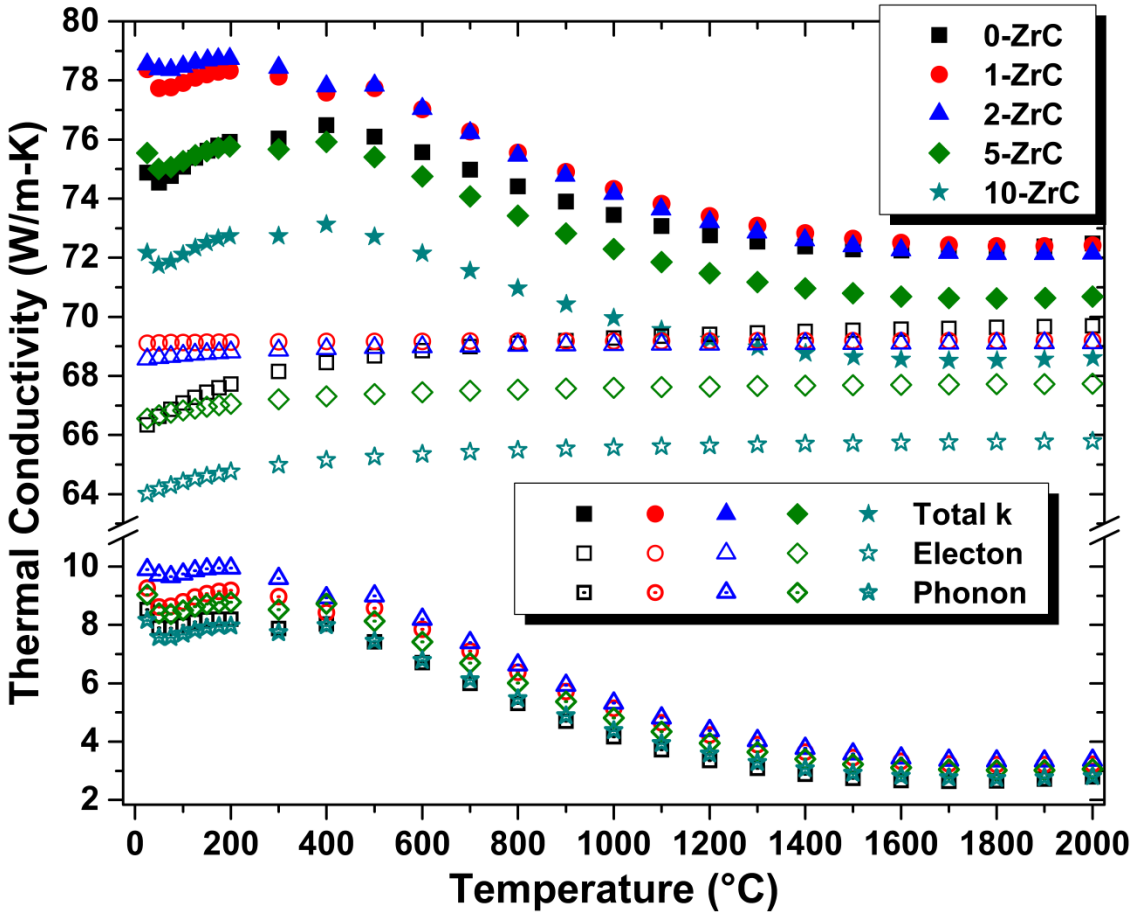

Fig. 7. The total (filled symbols), electron (open), and phonon (open dot) thermal conductivities are plotted as a function of temperature for each as processed composition.

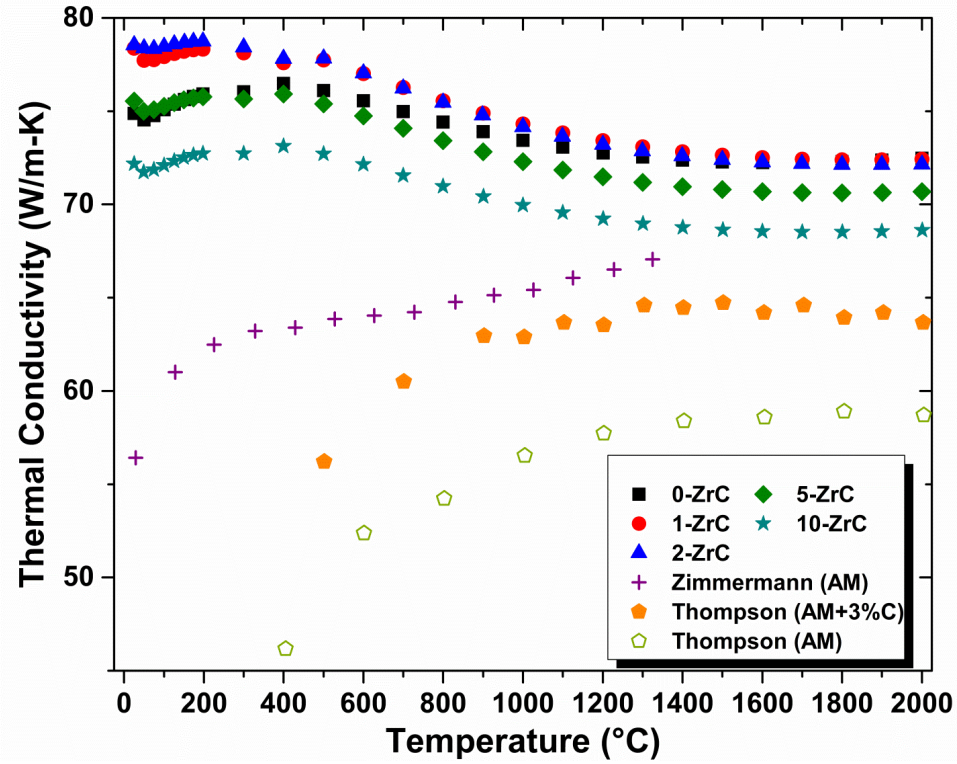

Fig. 8. Thermal conductivity as a function of temperature for the material from the current study displayed along with material by Zimmermann et al.[12] and Thompson et al.[13], which had been attrition milled (AM) with WC.

SECTION

3. SUMMARY AND CONCLUSIONS

The focus of this dissertation was to investigate the thermal and electrical properties of ZrB_2. Specific attention was paid to the underlying effects of processing, microstructure, and composition. A literature review of ZrB_2 reveals a wide range of reported thermal conductivities from 25 to 2000°C. Few researchers have discussed more than one or two materials within the same study. Therefore, little direct focus has been put towards the systematic analysis of various effects on the thermal conductivity of ZrB_2 based ceramics. In the present work, ZrB_2 ceramics were produced to systematically vary composition. These changes in composition were intended to alter the distribution of species either in solid solution or as second phases. Thermal conductivity and electrical resistivity were then evaluated for these materials and discussed in terms of the changes in composition. In addition, attention was paid to the differences and similarities between the current research and the established technical literature. This allowed for a more well-rounded understanding of the thermal conductivity of ZrB_2 to be developed than would have been possible from the current body of work alone.

3.1. SUMMARY

1. How do carbon and oxygen contents relate to the densification and resulting phase equilibria in the ZrB_2-C binary?

Carbon additions of 0 to 1 wt% were made to as received, commercial ZrB_2 powder that initially contained 0.088 wt% C and 1.25 wt% O (as measured before powder processing). Powder processing was performed to coat the ZrB_2 with phenolic

resin. The powder was subsequently pyrolyzed at 600°C to form a finely dispersed carbon second phase. After powder processing, carbon increased in proportion to the intended addition and oxygen increased between 0.37 and 0.99 wt%. Each composition was hot pressed at 2000 or 2100°C at 32 MPa until ram travel ceased for 10 minutes. Isothermal vacuum assisted reaction holds were performed at 1450 and 1600°C before hot pressing to allow the added carbon to react with the zirconium and boron oxides. Densification increased as a function of the addition of carbon and the increase in densification temperature. The highest density material was produced with 1 wt% C, achieving 98.5% of theoretical at 2100°C. Carbon contents after densification varied slightly, from 0.019 to 0.041 wt% between the 0 and 0.75 wt% C addition materials for both processing temperatures. Carbon contents increased more significantly for the 1 wt% C material. The final concentrations were 0.098 wt% (2000°C) and 0.071 wt% (2100°C). Boron carbide was formed in the 0.75 and 1 wt% C materials. All materials, with the exception of the highly porous , 0 wt% C composition hot pressed at 2000°C, had final oxygen contents decrease by >95%, to below ~0.08 wt%. Finally, 0.25, 1 and 5 wt% additions of ZrH_2 were made to ZrB_2 with 1 wt% added carbon. The formation of boron carbide was eliminated for the 1 wt% ZrH_2 addition, producing ZrB_2 with only carbon observable as a second phase.

2. What is the effect of carbon (with specific emphasis on the ZrB_2+C solid solution) on the thermal conductivity of ZrB_2 and its electron/phonon contributions to k?

With the lessons in processing learned from the first study. ZrB_2 was hot pressed with carbon additions spanning 0 to 2 wt% with 1 wt% ZrH_2 added to each composition. The materials were divided into three regimes, based on the resulting second phases

and solid solution content in order to interpret the resulting thermal conductivities. Regime I included the 0, 0.1, and 0.2 wt% C compositions which all had final carbon contents of ~0.026 wt%. These materials were characterized by a second phase of zirconia which decreased from 0.85 to 0.22 vol% as carbon content increased. In Regime I, the thermal conductivity increased with increasing carbon addition, achieving conductivities from 97 to 99 W/m-K. Regime II included the 0.2, 0.3, and 0.4 wt% C additions. No second phases were identified in the latter two materials. Carbon increased from 0.026 to 0.033 wt% across Regime II. Starting at 99 W/m-K (0.2 wt% C material), conductivities dropped to 94 and 92 W/m-K as carbon increased in Regime II. In Regime III, carbon was formed as a second phase. Final carbon contents increased from 0.26 vol% (0.05 wt%) to 4.68 vol% (1.36 wt%) between the 0.5 and 2 wt% C materials. In Regime III, k continued to decrease, resulting in the lowest room temperature conductivity for the study of 88 W/m-K at 25°C. The differences in k were most significant at room temperature, and the conductivities gradually converged to a more narrow range at high temperature (~2 W/m-K above 1300°C). The electron contribution to thermal conductivity decreased as carbon content increased, but the phonon conductivity became larger. For all compositions evaluated, k_e was between 84 and 95%, and increased as a function of temperature.

3. What is the achievable upper limit to the thermal conductivity of ZrB_2, produced from current commercial powders, when phase purity in the system is controlled? In addition, how do these results compare to the examples from the literature and what is causing the differences?

The highest conductivity material evaluated in this body of work (after porosity corrections were applied) was produced from H.C.Starck grade B powder and hot

pressed to 96% of theoretical at 2150°C with an addition of 0.2 wt% C and 1 wt% ZrH_2. Thermal conductivities of 99 W/m-K at 25°C and 75 W/m-K at 2000°C were calculated for this material. Before correcting for porosity, the same conductivities were 94 and 71 W/m-K. The only second phase identified in this material was 0.22 vol% of zirconia, and the solid solution carbon content was 0.0267 wt%. In addition, the content of several important impurity elements were evaluated (O (0.13 wt%), N (0.078 wt%), Co (<0.001 wt%), Fe (<0.001 wt%), Hf (1.65 wt%) and W (0.005 wt%)). The overall purity was 98.1%.

4. Does the electrical resistivity of ZrB_2 change linearly from room temperature to 2000°C?

Electrical resistivity was measured by the van der Pauw technique using a testing setup designed and fabricated especially for use inside a high temperature metal element furnace (more details are contained in section III and Appendix A). Attempts were made to measure electrical resistivity up to 2000°C but testing issues limited measurements to between 25 and 1860°C. In this range, 96% dense ZrB_2 with additions of 0.2 wt% C and 1 wt% ZrH_2 was evaluated. The room temperature resistivity was 7.3 μΩ-cm. Resistivity increased linearly with respect to temperature up to 36 μΩ-cm at 950°C. The slope in resistivity as a function of temperature increased above 950°C and can be fit to a second linear trend between 950 and 1860°C where a resistivity of 76 μΩ-cm was recorded.

5. Can the $(Zr,W)B_2$ solid solution resulting from WC milling contamination be mitigated to produce ZrB_2 with increased thermal conductivities and improved microstructures?

Both ZrB_2 and ZrC were attrition milled with WC and combined with 0.5 wt% C to produce compositions with 0, 1, 2.5, 5, and 10 vol% ZrC. The materials were all hot pressed to full density at 1900°C at 32 MPa. The average ZrB_2 grain size of the starting compositions was between 3.3 and 3.9 µm. After a four hour heat treatment at 2100°C the grain sizes increased to a maximum average size of 20 µm (0% ZrC) and a minimum average size of 6.3 µm (10% ZrC). The as processed ZrC lattice parameters were 4.666 Å (2.5% ZrC), 4.668 Å (5% ZrC), and 4.675 Å (10% ZrC). The starting ZrC had a lattice spacing of 4.691 Å. Tungsten carbide content within the ZrC was calculated to be 6.9 to 7.9 mol% for the 2.5% ZrC composition and decreased to 5.7 to 5.9 mol% for the 10% ZrC material. The percentage of W in the ZrB_2 removed from by the ZrC was 31-34% (2.5% ZrC), 68-71% (5% ZrC), and 71-90% (10% ZrC). Room temperature electrical resistivities were highest for the compositional extremes (10.9 µΩ-cm, 0% ZrC and 10.7 µΩ-cm, 10% ZrC). The 1% ZrC was the lowest resistivity material at 25°C (9.92 µΩ-cm) but at all other temperatures the 2.5% ZrC was lowest. Both 1 and 2.5% ZrC additions had the highest electrical conductivities (78 W/m-K at 25°C and 72 W/m-K at 2000°C). Thermal conductivities were 2 to 3 W/m-K lower for the 5%, and 4 to 6 W/m-K for the 10% ZrC materials. At room temperature, the conductivity of the 0% material was as low as the 5%, but as temperature increased, conductivity converged with the 1 and 2.5% materials, overlapping at 1500°C.

6. Is the theoretical Lorenz number valid for ZrB_2 and how can it be evaluated experimentally?

The electron and phonon contributions to the total thermal conductivity were evaluated for both the C and ZrC addition studies. All compositions in the former study resulted in negative k_p values using the theoretical Lorenz number (L_o) to calculate k_e. Negative values were calculated at every temperature for the lowest carbon additions (0, 0.1, and 0.2 wt%) and above 600 to 1100°C for the higher carbon additions. In the later study, no negative phonon conductivities were observed for the 0 and 1 vol% ZrC additions. The 2.5, 5, and 10% ZrC materials had negative conductivities from either from either 900 or 1000°C, and up. For the compositions in each study, experimental Lorenz values were calculated to re-evaluate k_e and k_p. Lorenz values between 2.04 x 10^{-8} and 2.26 x 10^{-8} $W \cdot \Omega \cdot K^{-2}$ were obtained for the carbon addition study with no systematic variation. The calculated Lorenz values for the ZrC study were 2.433 x 10^{-8}, 2.352 x 10^{-8} , 2.51 x 10^{-8}, 2.249 x 10^{-8}, and 2.261 x 10^{-8} $W \cdot \Omega \cdot K^{-2}$.

3.2. CONCLUSIONS

The following conclusions were reached based on the manuscripts presented and the questions in the previous Summary section.

1. Oxygen removal alone does not account for the effect of carbon on densification, as oxygen removal was independent of the carbon addition. Carbon additions are proposed to facilitate the improved densification of ZrB_2 by reducing the boron oxides on the surface of the raw powders. Left in the system, the boron oxides evaporate, reducing the oxygen content but contributing to a reduction in the driving force for densification by facilitating coarsening by vapor phase transport.

Boria reduction by carbon plays an interrelated role in the phase equilibria by leaving excess boron in the system. Once reduction reactions reach equilibrium, excess carbon additions can react with this boron producing a carbon rich, boron carbide. To produce ZrB_2 ceramics in the ZrB_2-C binary an additional source of zirconium is required and further additions will consume carbon to form ZrC. In general, depending on the desired second phase content, carbon additions should be controlled and the Zr/B stoichiometry modified accordingly.

2. The solid solution of carbon in ZrB_2 is limited (0.02 to 0.03 wt% C below 2100°C) and thought to form by substitution for boron in the lattice. As a second phase in ZrB_2, carbon forms a disordered graphitic structure that preferentially elongates along the grain boundaries. In either case, carbon reduces the thermal conductivity of ZrB_2 by reducing the electron contribution to conductivity for ZrB_2 ceramics. Phonon conduction does increase as a function of carbon content, but its contribution is less significant due the appreciable metallic nature of ZrB_2. The solid solution of carbon plays a minimal role in affecting thermal conductivity due to its limited solid solubility. Regardless, these results show the use of carbon in producing/densifying ZrB_2 should not be ignored when applications dictate maximizing thermal conductivity.

3. When producing ZrB_2 ceramics from typical commercial powders, porosity corrections indicate thermal conductivities as high as 99 W/m-K at 25°C and 75 W/m-K at 2000°C are achievable. In a real material, this will require densification to be improved to >99% as the experimental conductivities for the 96% dense material were 4 to 5 W/m-K lower before correcting for porosity. This nearly phase pure ZrB_2 (0.2 vol% zirconia) falls below the thermal conductivities of

some ZrB_2 materials from the literature, but most are lower. A majority of the differences arise from changes in the transition metal solid solution content. Tungsten contamination has resulted in ZrB_2 with lower thermal conductivities than the current research. On the other hand, ZrB_2 produced by reaction processing from the elements (B and Z or ZrH_2) is more likely to have reduced Hf contents. It is believed this leads to higher thermal conductivities than for ZrB_2 from commercial sources with higher naturally occurring Hf contamination. Other factors like grain size, while likely important, take a back seat to the effects of purity on the conductivity of ZrB_2.

4. The evaluation of electrical resistivity approaching 2000°C indicates ZrB_2 exhibits a shift in the slope of resistivity versus temperature at approximately 950°C. These results conflict with previous reports. However, the current work evaluated resistivity through a larger temperature range than all but one such study. This extended resistivity testing may be necessary for the observed trends to become evident.

5. A reduction in the $(Zr,W)B_2$ solid solution can be facilitated by the addition of ZrC, which forms a (Zr,W)C solid solution. Increased thermal conductivities at temperatures <1500°C were realized due to the sequestration of W from the ZrB_2 matrix to the ZrC second phase. This effect is limited by the negative effect of subsequent ZrC additions on thermal conductivity. Improved microstructures were achieved by maintaining higher thermal conductivities in two ways. First, compared to similar works in the literature, higher thermal conductivities were maintained while still reducing the grain size of the ZrB_2. This was facilitated by improving milling procedures to limit contamination, while still reducing particle

sizes. Second, the initial ZrC additions improved k below 1500°C and restricted coarsening of the ZrB_2 at elevated temperatures. In addition, the reduced k from the higher ZrC additions may be an acceptable tradeoff given the further reduction in coarsening at high temperatures.

6. The theoretical Lorenz number is not valid for all ZrB_2 materials. This is evidenced by the calculation of $k_p<0$ which is not physically possible. Compositions with reduced purity showed a tendency to deviate less from the Wiedemann-Franz law when using the theoretical Lorenz value. This was most obvious for the ZrB_2 attrition milled with WC with 0% added ZrC. The calculation of experimental Lorenz numbers from the thermal conductivity and electrical resistivity date were successful. The values made physical sense as the recalculation of k_e and k_p returned $k_e<k$ and therefore $k_p>0$. In addition, the calculated L values confirm that lower purity materials deviate less from Wiedemann-Franz, as the values for these materials were closest to the theoretical Lorenz number.

The research presented in this dissertation leads to one overarching theme with respect to the discussion of thermal conductivity for ZrB_2. That is, purity over all other factors dictates the magnitude of thermal conductivity in ZrB_2. Thermal conductivities will only be maximized by the elimination/removal of foreign species from the system, regardless of whether the species forms a solid solution or a second phase. Most often, improvements to thermal conductivity can come from optimizing processing to limit unnecessary contamination which isn't required for densification, or improving any other property. Commercial ZrB_2 sources, if not produced with reduced Hf contents, will always be limited in their potential thermal conductivity. The research presented also highlights the importance of understanding the Lorenz number for ZrB_2 ceramics.

Accurate values are not just necessary to separate the phonon and electron contribution to conductivity. They can also give insight into the phenomena controlling electron transport (electrical and thermal) in ZrB_2, which is very important due to the dominant nature of the electron contribution to the total thermal conductivity.

4. SUGGESTIONS FOR FUTURE WORK

Based on the research presented in this dissertation, many unanswered questions remain regarding the thermal conductivity, electrical resistivity, Lorenz number, and interrelated effects of purity which can be further investigated. The following suggestions are presented which may be of great value in further developing the understanding of thermal transport in ZrB_2 and other similar, conductive ceramics.

1. Continue the high temperature electrical resistivity testing of ZrB_2 and other similar materials. It may be fruitful to investigate the electrical resistivity of ZrB_2 with increased and decreased impurity contents (e.g. W and Hf, respectively) to see if they exhibit the same trends as the phase pure ZrB_2 discussed in this dissertation. Additions of tungsten are proposed, as linear trends in electrical resistivity as a function of temperature are reported, up to 1300°C, for ZrB_2 produced with WC contamination. Decreasing the impurity content of Hf from ZrB_2 is proposed based on the decreased electrical resistivities reported for low Hf content zirconium diboride. In addition, TiB_2 and HfB_2 would be ideal candidate materials for high temperature electrical resistivity testing. They should exhibit similar phenomena to ZrB_2 based on their identical bonding characteristics and crystal structure.
2. The observations of a change in the slope of electrical resistivity versus temperature for ZrB_2 must have an underlying mechanism. This phenomenon could be due to changes in the bonding characteristics, impurity distributions, or numerous other changes taking place at elevated temperatures. Modeling of electrical resistivity at high temperatures could be beneficial in answering questions regarding this phenomenon. In addition, modeling the resistivity would lend itself to calculating electron contributions to thermal conductivity.

3. The Lorenz number(s) for ZrB_2 are still not understood. Direct measurements of thermal conductivity and electrical resistivity under varied magnetic fields may yield a semi-direct evaluation of the Lorenz number. If successful, these results could open the door to additional, useful experiments to help broaden the understanding of the relationship between thermal and electrical conduction in ZrB_2 and other conductive materials.
4. The continued use of equation (43), from the literature review, to estimate the Lorenz number may also be beneficial in conjunction with the evaluation discussed above. In addition, this analysis could be used on previous studies that have presented thermal conductivities and electrical resistivities as a function of temperature, as these studies have assumed the theoretical Lorenz number to be valid. By calculating Lorenz values for ZrB_2 materials with obvious compositional or microstructural differences, trends in the data may become evident. From this, experiments may be designed to confirm the observations and validate any hypothesis.
5. Finally, the continued use of modeling would complement the experimental evaluations of the Lorenz number. The models may be able to answer questions regarding what controls the Lorenz number for ZrB_2 ceramics, if matched to the experimental observations.

APPENDIX

HIGH TEMPERATURE van der Pauw ELECTRICAL RESISTIVITY TESTING

As part of the research objectives of this dissertation, the development and fabrication of a system to measure electrical resistivity temperatures up to 2000°C was deemed critical. This system includes several individual parts including the electronics for measuring voltage and applying current, the computer and LabView software to control the electronics, an Excel spread sheet for data analysis, the high temperature metal element furnace, and finally the high temperature specimen test fixturing. Each of these systems will be discussed individually with a focus on general operating instructions for future researchers.

Computer, Electronics, and Software

The computer (Fig. 1a), switch box/voltage measurement equipment (Fig. 1b), testing power supply (Fig. 1c), and uninterruptable power supply (UPS; Fig. 1d) have been set up on a metal cart for ease of transport. It should be noted that the software and electronics can be used to measure electrical resistivity with any 4-point technique. The high temperature furnace and fixturing in G-2 Fulton will be discussed later but the measurement equipment can be taken to other possible testing setups. Mobility of the computer is also made easier by the accompanying USB Wi-Fi adaptor. The UPS has been included to maintain clean power and prevent issues with sudden power loss.

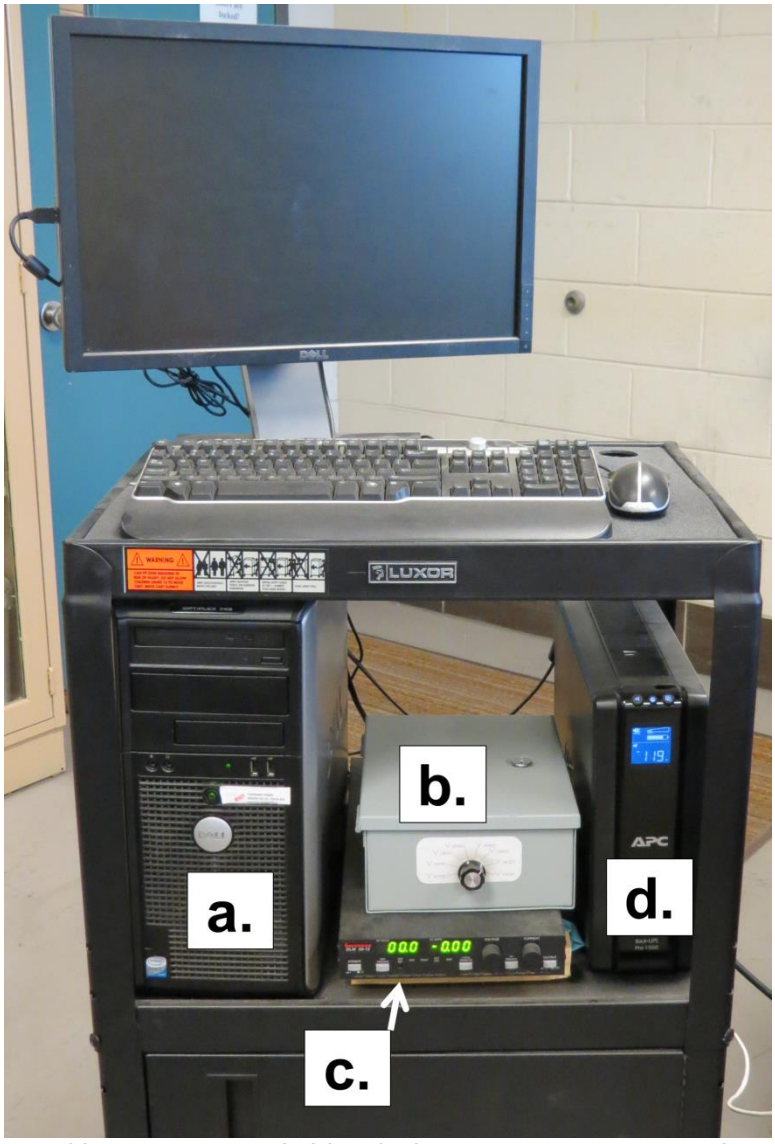

Fig. 1. Metal cart with computer, switchbox/voltage measurement equipment, DC power supply and UPS.

Switchbox and Voltage Measurement Equipment

An electrical box has been setup containing a DAQ device (data acquisition, Fig. 2a; NI 9211 DAQ w/NI USB-9162; National Instruments Corporation, Austin, TX), 0.005 Ω current sense resistor (Fig. 2b; CS3JR005E; Ohmite Mfg. Co., Arlington Heights, IL), and a rotary switch (Fig. 2c; four deck switch with 8 of 11 positions used, D4G0411N, Electroswitch, Raleigh, NC).

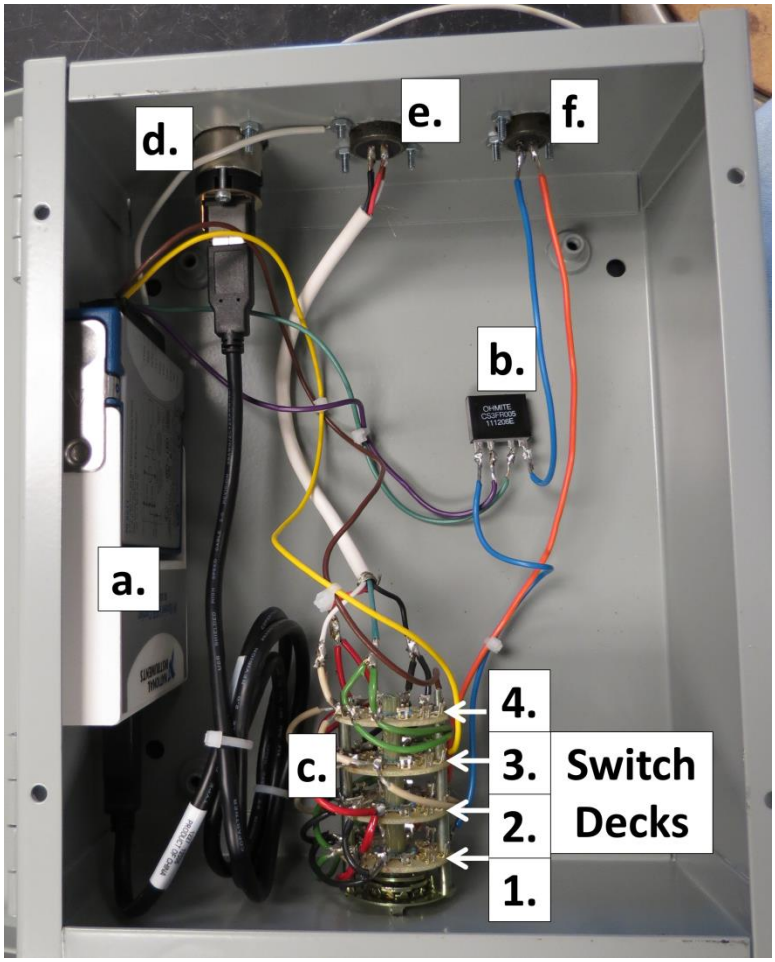

Fig. 2. Switch box with the DAQ (a), current sense resistor (b), rotary switch (c), USB feedthrough (d), 4-pole male electrical receptical (e), and 2-pole male electrical receptacle.

The rotary switch allows for the efficient switching between each permutation of the van der Pauw technique (see section 2.4.3.1.1 in the literature review). Each of the eight positions (permutations) is indicated at the switch control on the front of the box (Fig. 3). Each deck is labeled in Fig. 2 and in the electrical wiring diagram (Fig. 4). Decks 1 and 2, switch the positive and negative current coming from the DC power supply, which is fed into the box through the 2-pole electrical receptacle (Fig 2f). Decks 3 and 4, switch the positive (Fig. 5; TC0+) and negative (Fig. 5; TC0-) connections to the DAQ. These are the terminals used to measure the voltage drop across the sample during the

testing. The current sense resistor is also wired to the DAQ (TC1+ and TC1-; Fig. 5.) to enable the direct evaluation of the testing current.

Each of the eight positions of each deck is connected to one of four wires. These wires exit the box through the 4-pole electrical receptacle. The corresponding 4-pole plug is then connected to color coded wires on the outside which are eventually terminated by alligator clips (Fig. 6.). The clips can then be connected to any fixturing developed to make contact with a specimen. Ordering of the contacts is important and should be made concentrically around the sample as: red, white, green (or blue), and black.

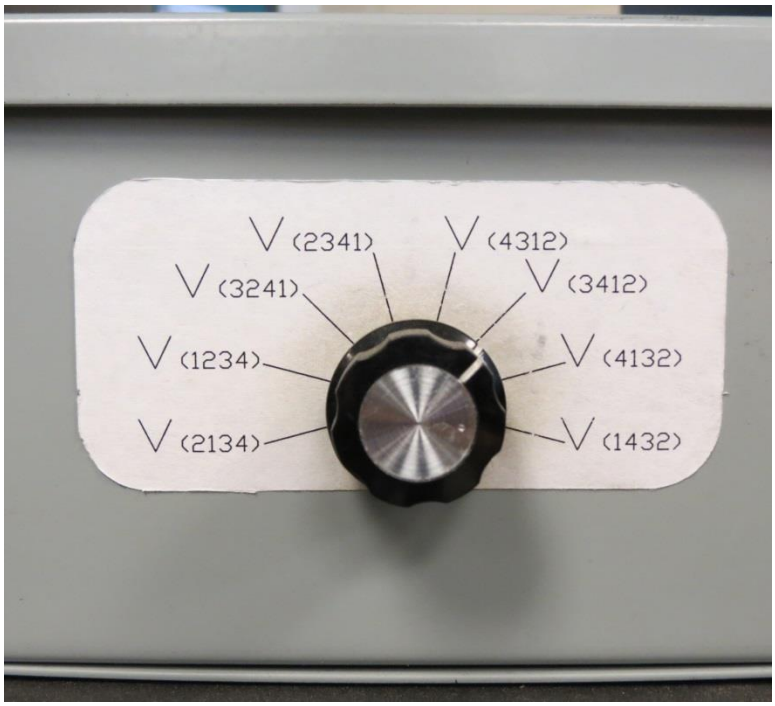

Fig. 3. Front of the switch box showing the eight positions which relate to the eight permutations of the sample contact positions necessary to perform the full van der Pauw technique.

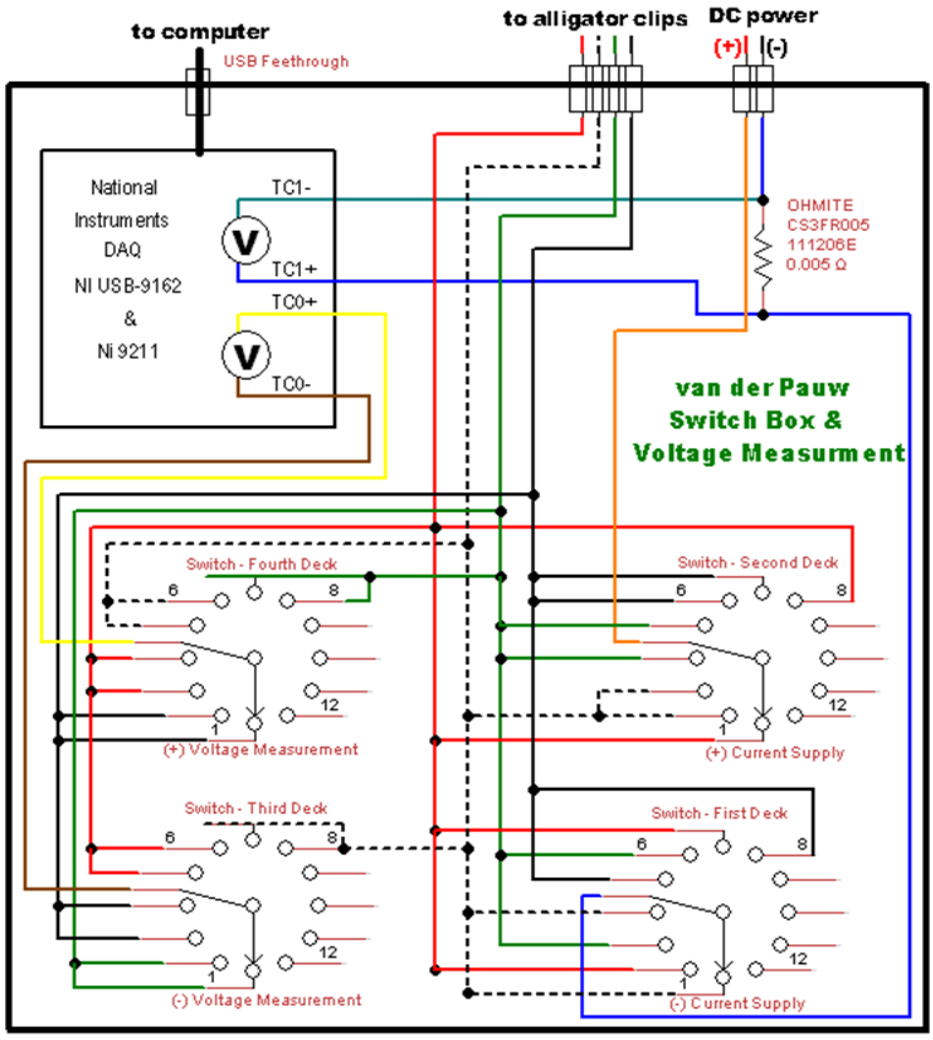

Fig. 4. Electrical diagram of the switch box detailing the wiring positions for each deck of the rotary switch, along with the connections they make in and outside of the box.

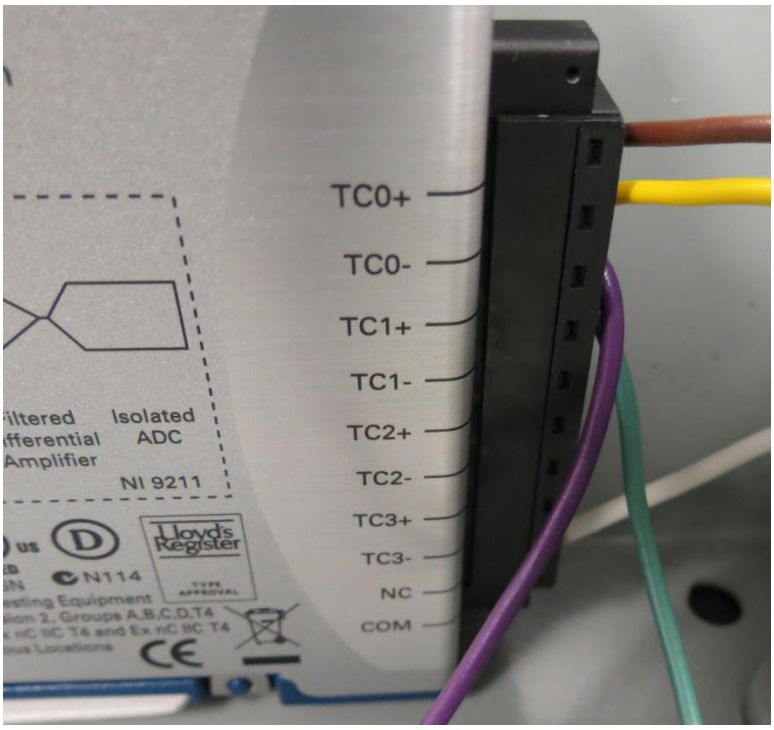

Fig. 5. Close-up view of the connections to the DAQ.

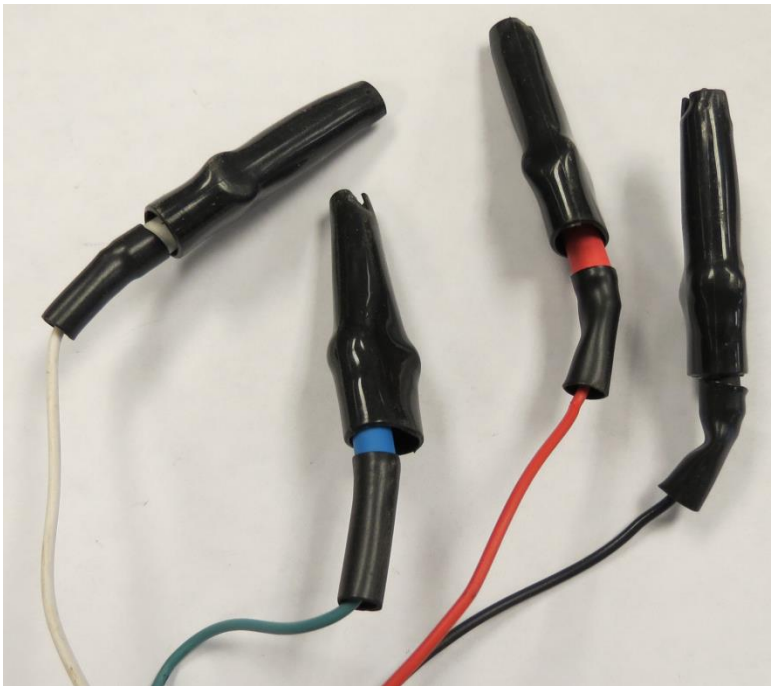

Fig. 6. Alligator clips used to connect the switch box to the test fixturing. They should always be ordered concentrically as: red, white, green (or blue), and black.

The DC power supply (DLM 40-15; Sorensen, AMETEK Corp., San Diego, CA) is shown in Fig. 7. This unit is connected to the 2-pole receptacle on the box by an accompanying 2-pole female plug. Communication between the power supply and the computer is made via a GPIB (IEEE 488.1) to USB interface adaptor (NI GPIB-USB-HS; National Instruments Corporation, Austin, TX) and is controlled automatically by the software. The front interface also allows for manual control if necessary.

Fig. 7. Front interface of the DC power supply which displays the applied current and corresponding voltage; and allows for manual control.

LabVIEW Electrical Testing Virtual Instrument (VI)

The computer is loaded with a campus license of LabVIEW (LabVIEW 12; National Instruments Corporation, Austin, TX). A LabVIEW script (DAQ-PowerSupply application.vi) has been written which enables the power supply to be automatically controlled and the measurement by the DAQ to be sampled and recorded. Special thanks should be given to Dr. Simon Lekakh for providing the initial program which was then expanded upon thanks to Brian Swift.

Before starting the program it is best to make sure that both the DAQ and power supply are connected to the computer and that the power supply is on. A walkthrough of the operation of the software will now be presented.

The two main features of this program are the live data graph and the operation controls (Fig. 8). During testing, the live graph will display both the voltage drop measured across the sample and the input current (the system has a correction equal to the resistance of the sense resistor applied in order to display a value of current). The operation controls are used to select the appropriate instrumentation (DAQ and power

supply), input testing parameters, and start/stop the program. The other features of this interface are not critical to the testing, but error out and error out 2 can help troubleshoot issues with the program. A red X will appear if the program experiences an error (instead of a green check) and the error code will be displayed.

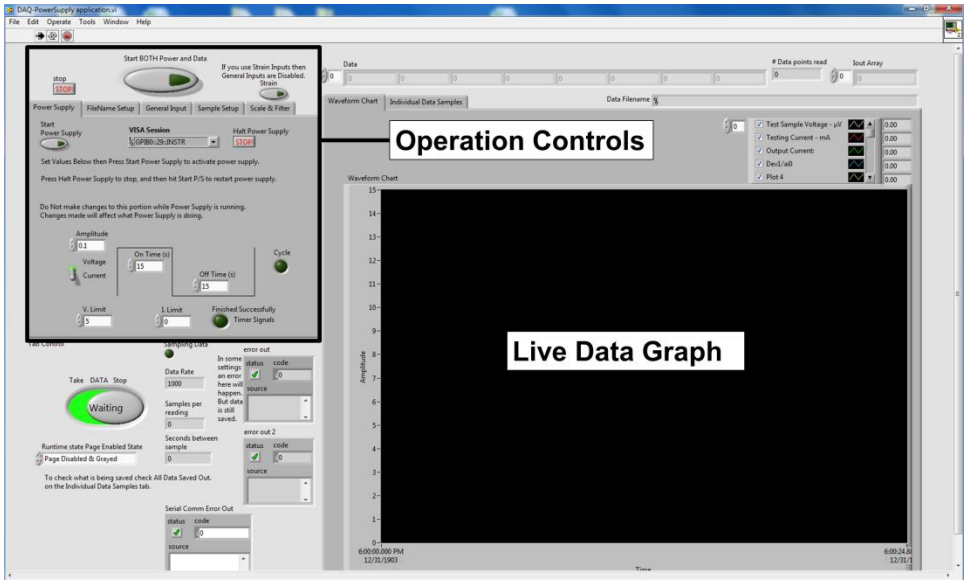

Fig. 8. Initial startup screen for the DAQ-PowerSupply application.vi testing program.

The program starts up with the “Power Supply” tab selected in the operation controls (Fig. 9). Some of the main testing parameters are set here and this tab is where the program is controlled during testing. Control of the power supply is set in the “VISA Session” drop down and GPIB0::29::INSTR should always be chosen. The system automatically operates the test by cycling the power supply on and off, allowing the experimental and baseline voltages to be measured for a given current and the zero current conditions. The system can be run using a constant voltage or a constant current. This is changed by the switch next to “voltage” and “current”. The resistivity testing should be run in the constant current setting. The magnitude of the current (or voltage) is set by the value in the “Amplitude” box. Currents between 0.1 and 0.6 amps are typically used. However, the necessary current will depend on the specimen resistivity and thickness. Depending on if the program is run using constant current or

constant voltage a corresponding limit can be set to the voltage (V. Limit) used to achieve the constant current or current allowable (I. Limit) to reach a given voltage.

The cycling times (in seconds) are set by the values in the “On Time (s)” and “Off Time (s)” boxes. Appropriate time lengths will depend on the signal quality, as better signal to noise ratios means fewer samples will need to be recorded to obtain an acceptable average. The “Cycle” light will illuminate when the program is running and will turn off after the program has been shut off and the off time has been completed. Data recording and current cycling are started simultaneously using the “Start BOTH Power and Data” button. Pressing this again will also stop the recording but “Halt Power Supply” must be pressed to stop the current source. Shutting down the power supply is usually done first and then the recording is stopped after the cycle light turns off. Operation of the power supply can be started separately using the “Start Power Supply” button.

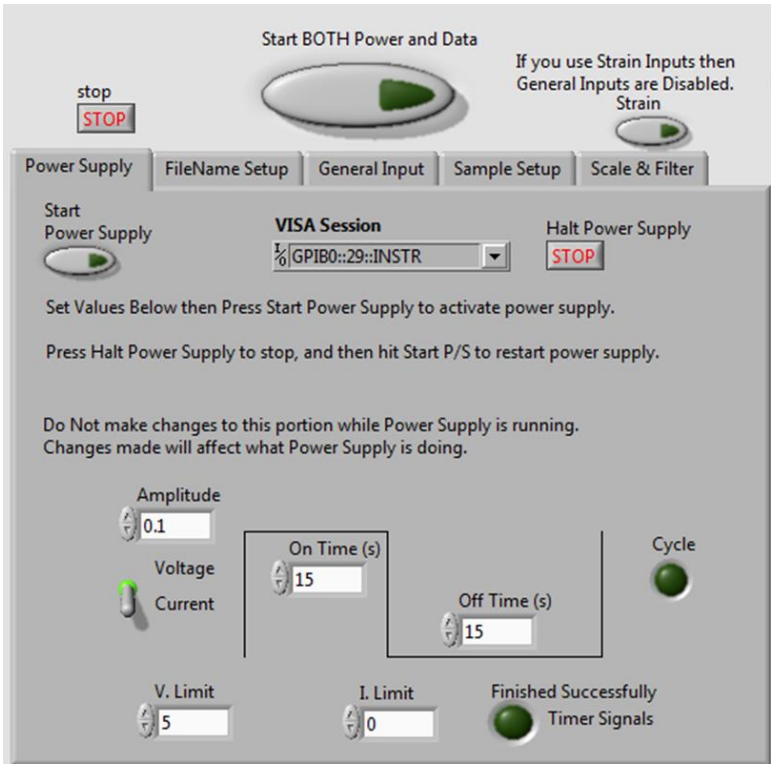

Fig. 9. The features of the “Power Supply” tab of the operation controls from Fig.9 are shown more closely.

The second tab in the operation controls is the “FileName Setup” tab (Fig. 10). Upon the startup of testing (turning on the “Start BOTH Power and Data” button) the program will create a text file in the specified path (see “Path to save to” dialog box) that is continuously written to as the data is collected. The text file is then finalized upon ending the data acquisition. The name of the file is dictated by the options selected in this tab and its final form, along with the complete directory path, are displayed in “Run Filename”. The boxes “Filename part 1”, “part 2”, and “File name part 3” specify three separate strings that will make up the full file name. Part 1 is usually the specimen name. Part 2 is a number that can be set to increment automatically after the testing is stopped. The increment feature can be turned off using the “Auto Increment” switch and the increment value specified in the “Increment” box. In the case of testing the eight separate switch positions for the van der Pauw method, part 2 is usually set to 1 and the increment is set to 1. In doing this, each switch position is a number 1 through 8 when starting at the left most position. Part 3 of the file name is a time/date stamp which can be turned on and off with the “Time – Date” switch.

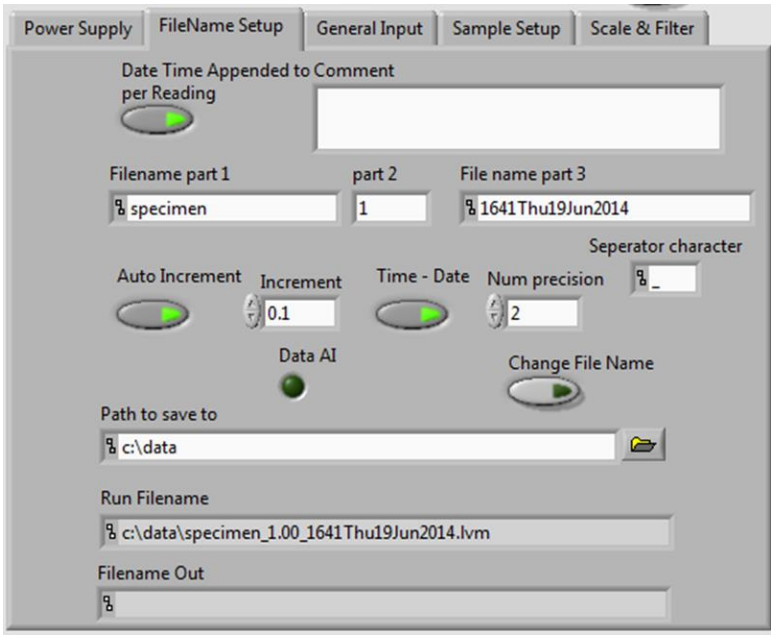

Fig. 10. The “FileName Setup” tab configures the name applied to the output text file.

Configuration of the “General Input” tab specifies the input devices/channels for the data acquisition (Fig. 11). The “Channel Type Enable for Physical Channels Dark for Global Channels” switch allows the user to select different types of channels. The physical channels are simply the input channels available from a given DAQ. As this feature does not allow the data input to be scaled and other features have to be input every time the program is started this switch is turned off. For this electrical testing procedure, two global channels “Test Sample Voltage - μV” and “Testing Current - Amps” have been established. These channels can be selected by first pressing the “DAQmx Global Channel” down arrow, then selecting “Browse…” from the drop down menu (Fig. 12), and then choosing in order from top to bottom, “Test Sample Voltage - μV” and “Testing Current - Amps” from the “Select item(s)” dialogue box (Fig. 13). The specific order in which these channels are chosen dictates which columns the output data are filled. This will become important when the columns are copied into the Excel spreadsheet designed to filter through the output data. Finally, the “Both Raw & Scaled”

switch should be highlighted for the Excel sheet to work properly after the output data has been pasted.

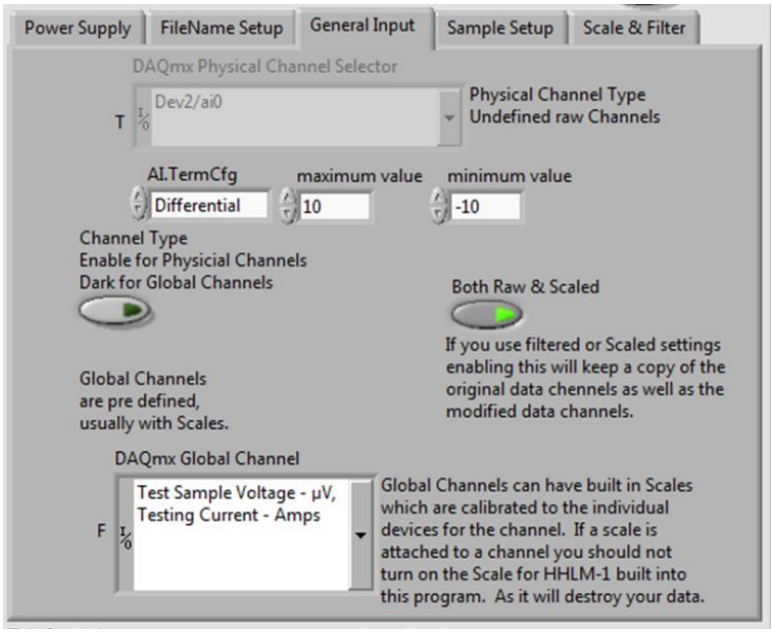

Fig. 11. The “General Input” tab configures the data collection from the DAQ.

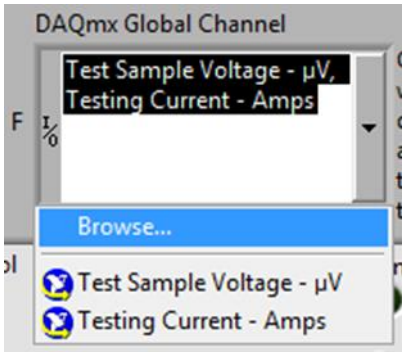

Fig. 12. Drop down list that appears by pressing the “DAQmx Global Channel” down arrow.

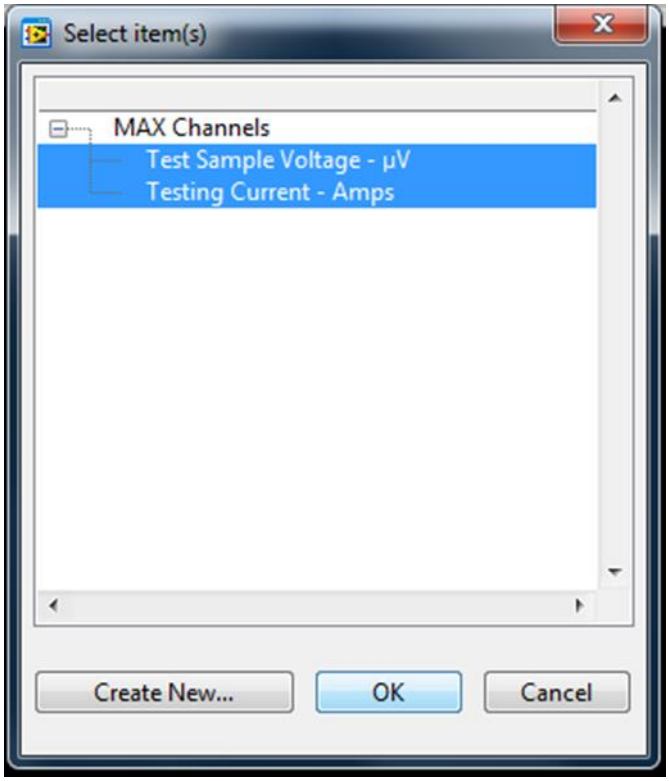

Fig. 13. Dialog box which appears after selecting the browse option from the "DAQmx Global Channel" down arrow.

The "Sample Setup" tab allows the data collection settings to be defined. The "Data Rate" parameter dictates how many data points are read every second. Each data point is composed of a given number of samples defined by the "Samples per time reading" dialog. Based on the limitations of the DAQ chosen, 4 is the maximum value for both of these parameters. The "Seconds between sample" will be defined as 0.25 once both of the other dialog boxes are established.

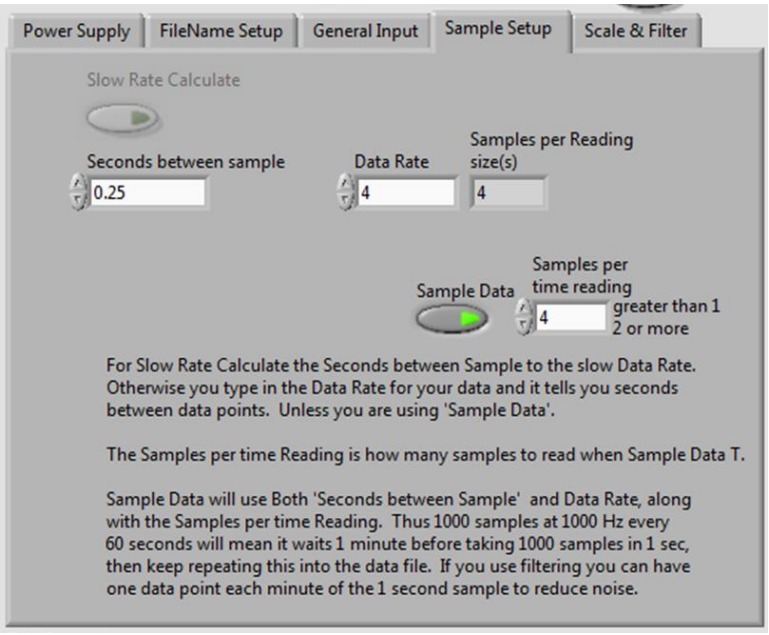

Fig. 14. The “Sample Setup” tab configures the data acquisition timing/sampling parameters.

The final part of the operation controls is the “Scale & Filter” tab (Fig. 15). Features at the top of this tab allow the output data to be scaled by a fixed factor. This serves no utility for the current testing and can be disregarded. The bottom options allow for the data to be filtered to average out noise from the testing and limit the number of data points to analyze by the Excel spreadsheet. This option is always used as seen in Fig. 15, with the switch below “All Data Points Filtered” set to the on position.

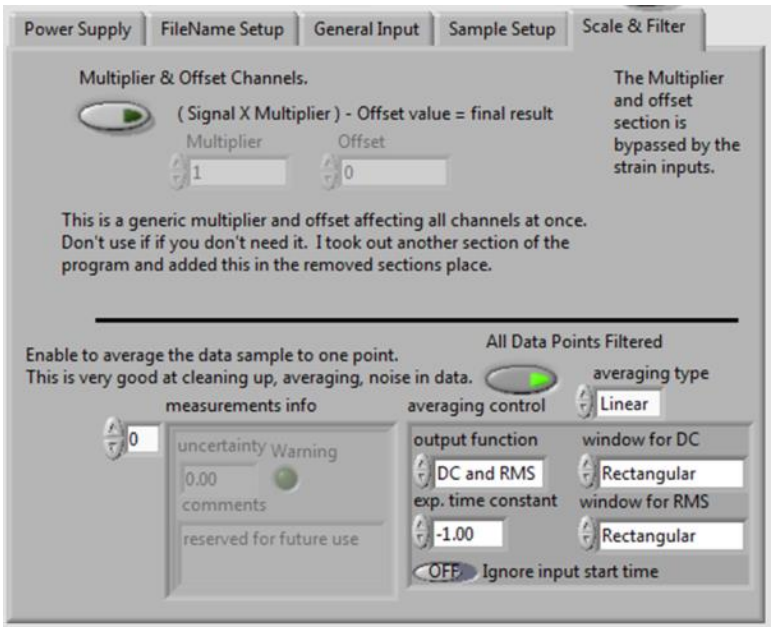

Fig. 15. The “Scale and Filter” tab allows the data from the channels to be scaled or filtered (to average out noise).

With all of the parameters of the operations controls set (and assuming the test fixturing is ready with the specimen in place) testing may proceed. Fig. 16 gives a representative view of the live data feed after one position has been tested. The system is allowed to cycle on and off multiple times and then without shutting the testing down the current is changed to two successively higher currents. Not only does this operation allow more data to be analyzed but a check of V/I at each current should yield a consistent value if all of the electrical contacts in the system are Ohmic. With the data from one position recorded shut off the power and then stop the data recording. The live data feed may be erased by right clicking in the black space and choosing the option “clear data”. Now, switch the dial on the switch box to the next position, reset the amplitude to the first testing current and repeat. When all eight positions have been recorded the data is ready to be analyzed.

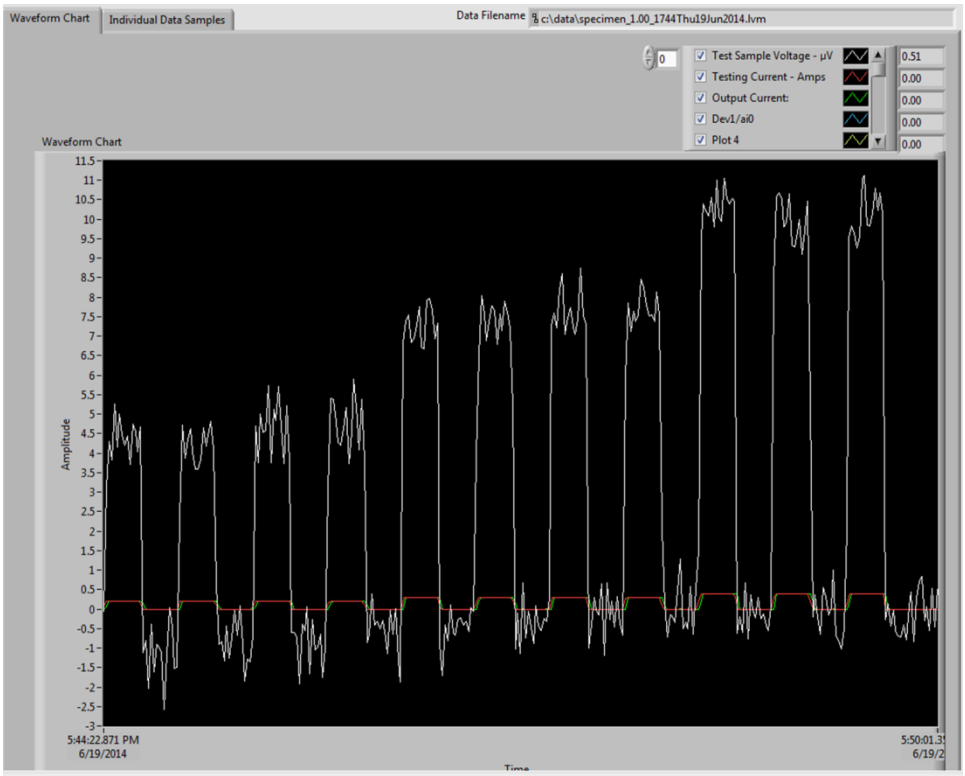

Fig. 16. Live data graph showing the on and off cycling of three separate applied currents which is typical of the electrical resistivity testing.

Excel Data Analysis and van der Pauw Calculation Spreadsheet

If the setup directions are followed up until this point the output data spreadsheet should look like the image in Fig. 17. An Excel spreadsheet titled “Electrical Resistivity Testing template” has been developed as a template to accept the output data. The template then automatically filters the inserted data to enable the calculation of electrical resistivity from the eight separate positions using the math outlined in ASTM Standard F-76-08. To begin filling the template, highlight all the data from the output file below and to the right of cell A23 (selecting A23 and then holding shift and ctrl while hitting the down arrow and right arrow will select the continuous data quickly) and copy it. With the appropriate voltage permutation tab selected in the template, paste the data into cell A11. This should populate the appropriate rows and columns (see Fig. 18). Repeat this step for each testing permutation and make sure the data from each testing position goes into the correct tab.

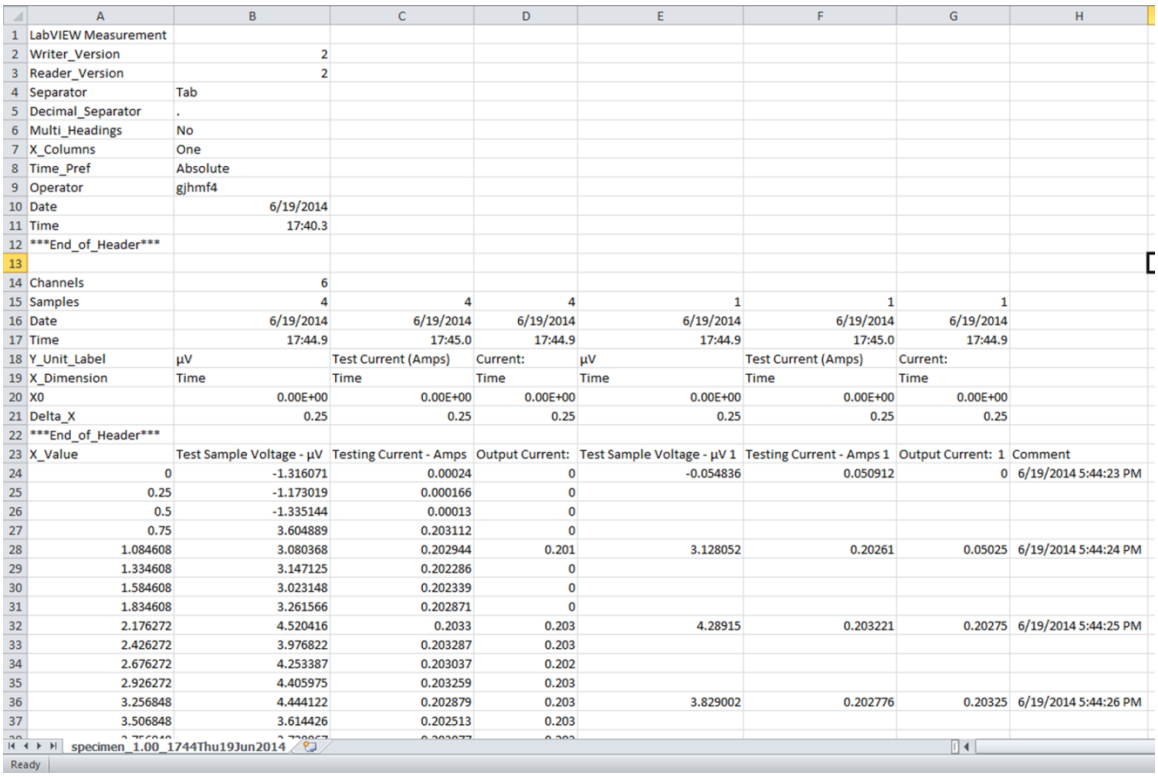

	A	B	C	D	E	F	G	H
1	LabVIEW Measurement							
2	Writer_Version	2						
3	Reader_Version	2						
4	Separator	Tab						
5	Decimal_Separator	.						
6	Multi_Headings	No						
7	X_Columns	One						
8	Time_Pref	Absolute						
9	Operator	gjhmf4						
10	Date	6/19/2014						
11	Time	17:40.3						
12	***End_of_Header***							
13								
14	Channels	6						
15	Samples	4	4	4	1	1	1	
16	Date	6/19/2014	6/19/2014	6/19/2014	6/19/2014	6/19/2014	6/19/2014	
17	Time	17:44.9	17:45.0	17:44.9	17:44.9	17:45.0	17:44.9	
18	Y_Unit_Label	µV	Test Current (Amps)	Current:	µV	Test Current (Amps)	Current:	
19	X_Dimension	Time	Time	Time	Time	Time	Time	
20	X0	0.00E+00	0.00E+00	0.00E+00	0.00E+00	0.00E+00	0.00E+00	
21	Delta_X	0.25	0.25	0.25	0.25	0.25	0.25	
22	***End_of_Header***							
23	X_Value	Test Sample Voltage - µV	Testing Current - Amps	Output Current:	Test Sample Voltage - µV 1	Testing Current - Amps 1	Output Current: 1	Comment
24	0	-1.316071	0.00024	0	-0.054836	0.050912	0	6/19/2014 5:44:23 PM
25	0.25	-1.173019	0.000166	0				
26	0.5	-1.335144	0.00013	0				
27	0.75	3.604889	0.203112	0				
28	1.084608	3.080368	0.202944	0.201	3.128052	0.20261	0.05025	6/19/2014 5:44:24 PM
29	1.334608	3.147125	0.202286	0				
30	1.584608	3.023148	0.202339	0				
31	1.834608	3.261566	0.202871	0				
32	2.176272	4.520416	0.2033	0.203	4.28915	0.203221	0.20275	6/19/2014 5:44:25 PM
33	2.426272	3.976822	0.203287	0.203				
34	2.676272	4.253387	0.203037	0.202				
35	2.926272	4.405975	0.203259	0.203				
36	3.256848	4.444122	0.202879	0.203	3.829002	0.202776	0.20325	6/19/2014 5:44:26 PM
37	3.506848	3.614426	0.202513	0.203				

specimen_1.00_1744Thu19Jun2014

Ready

Fig. 17. Representative output data file. The data to the right and below cell A23 get copied into the resistivity testing template.

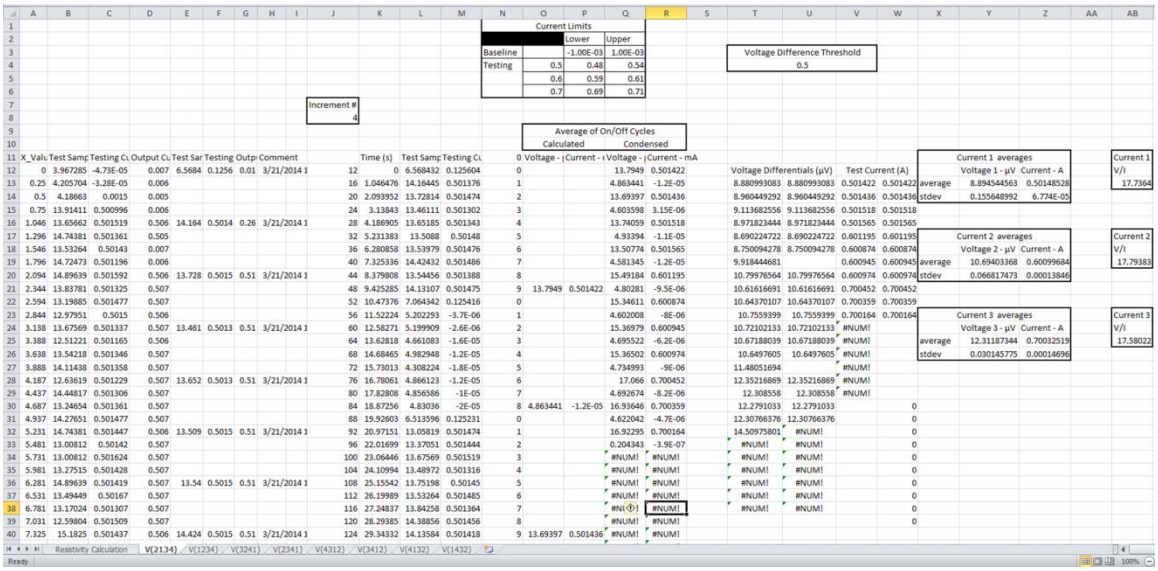

Current Limits

		Lower	Upper
Baseline		-1.00E-03	1.00E-03
Testing	0.5	0.48	0.54
	0.6	0.59	0.61
	0.7	0.69	0.71

Voltage Difference Threshold: 0.5

Increment #: 4

Average of On/Off Cycles

Calculated		Condensed	
Voltage - µV	Current - mA	Voltage - µV	Current - mA
0		13.7949	0.501422
1		4.863441	-1.2E-05
2		13.69397	0.501436
3		4.603598	3.15E-06
4		13.74059	0.501518
5		4.93394	-1.1E-05
6		13.50774	0.501565
7		4.581345	-1.2E-05
8		15.49184	0.601195
9	13.7949 0.501422	4.80281	-9.5E-06
0		15.34611	0.600874
1		4.602008	-8E-06
2		15.36979	0.600945
3		4.695522	-6.2E-06
4		15.36502	0.600974
5		4.734993	-9E-06
6		17.066	0.700452
7		4.692674	-8.2E-06
8	4.863441 -1.2E-05	16.93646	0.700359
0		4.622042	-4.7E-06
1		16.92295	0.700164
2		0.204343	-3.9E-07
3		#NUM!	#NUM!
4		#NUM!	#NUM!
5		#NUM!	#NUM!
6		#NUM!	#NUM!
7		#NUM!	#NUM!
8		#NUM!	#NUM!
9	13.69397 0.501436	#NUM!	#NUM!

Voltage Differentials (µV)	Test Current (A)
8.880993083	8.880993083 0.501422 0.501422
8.960449292	8.960449292 0.501436 0.501436
9.113682556	9.113682556 0.501518 0.501518
8.971823444	8.971823444 0.501565 0.501565
8.690224722	8.690224722 0.601195 0.601195
8.750094278	8.750094278 0.600874 0.600874
9.918444681	0.600945 0.600945
10.79976564	10.79976564 0.600974 0.600974
10.61616691	10.61616691 0.700452 0.700452
10.64370107	10.64370107 0.700359 0.700359
10.7559399	10.7559399 0.700164 0.700164
10.72102133	10.72102133 #NUM!
10.67188039	10.67188039 #NUM!
10.6497605	10.6497605 #NUM!
11.48051694	#NUM!
12.35216869	12.35216869 #NUM!
12.308558	12.308558 #NUM!
12.2791033	12.2791033
12.30766376	12.30766376
14.50975801	#NUM!
#NUM!	#NUM!
#NUM!	#NUM!
#NUM!	#NUM!
#NUM!	#NUM!
#NUM!	#NUM!

Current 1 averages		
	Voltage 1 - µV	Current - A
average	8.894544563	0.50148528
stdev	0.155648992	6.774E-05

Current 1 V/I: 17.7364

Current 2 averages		
	Voltage 2 - µV	Current - A
average	10.69403368	0.60099684
stdev	0.066817473	0.00013846

Current 2 V/I: 17.79383

Current 3 averages		
	Voltage 3 - µV	Current - A
average	12.31187344	0.70032519
stdev	0.030145775	0.00014696

Current 3 V/I: 17.58022

Resistivity Calculation | V(2134) | V(1234) | V(3241) | V(2341) | V(4312) | V(3412) | V(4132) | V(1432)

Ready

Fig. 18. Image of the van der Pauw permutation tab V(2134) which is the first position on the electrical switch box. The output data from this position starting from cell A23 gets copied into cell A11 on this sheet.

With all of the output data copied into the appropriate tabs, each tab should be checked to make sure the data is filtered correctly by evaluating the columns to the right

of “I”. A close up of these cells is shown in Fig. 19. The description of the function of each cell or column of cells will now be taken step by step to describe how the spreadsheet filters through the raw data.

- Cell J8 – sets the increment of cells J12 and below depending on how many cells in the filtered output data are skipped.
- Cells K12 and below – takes the time from column A associated with the number in column J of the same row as the cell in column K (cell K13 pulls in data from cell A16 because of the number in cell J13 is 16)
- Cells L12 and below – same as K12 but looks up the measured sample voltage
- Cells M12 and below – same as K12 but looks up the measured testing current
- Cells N12 and below –. Based on the current limits established in cells N1 through Q6 (the upper and lower limits bound the nominal testing currents (cells O4-O6) which are set in cells R1-R3 the “Resistivity Calculation” tab) this column looks for either an on current or off current from the data in cells M12 and below. Once a continuous set of currents is located which correspond to the limits set above, the cell increments, starting over when the opposite current cycle is detected.
- Cells O12 and below – averages the continuous string of on or off cycle voltages to produce a single value for one cycle. This column looks for a continuous set of non-zero numbers from cells N12 and below which tell the cell which rows in column L to pull from to form the average cycle voltage
- Cells P12 and below – same as O1 and below except this column averages the testing currents for a given on or off cycle.
- Cells Q12 and below – condenses the data in O12 and below to remove the empty cells
- Cells R12 and below – condenses the data in R12 and below to remove the empty cells
- Cells T13 and below – calculates the voltage difference between an off cycle and the preceding and following on cycles or between an on cycle and the preceding and following off cycles. This step is necessary as the DAQ measures a floating point voltage and the baseline has to be measured for reference.
- Cells U13 and below – Using the “Voltage Difference Threshold” value from cell U4 this column takes out the voltage difference which lies in between the change

in testing currents calculated in the cells T13 and below. This value will need to be changed periodically to obtain three individual sets of continuous voltage differentials associated with each testing current. If changing this value fails to automatically achieve this result the appropriate numbers may be manually input or deleted as necessary.

- Cells V13 and below – determines the average testing current associate with each set of on cycles
- Cells W13 and below – these cells use the “iserror” function to remove any #NUM! errors from the ending of cells V13 and below
- The bordered boxes in columns X, Y and Z calculate the average voltage difference and testing current for each of the three testing currents
- The bordered boxes in column AB calculate the ultimate V/I (resistance) for each testing currents. Any significant deviation in these values is an indication of non Ohmic contacts

It should be noted that certain changes in the quality of the output testing data may make it more difficult to analyze the data and more steps may need to be taken to manually filter though the data. However this sheet carries out most of the hard work when good signal to noise ratios are obtained and the order of testing is kept consistent.

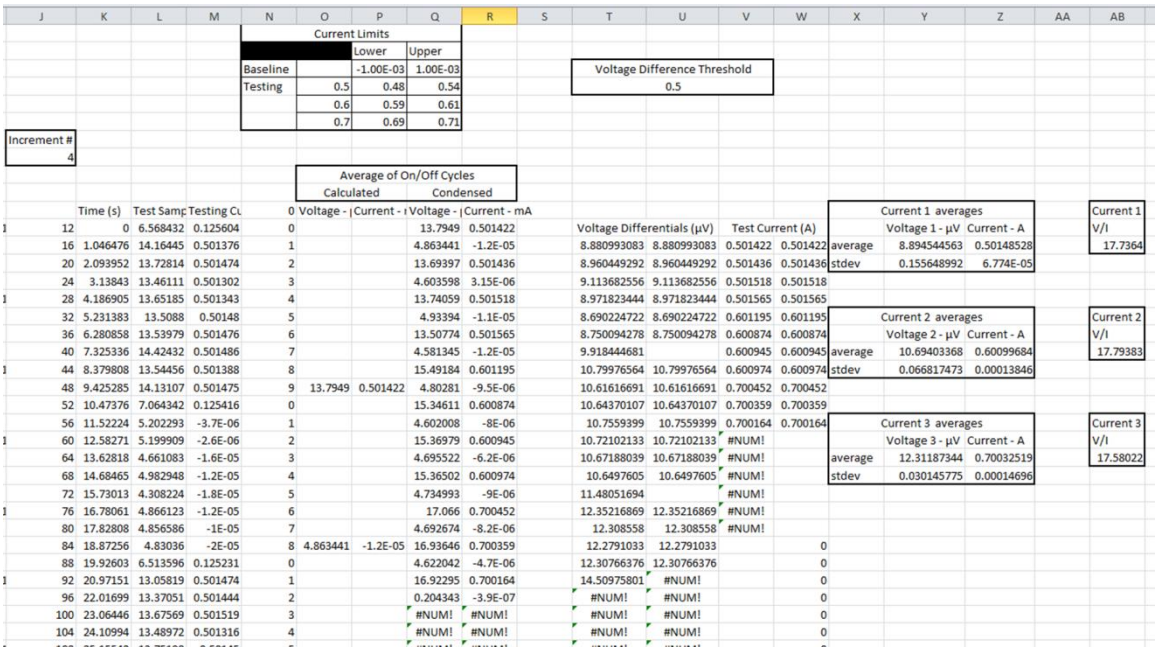

					Current Limits																
						Lower	Upper														
					Baseline		-1.00E-03	1.00E-03			Voltage Difference Threshold										
					Testing	0.5	0.48	0.54			0.5										
						0.6	0.59	0.61													
						0.7	0.69	0.71													
Increment #																					
4																					
						Average of On/Off Cycles															
						Calculated		Condensed													
		Time (s)	Test Samp	Testing Cu	0	Voltage -	Current -	Voltage -	Current - mA		Voltage Differentials (μV)		Test Current (A)			Current 1 averages				Current 1
1	12	0	6.568432	0.125604	0			13.7949	0.501422							Voltage 1 - μV	Current - A			V/I
	16	1.046476	14.16445	0.501376	1			4.863441	-1.2E-05		8.880993083	8.880993083	0.501422	0.501422	average	8.894544563	0.50148528			17.7364
	20	2.093952	13.72814	0.501474	2			13.69397	0.501436		8.960449292	8.960449292	0.501436	0.501436	stdev	0.155648992	6.774E-05			
	24	3.13843	13.46111	0.501302	3			4.603598	3.15E-06		9.113682556	9.113682556	0.501518	0.501518						
1	28	4.186905	13.65185	0.501343	4			13.74059	0.501518		8.971823444	8.971823444	0.501565	0.501565						
	32	5.231383	13.5088	0.50148	5			4.93394	-1.1E-05		8.690224722	8.690224722	0.601195	0.601195		Current 2 averages				Current 2
	36	6.280858	13.53979	0.501476	6			13.50774	0.501565		8.750094278	8.750094278	0.600874	0.600874		Voltage 2 - μV	Current - A			V/I
	40	7.325336	14.42432	0.501486	7			4.581345	-1.2E-05		9.918444681		0.600945	0.600945	average	10.69403368	0.60099684			17.79383
1	44	8.379808	13.54456	0.501388	8			15.49184	0.601195		10.79976564	10.79976564	0.600974	0.600974	stdev	0.066817473	0.00013846			
	48	9.425285	14.13107	0.501475	9	13.7949	0.501422	4.80281	-9.5E-06		10.61616691	10.61616691	0.700452	0.700452						
	52	10.47376	7.064342	0.125416	0			15.34611	0.600874		10.64370107	10.64370107	0.700359	0.700359						
	56	11.52224	5.202293	-3.7E-06	1			4.602008	-8E-06		10.7559399	10.7559399	0.700164	0.700164		Current 3 averages				Current 3
1	60	12.58271	5.199909	-2.6E-06	2			15.36979	0.600945		10.72102133	10.72102133	#NUM!			Voltage 3 - μV	Current - A			V/I
	64	13.62818	4.661083	-1.6E-05	3			4.695522	-6.2E-06		10.67188039	10.67188039	#NUM!		average	12.31187344	0.70032519			17.58022
	68	14.68465	4.982948	-1.2E-05	4			15.36502	0.600974		10.6497605	10.6497605	#NUM!		stdev	0.030145775	0.00014696			
	72	15.73013	4.308224	-1.8E-05	5			4.734993	-9E-06		11.48051694		#NUM!							
1	76	16.78061	4.866123	-1.2E-05	6			17.066	0.700452		12.35216869	12.35216869	#NUM!							
	80	17.82808	4.856586	-1E-05	7			4.692674	-8.2E-06		12.308558	12.308558	#NUM!							
	84	18.87256	4.83036	-2E-05	8	4.863441	-1.2E-05	16.93646	0.700359		12.2791033	12.2791033		0						
	88	19.92603	6.513596	0.125231	0			4.622042	-4.7E-06		12.30766376	12.30766376		0						
1	92	20.97151	13.05819	0.501474	1			16.92295	0.700164		14.50975801	#NUM!		0						
	96	22.01699	13.37051	0.501444	2			0.204343	-3.9E-07		#NUM!	#NUM!		0						
	100	23.06446	13.67569	0.501519	3			#NUM!	#NUM!		#NUM!	#NUM!		0						
	104	24.10994	13.48972	0.501316	4			#NUM!	#NUM!		#NUM!	#NUM!		0						

Fig. 19. Close up of the columns past "I" where the voltage permutation sheet needs to be checked in order to make sure the data is being sorted properly.

If the data in each permutation tab is calculated correctly and no errors exist, each voltage differential and affiliated testing current should automatically be populated in the "Resistivity Calculation" tab (Fig. 20). The calculations used here are all detailed in section 2.4.3.1.1 of the literature review and have been pulled from ASTM Standard F-76-08. Each set of voltages and currents is used along with the input thickness to calculate one of two complimentary resistivities for each current. The spread sheet displays the percentage difference between these resistivities so that compliance with the ASTM standard can be checked. The shape factor (f_A or f_B) must be calculated using the solver function which utilizes the sum of least squares to optimize the numbers. All of the input parameters to solve for the shape factor are saved in the solver in the template (Fig. 21). To solve for the shape factor just open the solver and press the solve button.

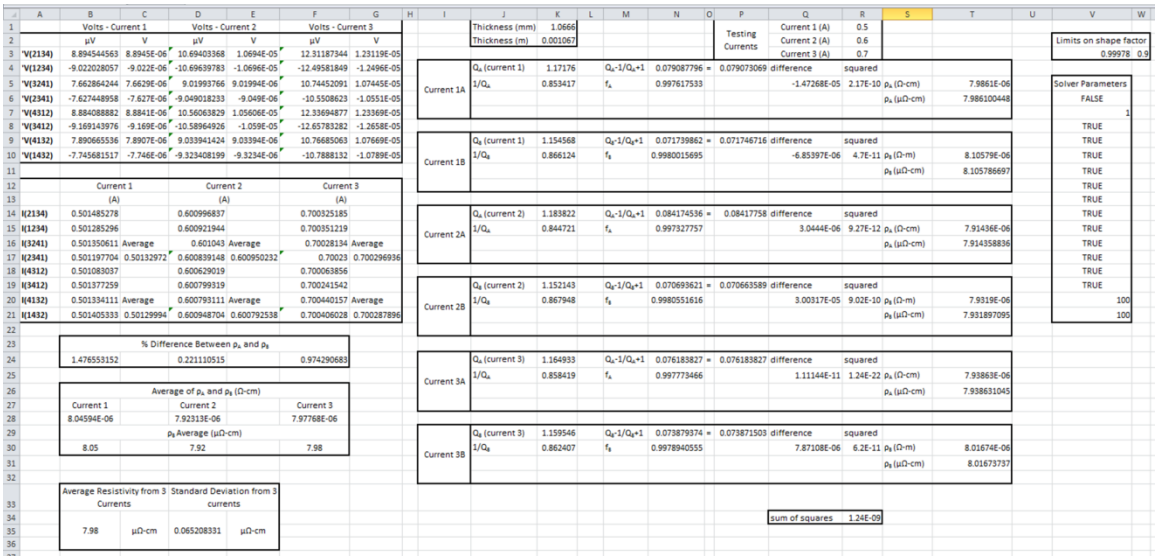

Fig. 20. “Resistivity Calculation” tab is shown. This is where the current and voltage data are used to calculate the final electrical resistivity.

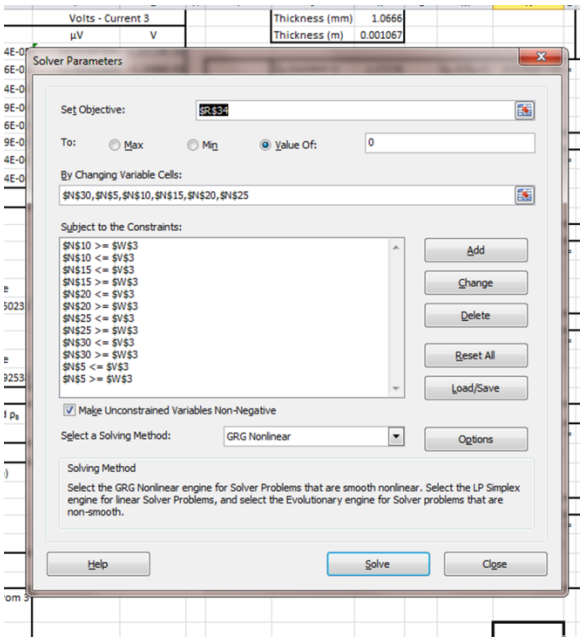

Fig. 21. The Excel solver add-in used to solve for the shape factors is displayed. All of the constraints should be prepopulated allowing ease of use of the template.

The resulting resistivity and standard deviation are calculated in the bottom left bordered box. This concludes the navigation the software. The remainder of the discussion will cover the high temperature fixturing and furnace.

High Temperature Electrical Fixturing and Furnace

The high temperature electrical fixturing is designed to work with the tungsten element furnace (1100-4080-W3; Thermal Technologies LLC) in G2 Fulton (Fig. 22a). The system makes use of the pneumatically operated elevator door (Fig. 22b) to be able to easily work on the assembly and then insert it into the furnace.

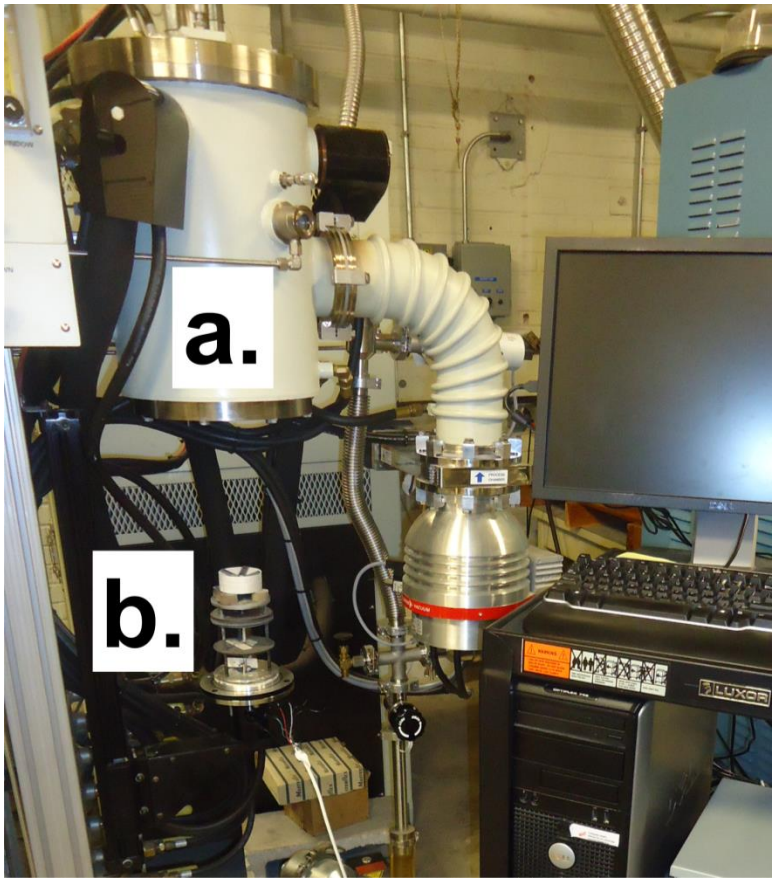

Fig. 22. Image of the furnace body (a) and bottom elevator door (b) where the electrical testing setup is installed.

A closer view of the assembly on the furnace elevator is shown in Fig. 23. The electrical testing fixturing (Fig. 23a) rests on top of some ZrB_2 cylinders to elevate it further into the hotzone. A tungsten hearth plate, tungsten shield pack and molybdenum shield pack support the fixturing while serving as the bottom thermal shielding (Fig. 23c). Tungsten wires (Fig. 23c; 0.75 mm diameter 99.95% pure W from Alpha Aesar) connect the electrical setup to the feedthrough wires at the bottom of the furnace (Fig. 23d). The

feed through wires and tungsten wires are mechanically clamped to each other with stainless steel nuts, bolts, and washers. The entire assembly rests on the aluminum elevator platform (Fig. 23e). A hermetic 4-wire electrical feedthrough is inserted in the bottom of the elevator platform (Fig. 24.) The electrical testing equipment hook to these wires using the alligator clips.

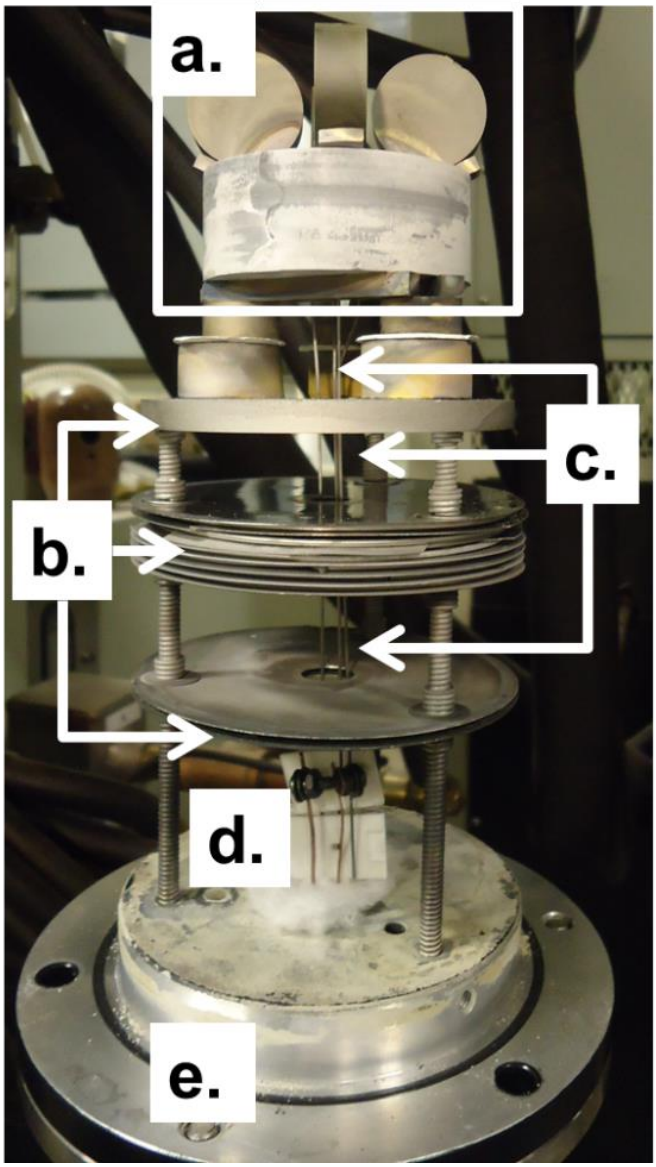

Fig. 23. The furnace bottom assembly the electrical test fixturing (a), heart and shield pack (b), tungsten wires (c), contacts to electrical feedthrough (d), and the bottom elevator door.

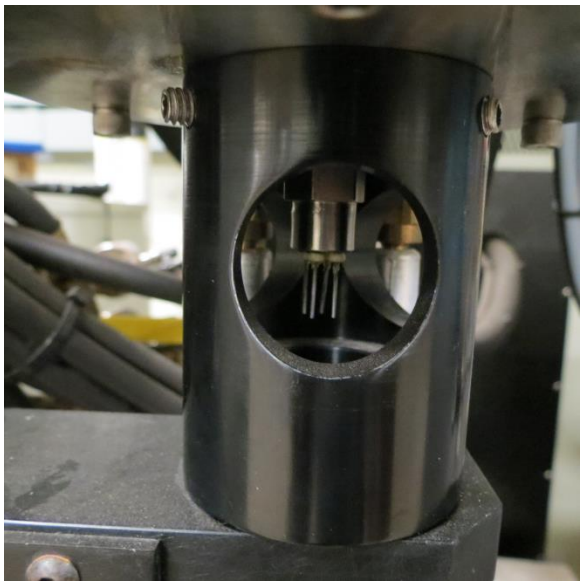

Fig. 24. Underside of the elevator door showing the electrical feedthrough which is attached via a ¼" NPT fitting.

The electrical fixturing in Fig. 23a is supported by an insulating hexagonal BN setter, machined with a conical depression on one side and four holes through the bottom for the tungsten wires (Fig. 25). ZrB_2 contacting bars rest in the cone of the setter and the tungsten wires are pinned into notches produced by EDM (Fig. 25). Fig. 26 offers a better view of the bend in the tungsten wire which hooks into the bar. This bend is put into the W wire by heating the wire on a hot plate to 300°C (a metal plate on the hot surface helps transfer heat) and then slowly working the tungsten around the tip of a needle nose pliers like a mandrel. Attempts to bend the wire without heating can be successful but are more problematic.

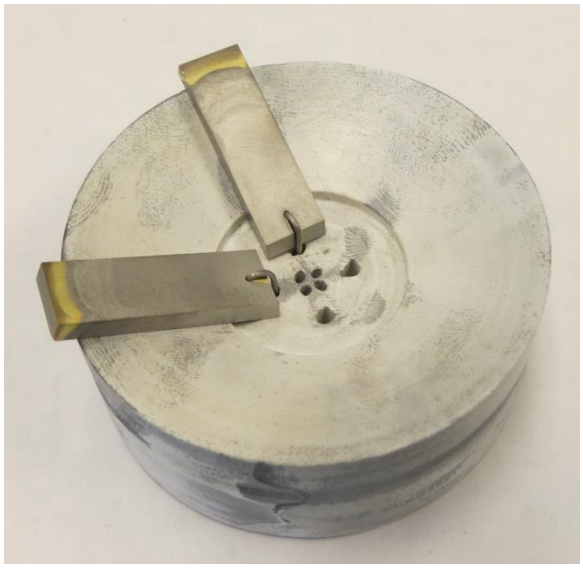

Fig. 26. Boron nitride setter with ZrB_2 contacting bars set in the conical depression. The bars can also be seen with tungsten wires inserted.

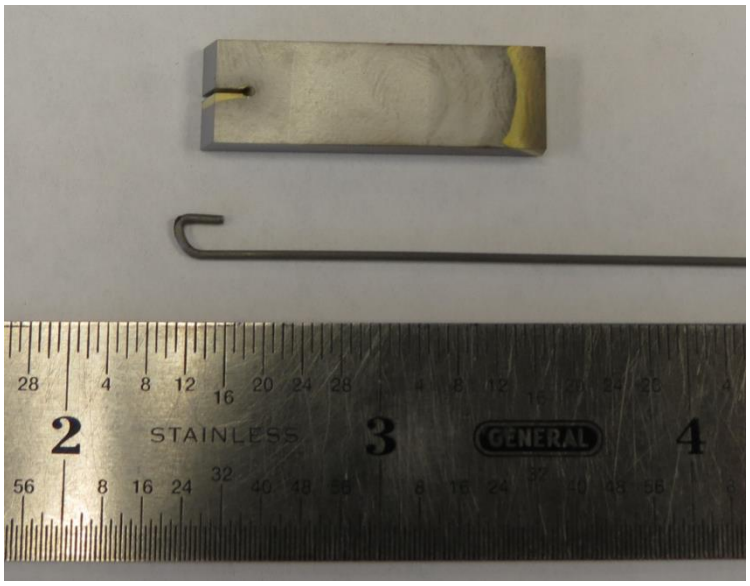

Fig. 26. ZrB_2 contacting bar and bent tungsten wire.

With the two other contacting bars in place the specimen is supported above them by a boron nitride “table top” and boron nitride shims, as necessary (Fig. 27.). ZrB_2 rollers are then used to make electrical contact between the specimen and the four contacting bars (Fig. 28.) The design of the rollers on the sloped bars allows for gravity to maintain the contacts, giving a way to compensate for thermal expansion of the

system. It should be noted that a similar setup has also been used which utilizes copper wires, bars, and rollers. This setup has been primarily used for low temperatures up to 800°C as the copper stays “clean” more easily than ZrB_2 in the low temperature furnace environment. The high temperature setup with the tungsten and ZrB_2 has been used successfully up to 1860°C but has been taken to 2000°C in attempts to make measurements.

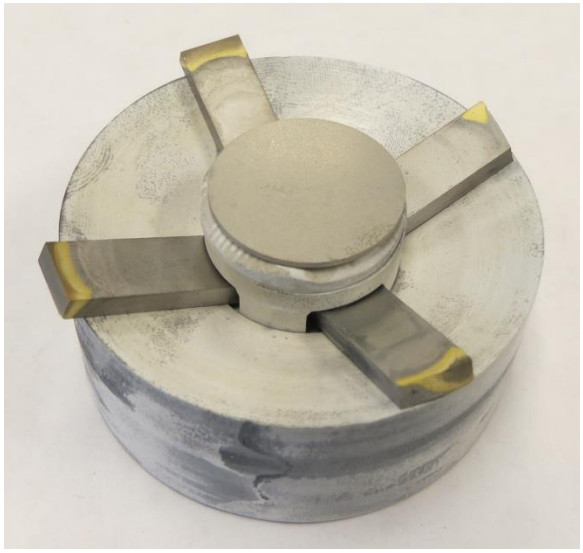

Fig. 27. The setter with all four bars, the sample support and sample.

Fig. 28. The completed electrical resistivity fixturing showing the ZrB_2 rollers in contact with the sample and their respective contacting bars.

Elevated temperature electrical testing is typically done under either Ar or He. In addition, either gas can be passed through the installed getter which utilizes Ti turnings in a quartz tube which are heated to 800°C. This furnace has been calibrated with an external thermocouple, which did not match the temperature displayed by the gauge.

Temperature measurement ≤800°C has utilized an extended length k-type thermocouple inserted through the main thermocouple feed through at the top of the furnace. This thermocouple is typically brought into direct contact and then backed off (~0.5”) to remain close to the sample but with more than enough room for thermal expansion. Manual operation of the furnace at temperatures below 400°C works best as the furnace is slow to respond at these temperatures. High temperature operation utilizes a shorter c-type thermocouple in place of the k-type. The thermocouple will remain inserted up until 1400°C at which point the optical pyrometer attached to the back of the furnace will take over full control.

Concluding Remarks and Areas to Improve

This concludes the overview of the electrical testing setup. The details given are by no means complete but they should aid in familiarization with equipment as it has been established. This is by no means a flawless system but trial and error has driven it to its current form.

Several improvements could make setup and testing better for future researchers. The use of thinner tungsten wire could allow forming the needed bends to be faster with less necessity for the application of heat. Molybdenum wire is also another possibility to try. ZrB_2 bars were chosen due to their compatibility with boron nitride (bloating of the tungsten wires where they pass through the setter had been noticed) and ZrB_2 rollers were used to prevent possible inter-diffusion between the ZrB_2 specimens and the possible choices for refractory materials. However, at temperatures below 950 to 1000°C the ZrB_2 tends to oxidize. Tungsten rollers could prove effective and cladding the ZrB_2 bars with a piece of tungsten sheet may keep the contacts in better shape through the entire temperature range.

The electrical testing could be improved by implementing more automation in the process. LabVIEW could be modified to automatically switch the testing current so that the user would not need to interact with the testing every few minutes. In addition, with the correct DAQ, LabVIEW would be able control a set of electronic switches which could replace the rotary switch. With these two modifications, the user could establish the temperature hold and set the program to test multiple currents, while switching through the eight permutation of the van der Pauw method. This would free up valuable time as each test takes 30 to 45 minutes depending on the length of the on/off cycles. Finally, use of Excel is by no means the ideal way to analyze the raw output data. A level of programming experience would be required but software that could take in and

process the raw data automatically would go a long way in streamlining the testing process.

REFERENCES

1. E. Rudy and S. Windisch, ACerS-NIST, *Figure 08824 - Zr-B System*, *ACerS-NIST Phase Equilibria Diagrams. CD-ROM Database, Ver. 3.0.1,* Westerville, OH, (2004).

2. W.G. Fahrenholtz, G.E. Hilmas, I.G. Talmy, and J.A. Zaykoski, "Refractory Diborides of Zirconium and Hafnium," *J. Am. Ceram. Soc.,* **90** [5] 1347-64 (2007).

3. C. Mroz, "Zirconium Diboride," *Am. Ceram. Soc. Bull.,* **73** [6] 141-2 (1994).

4. N. Kaji, H. Shikano, and I. Tanaka, "Develpment of ZrB_2-Graphite Protective Sleeve for Submerged Nozzle," *Taikabutsu Overseas,* **14** [2] 39-43 (1992).

5. A.L. Chamberlain, W.G. Fahrenholtz, G.E. Hilmas, and D.T. Ellerby, "High-Strength Zirconium Diboride-Based Ceramics," *J. Am. Ceram. Soc.,* **87** [6] 1170-2 (2004).

6. P. Rogl and H. Bittermann, "On the Ternary System Hafnium–Boron–Carbon," *J. Solid State Chem.,* **154** [1] 257-62 (2000).

7. *Ceradyne Boron Products LLC., Ceradyne, Inc. Announces $18.3 Million Contract Award for Enriched Zirconiumm Diboride*, http://www.ceradyneboron.com/news/newsreleasedetails.aspx?id=221, (2011).

8. V.A. Gasparov and A. Suslov, "Electron Transport and Superconducting Properties of ZrB_{12}, ZrB_2 and MgB_2," *AIP Conference Proceedings,* **850** [1] 637-8 (2006).

9. N.L. Okamoto, M. Kusakari, K. Tanaka, H. Inui, M. Yamaguchi, and S. Otani, "Temperature dependence of thermal expansion and elastic constants of single crystals of ZrB_2 and the suitability of ZrB_2 as a substrate for GaN film," *J. Appl. Phys.,* **93** [1] 88-93 (2003).

10. E.W. Neuman, G.E. Hilmas, and W.G. Fahrenholtz, "Strength of Zirconium Diboride to 2300°C," *J. Am. Ceram. Soc.,* **96** [1] 47-50 (2013).

11. M.M. Opeka, I.G. Talmy, and J.A. Zaykoski, "Oxidation-based materials selection for 2000°C + hypersonic aerosurfaces: Theoretical considerations and historical experience," *J. Mater. Sci.,* **39** [19] 5887-904 (2004).

12. M.J. Gasch, D.T. Ellerby, and S.M. Johnson, "Ultra High Temperature Ceramic Composites," pp. 197-224 in *Handbook of Ceramic Composites.* Edited by N.P. Bansal. Springer, New York, 2005.

13. E. Wuchina, E. Opila, M. Opeka, W. Fahrenholtz, and I. Talmy, "UHTCs: ultra-high temperature ceramic materials for extreme environment applications," *The Electrochemical Society Interface,* **16** [4] 30 (2007).

14. T.R.F. Nonweiler, "Heat shield design for re-entry and launch. The use of conduction-assisted radiation on sharp-edged wings," *Philosophical Transactions of the Royal Society of London. Series A: Mathematical, Physical and Engineering Sciences,* **357** [1759] 2197-225 (1999).

15. T.H. Squire and J. Marschall, "Material property requirements for analysis and design of UHTC components in hypersonic applications," *J. Eur. Ceram. Soc.,* **30** [11] 2239-51.

16. D.M. Van Wie, D.G. Drewry, D.E. King, and C.M. Hudson, "The hypersonic environment: Required operating conditions and design challenges," *J. Mater. Sci.,* **39** [19] 5915-24 (2004).

17. W.D. Kingery, "Factors Affecting Thermal Stress Resistance of Ceramic Materials," *J. Am. Ceram. Soc.,* **38** [1] 3-15 (1955).

18. S. Guo, T. Nishimura, and Y. Kagawa, "Preparation of zirconium diboride ceramics by reactive spark plasma sintering of zirconium hydride-boron powders," *Scripta Mater.,* **65** [11] 1018-21 (2011).

19. D.L. McClane, W.G. Fahrenholtz, and G.E. Hilmas, "Thermal Properties of (Zr,TM)B_2 Solid Solutions with TM = Hf, Nb, W, Ti, and Y," *J. Am. Ceram. Soc.,* **97** [5] 1552-8 (2014).

20. B.A. Fridlender, V.S. Neshpor, S.S. Ordan'yan, and V.I. Unrod, "Thermal Conductivity and Diffusivity of Binary Alloys of the ZrC-ZrB_2 System at High Temperatures," *High Temperature,* **17** [6] 1001-5 (1980).

21. E.V. Clougherty, K.E. Wilkes, and R.P. Tye, "Research and Development of Refractory Oxidation-Resistant Diborides, Part II, Volume V: Thermal, Physical, Electrical, and Optical Properties," *Air Force Materials Laboratory, Air Force Systems Command, Wright-Patterson Air Force Base, Ohio, Technical Report AFML-TR-68-190, Part II, Volume V,* (1969).

22. H.M. Chen, F. Zheng, H.S. Liu, L.B. Liu, and Z.P. Jin, ACerS-NIST, *Figure 14217 - Zr-B System*, *ACerS-NIST Phase Equilibria Diagrams. CD-ROM Database, Ver. 3.0.1,* Westerville, OH, (2004).

23. T. Tokunaga, K. Terashima, H. Ohtani, and M. Hasebe, ACerS-NIST, *Figure 14141 - Zr-B System*, *ACerS-NIST Phase Equilibria Diagrams. CD-ROM Database, Ver. 3.0.1,* Westerville, OH, (2004).

24. P. Rogl and P.E. Potter, ACerS-NIST, *Figure 08825 - Zr-B System*, *ACerS-NIST Phase Equilibria Diagrams. CD-ROM Database, Ver. 3.0.1,* Westerville, OH, (2004).

25. D.D. Radev and M. Marinov, "Properties of titanium and zirconium diborides obtained by self-propagated high-temperature synthesis," *J. Alloys Compd.,* **244** [1–2] 48-51 (1996).

26. E.A. Knyshev, V.M. Novgorodtsev, U.S. Plyshevski, V.A. Kobyakov, Z.G. Stepanova, V.V. Svistunov, and A.R. Becketov, "Synthesis of transition metal borides and their properties," *J Less Common MET,* **47** [0] 273-8 (1976).

27. S. Ran, O. Van Der Biest, and J. Vleugels, "ZrB_2 Powders Synthesis by Borothermal Reduction," *J. Am. Ceram. Soc.,* **93** [6] 1586-90 (2010).

28. P. Peshev and G. Bliznakov, "On the borothermic preparation of titanium, zirconium and hafnium diborides," *J Less Common MET,* **14** [1] 23-32 (1968).

29. R. Thompson, "Production, Fabrication and Uses of Borides," pp. 113-20 in NATO ASI Series, Vol. 185, *The Physics and Chemistry of Carbides, Nitrides and Borides.* Edited by R. Freer. Springer Netherlands, 8, 1990.

30. A.I. Karasev, "Preparation of technical zirconium diboride by the carbothermic reduction of mixtures of zirconium and boron oxides," *Sov. Powder Metall.,* **12** [11] 926-9 (1973).

31. S.K. Mishra, S. Das, and L.C. Pathak, "Defect structures in zirconium diboride powder prepared by self-propagating high-temperature synthesis," *Materials Science and Engineering: A,* **364** [1–2] 249-55 (2004).

32. V.F. Funke and S.I. Yudkovskii, "Preparation of zirconium boride," *Sov. Powder Metall.,* **2** [4] 293-6 (1964).

33. H. Zhao, Y. He, and Z. Jin, "Preparation of Zirconium Boride Powder," *J. Am. Ceram. Soc.,* **78** [9] 2534-6 (1995).

34. W.-M. Guo and G.-J. Zhang, "Reaction Processes and Characterization of ZrB_2 Powder Prepared by Boro/Carbothermal Reduction of ZrO_2 in Vacuum," *J. Am. Ceram. Soc.,* **92** [1] 264-7 (2009).

35. C.B. Carter and G. Norton, *Ceramic Materials: Science and Engineering*. Springer, 2013.

36. T. Lundstrom, "Transition Metal Borides," in *Boron and Refractory Borides.* Edited by G.V. Samsonov, P. Hagenmuller, V.I. Matkovich, and T. Lundstrom. Springer London, Limited, 2012.

37. C. Mroz, "Processing and Properties of Microcomposite TiZrC and $TiZrB_2$ Materials," *Am. Ceram. Soc. Bull.,* **73** [4] 78-81 (1994).

38. D. Sciti, S. Guicciardi, A. Bellosi, and G. Pezzotti, "Properties of a Pressureless-Sintered ZrB_2–$MoSi_2$ Ceramic Composite," *J. Am. Ceram. Soc.,* **89** [7] 2320-2 (2006).

39. S.-H. Lee, Y. Sakka, and Y. Kagawa, "Dispersion Behavior of ZrB_2 Powder in Aqueous Solution," *J. Am. Ceram. Soc.,* **90** [11] 3455-9 (2007).

40. T. Baldridge, M.C. Gupta, and C.-N. Sun, "Nanostructures from Zirconium Diboride and Alumina Ceramics," *J. Am. Ceram. Soc.,* **93** [9] 2891-6 (2010).

41. Treibacher Industrie Ag, *Zircnoium Diboride data sheet/chemical analysis*.

42. "Fundamentals: Hafnium," *Metal Bulliten Monthly,* 44-5 (2007).

43. S.F. Mughavghav, "Thermal Neutron Capture Cross Sections Resonance Intergrals and G-Factors," *INDC(NDS)-440,* (2003).

44. S. Otani, T. Aizawa, and N. Kieda, "Solid solution ranges of zirconium diboride with other refractory diborides: HfB_2, TiB_2, TaB_2, NbB_2, VB_2 and CrB_2," *J. Alloys Compd.,* **475** [1–2] 273-5 (2009).

45. B. Post, F.W. Glaser, and D. Moskowitz, "Transition metal diborides," *Acta Metall.,* **2** [1] 20-5 (1954).

46. P.S. Kisliy, M.A. Kuzenkova, and O.V. Zaveruha, "On the Sintering Process of Zirconium Diboride with Tungsten," *Physics of Sintering,* **3** [1] 29-44 (1971).

47. E. Rudy and S. Windisch, ACerS-NIST, *Figure 08874-C - ZrB_2-C Binary*, *ACerS-NIST Phase Equilibria Diagrams. CD-ROM Database, Ver. 3.0.1,* Westerville, OH, (2004).

48. E. Rudy and S. Windisch, ACerS-NIST, *Figure 08874-D - ZrB_2-B_4C Binary*, *ACerS-NIST Phase Equilibria Diagrams. CD-ROM Database, Ver. 3.0.1,* Westerville, OH, (2004).

49. S.S. Ordan'yan and V. Unrod, ACerS-NIST, *Figure 08875 - ZrB_2-ZrC - Quasibinary phase diagram*, *ACerS-NIST Phase Equilibria Diagrams. CD-ROM Database, Ver. 3.0.1,* Westerville, OH, (2004).

50. H.P. Klug and L.E. Alexander, *X-Ray Diffraction Procedures: For Polycrystalline and Amorphous Materials*. Wiley, New York, 1974.

51. J. Goldstein, D.E. Newbury, P. Echlin, D.C. Joy, A.D. Romig, C.E. Lyman, C. Fiori, and E. Lifshin, *Scanning Electron Microscopy and X-Ray Microanalysis,* Third ed. Springer US, 2003.

52. W.H. Weber and R. Merlin, *Raman Scattering in Materials Science*. Edited by R. Hull, R.M. Osgood Jr., H. Sakaki, and A. Zunger. Springer, New York, 2000.

53. H.A. Szymanski, *Raman Spectroscopy: Theory and Practice,* Vol. 2. Plenum Press, New York, 1970.

54. D.J. Gardiner, P.R. Graves, and H.J. Bowley, *Practical Raman spectroscopy*. Springer-Verlag, 1989.

55. D.A. Long, *The Raman Effect: A Unified Treatment of the Theory of Raman Scattering by Molecules*. Wiley, 2002.

56. H. Werheit, U. Kuhlmann, H.W. Rotter, and S.O. Shalamberidze, "Isotopic effects on the phonon modes in boron carbide," *Journal of physics. Condensed matter : an Institute of Physics journal,* **22** [39] 395401 (2010).

57. H. Werheit, *Boron compounds, Landolt-Borstein,* Vol. 41D*;* pp. 1-491. Springer, Berlin, 2000.

58. U. Kuhlmann and H. Werheit, "Raman effect of boron carbide ($B_{4.3}C$ to $B_{10.37}C$)," *J. Alloys Compd.,* **205** [1–2] 87-91 (1994).

59. D.R. Tallant, T.L. Aselage, A.N. Campbell, and D. Emin, "Boron carbide structure by Raman spectroscopy," *Physical review. B, Condensed matter,* **40** [8] 5649-56 (1989).

60. H.J. Brown-Shaklee, W.G. Fahrenholtz, and G.E. Hilmas, "Densification Behavior and Microstructure Evolution of Hot-Pressed HfB_2," *J. Am. Ceram. Soc.,* **94** [1] 49-58 (2011).

61. M.J. Thompson, W.G. Fahrenholtz, and G.E. Hilmas, "Elevated Temperature Thermal Properties of ZrB_2 with Carbon Additions," *J. Am. Ceram. Soc.,* **95** [3] 1077-85 (2012).

62. A.C. Ferrari and J. Robertson, "Interpretation of Raman spectra of disordered and amorphous carbon," *Phys. Rev. B,* **61** [20] 14095-107 (2000).

63. E. Antunes, A. Lobo, E. Corat, V. Trava-Airoldi, A. Martin, and C. Verissimo, "Comparative study of first-and second-order Raman spectra of MWCNT at visible and infrared laser excitation," *Carbon,* **44** [11] 2202-11 (2006).

64. P. Vajeeston, P. Ravindran, C. Ravi, and R. Asokamani, "Electronic structure, bonding, and ground-state properties of AlB_2-type transition-metal diborides," *Phys. Rev. B,* **63** [4] 045115-(1-12) (2001).

65. K.E. Spear, "Chemical bonding in AlB_2-type borides," *J Less Common MET,* **47** [0] 195-201 (1976).

66. I.R. Shein and A.L. Ivanovskii, "Band structure of ZrB_2, VB_2, NbB_2, and TaB_2 hexagonal diborides: Comparison with superconducting MgB_2," *PhSS,* **44** [10] 1833-9 (2002).

67. W. Chu, Z. Wu, W. Liu, N.L. Saini, A. Bianconi, T. Hu, and Y. Xie, "Lattice dynamics study of AlB2-type 4d transition-metal diborides by extended X-ray-absorption fine structure," *Radiat. Phys. Chem.,* **75** [11] 2080-4 (2006).

68. R.E. Newnham, *Properties of Materials : Anisotropy, Symmetry, Structure: Anisotropy, Symmetry, Structure*. OUP Oxford, 2004.

69. X. Zhang, X. Luo, J. Han, J. Li, and W. Han, "Electronic structure, elasticity and hardness of diborides of zirconium and hafnium: First principles calculations," *Computational Materials Science,* **44** [2] 411-21 (2008).

70. S.M. Sichkar, V.N. Antonov, and V.P. Antropov, "Comparative study of the electronic structure, phonon spectra, and electron-phonon interaction of ZrB_2 and TiB_2," *Phys. Rev. B,* **87** [6] 064305 (2013).

71. J.W. Lawson, C.W. Bauschlicher, and M.S. Daw, "Ab Initio Computations of Electronic, Mechanical, and Thermal Properties of ZrB_2 and HfB_2," *J. Am. Ceram. Soc.,* **94** [10] 3494-9 (2011).

72. M.A. Kuzenkova and P.S. Kislyi, "The mechanism of shrinkage of zirconium diboride during sintering," *Sov. Powder Metall.,* **5** [2] 114-21 (1966).

73. W.G. Fahrenholtz, G.E. Hilmas, S.C. Zhang, and S. Zhu, "Pressureless Sintering of Zirconium Diboride: Particle Size and Additive Effects," *J. Am. Ceram. Soc.,* **91** [5] 1398-404 (2008).

74. M.N. Rahaman, *Ceramic Processing*. CRC/Taylor & Francis, Boca Raton, 2007.

75. R. Hayami, M. Iwasa, and M. Kinoshita, "Effects of Applied Pressure on Hot-Pressing of ZrB_2," *Journal of the Ceramic Association, Japan,* **86** [996] 352-9 (1978).

76. M. Thompson, W.G. Fahrenholtz, and G. Hilmas, "Effect of Starting Particle Size and Oxygen Content on Densification of ZrB_2," *J. Am. Ceram. Soc.,* **94** [2] 429-35 (2011).

77. S.L. Dole, S. Prochazka, and R.H. Doremus, "Microstructural Coarsening During Sintering of Boron Carbide," *J. Am. Ceram. Soc.,* **72** [6] 958-66 (1989).

78. S. Baik and P.F. Becher, "Effect of Oxygen Contamination on Densification of TiB_2," *J. Am. Ceram. Soc.,* **70** [8] 527-30 (1987).

79. S. Zhu, W.G. Fahrenholtz, G.E. Hilmas, and S.C. Zhang, "Pressureless sintering of carbon-coated zirconium diboride powders," *Materials Science and Engineering: A,* **459** [1–2] 167-71 (2007).

80. S. Zhu, W.G. Fahrenholtz, G.E. Hilmas, and S.C. Zhang, "Pressureless Sintering of Zirconium Diboride Using Boron Carbide and Carbon Additions," *J. Am. Ceram. Soc.,* **90** [11] 3660-3 (2007).

81. S.C. Zhang, G.E. Hilmas, and W.G. Fahrenholtz, "Pressureless Densification of Zirconium Diboride with Boron Carbide Additions," *J. Am. Ceram. Soc.,* **89** [5] 1544-50 (2006).

82. S. Zhu, "Densification, Microstructure, and Mechanical Properties of Zirconium Diboride Based Ultra-High Temperature Ceramics"; PhD Thesis. Missouri University of Science and Technology, 2008.

83. S.M. Kats, S.S. Ordan'yan, and V.I. Unrod, "Compressive creep of alloys of the ZrC-ZrB2 and TiC-TiB2 systems," *Sov. Powder Metall.,* **20** [12] 886-90 (1981).

84. V.M. Gropyanov and L.M. Bel'tyukova, "Sintering and recrystallization of ZrC-ZrB_2 compacts," *Sov. Powder Metall.,* **7** [7] 527-33 (1968).

85. E.W. Neuman, "Elevated Temperature Mechanical Properties of Zirconium Diboride Based Ceramics"; PhD Thesis. Missouri University of Science and Technology, 2014.

86. T. Tsuchida and S. Yamamoto, "Spark plasma sintering of ZrB_2–ZrC powder mixtures synthesized by MA-SHS in air," *J. Mater. Sci.,* **42** [3] 772-8 (2007).

87. M.J. Thompson, "Densification and Thermal Properties of Zirconium Diboride Based Ceramics"; PhD Thesis. Missouri University of Science and Technology, 2012.

88. A.L. Chamberlain, W.G. Fahrenholtz, and G.E. Hilmas, "Pressureless Sintering of Zirconium Diboride," *J. Am. Ceram. Soc.,* **89** [2] 450-6 (2006).

89. J.W. Zimmermann, G.E. Hilmas, W.G. Fahrenholtz, R.B. Dinwiddie, W.D. Porter, and H. Wang, "Thermophysical Properties of ZrB_2 and ZrB_2–SiC Ceramics," *J. Am. Ceram. Soc.,* **91** [5] 1405-11 (2008).

90. S.-K. Choi, S.-W. Ui, I.-S. Choi, and S.-C. Choi, "Densification behavior of ZrB_2 with Co-WC as additives," *J. Ceram. Soc. Jpn.,* **122** [1423] 198-203 (2014).

91. A. Bellosi and F. Monteverde, "Fabrication and Properties of Zirconium Diboride-based Ceramics for UHT Applications," *Proc. 4th European Workshop, 'Hot Structures and Thermal Protection Systems for Space Vehicles',* 26-9 (2002).

92. N.W. Ashcroft and N.D. Mermin, *Solid State Physics*. Cengage Learning, 2011.

93. C. Uher, "Thermal Conductivity of Metals," pp. 21-91 in *Thermal Conductivity: Theory, Properties, and Applications.* Edited by T.M. Tritt. Springer, 1.2, 2004.

94. G.S. Kumar, G. Prasad, and R.O. Pohl, "Experimental determinations of the Lorenz number," *J. Mater. Sci.,* **28** [16] 4261-72 (1993).

95. G. Grimvall, *Thermophysical Properties of Materials*. Elsevier Science, 1999.

96. Y. Kumashiro, *Electric Refractory Materials*. Taylor & Francis, 2000.

97. F.J. Blatt, *Physics of electronic conduction in solids*. McGraw-Hill, 1968.

98. G.A. Slack, "The Thermal Conductivity of Nonmetallic Crystals," pp. 1-71 in Vol. Volume 34, *Solid State Physics.* Edited by F.S. Henry Ehrenreich and T. David. Academic Press, 1979.

99. W.D. Kingery, H.K. Bowen, and D.R. Uhlmann, *Introduction to ceramics*. John Wiley and Sons, New York, 1976.

100. G.V. Samsonov and V.S. Sinel'nikova, "The resistivity of refractory compounds at high temperatures," *Sov. Powder Metall.,* **1** [4] 272-4 (1962).

101. L. Zhang, D.A. Pejaković, J. Marschall, and M. Gasch, "Thermal and Electrical Transport Properties of Spark Plasma-Sintered HfB_2 and ZrB_2 Ceramics," *J. Am. Ceram. Soc.,* **94** [8] 2562-70 (2011).

102. L. Fail, "Narcolepsy and neurosis," *Med. J. Aust.,* **2** [5] 223-5 (1973).

103. M. Rahman, C.C. Wang, W. Chen, S.A. Akbar, and C. Mroz, "Electrical Resistivity of Titanium Diboride and Zirconium Diboride," *J. Am. Ceram. Soc.,* **78** [5] 1380-2 (1995).

104. L.J. Van Der Pauw, "A method of measuring specific resistivity and Hall effect of discs of arbitrary shape," *Philips Res.Rep,* **13** [1] (1958).

105. *ASTM Standard F76, 2008, "Standard Test Methods for Measuring Resistivity and Hall Coefficient and Determining Hall Mobility in Single-Crystal Semiconductors"*. ASTM International, West Conshohocken, PA, 2008, DOI: 10.1520/F0076-08.

106. S.J. Sindeband and P. Schwarzkopf, "The Metallic Nature of Metal Diborides," *Powder Metallurgy Bulletin,* **5** [3] 42-3 (1950).

107. D.S. Neel, C.D. Pears, and S. Oglesby Jr., "The Thermal Properties of Thirteen Solid Materials to 5000°F for Thier Destruction Temperatures," *Contract No. AF 33(616)-6312, Southern Research Institute, WADD TR 60-924, February,* (1962).

108. G.V. Samsonov, B.A. Kovenskaya, T.I. Serebryakova, and E.Y. Tel'nikov, "Thermal Conductivity of Diborides of Group IV-VI Transition Metals," *High Temp,* **10** [6] 1193-5 (1972).

109. T.M. Branscomb and J.O. Hunter, "Improved Thermal Diffusivity Method Applied to TiB_2, ZrB_2, and HfB_2 from 200°--1300°C," *J. Appl. Phys.,* **42** [6] 2309-15 (1971).

110. R.A. Andrievskii, L.A. Korolev, V.V. Klimenko, A.G. Lanin, I.I. Spivak, and I.L. Taubin, "Effect of zirconium carbide and carbon additions on some physicomechanical properties of zirconium diboride," *Powder Metall. Met. Ceram.,* **19** [2] 93-4 (1980).

111. H. Kinoshita, S. Otani, S. Kamiyama, H. Amano, I. Akasaki, J. Suda, and H. Matsunami, "Zirconium diboride (0001) as an electrically conductive lattice-matched substrate for gallium nitride," *Japanese Journal of Applied Physics, Part 2: Letters,* **40** [12 A] L1280-L2 (2001).

112. R. Loehman, E. Corral, H.P. Dumm, P. Kotula, and R. Tandon, "Ultra High Temperature Ceramics for Hypersonic Vehicle Applications," *Sandia Report (SAND 206-2925), Sandia National Laboratories, Albuquerquie, New Mexico and Livermore, California,* (2006).

113. M. Ikegami, K. Matsumura, S.Q. Guo, Y. Kagawa, and J.M. Yang, "Effect of SiC particle dispersion on thermal properties of SiC particle-dispersed ZrB_2 matrix composites," *J. Mater. Sci.,* **45** [19] 5420-3 (2010).

114. A. Snyder, Z. Bo, S. Hodson, T. Fisher, and L. Stanciu, "The effect of heating rate and composition on the properties of spark plasma sintered zirconium diboride based composites," *Materials Science and Engineering: A,* **538** [0] 98-102 (2012).

115. D. McClane, W.G. Fahrenholtz, and G.E. Hilmas, "Thermal Properties of Zirconium Diboride with Transition Metal Diboride Additions," *J. Am. Ceram. Soc.,* (2013).

116. W.J. Parker, R.J. Jenkins, C.P. Butler, and G.L. Abbott, "Flash Method of Determining Thermal Diffusivity, Heat Capacity, and Thermal Conductivity," *J. Appl. Phys.,* **32** [9] 1679-84 (1961).

117. T.M. Tritt and D. Weston, "Measurement Techniques and Considerations for Determing Thermal Conductivity of Bulk Materials," pp. 187-203 in *Thermal Conductivity: Theory, Properties, and Applications.* Edited by T.M. Tritt. Springer, 2.1, 2004.

118. R.D. Cowan, "Pulse Method of Measuring Thermal Diffusivity at High Temperatures," *J. Appl. Phys.,* **34** [4] 926-7 (1963).

119. L.M. Clark Iii and R.E. Taylor, "Radiation loss in the flash method for thermal diffusivity," *J. Appl. Phys.,* **46** [2] 714-9 (1975).

120. R.C. Heckman, *Error analysis of the flash thermal diffusivity technique;* p. Medium: ED; Size: Pages: 21. 1973.

121. J.A. Koski, "Improved Data Reduction Method for Laser Pulse Diffusivity Determination with the Use of Minicomputers," in *8th Symposium on Thermophysical Properties.* The American Society of Mechanical Engineers, 1981.

122. H.L. Schick , Avco Corporation Research and Advanced Development Division, Air Force Materials Laboratory. Materials Physics Division, *Thermodynamics of certain refractory compounds*. Edited by A.F.M.L.M.P.D. Avco Corporation Research and Advanced Development Division. Academic Press, New York, 1966.

123. A.S. Bolgar, E.A. Guseva, A.G. Turchanin, and V.V. Fesenko, *"Thermodynamic properties of zirconium diboride," in: Thermophysical Propeties of Solid Substances [in Russian]*. Nauka, Moscow, 130-132, 1976.

124. M.W. Chase, *NIST-JANAF Thermochemical Tables. American Chemical Society and the American Institute of Physics,* 4th ed.*;* p. 1951. Woodbury, NY, 1998.

125. A. Roine, HSC Chemistry for Window, Version 5.11., [Computer Program] Outokumpu Research, Oy, Pori, Finland, 2006.

126. M. Gasch, D. Ellerby, E. Irby, S. Beckman, M. Gusman, and S. Johnson, *Processing, properties and arc jet oxidation of hafnium diboride/silicon carbide ultra high temperature ceramics,* Vol. 39*;* p. 13. Springer, Heidelberg, ALLEMAGNE, 55-60, 2004.

127. D. Gosset, G.-M. Decroix, and B. Kryger, "Improvement of Thermo-Mechanical Properties of Boron-Rich Compounds," *Japanese Journal of Applied Physics, Proceedings of the 11th International Symposium on Boron, Borides, and Related Compounds, Tsukuba, Japan,* 216-19 (1993).

128. K. Shinzato and T. Baba, "A laser flash apparatus for thermal diffusivity and specific heat capacity measurements," *J. Therm. Anal. Calorim.,* **64** [1] 413-22 (2001).

129. *ASTM Standard E1461-13, 2013, "Standard Test Method for Thermal Diffusivity by the Flash Method"*. ASTM International, West Conshohocken, PA, 2013, DOI: 10.1520/E1461-13.

130. Y.S. Touloukian, R.K. Kirby, R.E. Taylor, and P.D. Desai, *Thermal Expansion: Nonmetallic Solids,* Vol. 13. Edited by Y.S. Touloukian. IFI/Plenum, 1977.

131. W.D. Kingery and M.C. Mcquarrie, "Thermal Conductivity: I, Concepts of Measurement and Factors Affecting Thermal Conductivity of Ceramic Materials," *J. Am. Ceram. Soc.,* **37** [2] 67-72 (1954).

132. W. Voigt, *Lehrbuch der kristallphysik,* Vol. 34. BG Teubner, 1910.

133. J.L. Nichols, "Orientation and Temperature Effects on the Electrical Resistivity of High-Purity Magnesium," *J. Appl. Phys.,* **26** [4] 470-2 (1955).

134. H. Zhang, Y. Yan, Z. Huang, X. Liu, and D. Jiang, "Properties of ZrB_2–SiC Ceramics by Pressureless Sintering," *J. Am. Ceram. Soc.,* **92** [7] 1599-602 (2009).

135. Z. Wang, C. Hong, X. Zhang, X. Sun, and J. Han, "Microstructure and thermal shock behavior of ZrB_2–SiC–graphite composite," *Mater. Chem. Phys.,* **113** [1] 338-41 (2009).

136. J. Zou, G.-J. Zhang, H. Zhang, Z.-R. Huang, J. Vleugels, and O. Van Der Biest, "Improving high temperature properties of hot pressed ZrB_2–20vol% SiC ceramic using high purity powders," *Ceram. Int.,* **39** [1] 871-6 (2013).

137. M. Mallik, A.J. Kailath, K.K. Ray, and R. Mitra, "Electrical and thermophysical properties of ZrB_2 and HfB_2 based composites," *J. Eur. Ceram. Soc.,* **32** [10] 2545-55 (2012).

138. W.-B. Tian, Y.-M. Kan, G.-J. Zhang, and P.-L. Wang, "Effect of carbon nanotubes on the properties of ZrB_2–SiC ceramics," *Materials Science and Engineering: A,* **487** [1–2] 568-73 (2008).

139. R. Tu, H. Hirayama, and T. Goto, "Preparation of ZrB_2-SiC composites by arc melting and their properties," *J. Ceram. Soc. Jpn.,* **116** [1351] 431-5 (2008).

140. S. Guo, "Thermal and electrical properties of hot-pressed short pitch-based carbon fiber-reinforced ZrB_2–SiC matrix composites," *Ceram. Int.,* [0] (2013).

141. F. Monteverde, "The addition of SiC particles into a $MoSi_2$-doped ZrB_2 matrix: Effects on densification, microstructure and thermo-physical properties," *Mater. Chem. Phys.,* **113** [2–3] 626-33 (2009).

142. S. Guo, Y. Kagawa, T. Nishimura, and H. Tanaka, "Thermal and Electric Properties in Hot-Pressed ZrB_2–$MoSi_2$–SiC Composites," *J. Am. Ceram. Soc.,* **90** [7] 2255-8 (2007).

143. S.-Q. Guo, Y. Kagawa, T. Nishimura, and H. Tanaka, "Pressureless sintering and physical properties of ZrB_2-based composites with $ZrSi_2$ additive," *Scripta Mater.,* **58** [7] 579-82 (2008).

144. S.R.P. Silva, *Properties of amorphous carbon*. INSPEC, London, 158-162, 2003.

145. D. Lide, *CRC Handbook of Chemistry and Physics,* 88th ed. CRC, Boca Raton, 2007.

146. T. Dasgupta and A.M. Umarji, "Thermal properties of $MoSi_2$ with minor aluminum substitutions," *Intermetallics,* **15** [2] 128-32 (2007).

147. R.P. Tye and E.V. Clougherty, "The Thermal and Electrical Conductivities of Some Electrically Conducting Compounds," *Proceedings of the Fifth Symposium on Thermophysical Properties, Newton Massachusetts, September 30 - October 2,* 396-401 (1970).

148. K.C. Lukas, W.S. Liu, G. Joshi, M. Zebarjadi, M.S. Dresselhaus, Z.F. Ren, G. Chen, and C.P. Opeil, "Experimental determination of the Lorenz number in $Cu_{0.01}Bi_2Te_{2.7}Se_{0.3}$ and $Bi_{0.88}Sb_{0.12}$," *Phys. Rev. B,* **85** [20] 205410 (2012).

149. R.G. Sharma, M.S.R. Chari, and D.K. Reddy, "The electronic Lorenz number in some transition metals at high temperatures," *J. Phys. F,* **16** [5] 603-7 (1986).

150. P.E.D. Morgan, "Wiedemann-Franz-Lorenz Relation in Metallic Conducting Ceramics," *J. Am. Ceram. Soc.,* **58** [7-8] 349 (1975).

VITA

Greg Harrington was born on August 12, 1985 in Michigan City, Indiana. He lived in Union Mills, Indiana until 2004 when he graduated from South Central High School. In the fall of 2004, Greg enrolled in Freshmen Engineering at Purdue University in West Lafayette, Indiana. By spring, he had selected Materials Science and Engineering as his official major. During his five years at Purdue, Greg spent four rotations as a co-op student, working at GE Aviation in Cincinnati, Ohio. In the spring of 2006, he joined the Purdue chapter of Triangle Fraternity and would become the financial director during his senior year.

In 2007 Greg met his future wife, Heather, while taking summer classes at Purdue. Greg spent the summer before his senior year interning at Littelfuse Inc. in Des Plaines, Illinois. After graduating from Purdue in 2009, he and Heather moved to Rolla so he could begin his graduate research at Missouri University of Science and Technology. Under the advisement of Drs. Gregory E. Hilmas and William G. Fahrenholtz, Greg would study the thermal properties of ultra-high temperature ceramics with a focus on zirconium diboride. While at MST he presented his work nationally and internationally at seven conferences, has published one manuscript with four pending and coauthored a book chapter. Heather and Greg married on April 28th, 2012 and almost a year later on April 26th, 2013 they had their first child, Owen Gregory. In December 2014, Greg earned his Ph.D. in Ceramic Engineering at Missouri University of Science and Technology. After his time in Rolla, Greg moved with family to Oregon to work as a process engineer in the D1D Fab at Intel in Hillsboro, Oregon.